Conductance Quantization of Massless Dirac Fermions and the Synthesis, Characterization, and Manipulation of Graphene

by

Caglar Girit

A dissertation submitted in partial satisfaction of the

requirements for the degree of

Doctor of Philosophy

in

Physics

in the

Graduate Division

of the

University of California, Berkeley

Committee in charge:

Professor A. Zettl, Chair

Professor Irfan Siddiqi

Professor Jeffrey Bokor

Spring 2010

Conductance Quantization of Massless Dirac Fermions and the Synthesis, Characterization, and Manipulation of Graphene

Caglar Girit

Abstract

Conductance Quantization of Massless Dirac Fermions and the Synthesis, Characterization, and Manipulation of Graphene

by

Caglar Girit

Doctor of Philosophy in Physics

University of California, Berkeley

Professor A. Zettl, Chair

Graphene, a two-dimensional carbon allotrope, has interesting electronic properties resulting from its unique hexagonal mono-atomic lattice. Electronic quasiparticles in graphene, called massless Dirac fermions, are described by the Weyl equation in which the effective speed of light is the Fermi velocity, approximately $c/300$. Thus graphene provides a solid-state system in which to study the physics of high-energy electrons or neutrinos, including interesting relativistic quantum phenomena such as Zitterbewugung, atomic collapse, and Klein tunneling. The comparison of graphene's quasiparticles to free space neutrinos is limited by the fact that scattering in the solid reduces the mean free path to about a micron. However, by fabricating clean graphene devices with closely spaced electrodes, one can probe the intrinsic properties of massless Dirac fermions in the ballistic regime where these quasiparticles do not undergo scattering.

The theory of the Dirac equation, the band structure of graphene, and the Landauer formalism for electronic transport is explained. Techniques are presented for the extraction of graphene, synthesis of chemical-vapor deposited graphene, and fabrication of graphene devices for both characterization and electronic transport measurements. The various characterization methods include Raman spectroscopy, atomic force microscopy, and transmission electron microscopy. Experiments approaching the ballistic transport limit in graphene devices such as point contacts, Josephson junctions, and short-and-wide junctions are described.

For my father,
Cem Girit,
who answered "Why?"

Contents

List of Figures

Acknowledgments

Above all to those who made graduate school possible. Claire Wyart, who supported me from the beginning in countless ways, through hardship and happiness. The National Science Foundation, whose Graduate Research Fellowship turned the tables. Anne Takizawa, who listened, understood, and connected the pieces. To my family: Claire, the ever-shining sun and source of mischief, a wonderful partner, mother, and child; Uzay, as old as my graduate studentship, kind curious and sage, who played games and watched cartoons with me at the end of the day; (Lou), the little daughter to be, ending this chapter and opening the next. To my parents, Emel and Cem, who will never be thanked enough by ungrateful children, and who are always willing to give more. It started with you: dinnertime questions and fun with liquid nitrogen and micro-pipettes. To my brother, Başar, the constant inspiration from afar. Türkiye deki ailem, haber vermiyorsam bile, sizi hiç unutmiyorum. To Françoise, toujours preuve que *tout est possible*. To Pierre-Gilles, his smile and laugh always ready, his life and work a constant presence and muse; you are greatly missed. To my adviser, Alex. Your wisdom, subtlety, kindness, and support will be irreplaceable. I wish you the best in your quest and hope our paths will cross again. To Irfan, who taught me how to crimp a wire and run a fridge, with smarts, charm, and perseverance you will catch those quantum kittens. To Vincent, for the brainstorms, the good advice, a like mind, and a long and fruitful collaboration. On l'ameliora ensemble. To the patient teachers, the postdocs: András Kis, Yuanbo Zhang, and Ofer Naaman. I did not and can never thank you enough. To Kenny and Victor, fellow basement dwellers, colleagues at work and home. Keep your minds open and your thoughts big–when do we form our startup? To Benji and Brian, partners in crime. To Stefanos: ela my PhD brother and physics buddy. Play your tune and it will lead you. To Anne and Gee Gee, the behind-the-scene warriors. Thank you. Finally, to you the reader, enjoy. May you find something worthwhile.

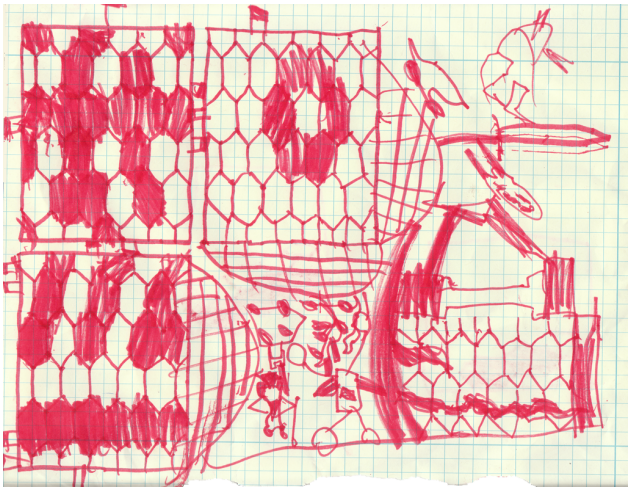

A picture with hexagons. Uzay Girit.

Part I

Graphene Fundamentals

Chapter 1

Introduction

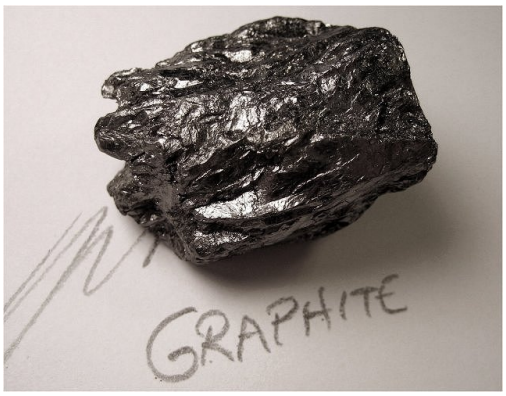

Figure 1.1: Graphite photo. Courtesy R. Weller, Cochise College.

The crystal structure of graphite (Fig. 1.2), commonly found in pencil lead, consists of planar layers of carbon atoms bonded in a hexagonal lattice. A single atomic layer of graphite is called *graphene*. Although graphite itself has been under scientific study for at least one hundred years, it was not until 2004 that graphene was extracted from graphite by a simple technique requiring only tape [117].

As a stable two-dimensional, crystalline, atomically thin material, graphene is interesting from a mechanical point of view. The covalent sigma bonds holding the hexagonal lattice together are strong, and the atoms are relatively light. This leads to a high melting point, high thermal conductivity, and large Debye temperature. Graphene's elastic properties have been thoroughly characterized [96], and indicators of its exceptional strength include the ability to sustain large strains before breaking. As a material for nanoelectromechanical systems (NEMS), graphene has several favorable qualities. The low mass density, large tensile strength, and electrical conductivity allow fabrication of high-frequency, large-amplitude resonators with electric-field tunable resonant frequencies [19, 25].

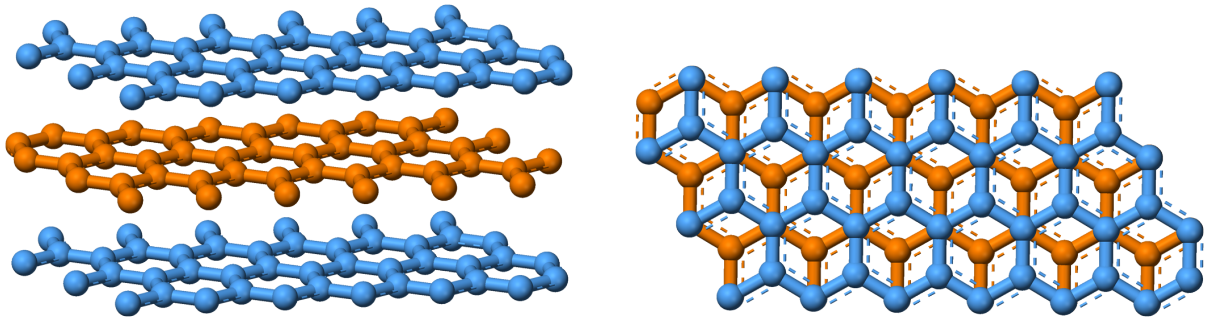

(a) Side view (b) Top view

Figure 1.2: Crystal structure of graphite, showing stacking of graphene layers. Wikipedia.

For fundamental studies of mechanical systems at the quantum limit, where only the ground state of a vibrational mode is occupied, graphene seems ideal. Graphene resonators with small dimensions or under large strains should easily have resonant frequencies in the GHz [25]. At such frequencies, a dilution refrigerator is sufficient to provide temperatures such that $kT < \hbar\omega$ and the resonator will be in its ground state. In addition the zero-point motion, $x_0 = \sqrt{\frac{\hbar}{2m\omega}}$, which corresponds to the RMS amplitude of vibrations in the ground state is large compared to bulk resonators at similar frequencies ω and thus easier to detect. This is due to the atomic thickness of graphene, less than one angstrom, which is at least one-thousandth the thickness of even a thin-film NEMS resonator, and the atomic mass, which is at least half that of commonly used NEMS materials (Si, Al, GaAs). In general, the scaling of resonant frequency, total mass, and zero-point motion with size favors graphene for NEMS applications and experiments in comparison to other materials.

Graphene's electronic structure is just as exciting if not more than its exceptional mechanical properties [23]. Carbon, as a result of having atomic number $Z = 6$, occupies a special position in the periodic table. Since it has four valence electrons and only one filled shell ($1s^2$), its orbitals can hybridize to form sp^2 and sp^3 bonds that yield several different allotropes: graphite and diamond, being the most common in bulk, and fullerenes, nanotubes, and graphene at the nano-scale. In two dimensions, sp^2-bonding allows the formation of the highly symmetric hexagonal lattice found in graphene. Calculation of the band structure for such a lattice (Chapter A) shows that it is a zero-bandgap semiconductor with quasiparticles, called massless Dirac fermions, that have a linear light-like dispersion relation, instead of the conventional parabolic dispersion. In effect, the quasiparticles in graphene behave like massless, spin-half particles such as ultrarelativistic electrons or neutrinos. Their effective speed of light is roughly $c/300$. This "relativistic" property of the quasiparticles in graphene is what makes it an electronically interesting material. The possibility of observing and manipulating quasi-relativistic particles in a two-dimensional solid-state system has driven much of the research in graphene.

The first electronic measurements on graphene devices demonstrated the electric-field effect [117]. Two electrodes were deposited onto a microscopic graphene sheet and the resistance measured as a function of the gate voltage on a nearby conducting backplane. In this field-effect transistor device geometry, the charge density is tuned with the electric field produced by the gate voltage. Such graphene transistors cannot be switched off, but conduction is bipolar–the Fermi level can be tuned from p-type to n-type conduction. Soon afterwards, the integer quantum hall effect (QHE), the hallmark of two-dimensional electron gas (2DEG) physics, was observed [116, 164] at low temperatures and high magnetic fields in graphene hall-bar devices. Two features distinguish the QHE in graphene from that in conventional 2DEG materials such as GaAs quantum wells. The gapless, linear density of states modifies the Landau level energy spectrum and creates a novel zeroth level which mixes both electrons and holes. In addition the Hall conductivity plateaus are shifted by a half-integer. More recently, the fractional quantum hall effect was observed in suspended samples [42, 16] and a study of those states as well as the zeroth Landau level are exciting future research directions.

Besides the quantum Hall effect, another hallmark of mesoscopic 2DEG physics is conductance quantization. In a one-dimensional ballistic wire, where charge carriers do not scatter, the conductance is not infinite but has a quantized value of e^2/h (per spin or other degeneracy) when the wire is connected to macroscopic contacts. This was originally observed in GaAs [150] and it was later confirmed that all of the voltage drop occurs at the interfaces between the contacts and wire [35]. The mobility of the molecular-beam-epitaxy (MBE) grown GaAs used in these experiments were in the millions of $\mathrm{cm^2\,V^{-1}\,s^{-1}}$ with mean free paths in the tens of microns. Despite increases in mobility of graphene devices on silicon dioxide from early values of $5000\,\mathrm{cm^2\,V^{-1}\,s^{-1}}$ up to more recent measurements of $20\,000\,\mathrm{cm^2\,V^{-1}\,s^{-1}}$, and the observation of mobilities as high as $200\,000\,\mathrm{cm^2\,V^{-1}\,s^{-1}}$ in suspended devices, these values are still at most one-tenth that of high-quality GaAs. However the graphene field is still in its infancy and it is expected that suspended sample quality can be improved[1] and possibly match that of GaAs. The room-temperature mobility of graphene however greatly exceeds that of GaAs and combined with the modified Landau level energy spectrum of massless Dirac fermions the quantum Hall effect has even been observed at room temperature in high field (45 T) [119]. In contrast conduction quantization is a zero-field phenomenon that despite being less robust than the quantum Hall effect would lead to several novel ballistic electronic devices [136, 128, 122]. These quantum devices could potentially operate at room temperature without the need for high magnetic fields if graphene mean free paths at 300 K exceed one micron.

Beyond their applications possibilities, ballistic graphene devices are interesting as a means to investigate the intrinsic physical properties of massless Dirac fermions. In the presence of scattering, transport measurements of graphene always include the effects of an unknown scattering potential. It is only in the ballistic limit that intrinsic properties can be probed. Despite advances toward fabricating ballistic devices [41], a clear sign of

[1] E. Andrei, condensed matter seminar (290k), University of California, Berkeley, 2010.

conductance quantization of Dirac fermions is lacking. Once this goal is achieved, a variety of "relativistic" quantum mechanical phenomena such as Zitterbewugung, atomic collapse, and Klein tunneling [84, 159, 134] can be properly explored by applying controlled external potentials. In this limit, electronic transport measurements in graphene will be analogous to high-energy physics experiments probing relativistic quantum mechanics by accelerating and colliding single electrons at GeV scales. However in ballistic graphene the applied external potentials can easily be comparable to the quasiparticle energies, which would be extremely difficult for ultrarelativistic electrons.

The goal of this thesis is to provide a theoretical understanding of conductance quantization of massless Dirac fermions, to describe the fabrication and characterization of graphene devices, and to present experimental results on the route to measuring this phenomenon. It is hopeful that the experimental signatures of conductance quantization will soon be observed in graphene and that this will open the door to further exciting experiments.

Chapter 2

Synthesis

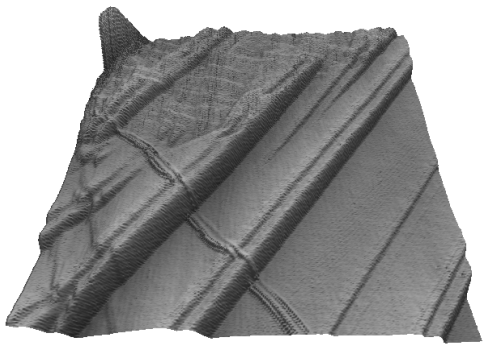

Figure 2.1: Atomic force micrograph of graphene grown on copper foil.

The first difficulty in doing experiments on graphene is synthesis. Luckily, synthesis of graphene is much easier than producing high-mobility GaAs/AlGaAs quantum wells by molecular-beam epitaxy (MBE). This is partly the reason why interest in graphene grew so quickly. Researchers realized that a single graduate student would be enough to "peel graphite" and repeat the same experiments as before–this time with graphene instead of a carbon nanotube, silicon nanowire, high-T_c superconductor, metallic thin film, etc. There are currently two main techniques for graphene synthesis. Both will be covered in this chapter.

The first is actually graphene *extraction* instead of synthesis, and was discovered by Novoselov and Geim [117] who referred to it as "micromechanical exfoliation". It is more commonly referred to as the Scotch-tape technique, in that common adhesive tape is used to repeatedly peel layers of a bulk graphite source in order to eventually produce single-layer, graphene samples. Such a description does not do justice to the technique required in peeling–indeed initial attempts, over several weeks, at reproducing this "simple" technique produced no single-layer samples for the author. Only with practice, perseverance, and help

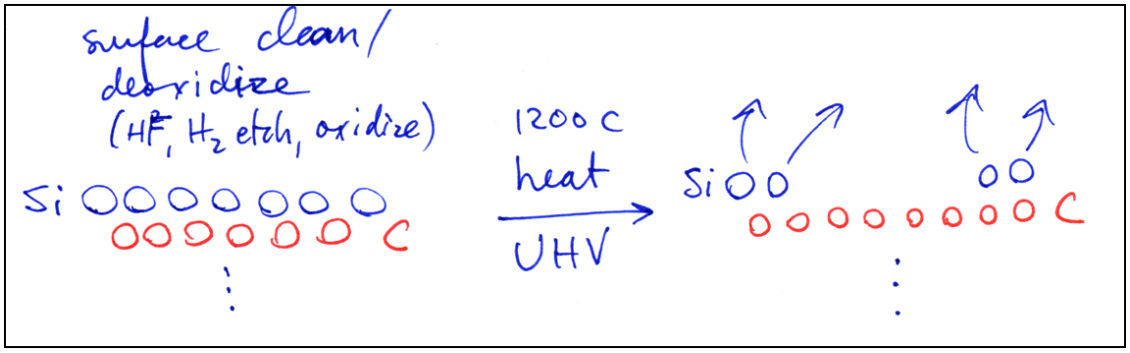

Figure 2.2: Schematic of SiC graphene synthesis.

from others does it become a commonplace occurrence to obtain graphene. This is made evident from the increase in sample size in published articles from the conception of the technique in 2004. Initially, lateral sample dimension was limited to 10 µm. Now samples with 50 µm–100 µm lengths are common, with the largest samples up to a millimeter in size. In addition, it is no longer necessary to make samples oneself–there is a company that sells exfoliated graphene[1], although it is quite expensive.

The second technique to produce graphene *is* a synthesis technique, chemical vapor deposition (CVD), which is commonly used to produce carbon nanotubes and silicon oxide thin films. There is a long history of vapor-phase deposition of "monolayer graphite" [121], as graphene was referred to prior to 2004. Unfortunately, these techniques were not widespread or well known because ultra-high-vacuum (UHV) processing and high-quality single-crystal catalyst substrates were required, and no one had attempted to isolate the graphene produced in this manner. More recently, near-ambient pressure, tube-furnace CVD synthesis of few-layer graphite on nickel foils was rediscovered [88] after having been investigated thoroughly previously [82]. Again, the major advance in the recent work was not synthesizing the few-layer graphite, but etching away the nickel and isolating the graphite post-synthesis. Finally, in 2009, a CVD tube-furnace technique using copper instead of nickel foils was developed that produced uniform, large-area, single-layer graphene [98]. It is this technique that shows most promise for graphene-based applications, although the electronic quality of samples is not yet as good as that of exfoliated graphene.

Several other graphene synthesis techniques exist, which include vacuum graphitization of silicon carbide [13] and liquid-phase intercalation and chemical exfoliation of graphite [151, 100, 71]. I briefly describe here the first technique, graphitization of silicon carbide (Fig. 2.2), which has resulted in high mobility samples for scanning tunneling microscope (STM) studies and could potentially be used for graphene electronics applications.

The "substrate" for graphene growth by vacuum graphitization are wafers of crystalline

[1] Graphene Research, Ltd., `http://www.grapheneresearch.com`. The current price is roughly $20\,¢/\mu m^2$ with sample areas in the $400\,000\,\mu m^2$ ($20,000) and larger.

silicon carbide purchased commercially[2] Several polytopes or stacking orders exist for silicon carbide, with 4H-SiC and 6H-SiC commonly used for graphene synthesis. Both silicon carbides are layered compounds, with alternating carbon and silicon planes in the bulk and oxidized silicon at the surfaces. A silicon carbide wafer or chip is placed in a UHV chamber and pumped to low pressure. As graphitization requires a clean, oxygen-free surface, immediately before pumping down the SiC, it is dipped in HF to hydrogen-terminate the surface. Once the chamber is pumped to ultra-high vacuum, the surface is again cleaned by a hydrogen plasma etch. Subsequently, the wafer is heated to 1200 °C, which results in desorption of the silicon atoms near the surface. The silicon-carbon bonds are broken and carbon-carbon bonds form, graphitizing the exposed carbon layer and producing graphene sheets on top of the silicon carbide bulk. Although graphitization can produce large domains [48], the number of layers cannot be well controlled. However, since the stacking order of the layers random they are decoupled electronically and ideal graphene electronic properties have been observed by surface sensitive probes such as STM [112] and angular-resolved photo-emission spectroscopy (ARPES) [137].

2.1 Micromechanical Exfoliation

The micromechanical exfoliation, or Scotch-tape, technique produced the first samples for electronic transport measurements in graphene. The technique takes advantage of the weak interplanar bonding in graphite–although the in-plane sigma bond is strong, the out-of-plane pi bond is weak. This results in the slippery feel of graphite and the ease with which it can be cleaved. Adhesive tape can be used to repeatedly cleave or peel a graphite flake, "thinning" it down and distributing a thick stack over a wide area of tape. The tape is then pressed onto an oxidized silicon wafer, thereby transferring some graphite from the tape onto the wafer. Some transferred graphite will have only a few layers, and optical contrast and color on the wafer can be used to identify single layers. The exfoliation and transfer procedure, graphite/tape sources, and substrate choice and preparation are described below.

Some "recipes" by others can be found online, including videos:

- Zettl Group, UC Berkeley: Graphene Exfoliation Wiki
- McEuen Group, Cornell: Graphene Fabrication Wiki
- Özyilmaz Group, Singapore: Making Graphene 101 YouTube video
- Jarillo-Herrero Group, MIT: DIY Graphene at Scientific American

[2] Cree, Inc. (`http://www.cree.com`) supplies high quality silicon carbide wafers. A 6H-SiC n-type 50 mm wafer cost $753 in Fall 2005.

2.1.1 Exfoliation and Transfer Procedure

The following should be considered guidelines, as they have worked for the author, but they may not necessarily work for anyone else! This "synthesis" technique is inherently random: there is minimal control of how much graphene will be produced and where it will be located. This is why one should not really call it synthesis, but rather extraction. In addition, there are many factors that one ignores, such as temperature, humidity, tape aging, aging of graphite source, precise substrate surface preparation, and so on. Ideally clean-room conditions can fix most of these parameters, but that requires convenient access to a clean-room facility which allows "dirty" processes. Even with precisely controlled environmental conditions, the yield of graphene can vary significantly based on who is doing the exfoliation and transfer. Yield *will* improve with practice and good note-keeping. The "theory" of exactly what allows the transfer of an isolated single layer versus many layers is not clear and so it is difficult to optimize the recipe. Some thoughts on this question are discussed at the end of this section.

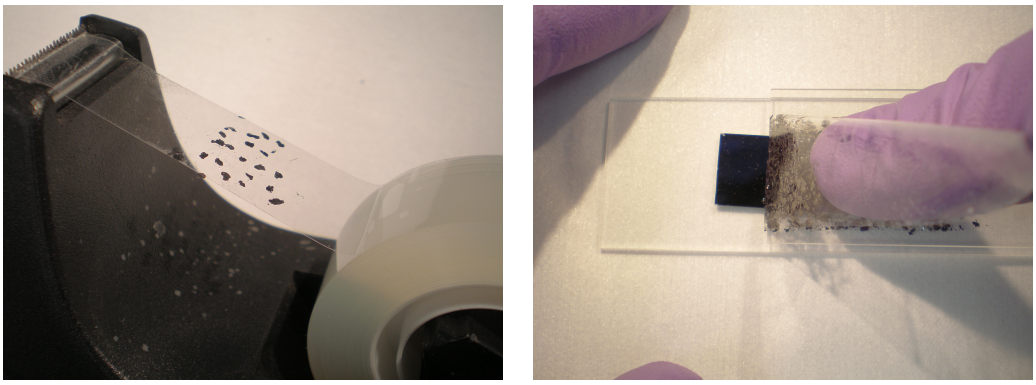

(a) Graphite transfer to tape (b) Graphite exfoliation onto wafer

Figure 2.3: Graphene exfoliation and transfer procedure.

1. **Graphite Transfer to Tape**
   The spool of tape should be loaded onto a standard dispenser, as this will provide a support for transferring the graphite onto the tape. After donning gloves, remove and discard the segment of tape on the dispenser that had been exposed to air, revealing a fresh segment. Ensure that the tape is taut between the spool and the cutter. Set the dispenser upside-down so that the exposed tape faces upward. Now the graphite source can be transferred onto the tape with tweezers. Certain tweezers will not work well for picking up graphite flakes due to electrostatic charging–carbon-fiber or carbon-fiber tipped ones seem to minimize "jumping away" of flakes. Use the tweezers to transfer flakes to the center area of the exposed tape, halfway between the spool and the cutter.

They should stick as soon as they touch the tape, but gently pat them down if they are not flat. It is not necessarily the number of flakes taped on that matters, but the volume of graphite which is subsequently cleaved to produce the proper "contrast" of graphite on the tape (next step). If the graphite flakes are extremely thin to begin with (<0.1 mm) and have lateral dimension of several millimeters, roughly three to five flakes should suffice for a tape length of 8 cm between spool and cutter. Now detach the tape segment, ensuring that there is enough space at the tail-end to be able to firmly hold it. Avoid touching the graphite flakes and surrounding region with gloves, as even "powder-free" gloves leave residues on the tape and may reduce its tack.

2. **Cleaving of Graphite**
   Now hold the tape with graphite flakes attached in the central region firmly at both ends. Fold the tape onto itself, taking care to avoid folding the graphite flakes onto each other. A gentle folding without applying pressure should be sufficient to stick the tape onto the exposed side of the graphite flakes. Gently unpeel the tape from itself, and there should be two copies of the initial pattern of graphite flakes. Repeat this process three or four times, avoiding taping the graphite onto itself as much as possible. This will require folding the tape onto itself at various angles and distances from the middle. At this point, most of the central region of the tape should be covered in dark gray graphite. Repeat the cleaving process several more times in order to obtain a contrast and coverage similar to that in Fig. 2.5 (b).

3. **Taping onto Substrate**
   With proper graphite flake coverage on the tape, it is time to tape onto the substrate. If the substrate is an oxidized silicon wafer, it should be cleaved into a rectangle or square with a width comparable to the tape width and a length shorter than the tape segment. Place the wafer chip onto a flat surface and press one end of the tape segment onto the surface near the short edge of the chip. Align the chip or tape segment so that the center of the graphite region on the tape will contact the center of the chip when the tape is lowered. Hold the tape taut with one hand (right hand for right-handed persons) and use the other hand to press it down onto the chip, moving slowly upward toward the end held with the right hand. Tape it down uniformly, to avoid trapping air bubbles. The rounded end of a razor-blade or other tool can be used instead of a finger to push the tape down and over the chip. Press the tape segment completely onto the flat surface–the tape on both ends of the chip should hold it down firmly against the chip surface. Now apply pressure with your finger or a rubber eraser on top of the chip, bringing the tape into closer contact with the chip surface. Experiment with the applied pressure and time. About a minute of "moderate" finger-pressure should be adequate.

4. **Tape Removal**
   Before removing the tape from the chip, a waiting period of several hours to days can be beneficial in improving the yield of graphene sheets. It is possible that small

differential thermal contractions of the tape-on-substrate due to normal temperature variations can improve the adhesion of graphite to the substrate. Once the tape is ready for removal, detach one end from the flat surface next to the chip. Lift it vertically and slowly peel the tape off the substrate, holding the substrate down so it does not rise up (Fig. 2.3(b)). One can experiment with both the angle the tape makes when lifting off the substrate and the peel-off time. Many different combinations where tried, from normal peel-angle to nearly flat, as well as rapid peel-off and very slow (several minutes) peel-off. Slow seems better than rapid, and nearly flat better than normal angle. However, no attempt was made to evaluate these parameters systematically either qualitatively or quantitatively, but that would be a direction worth pursuing with a capable undergraduate assistant. This process usually yields several graphene samples of lateral dimensions $>100\,\mu m$ in a $1\,cm^2$ substrate area. Identification of graphene samples on conventional silicon oxide substrate by optical microscopy (Section 3.1) and Raman spectroscopy (Section 3.2) is discussed starting page 33.

In the preceding recipe, various parameters are involved, some implicit (temperature, humidity) and others explicit (pressure, contrast of cleaved graphite on tape). Systematic analysis of their effects is not an interesting task, and as long as the process works producing several graphene sheets each time, the researcher can move forward with experiments.

However, it may be worthwhile to imagine the process by which a single atomic layer of graphite is transferred to the substrate from the graphitic mass on the tape, either toward improving yield or suggesting alternative synthesis routes. Although it seems reasonable that a plane of graphite would "stick" more readily to the polymer goo forming the adhesive coating on tape rather than to another layer, why it would prefer to stick to a substrate such as silicon oxide is not clear. Surface preparation of the substrate (Section 2.1.3) has a strong effect on graphene adhesion and understanding the graphite/substrate interaction would be useful. It is possible that the tape-based cleaving process produces graphene sheets on the surface of the graphite flakes that are misaligned, out-of-plane, or otherwise poorly coupled, and as a result prefer to stick to the substrate upon contact. Sometimes tape residues will appear at the edges of a transferred graphene sample, and perhaps even under a sample, and this could also play a role in the "stickiness" to the substrate. Also shear forces may play an important role in the transfer of a graphene sheet, perhaps due to relative thermal expansion of the tape on the substrate. Investigations along these directions may be useful in obtaining larger exfoliated samples or better yield.

2.1.2 Graphite and Tape Sources

Graphite

There are two major pure sources of graphite: Kish graphite and highly-oriented pyrolytic graphite (HOPG). Kish graphite is thought to be recovered from the iron smelting process: excess carbon precipitates and graphitizes during the cooling of molten steel. Kish graphite

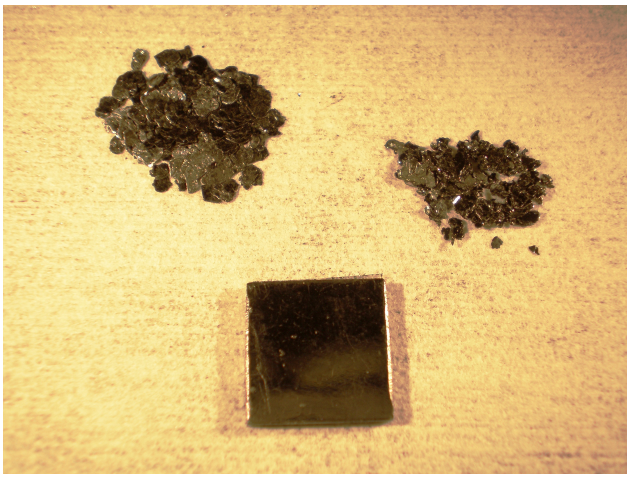

Figure 2.4: Graphite Sources.
Upper left: natural graphite flakes from NGS Naturgraphit GmbH. Upper right: Kish graphite flakes from Covalent Materials Corporation. Bottom: HOPG square from AIST-NT, Inc. The HOPG is 1 cm on a side.

is sometimes called graphite flakes, or natural graphite, and the quality depends highly on the source. It is usually sold in a vial or bag of hundreds to thousands of flakes (weighing from 10 g to 1 kg), each flake having rough dimensions of 3 µm × 3 µm × 0.2 µm.

HOPG is graphite synthesized in a high-temperature, high-pressure process, forming large (10 mm × 10 mm × 1 mm) blocks that are extremely flat and smooth. It is often used for calibration in X-ray crystallography and is closest in structure to what is imagined of graphite. It is also used for STM studies, being one of the few materials with which one can obtain atomic resolution in air, due to the relative inertness of the surface. Although HOPG can be used for graphene synthesis by exfoliation, better results are obtained with Kish, perhaps because it has more defects and cleaves easier or with smaller domains.

There are several commercial sources for both Kish and HOPG. Figure 2.4 is a picture of Kish graphite, natural graphite, and HOPG.

- Covalent Materials Corp. (`http://www.covalent.co.jp`), in Japan, sells very high quality Kish graphite for exfoliation, and is the recommended source by Yuanbo Zhang. They were formerly Toshiba Ceramics. Product name is `AP70 PV KISH GRAPHITE`. Information page here. As of 2006, pricing was $250 per gram.

  ```
  Covalent Materials Corporation
  Nissei Bldg.
  6-3, Ohsaki 1-chome
  Shinagawa-ku
  Tokyo 141-0032, Japan
  ```

TEL : +81-3-5437-8411
FAX : +81-3-5437-7172

Allen Okamoto
Senior Sales Mgr
Covalent Materials USA Inc
2010 North First Street, Suite 400
San Jose, CA 95131-2018
Ph 408-467-0515
Fax 408-467-0510
alleno@toceram.com (?)

- NGS Naturgraphit GmbH (http://graphit.de) is a common provider of Kish graphite for the graphene synthesis community. As of 2007, the rate was $2 per gram of highest purity, highest crystallinity Kish graphite.

  Hubert Meisner
  NGS Naturgraphit GmbH
  Winner Strae 9
  D-91227 Leinburg
  Fon: 0049 9187 5278
  Fax: 0049 9187 6130
  email@graphit.de

- AIST-NT, Inc. (http://nanoprobes.aist-nt.com) or "Advanced Integrated Scanning Tools for Nano Technology" sells highly-oriented pyrolytic graphite (HOPG). Direct link to product here. The Z grade is the highest quality for scanning probe microscopy or diffraction, but is not necessary for graphene exfoliation use.

  AIST-NT Inc.
  353 Bel Marin Keys Blvd., Suite 7-8
  Novato, CA 94949, USA
  Phone: (415) 884-9500
  Fax:(415) 884-9500
  sales@aist-nt.com

Tape

Many different kinds of tape were tested by an undergraduate assistant, Ru-Ern Chee (whoelse@gmail.com). It was found that classic 3M #600 Scotch tape (Fig. 2.5(a)) worked best. This can be purchased through McMaster-Carr (http://www.mcmaster.com/#7772a16), product number 7772A16, or at most office supply stores.

(a) 3M #600 Scotch Tape (b) Tape with exfoliated graphite

Figure 2.5: Graphite exfoliation with adhesive tape.

2.1.3 Substrate Sources and Preparation

There are several factors to consider when choosing the proper substrate and substrate preparation for experiments on exfoliated graphene. Obviously the substrate must allow easy identification, optical or otherwise, of the transferred graphene. Certain oxide thicknesses make it very easy to identify graphene with the human eye and a microscope. In addition, and also obviously, the substrate must suit the experiment to be done! For example, for low temperature electronic studies (below 4 K) the resistivity of a doped-semiconductor serving as a backgate must be low enough so that the backgate stays conducting when thermal carrier occupation is virtually zero. In other words, the backgate must be on the metallic side of the metal-insulator transition for the doped semiconductor. On the other hand, for optical measurements in transmission mode, the resistivity should be high to reduce absorption in the silicon. Also the wafer should be double-side polished (DSP) instead of having the standard oxide backseal which leads to diffuse scattering.

The transfer of exfoliated graphene is strongly dependent on the surface chemistry. For example, piranha etched silicon oxide wafers result in much better yield than oxygen etched ones, which results in hardly any graphite transfer at all. Piranha etching is described below.

Substrate Sources

For electronic transport measurements down to the lowest temperatures (milliKelvin and below) on back-gated samples, degenerately-doped wafers are required. For n-type, arsenic doped (N/As) silicon‘, the resistivity should be less than $0.005\,\Omega\,\mathrm{cm}$ for degenerate-doping and proper backgate function at low temperature. The oxide grown on the semiconductor also needs to be of high quality in order to minimize charge traps and charged impurities that could lead to shorter mean free paths in unsuspended graphene devices. The highest quality oxide is grown by a dry thermal process which has a slower growth rate than the lower quality wet process. The dry-growth oxide is sometimes referred to as electronic grade,

or "gate"-quality. Dry oxide growth needs to be specified in the purchase order, and is more expensive than the wet growth. The best oxidation process I found is referred to as "ultra pure CMOS Dry Chlorinated Thermal Oxidation." The higher quality oxides should also have higher dielectric breakdown fields, allowing application of higher gate voltages and a wider experimental range for the graphene Fermi level. Silicon wafers were used in all the experiments reported here, but other semiconductors or metals could also serve as backgate material. The ease with which silicon can be oxidized makes it appealing however. Few silicon wafer growth and oxidation companies will have degenerately doped wafers on hand as well as the capability of doing dry oxidation. Below are potential sources. University Wafers, Inc. is not recommended.

For easy optical identification of graphene, the oxide thickness should be either 285 nm or 90 nm (see Fig. 3.3). In the latter case care needs to be taken when applying the gate voltage, as dielectric breakdown will occur at a smaller voltage (roughly 50 V). In the case of 285 nm high-quality oxide, the breakdown voltage can be as high as 200 V.

- For degenerately doped wafers, Helitek Company, Ltd. (`http://www.helitek.com`), is a good source. They have fast turn around and are located in Fremont, CA. The price for arsenic doped (n-type) wafers of resistivity $<0.005\,\Omega\,\mathrm{cm}$ was \$12.50 per wafer (2008).

  ```
  Clair Wang
  Helitek Company Ltd.
  A Division of Wafer Works Corp.
  47338 Fremont Blvd.
  Fremont, CA 94538
  Tel. 510-933-7688    Fax. 510-933-7689
  http://www.helitek.com
  ```

- Silicon Valley Microelectronics, Inc., or SVM (`http://www.svmi.com`), can do dry thermal oxidation and has had degenerately doped wafers on hand (N/As, $1\,\mathrm{m}\Omega\,\mathrm{cm}$ to $5\,\mathrm{m}\Omega\,\mathrm{cm}$) in the past (2009). The cost of six-inch wafers is \$27.60 each or \$44.50 each with the ultra-pure CMOS dry chlorinated thermal oxidation.

  ```
  Sharon Kunkel <Skunkel@svmi.com>
  Silicon Valley Microelectronics, Inc. (SVM)
  2985 Kifer Road
  Santa Clara, CA 95051-0802 USA
  Phone 408.844.7100
  Email: sales@svmi.com
  ```

- Silicon Quest International, Inc., or SQI (`http://www.siliconquest.com`), can do dry chlorinated thermal oxidation and has had degenerately doped wafers on hand (N/As,

1 mΩ cm to 5 mΩ cm) in the past (2009). The cost of four-inch wafers is $19.50 each and $36.50 with the oxidation. Note that this is more expensive than the six-inch wafers above from SVM.

```
Len Anderson
Sales Representative
Silicon Quest International
Phone: 800-959-3556 x111 or 408-496-1000 x111
Fax: 408-496-1133
email: len@siliconquest.com
```

- MEMS Exchange (`https://www.mems-exchange.org`) produces the highest quality oxidized silicon wafers, but it is also the most expensive. Their process is called "gate quality dry oxidation + forming gas anneal with Trans-LC". Trans-LC is a chlorine source for silicon oxidation. Their price is roughly $130 per wafer with oxidation.

```
Mehmet Ozgur, D.Sc.
Senior MEMS Engineer
MEMS and Nanotechnology Exchange / CNRI
1895 Preston White Dr. Suite #100
Reston, VA, 20191
Ph:  703 -262 5368 (x5366)
Fax: 703 -262 5367
```

Substrate Preparation

Several different oxide surface preparation techniques were tried in order to improve graphene yield from micromechanical exfoliation as well as resultant device mobilities. These techniques are oxygen tube-furnace anneal, hydrogen tube-furnace anneal, oxygen reactive ion etch (RIE), UV ozone, and piranha etch. The last one was the only one to show any improvement in graphene yield. The hydrogen tube-furnace anneal seemed to result in improved mobilities, but the data on exfoliated samples is small and inconclusive.

The piranha etch involves subjecting an oxidized silicon wafer to a 3:1 heated mixture of sulfuric acid and hydrogen peroxide. This is an explosive, exothermic combination and care must be taken when performing this process. The reason it is called "piranha" is because the solution rapidly dissolves organic matter, converting it to gaseous carbon oxides. Acid-resistant gloves, lab coat, face shield, and acid handling safety awareness are required when doing a piranha etch.

The chemical reaction is

$$\mathrm{H_2SO_4} + \mathrm{H_2O_2} \longrightarrow \mathrm{H_3O^+} + \mathrm{HSO_4^-} + \mathrm{O} \tag{2.1}$$

which produces extremely reactive atomic oxygen which allows oxidation of carbon. The piranha etch not only serves to clean away organic residues on the oxidized silicon wafer, but

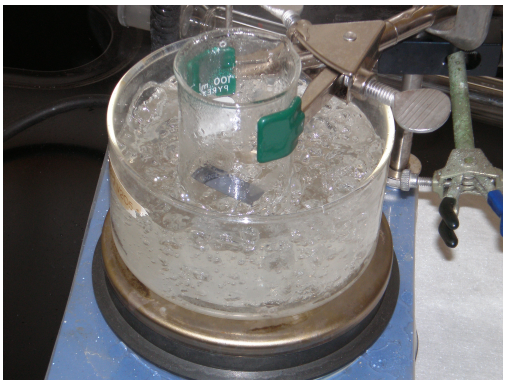

Figure 2.6: Photograph of Piranha etch of silicon wafer.

also to hydroxylate the surface SiO_2, terminating it with -OH groups. A successful piranha etch will leave the oxidized silicon free of any residues and completely hydrophilic–water should form a thin continuous film covering the entire surface. Pre-piranha, the surface is extremely hydrophobic and this is the state the etched surface will return to after a long period of time in storage.

It is best to have someone show how to perform a piranha etch instead of following written directions. After donning protective gear, first prepare a water bath to boiling. Then pour three parts concentrated sulfuric acid (usually 15 mL) into a graded pyrex beaker. Place cleaved silicon oxide wafer chips into beaker. It may be necessary to gently shake the beaker so that the chips are submerged and fall to the bottom. Load the beaker onto a lab clamp and stand, and submerge it partially in the boiling water bath. Now pour the remaining one part hydrogen peroxide (purchased as 30% H_2O_2 in water) slowly into the beaker. This step will release a large amount of heat and possibly vapor. After about one half-hour, stop the heat bath and remove the beaker. Empty the piranha solution into an acid waste container and flush the beaker and chips with deionized water several times. Remove the chips from the beaker with clean tweezers and spray with deionized water. The water should form a thin continuous film on the oxide surface. Blow-dry with nitrogen and proceed to tape on with exfoliated graphene. Immediate use ensures that the surface is completely hydroxylated and should give a higher graphene yield.

Hydrogen tube-furnace annealing consists of putting oxidized silicon chips in a tube furnace, described below, and heating to 1100 °C in a hydrogen environment (flow rate of 5-10 sccm should be sufficient). This may help remove charge traps in the silicon oxide and has led to reduced gate-voltage hysteresis and improved device mobility.

2.2 Chemical Vapor Deposition

Chemical vapor deposition (CVD) is a vapor-phase synthesis technique. Gases, including synthesis precursors and possibly inert carriers, are flown into a heated chamber, reacting

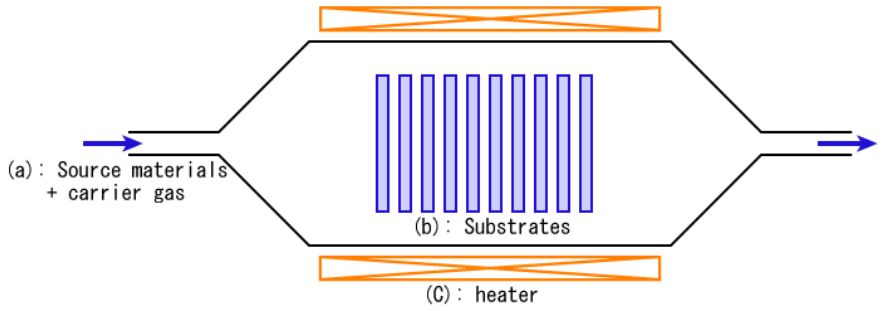

Figure 2.7: Chemical vapor deposition schematic, Wikipedia.

with each other as well as chamber walls and the substrate, ultimately depositing the desired material on the substrate (Fig. 2.7). CVD is often used to grow silicon or silicon-oxide thin films. The precursor gas for silicon growth is silane (SiH_4), and oxygen for oxidizing silicon to produce silicon oxide. Inert carrier gases include nitrogen and argon. Before CVD graphene synthesis became commonplace, it was often used in a laboratory setting for the growth of carbon nanotubes, using nanoscale transition-metal islands as catalyst and methane or other hydrocarbon gases as carbon source gas. Many variants on CVD exist, including low-pressure CVD (LP-CVD), microwave plasma-assisted CVD (MP-CVD), and plasma-enhanced CVD (PE-CVD).

2.2.1 CVD Synthesis

CVD graphene synthesis was implemented in the Zettl group in a low-pressure, tube-furnace system, which has three main components: a gas delivery manifold consisting of mass flow controllers connected to gas cylinders on the intake side and a tube furnace at the output; a tube furnace capable of reaching 1200 °C with a 1.5 inch diameter tube housing (Lindberg/Blue M); a rough pump connected to the furnace output providing downstream pressures from 30 mTorr to 1000 mTorr (Fig. 2.8).

Here the copper-foil graphene CVD synthesis recipe, developed in conjunction with Baisong Geng, visiting student in the Feng Wang group, and Lorenzo Maserati, visiting student in the Michael Crommie Group, is presented. It follows closely the recipe of Li et al. [98], shown in Fig. 2.9. The general Zettl group CVD setup was constructed by graduate students Michael Rousseas, David Okawa, Brian Kessler, and help from undergraduates.

1. **Copper foil preparation**
   Copper foil (Alfa Aesar, 99.9%, 25.4 µm thick) is cleaned with isopropanol and then cut into small squares (roughly 2 cm × 2 cm). Citric acid cleaning has also been reported to be helpful. The squares are then mounted vertically onto a rectangular ceramic substrate holder, with thin notches cut into it to support the squares. Multiple squares can be processed simultaneously by putting multiple notches on the holder. The ceramic

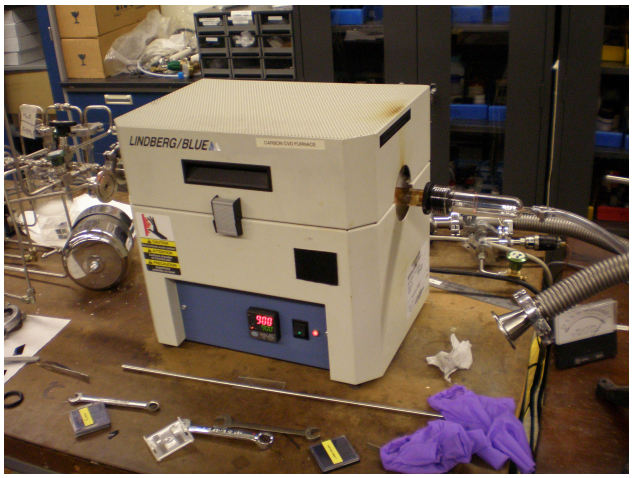

(a) Tube furnace

(b) Gas cylinders

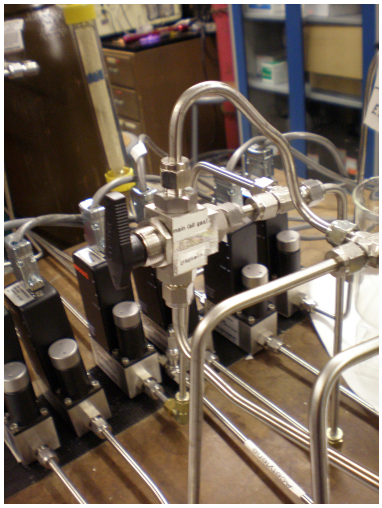

(c) Mass flow controllers

Figure 2.8: Photographs of Zettl Group CVD setup, from Zettl Wiki.

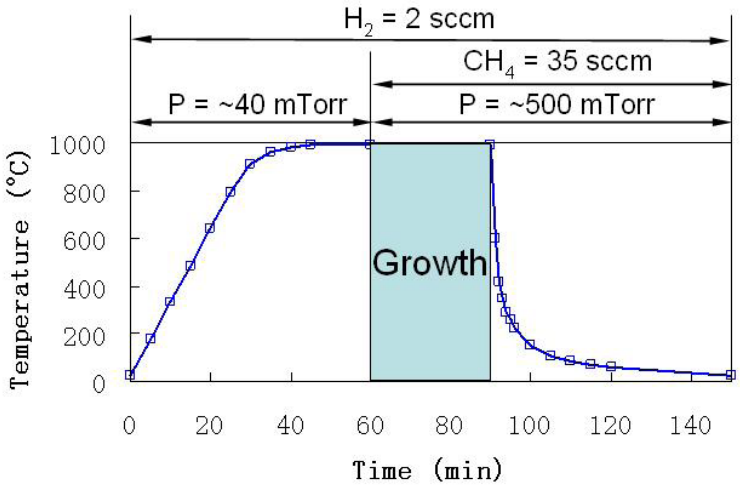

Figure 2.9: Recipe for CVD graphene synthesis on copper foil. Supplementary Fig. S1, Li et al. [98].

substrate holder with vertically-oriented copper foil squares is then inserted into the 1.5 inch diameter quartz tube, already loaded into the open tube furnace. Care should be taken that the copper squares are not so large that they are bent when inserted in the tube. The tube should be clean and the substrate holder pushed to the hot zone with a clean rod (stainless steel tubing works well).

2. **Furnace preparation**
   Once the copper foils have been mounted inside the quartz tube, the vaccuum fittings are connected on both sides of the tube. It is important to have a good vacuum, as gas leaks, especially oxygen can have an adverse effect on graphene growth. Stainless steel tube fittings with frequently replaced o-rings should be used. The fittings on the Zettl group setup have lock-rings to grip the quartz tube on one side and KF-25 on the other side to interface with the stainless steel lines leading to the mass flow controllers (MFC) regulating gas flow.

   At this point, the hydrogen and methane gas cylinders should be opened, but the MFCs should be set to no flow. Now the tube should be pumped down with the rough pump connected at its output, until a vacuum of around 30 mTorr is achieved. A standard vacuum gauge that goes down to 1 mTorr connected between the tube and pump is sufficient. Then the tube should be flushed briefly with about 10-30 sccm of hydrogen, with the pressure rising close to 1 Torr. Once the hydrogen flow is turned off, wait until the system is pumped down to 30 mTorr, and then repeat several times to ensure all oxygen and residual gases are evacuated.

3. **Foil annealing**

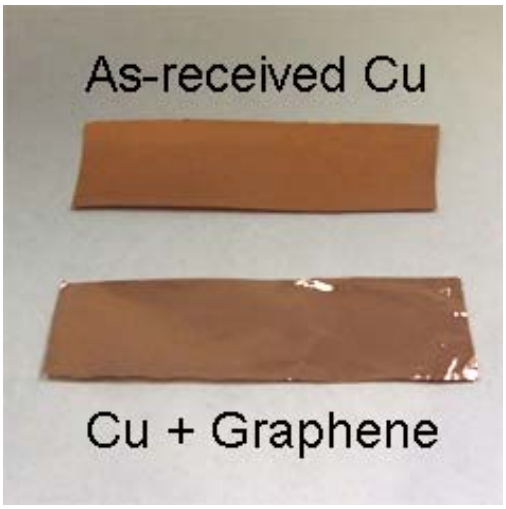

Figure 2.10: Comparison of copper foil before and after CVD graphene growth. Supplementary Fig. S2, Li et al. [98]

Now the hydrogen flow should be set to 2 sccm, resulting in a small rise in the tube pressure. The furnace lid should be closed, clamped, and then the furnace programmed for 1000 °C. It will take about an hour to reach this temperature, and the pressure will fluctuate as gases are desorbed from the quartz tube, substrate holder, and copper foils. Once the operating temperature is reached, the foils should be annealed for at least 30 min. This will help clean the foil as well as increase the size of crystal grains.

4. **Graphene growth**
   When the annealing is complete, set the methane MFC to 35 sccm and time the growth for about 10 min. At this point, open the lid to the furnace, which will stop the heating elements and quickly cool the system down. The methane should be left running during the cooldown. It will take about 10 min to cool to 200 °C to 300 °C, at which point the pump can be stopped and the system vented. Turn off the MFCs and the gas cylinders. Remove the tube from the furnace with heat-resistant gloves as it will still be hot. When the tube is cool enough, remove the substrate holder. The copper foils, now covered in graphene on all sides, should be bright and shiny, and should not lose their luster (Fig. 2.10). The graphene serves as an oxidation-resistant coating.

5. **Copper etch**
   The copper must be etched away to separate the graphene for transfer to another substrate. If the graphene coated copper foils is placed as-is in a ferric chloride ($FeCl_3$) or sodium persulfate ($Na_2(SO_4)_2$) etchant solution, once the copper is dissolved, the graphene will curl up and it will not be possible to transfer it. In order to do so, a polymer (PMMA or polystyrene) must first be spin coated onto the graphene/Cu.

Spin coat fresh, clean PMMA A4 (Microchem, Inc.) at 3000 RPM onto one face of the copper squares, taking care not to have the polymer run over onto the backside. If the PMMA coats both sides of the square, the etchants will not work as they cannot penetrate PMMA. Bake the PMMA/graphene/Cu directly on a hotplate at 180 °C for 30 min. Once the square is cool, cut a few millimeters off the sides to remove any PMMA that has crept onto the backside. Keeping the PMMA-coated side up, place the squares into the etchant solution. Ferric chloride is prepared by mixing 1:1 weight ratio with deionized water. Sodium persulfate is a cleaner etchant, but takes longer as the ions do not easily pass through the graphene. It can be prepared in the lab or purchased (M.G. Chemicals).

6. **Graphene transfer**
   In about an hour with the ferric chloride, or longer with the sodium persulfate, the solution should change color and a transparent square of PMMA should be floating on top. The graphene is stuck to the underside of the PMMA. Delicately use a plastic spoon to fish the PMMA square out of the etchant solution and into a clean deionized water bath. Transfer several times to fresh water baths to disperse etchant solution remaining on the PMMA/graphene. Now the PMMA/graphene can be removed from the solution and onto the substrate. Dip the substrate into the water bath and delicately approach the side of the PMMA/graphene square. Because of the hydrophobicity of the PMMA/graphene, it should stick to most substrates. Gently pull it out, taking care to avoid folding. Bake the PMMA/graphene/substrate for an hour at 180 °C to remove any residual water. Then dissolve the PMMA in acetone and rinse with isopropanol. If everything went well, there should be a cm-scale continuous graphene sheet on the substrate (Fig. 2.11).

The procedure for few-layer graphite deposition onto nickel thin films is similar, and gives results shown in Figure 2.12.

Despite the simplicity of the copper foil graphene CVD technique, the Achilles heel compromising sample quality is the transfer step. From Fig. 2.11(c), an atomic force microscopy scan of the graphene/Cu foil, it is clear that post-synthesis, the foil is extremely clean. No adsorbates can be identified and the graphene beautifully covers the entire well-terraced surface of the copper. On the other hand, once such a sample is transferred to silicon oxide, many particles cover the surface of the graphene (Fig. 2.13), either as a result of the etch step or the PMMA coating. Many different workarounds to this problem were investigated by Baisong Geng, but the results are not conclusive. It appears that concentrated nitric acid can improve the graphene cleanliness, at least on suspended samples transferred on transmission electron microscopy grids.

2.2.2 Deposition Mechanism

Two variants of CVD graphene synthesis exist, distinguished by the substrate material. If a nickel substrate is used, few-layer graphite is deposited. If a copper substrate is used,

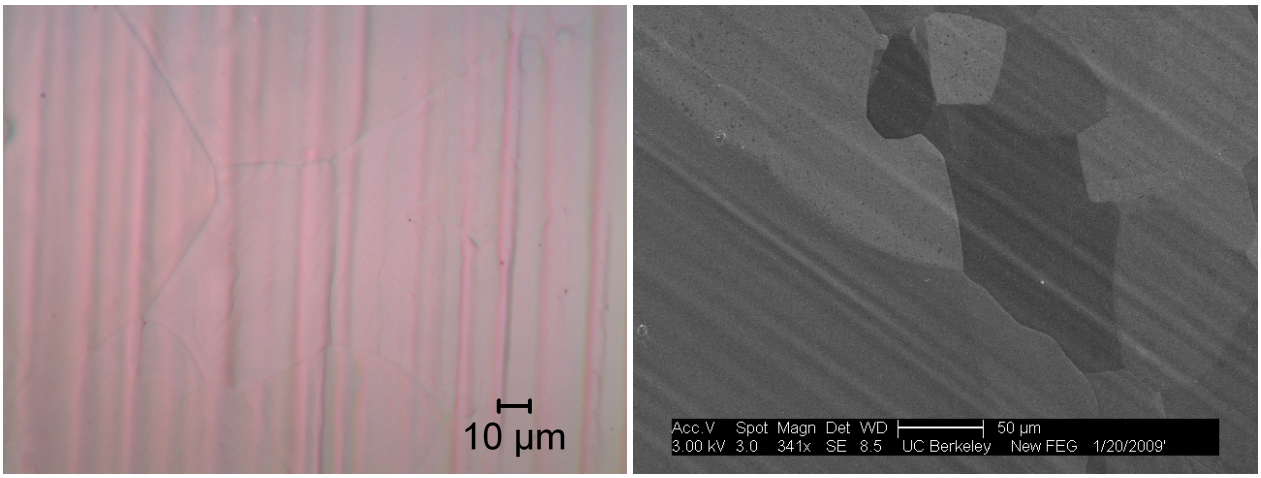

(a) Optical image

(b) Scanning electron micrograph

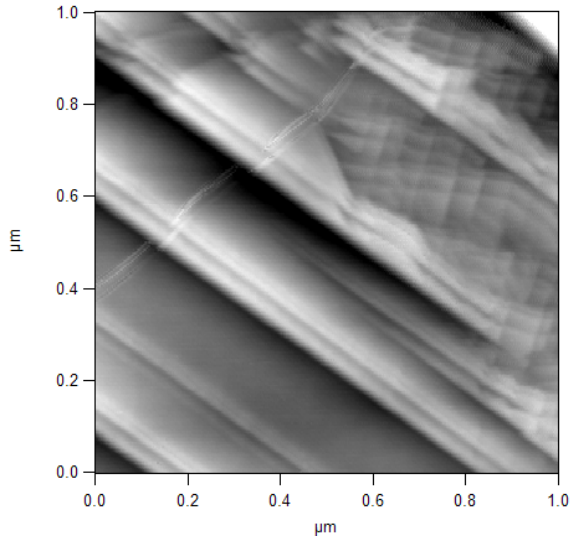

(c) Atomic force micrograph

Figure 2.11: Images of graphene grown on copper-foil by CVD. SEM and optical images courtesy Baisong Geng.

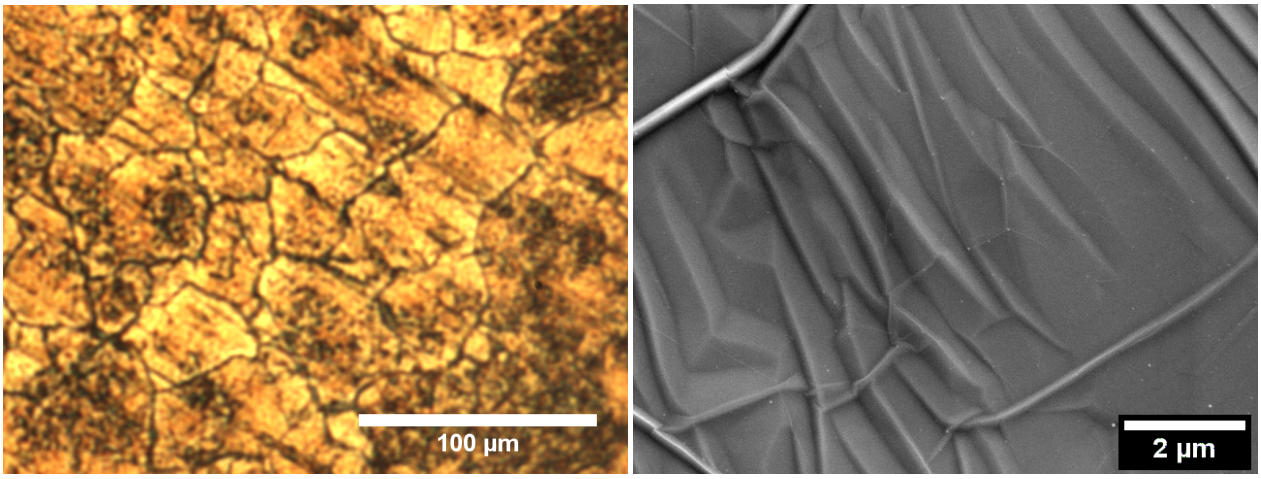

(a) Optical Image (b) Scanning Electron Micrograph

Figure 2.12: Images of few-layer graphite grown by nickel CVD.

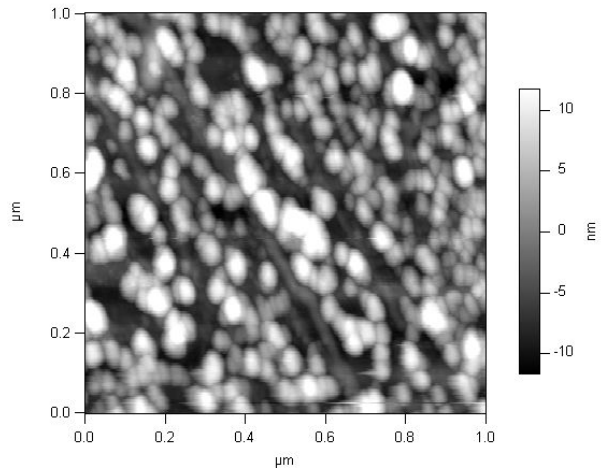

Figure 2.13: Atomic force microscope image of particles, likely PMMA residues, on transferred CVD graphene.

coverage is virtually monolayer. Using copper instead of a transition metal to produce only monolayer graphene was the major advance of Li et al. [98]. The reason why copper produces a single layer while nickel produces more layers can be understood from the solubility phase of diagrams of carbon in the two metals, Figure 2.14. In weight percent, the solubility of carbon at the melting point of copper, 1085 °C, is only 0.0076%. This low solubility of carbon is a common feature of the noble metals (Fig. 2.15). On the other hand, the solubility of carbon in the transition metal nickel at its melting point of 1455 °C is 0.6 wt%! Even at 1085 °C, this solubility is still orders of magnitude higher than in copper. The carbon solubility at the maximum furnace temperature will determine the amount of carbon contained in the substrate which will have to desorb or precipitate into the deposit on its surface as the furnace is cooled.

In the case of nickel, carbon is significantly dissolved in the bulk, and then precipitates and graphitizes as the furnace is cooled, leading to coverages much greater than a monolayer. When the cooling or heating cycles are performed out-of-equilibrium it is possible to obtain thinner coverage. This is the trick employed by Kim et al. [88]–rapid cooling–to obtain small single-layer graphite regions on nickel foils. Unfortunately, the coverage is non-uniform, and the nickel CVD synthesis is not suitable for experiments or applications requiring absolutely one layer. However, it can be very useful for making thin graphite films, where the layer number is not critical. Scanning-electron and optical images of few-layer graphite grown by CVD on nickel thin films (200 nm) evaporated on oxidized silicon substrates is shown in Fig. 2.12.

Copper, with its lower solubility, can produce uniform monolayers because carbon is not dissolved significantly in the bulk. Graphene production occurs by graphitization of surface adsorbed carbon, and is a surface-limited process. Although small patches of double- or triple-layer graphene can be produced if the high-temperature hold time is long, under normal conditions the entire copper foil area will be monolayer.

The difference between the two growth methods, nickel vs. copper, were clearly elucidated by Li et al. [99] in a carbon isotope Raman study. They used both normal and isotopic methane ($^{13}CH_4$) as the precursor gas for synthesis, and timed their delivery. Scanning micro-Raman spectroscopy (Section 3.2) on the resultant graphene/Ni and graphene/Cu could identify the isotopic composition spatially on a micron scale. It was observed that the isotopic composition was completely random for the few-layer graphite on nickel, indicating that the carbon did not graphitize before being first dissolved and mixed in the bulk and then precipitating to the surface. On the other hand for graphene on copper, the isotope spatial distribution was connected, forming circular rings indicating that graphitization occurred as carbon atoms adsorbed on the surface. From this data, a radial graphene growth rate could be determined of roughly 3 µm/min, whereas for bilayer and trilayers the growth rates are much lower, <160 nm/min and <40 nm/min, respectively.

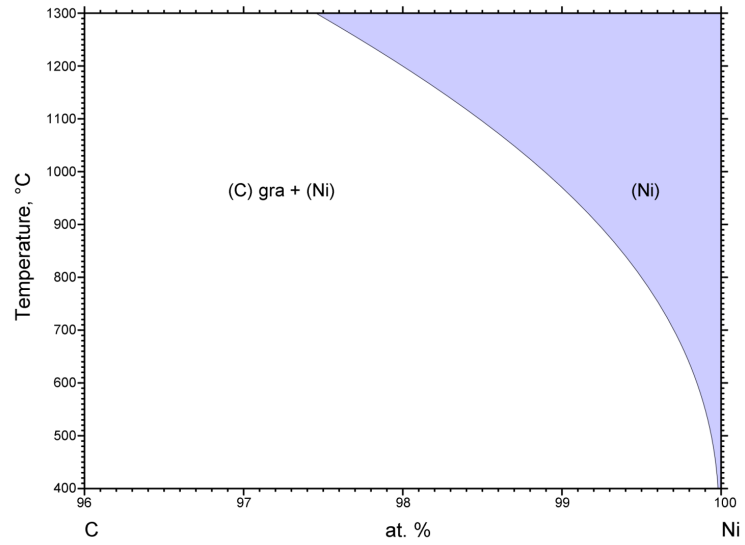

(a) Nickel

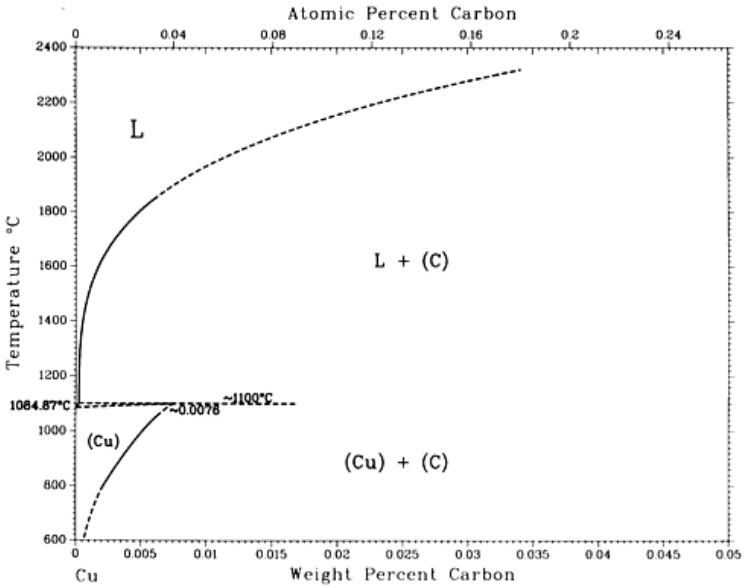

(b) Copper

Figure 2.14: Carbon solubility phase diagrams. Copyright ASM International.

Alternative Substrates

If the important factor for CVD graphene synthesis is the substrate's carbon solubility, are there alternatives to copper? Arnoult and Mclellan [6] studied the solubility of carbon in different metals in the dilute limit in 1972. They found that the solubility θ for the transition metals Rh, Ru, Ir, Re; the noble metals Au, Cu, Ag; and Pd are well described by a thermodynamic model by Mclellan called the "quasi-regular approximation" [105]:

$$\theta = e^{-\frac{\Delta\bar{H}}{kT}} e^{\frac{\Delta\bar{S}}{k}} \tag{2.2}$$

where $\Delta\bar{H}$ is the relative partial enthalpy of a carbon atom in solution and $\Delta\bar{S}$ is the relative partial excess entropy. These quantities are determined by fitting to measured data and given in Arnoult and Mclellan's paper [6]. The solubilities can then be plotted as a function of temperature (Fig. 2.15).

From these curves, we can see that the noble metals have an extremely low carbon solubility, with copper having the lowest solubility in the temperature range above 970 °C, and gold beating copper at lower temperatures. Hence at the high temperatures necessary to allow dehydroxylation of methane on the substrate surface and resultant carbon graphitization, copper is ideal. Of the transition metals, the ones with the lowest carbon solubility are those plotted. Although in comparison to nickel, they have orders of magnitude less solubility, this solubility is still a factor ten larger than that of the noble metals.

Despite copper's low carbon solubility, it is not the ideal substrate for certain experiments and electronic applications with CVD graphene. The melting points of copper (1085 °C) and the other noble metals (Au, 1064 °C and Ag, 962 °C) are relatively low compared to the transition metals. This means that it is not possible to use thin films (<100 nm) of the noble metals, grown for example by electron-beam evaporation onto an oxidized silicon wafer, as a substrate for graphene growth. At temperatures much less than the melting point, metallic thin films tend to ball up and form discontinuous islands due to surface tension (Fig.2.16). This is the reason copper foils of at least several micron thickness are necessary for CVD synthesis. The minimum thickness for a copper thin film on silicon oxide substrate that can produce a continuous graphene sheet is 500 nm (personal communication, Yuegang Zhang, Molecular Foundry, LBL).

Ideally, such a graphene/metal-thin-film/SiO_2/Si^{++} stack would be patterned directly into devices and etched, the metal thin film in the unetched areas serving as electrodes. This has several advantages: the graphene does not have to be transferred to another substrate, the graphene/electrode contact is expected to be extremely good as the graphene is grown directly on the contact, and the graphene in the active region is suspended, leading to higher mobilities. This process is shown in Figure 2.2.2.

The problem with using a half micron copper thin film is that, due to the isotropic nature of the wet etch process, the film thickness sets the minimum device feature size. For ballistic transport experiments and electronic device applications, this large feature size and thus copper usage is unacceptable. However, this technique has been used to make large micron-scale devices [97]. In order to have smaller feature sizes, a metal thin film with a higher

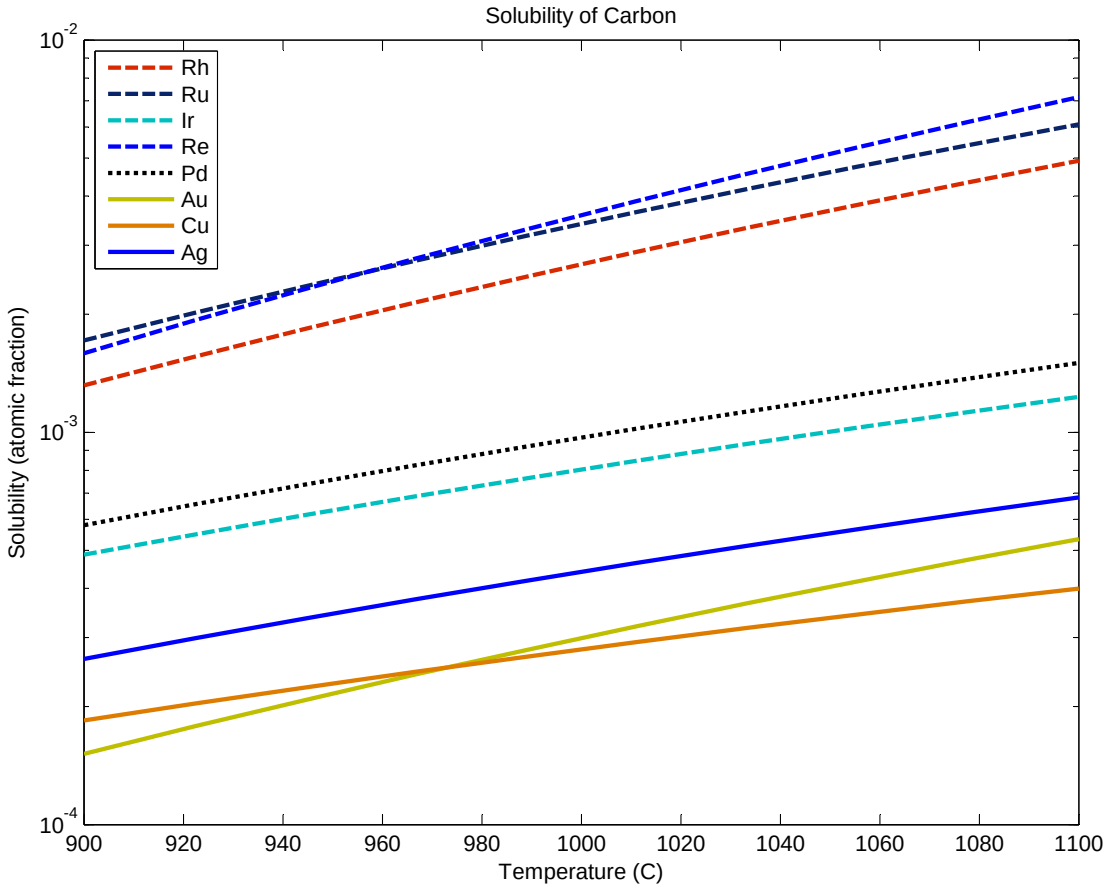

Figure 2.15: Solubility of carbon in selected transition and noble metals.

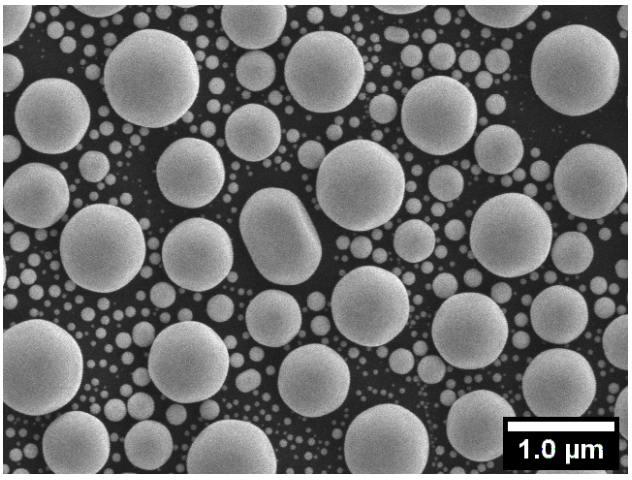

Figure 2.16: Indium island formation.

melting temperature and low carbon solubility is required.

From the carbon solubility curves (Fig. 2.15), good candidates for such metals are palladium (melting point 1555 °C) or one of the rare transition metals rhodium (Rh), rhenium (Re), iridium (Ir), or ruthenium (Ru), all of which have melting points well above 2000 °C. Palladium's melting point is unfortunately not high enough for the processing of 100 nm thin films at 1000 °C–discontinuous islands are formed. Of the rare transition metal alternatives, most are both prohibitively expensive *and* have such high melting points that electron-beam evaporation of thin films is not possible. Ruthenium, with the lowest melting point of the group, at 2334 °C, can be electron-beam evaporated and thin films up to 200 nm were produced on oxidized silicon. Unfortunately several attempts at graphene growth on these films was not successful, likely as a result of contamination (Fig. 2.18). Others have had success growing graphene on $Ru/SiO_2/Si^{++}$ [139, 140], but no etching or device fabrication has been attempted. This is a promising direction to pursue as well as attempting CVD graphene growth with sputtered films of iridium or the other transition metals. It is essential for ballistic transport experiments in graphene to have suspended short-gap junctions with good, transparent contacts, and this route seems like a promising one.

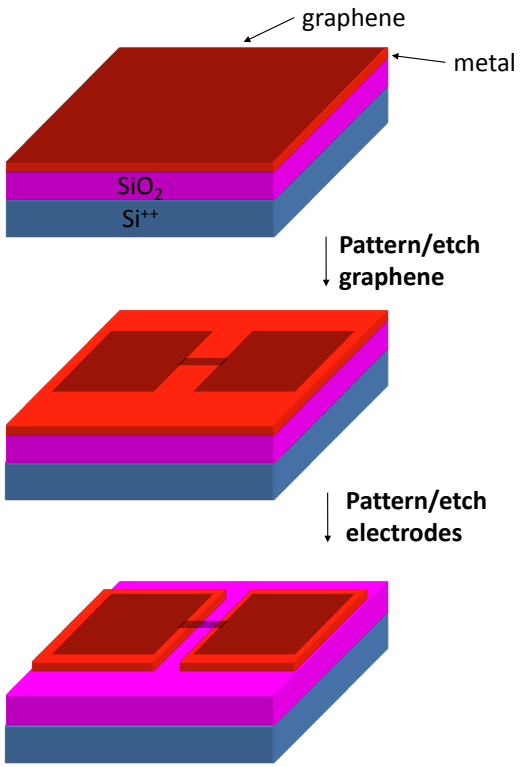

Figure 2.17: Schematic process for ideal CVD graphene device fabrication. Graphene is grown by CVD on a metal thin film deposited on an oxidized silicon wafer. The graphene is then patterned by electron or optical lithography and etched by an oxygen reactive ion etch. Finally, the metal thin film is patterned and etched chemically, resulting in a suspended graphene device with a high quality contact.

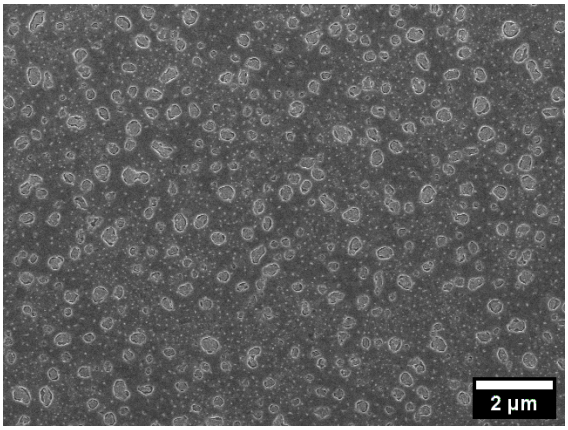

(a) SEM micrograph 1

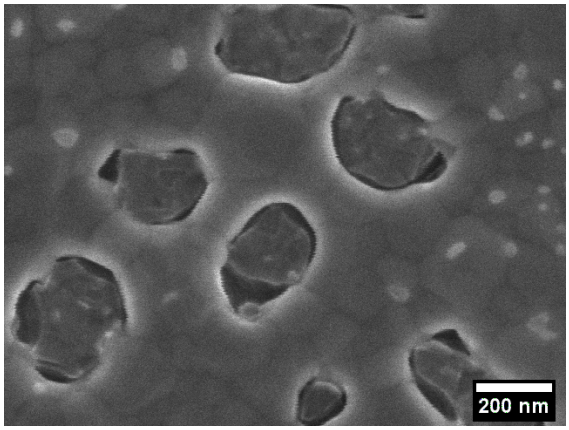

(b) SEM micrograph 2

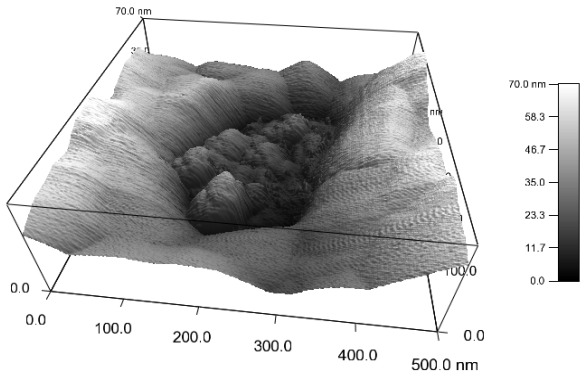

(c) AFM 3D plot of defect

Figure 2.18: Graphene growth attempt on ruthenium thin film.

Chapter 3

Characterization

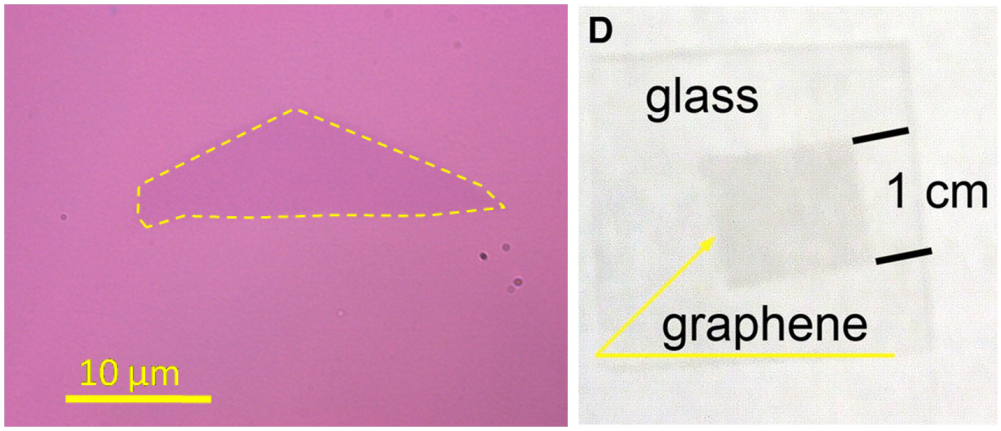

(a) Exfoliated graphene flake on SiO_2/Si^{++}

(b) Large-area CVD graphene on glass, Li et. al [98]

Figure 3.1: Optical microscopy of graphene.

As an atomically thin material, it is not obvious that graphene can be easily detected, either optically or by other means. But in fact a large enough sheet of graphene can actually be seen by the human eye alone and smaller samples with the aid of a microscope (Fig. 3.1), with a contrast $\pi\alpha \simeq 2.3\%$ at normal transmission over a broad range of wavelengths, where α is the fine-structure constant $e^2/hc \simeq 1/137$ [113].

In this chapter specific aspects of different methods of detecting graphene will be covered, in order of increasing instrumentation complexity. All techniques can identify single-layer sheets but each has in addition unique capabilities. Optical microscopy is the quickest way to determine whether one has single-layer graphite and can be used to precisely determine the number of layers for stacks of up to about ten layers. Raman spectroscopy is a very powerful graphene characterization tool that can give information on parameters such as the

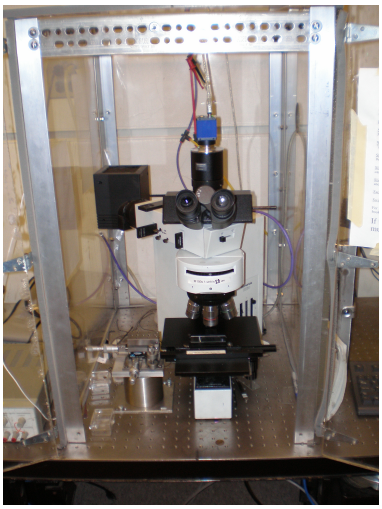

Figure 3.2: Olympus BX-50 optical microscope, Zettl group.
Three long working distance objectives are visible, along with CCD camera (blue), and three-axis micromanipulation stage (left of microscope) mounted to optical table. The entire setup is enclosed in a plexiglass dust protection box.

electronic doping, sample disorder, and strain [1]. Atomic force microscopy (AFM), in addition to determining the number of layers in arbitrarily large stacks, can be used to locally probe the work function, force constants, electric potential drop, or other properties. Transmission electron microscopy (TEM), especially its aberration corrected incarnation, can be used to study atomic-scale defects and dynamics in graphene sheets.

3.1 Optical Microscopy

Optical identification of graphene, even 10 µm exfoliated samples, should be easy with any optical microscope equipped with at least a 20x objective and 10x eyepieces. However, there are many additional accessories or upgrades to a standard optical microscope that are both useful for graphene characterization as well as manipulation. If possible, the series of objective magnifications should be 2x, 5x, 10x, 20x, 50x, and 100x. For a microscope with a five objective limit, abandon one of the 2x or 5x objectives. The higher magnifications are useful to look at features in graphene sheets such as folds, corners, edges, defects, or adsorbates; and also serve to inspect lithographed graphene devices. The lower magnification objectives, especially 10x, are suited for quickly scanning large substrate areas for large (>100 µm diameter) exfoliated samples. If possible, although much more expensive, the objectives should have a long working distance (Mitutuyo). These objectives allow inserting

[1] Carbon Raman spectroscopy specialist, Andrea C. Ferrari, of Cambridge University will tell you that Raman can tell you anything you want to know about graphene.

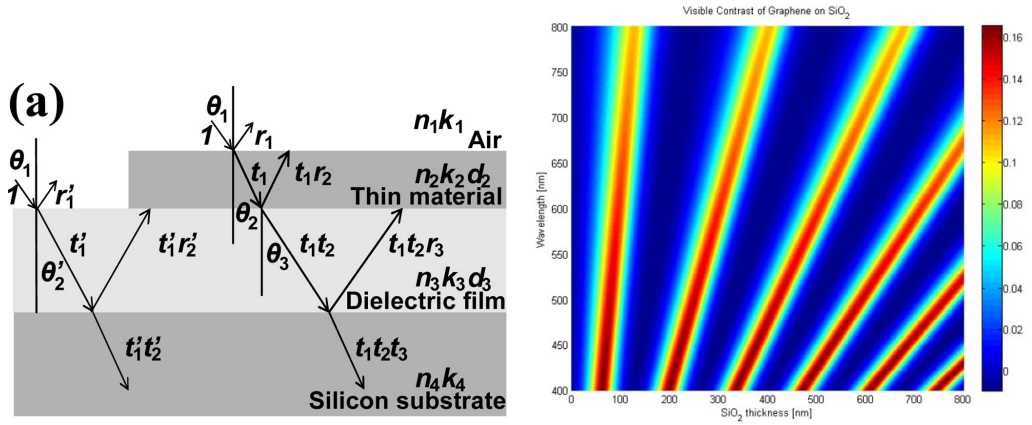

(a) Optical path geometry and parameters, from [83].

(b) Optical contrast, from McEuen Wiki

Figure 3.3: Optical contrast of graphene on SiO_2.

micromanipulation probes between the objective and sample, which is useful, among other things, for mechanically manipulating graphene, making alignment marks for lithography (Section 4.1), soldering micro-contacts (Section 4.2.3), or positioning shadow masks for resist-free lithography (Section 4.2.2). For these purposes, described in detail in Chapter 4, a three-axis micromanipulation stage, such as the Newport 561 ULTRAlign, can be mounted next to the microscope on an optical table (Fig. 3.2).

A good CCD camera is also a necessity for both cataloging samples and making a precise identification of the number of layers in graphene stacks. Images of graphene samples shown here were recorded with a Matrix Vision mvBlueFOX 121C, which is a 24-bit color CCD camera with 1/3 inch sensor.

3.1.1 Graphene Identification

The contrast of a graphene sheet on SiO_2/Si^{++} or other dielectric stacks was calculated by several groups in 2007 [1, 83, 115, 126]. The reflected light intensity is obtained from the interference of multiple optical paths through the stack (Fig. 3.3(a)). The contrast, c, can be expressed as the difference in the reflected intensities with and without the graphene sheet divided by the sum of the intensities:

$$c = \frac{R - R_g}{R + R_g} \tag{3.1}$$

where R (R_g) is the reflected intensity without (with) the graphene [83]. This quantity is referred to as the Michelson contrast.

The technique to optimize contrast for graphene is similar to that used in anti-reflection coatings on glasses. For a given wavelength, if the the optical path through substrate plus

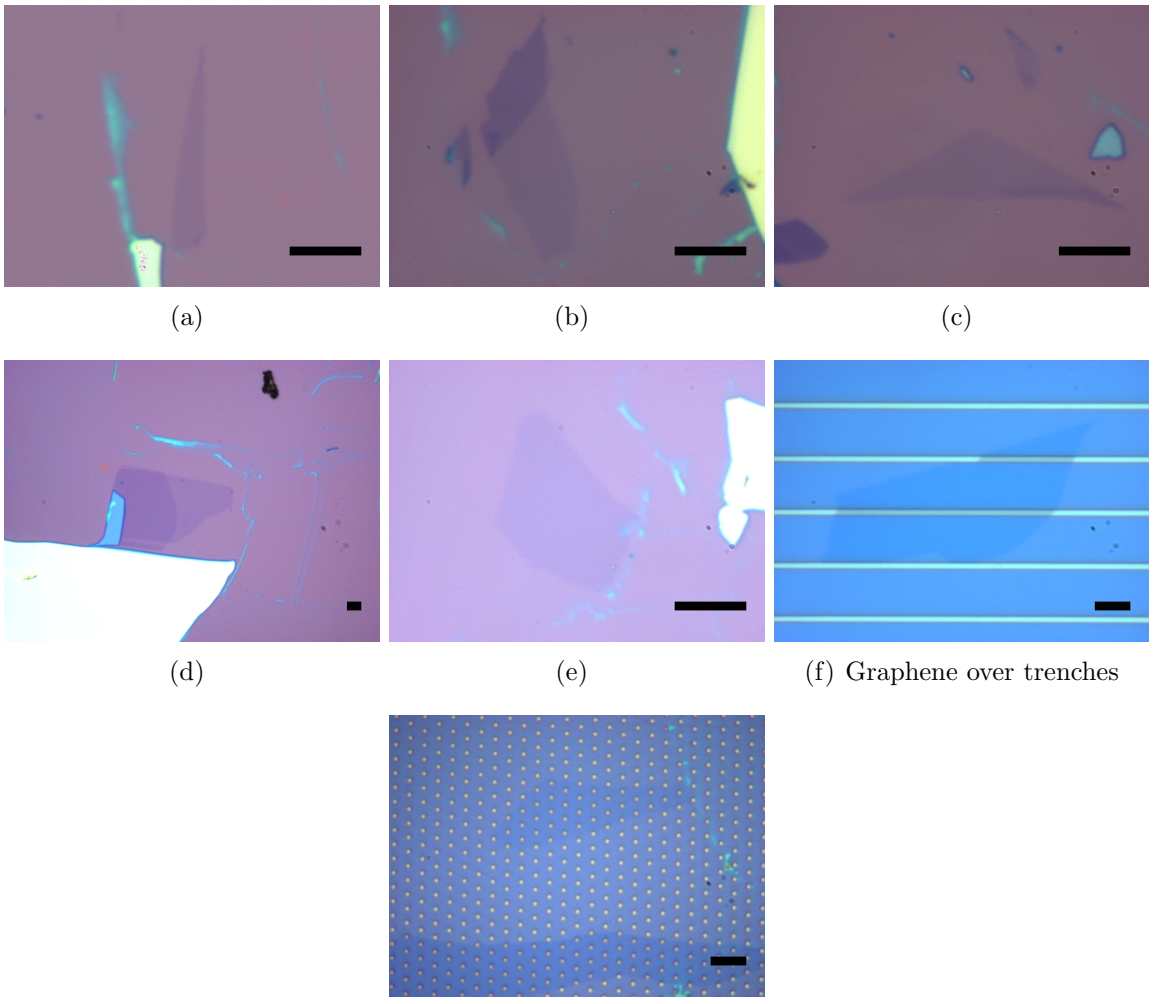

(a) (b) (c)

(d) (e) (f) Graphene over trenches

(g) Graphene over holes

Figure 3.4: Optical images of graphene. All scale bars 10 µm.

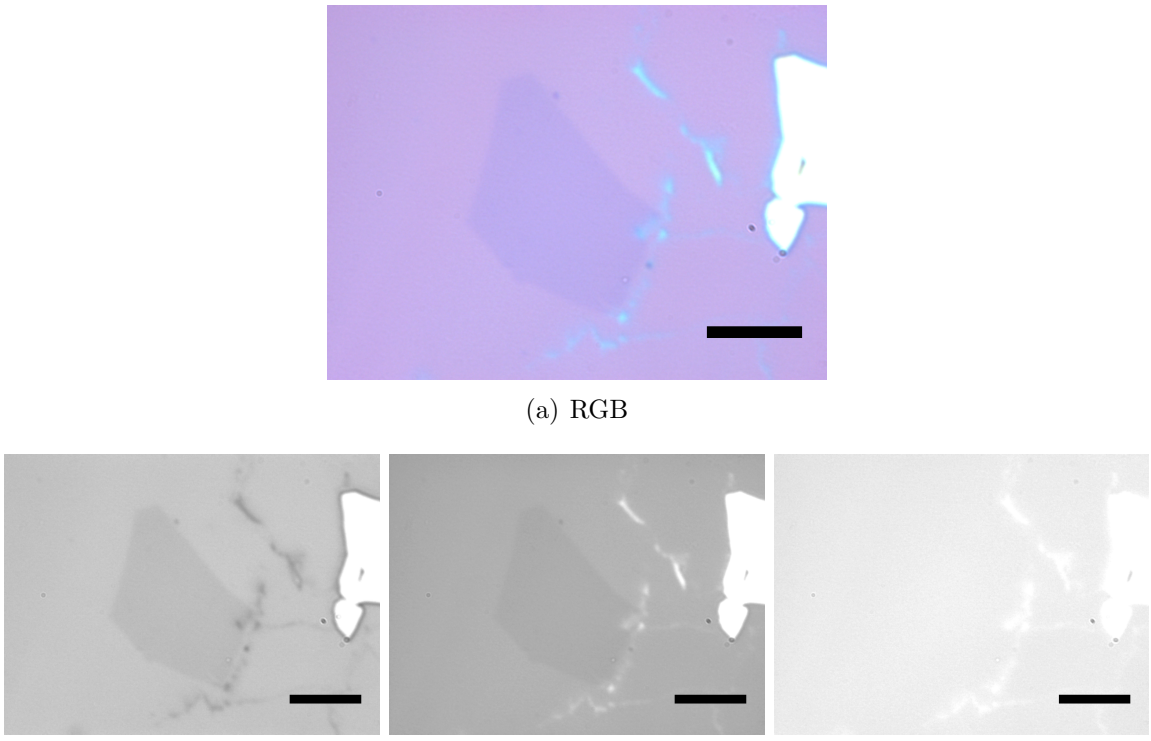

(a) RGB

(b) Red (c) Green (d) Blue

Figure 3.5: Wavelength dependence of graphene contrast. Scale bar 10 µm.

graphene causes destructive interference with the light reflected at the graphene, the intensity difference can be large. For graphene on thin films of SiO_2, the optimal oxide thicknesses are 90 nm and 285 nm, which maximize the contrast in the visible part of the optical spectrum (Fig. 3.3(b)). For the thinner oxide, the contrast is larger over a wider spectral range. For the thicker oxide, the peak in contrast is between 600 nm to 650 nm, which corresponds to a yellow/orange color. A slightly thicker oxide (above 285 nm) will push the peak contrast value toward red, and a thinner oxide toward green. All exfoliated graphene samples presented here were peeled onto wafers with oxide thickness in the range 280 nm to 300 nm. Despite a range of only 20 nm, as a result of the significant dependence of contrast on wavelength and oxide thickness in that interval, as well as the variation in microscope settings, graphene can appear quite different in RGB images (Fig. 3.4).

Taking one graphene RGB image (Fig. 3.4(e)) and splitting the channels into red, blue, and green the contrast is maximum for the red channel at roughly 630 nm, Figure 3.5), as expected from the contrast map (Fig. 3.3(b)) for an oxide thickness closer to 300 nm. The blue channel, at a wavelength near 430 nm, can hardly be used to identify the graphene as the contrast is virtually zero.

In order to quantitatively determine the contrast, an accurate method is to take a histogram of the sample plus substrate, which should give a bimodal distribution, Figure 3.6.

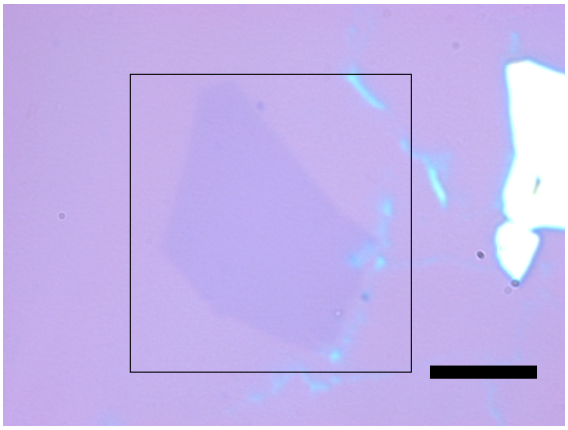

(a) Area for histogram calculation, sample Fig. 3.4(e)

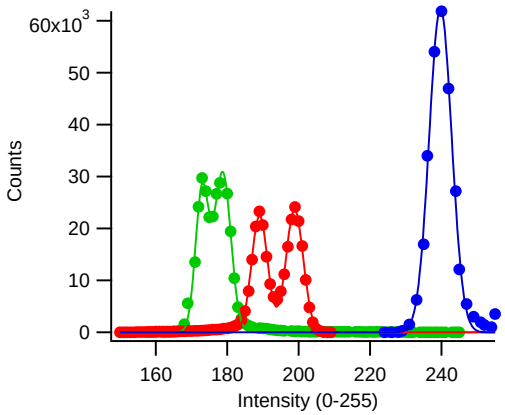

(b) Histogram of RGB Channels, sample Fig. 3.4(e)

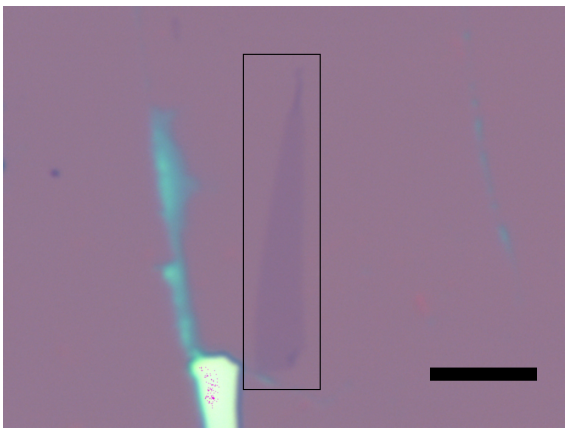

(c) Area for histogram calculation, sample Fig. 3.4(d)

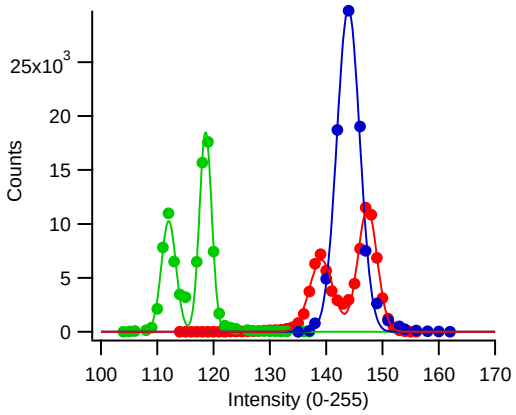

(d) Histogram of RGB Channels

Figure 3.6: Identifying graphene in optical images by analyzing histograms.

The histogram of a region surrounding the graphene sample is calculated for each channel separately. Two peaks are found in the red and green channels, with the higher intensity peak corresponding to the substrate without graphene, and the lower intensity peak to substrate plus graphene. In the blue channel, although there should be two distinct peaks, it appears as one because the peak separation is smaller than the intensity resolution and peak widths. The areas under the peaks correspond to the areas in pixels of the graphene and substrate in the histogram region. By choosing the histogram region carefully, the two peak heights and areas should be comparable.

Gaussians fit the peaks well and one can extract the peak positions to determine the Michelson contrast. This gives 2.56% (red) and 1.59% (green) for the sample in Fig. 3.4(e); 2.96% (red) and 2.89% (green) for the sample in Fig. 3.4(d). These are typical contrast

values for graphene on SiO_2/Si in the oxide thickness range of our wafers. One can see that for these two samples imaged under different conditions, the absolute intensity values differ markedly, about sixty grayscale values. Although the absolute values will depend on the imaging conditions, the contrast should depend only on the oxide thickness. As will be seen below, the contrast from few-layer graphite (with more than one layer) will have at least twice the contrast of graphene. For a silicon dioxide thickness of roughly 285 nm, one can reliably conclude that a sample is graphene if the red-channel contrast is between two and three percent.

3.1.2 Multilayer Identification

The widths of the intensity peaks are determined by the microscope optics settings and detector noise. The noise from a good CCD detector should not be more than several grayscale values with standard illumination and exposure times. Thus the peak widths are dominated by nonuniformities in the image due to the aperture and alignment settings. By adjusting the apertures, one can maximize contrast near the center of the field of view while compromising illumination uniformity over the entire field-of-view. This illumination nonuniformity can widen the peak widths in the calculated histograms. If the peaks are too wide, one can not quantitatively resolve the contrast difference between a graphene sheet and the substrate, as with the blue channel image, or different layers of a few-layer graphite sample. For the case of a single graphene sheet, the illumination nonuniformity should not hamper detection with the red or green channels because the contrast is relatively large: a few percent. It would take extremely poor imaging conditions to have peaks wide enough to hide the peak positions for those channels.

However, for the case few-layer graphite, the intensity difference between n layers and $n+1$ layers goes down as n increases. When one wants to accurately determine optically the number of layers in a few-layer graphite sample above, say four layers, the peak widths in the histogram are extremely important. If the peak width greatly exceeds the intensity difference between n and $n \pm 1$ layers, the layer number determination will not be accurate. Thus illumination uniformity should be optimized as much as possible when searching for large-n flakes.

Sometimes, even if the illumination is not optimized for uniformity and fixed for reproducibility, one can use image processing to correct these errors and reduce the peak widths. In this manner, one can determine the number of layers in thicker graphene stacks. One technique to correct illumination nonuniformity is lowpass filtering, but there are other techniques also such as background subtraction. The length scale for variation in the illumination due to optical settings is usually large, on the order of the image size, whereas the variation in contrast due to a graphene sheet on a substrate is several pixels. By filtering out large-wavelength components of the image, we can correct the illumination nonuniformity as a result of optical settings. ImageJ, an image processing and analysis program developed at NIH predominantly for biology applications, is free and easy-to-use, and comes with both background subtraction and bandpass filtering routines.

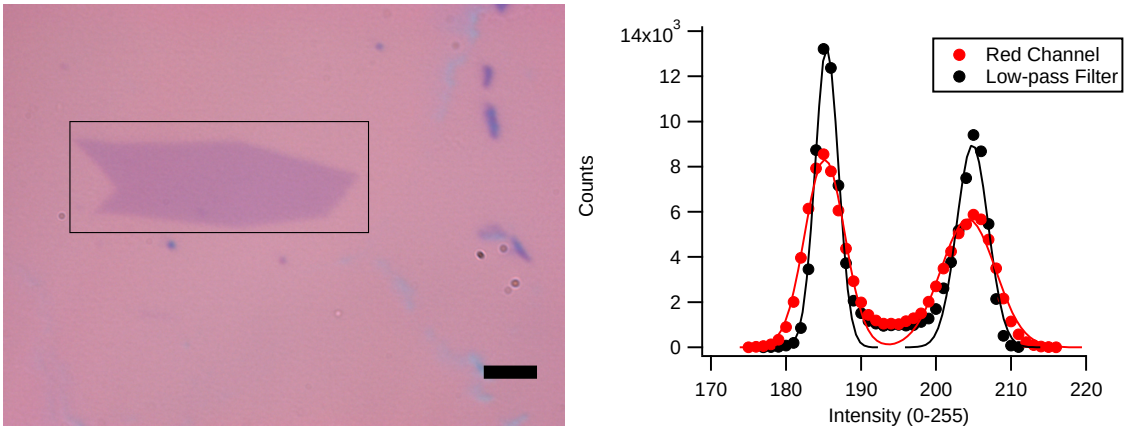

(a) Bilayer graphene sample

(b) Histogram comparison

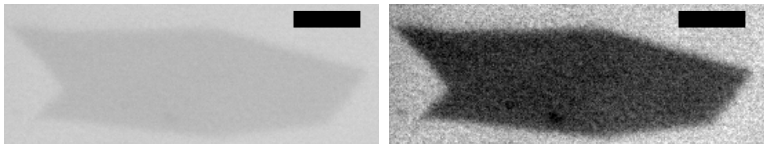

(c) Green channel

(d) Auto contrast

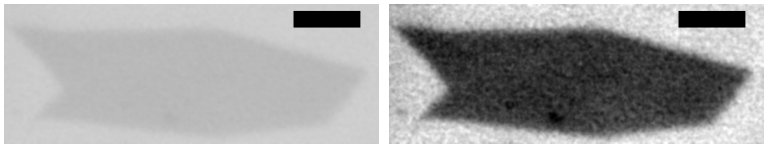

(e) Lowpass Filter

(f) Lowpass filter and auto contrast

Figure 3.7: Lowpass filtering correction of illumination nonuniformity. Scale bar 5 µm.

It is illustrative to demonstrate the peak narrowing effect as a result of lowpass filtering on a bilayer graphene sample. Figure 3.7(a) shows a bilayer graphene sample with a rectangle indicating the region where the red channel image (Fig. 3.7(c)) histogram is calculated, Fig. 3.7(b). The effect of auto-contrasting for better comparison is shown in Fig. 3.7(d). To apply the lowpass filter, the bandpass function of ImageJ (menu "Process; FFT; Bandpass Filter...") is used, with a low-frequency cutoff of 500 pixels, and a high frequency cutoff of 3 pixels. The low-frequency cutoff is roughly the width of the region of interest, and should remove large-scale illumination nonuniformity. The high-frequency cutoff will reduce pixel noise. Figure 3.7(e) shows the lowpass filtered image and is auto-contrasted in Figure 3.7(f). The eye can hardly discern the effect of the lowpass filter, but the histogram Fig. 3.7(b), makes it evident. The full width at half max (FWHM) of the unfiltered peaks for bilayer and substrate are 6.25 ± 0.08 and 8.59 ± 0.14 respectively. After lowpass filtering these widths are almost halved to 3.65 ± 0.07 (bilayer) and 4.94 ± 0.11 (substrate). The contrast for the bilayer is 5.0%, roughly twice that of the previous graphene samples.

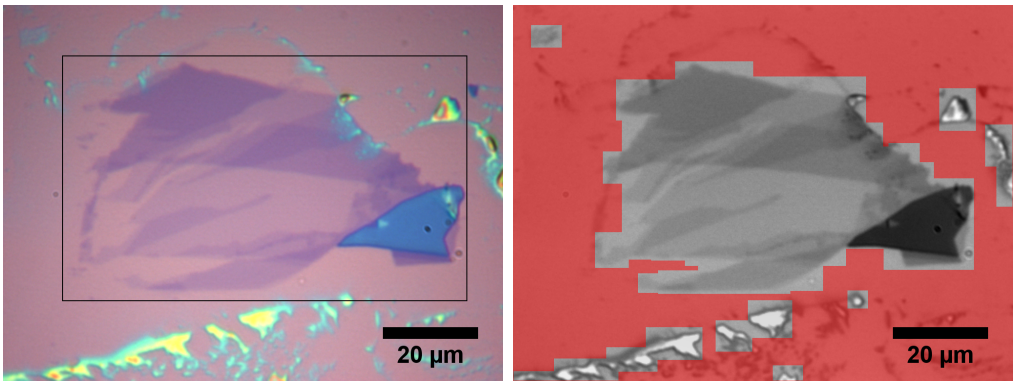

(a) Few-layer graphite sample (b) Masked region (red channel)

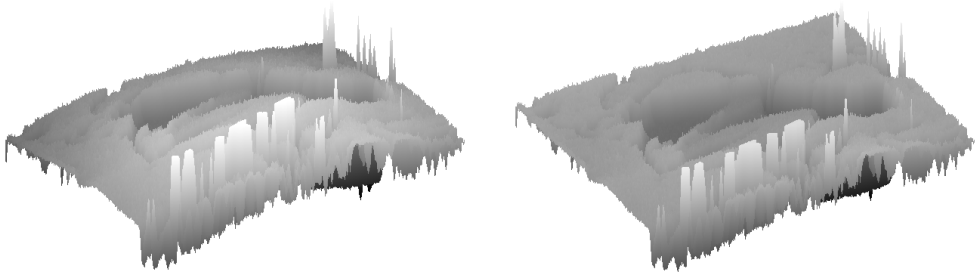

(c) 3D surface plot (d) Flattened 3D surface plot

Figure 3.8: Fixing illumination nonuniformity for multilayer identification by paraboloid flattening.

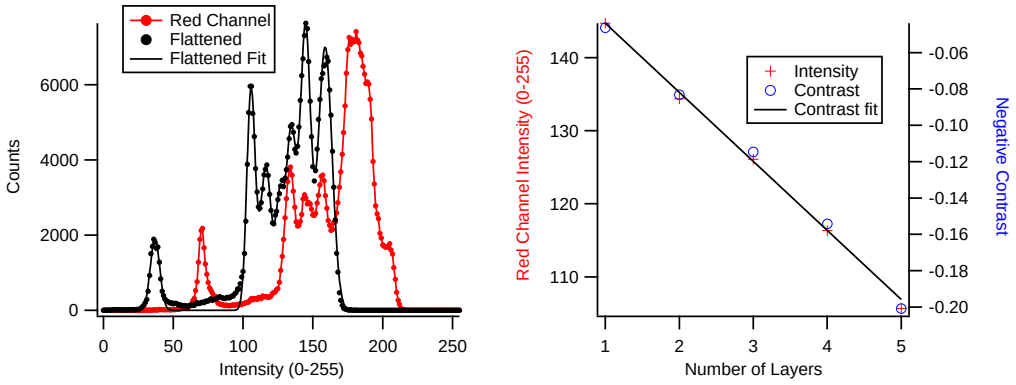

(a) Histogram of red channel, Fig. 3.8(a) (b) Contrast per layer 3.8%

Figure 3.9: Determining contrast as a function of layer number. Channels red, green, blue (left to right). Scale bar 20 µm

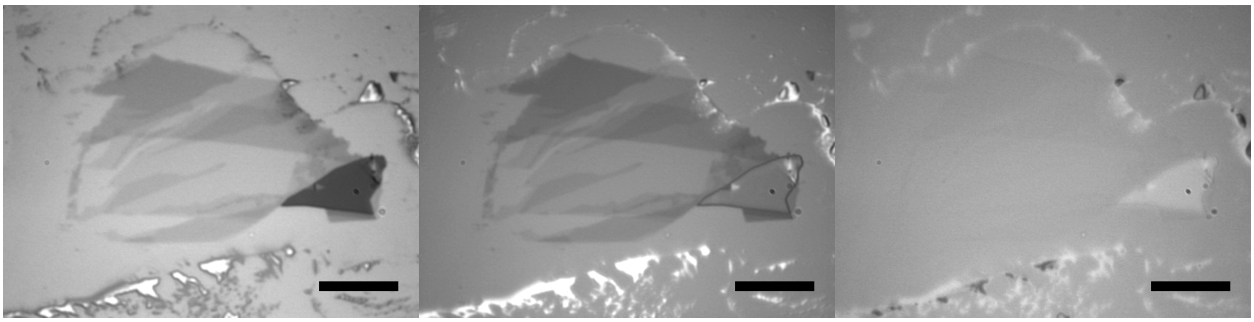

Figure 3.10: Inversion of contrast for thick regions at shorter wavelengths.

Moving on to thicker multilayer samples, the effect of illumination nonuniformity is clearly shown in Figure 3.8. The sample is large and the objective used when taking the image was 50x. If the microscope apertures had been constricted to optimize contrast for the 100x objective, this can result in darkening of the image boundary at subsequent lower magnification imaging, as seen in the 3d surface plot Fig. 3.8(c). A paraboloid background is clearly visible, due to higher illumination at the center of the image. One can correct such errors by fitting a second order polynomial to the silicon oxide substrate, which is flat and under uniform illumination should give uniform optical intensity. The region to be fit is masked, shown in red in Fig. 3.8(b). After subtracting the paraboloid background and adding the mean intensity value, one obtains Fig. 3.8(d), which shows that the substrate region is now planar as it should be. Gwyddion, free software designed for processing and analysis of scanning probe microscopy data, was used to perform the fitting and background subtraction (menu "Data Process; Level; Polynomial Background..."). Gwyddion has many options, including higher-order polynomials and sphere fitting for leveling of images, but a paraboloid should be sufficient for the Gaussian illumination profile one expects in optical images.

One additional algorithm which is useful for image flattening of terraced structures such as multilayer graphite flakes is facet leveling (Gwyddion menu "Data Process; Level; Facet Level"). This algorithm fits planes to a series of terraces. The inverse of the masked region in Fig. 3.8(b) is selected and the facets leveled. The effect of flattening by both paraboloid fitting and facet leveling on the histogram of the rectangular region in Fig. 3.8(a) is shown in Figure 3.9(a). The histogram has shifted with flattening due to correcting the entire image with the mean of the fitted paraboloid. More importantly, the histogram area which must be conserved, has redistributed to better resolve the peaks. The peaks corresponding to the substrate and different graphene layers are distinct in the flattened histogram for all but the trilayer, at intensity level 127. Plotting the grayscale values and contrast versus layer number , Fig. 3.9(b), we obtain a contrast of $3.80 \pm 0.15\%$ per layer. This value should be accurate up to thicknesses much smaller than a quarter wavelength for red traveling in the graphene. The thickest part of the flake in Fig. 3.8(a) is calculated to be 16.3 layers. Care must be taken when extrapolating this contrast dependence to higher layers, especially with

shorter wavelength light, Fig. 3.10. The contrast is inverted (lighter intensity than substrate) for the blue channel and close to zero for the green channel in the thick region of the flake.

3.2 Raman Spectroscopy

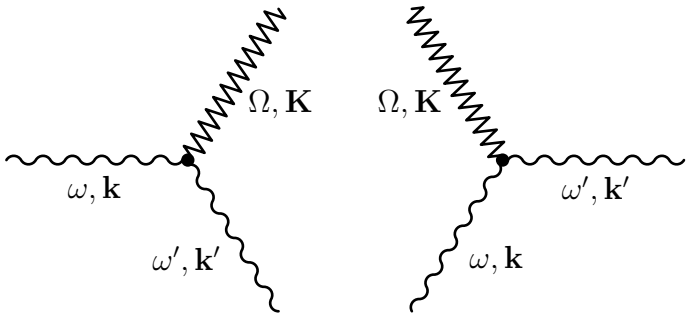

(a) Stokes (b) anti-Stokes

Figure 3.11: Raman scattering Feynman diagrams.

Raman spectroscopy is a technique which uses inelastically backscattered light to probe atomic vibrations as well as electronic structure in materials including crystals, amorphous solids, and molecules. In what is called a first-order Stokes process, a photon of energy $\hbar\omega$ and wavevector $\mathbf{k}$ incident on a crystal sample creates a phonon (energy $\hbar\Omega$, wavevector $\mathbf{K}$) and emits a photon of reduced energy $\hbar\omega' < \hbar\omega$ and wavevector $\mathbf{k}'$. In an anti-Stokes process, an incident photon combines with a crystal phonon and a photon of higher energy is emitted ($\hbar\omega' > \hbar\omega$). Both processes are schematized in Figure 3.11. The selection rules are $\omega = \omega' \pm \Omega$ and $\mathbf{k} = \mathbf{k}' \pm \mathbf{K}$. In actuality, the incident photon in Stokes scattering excites an electron-hole pair which drops to a lower energy by emitting a phonon and then recombines to produce the outgoing photon. A similar process occurs for anti-Stokes scattering. Raman scattering is described in detail in Yu and Cardona [160]. The Raman shift is given in wavenumbers (cm^{-1}) with positive wavenumbers corresponding to phonon emission (Stokes) and negative wavenumbers corresponding to phonon absorption (anti-Stokes). Higher order and resonant Raman processes can also occur, where multiple phonons are involved and special selection rules are met.

Raman spectroscopy of small samples, where a laser beam is focused through objectives onto a micron-scale sample, is often called micro-Raman. Such a Raman spectrometer consists of a laser light source, usually at 514 nm or 633 nm for graphene measurement; an optical path to guide the laser light into a microscope and onto the sample; a holographic notch filter to remove the high-intensity backscattered light at the incident wavelength; and a grating and CCD camera to measure the distribution and wavelengths of the Raman shifted reflected light. A typical micro-Raman setup is shown in Fig. 3.12, the Zettl group spectrometer from Renishaw. Four solid-state lasers rest on an optical table behind the

Figure 3.12: Zettl group micro-Raman spectrometer. Zettl group Wiki.

spectrometer assembly. The laser light is guided through the spectrometer and into the microscope at left, which is used to locate samples and focus the light. The motorized stage on the microscope can be used to acquire spectral maps of samples, as shown below. The reflected light returns to the spectrometer where it is filtered and reflected off the grating and onto the CCD camera. The entire system is automated and controlled via a computer (not shown) but occasional optical realignment inside the assembly is necessary.

3.2.1 Graphene Identification

The Raman spectroscopy signature of graphene was clearly identified by Ferrari et al [51]. Although others also measured Raman spectra of graphene around the same time [66, 63], Ferrari was able to use electron diffraction data to conclusively establish that his sample was single layer. There are two main spectroscopic features of graphene, shown in Figure 3.13, called the G band, or G peak, around $1580\,\mathrm{cm}^{-1}$ and the 2D band around $2700\,\mathrm{cm}^{-1}$ [50]. In the presence of disorder there is a third peak called the D band at $1350\,\mathrm{cm}^{-1}$.

The "G" in G band (Fig. 3.13(c)) refers to graphite because this peak is present in all carbon materials with sp^2 bonding. The G band Raman interaction corresponds to in-plane stretching of the sp^2 bonds. In solid-state terms, it is an excitation of the in-plane transverse and longitudinal optical phonon at the Γ point, in which the carbon atoms at the A and B sublattices move in opposite directions. This process is schematized in Figure 3.14 (a1), where the crossed linear bands correspond to an idealized graphene band structure (ignoring trigonal warping). The line connecting the upper and lower halves of the Dirac cone corresponds to the production of an electron-hole pair by the incident photon, the short line (small wavevector q) is the emitted zone-center phonon, and the vertical line pointing to the valence band is the virtual transition de-exciting the electron and emitting the Raman shifted photon.

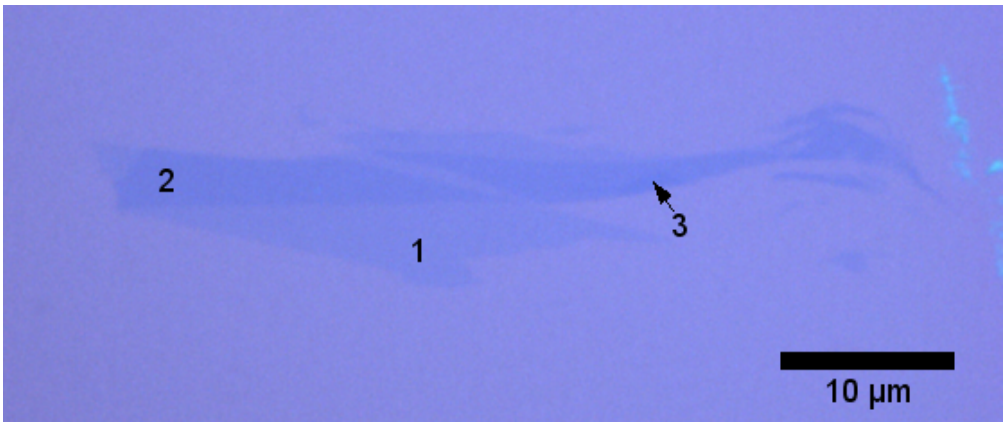

(a) Few layer graphite sample

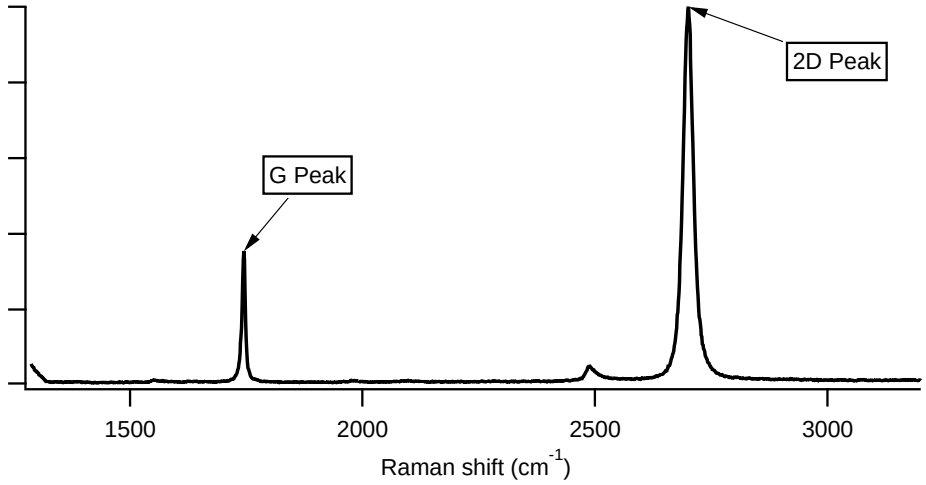

(b) Raman spectrum of graphene

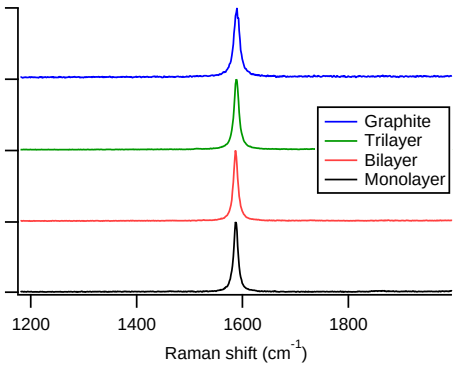

(c) G peak

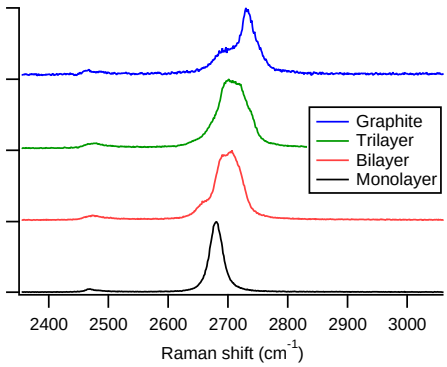

(d) 2D peak

Figure 3.13: Raman spectroscopy features of graphene, bilayer, trilayer, and graphite. Graphite sample not pictured.

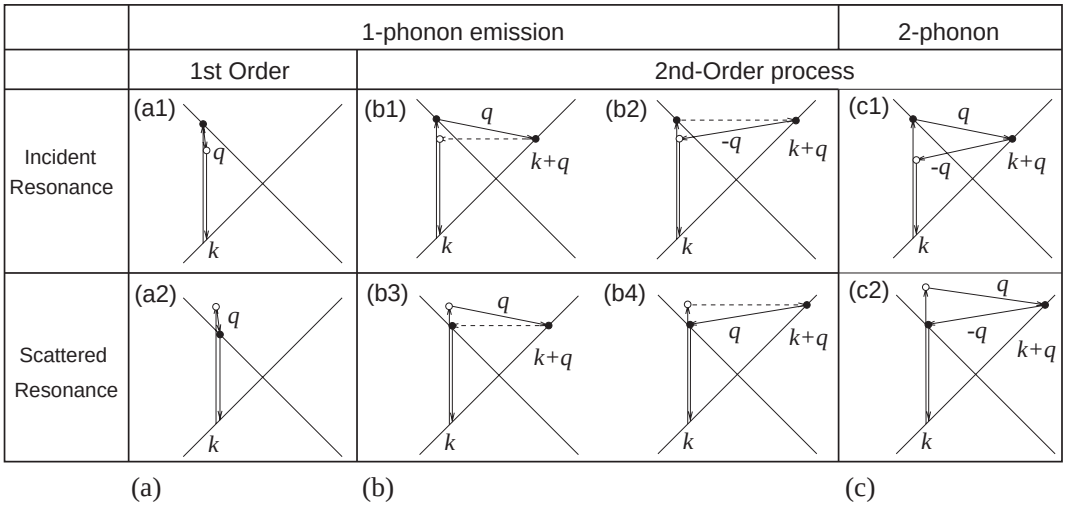

Figure 3.14: Raman scattering processes in graphene [38].

The 2D band ((Fig. 3.13(d)) arises from a doubly resonant Raman process involving two phonons (similar to Fig. 3.14 (c1)). The incident photon first excites an electron near the K point in the electronic band structure. The electron scatters from one branch in the K valley to the opposite branch in the K' valley, where there is a real electronic state at wavevector $k+q$, by emitting a phonon of wavevector q. An identical phonon with opposite momentum $-q$ is subsequently emitted, which brings the electron back to a virtual state below the conduction band at k. At this point the electron-hole pair recombines to emit a photon reduced in energy by almost twice the K point optical phonon ($1350\,\mathrm{cm}^{-1}$) [123]. The important difference with the process in Fig. 3.14 (c1) is that the 2D band comes from intervalley scattering of the excited electron, whereas the picture depicts intravalley scattering. This process is resonant in that the Raman scattering cross section is greatly enhanced when the quasiselection rule $q \simeq 2k$ (wavevectors referenced to the K point) is satisfied, and hence the 2D band can be observed even though it is a second order, two-phonon process [129, 51].

Identifying graphene from the Raman spectrum is extremely easy. The shape of the 2D peak in monolayer graphite should be a single Lorentzian/Gaussian, Figure 3.15(a), whereas it has four components in the case of bilayer graphite (Fig. 3.15(b)), and more for thicker samples [51]. The reason graphene has one peak is because all but the single $q > K$ double resonance process are repressed–the scattering phonon only connects to the opposite branch at the K' point, and to none of the other three possibilities. For bilayer, the electronic bands split to produce four bands, and double resonant scattering with four different phonons takes place, resulting in four peaks for the 2D band in the Raman spectrum.

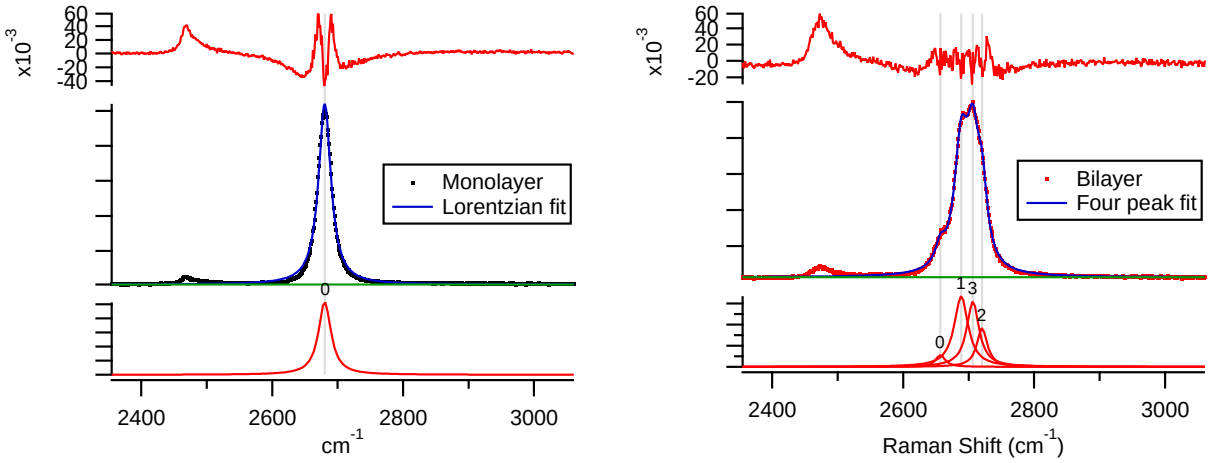

(a) Monolayer Lorentzian fit

(b) Bilayer four Lorentzian fit

Figure 3.15: Identifying monolayer and bilayer graphite by fitting Raman 2D peak. Shown are fits (middle panels), residuals (upper panels), and fit components (bottom panels).

3.2.2 X-Ray Irradiation

The last prominent feature, apparent only in defected graphene, is the D band, shown below. This process is depicted in Fig. 3.14 (b1), except once again in actuality the phonon should connect a state on the Dirac cone at K to a state on the Dirac cone at K'. When there are defects in the graphene, the electron can elastically scatter back, shown by the horizontal dashed line, to the virtual state at k near the K point. This is a second order process where one inelastic and one elastic scattering event occurs. This is different from the overtone 2D band where two *inelastic* scattering events take place. The D band to G band intensity ratio, determined from the peak areas, measures the degree of disorder in the sample and should be zero for good quality samples. This ratio is inversely related to a length scale describing the separation between defects [130, 22],

$$L_a(\text{nm}) = \frac{560}{E_{\text{laser}}^4}(I_{\text{D}}/I_{\text{G}})^{-1}, \tag{3.2}$$

where the defect-free crystallite size is L_a in nm and the energy of the Raman excitation laser is $E_{\text{laser}} = hc/\lambda$ in eV. It is not clear how appropriate this is for graphene samples as the numerical prefactor 560 was determined from correlating D/G ratios to the size of *nanographites* measured with scanning tunneling microscopy [22].

In Figure 3.16, the effect of soft X-ray exposure on the same sample (Fig. 3.13(a)) where the previous pristine spectrum were obtained (Fig. 3.13) is shown. Although a D peak was not discernible in any of the pristine spectra, here the D peak is large and more than twice the intensity of the G peak for the monolayer. The D to G integrated intensity ratio increases as the layer number goes down, indicating that the damage may be confined near the surface

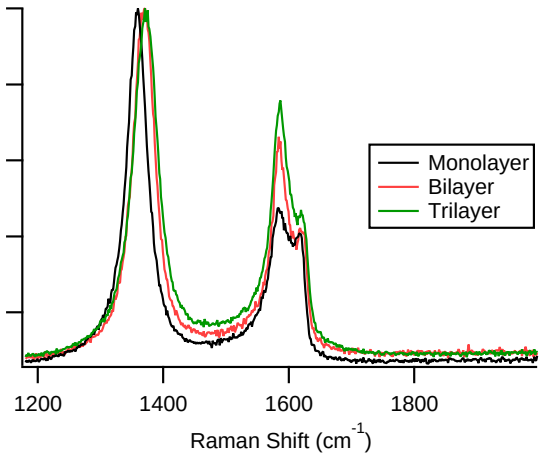

Figure 3.16: Appearance of D peak in few layer graphite as a result of soft X-ray exposure.

of the sample. An understanding of the origin of this damage and its occurrence in both suspended and non-suspended samples is presented in Zhou, Girit, et al [165].

3.2.3 Electron Irradiation

An important use of Raman spectroscopy is to characterize disorder in graphene samples. Unlike X-ray exposure, one source of disorder that is relevant to graphene device fabrication is electron beam exposure. When a device is made out of graphene using electron-beam lithography critical regions of the sheet under the contacts as well as edges of patterned samples are inevitably exposed to high-energy (kilovolt) electrons at high dosages (>10 electrons per nm^2). Although the effect of this exposure on experimental results obtained in such samples is not addressed, it is possible that this disorder could influence electronic transport properties.

In order to study the effects of electron beam exposure on graphene, Raman spectroscopy was performed on half-suspended graphene and bilayer samples before and after electron beam exposure. Micromechanical exfoliation of Kish graphite onto a SiO_2/Si^{++} substrate prepatterned with 1.8 µm diameter holes and roughly 4 µm pitch yielded >50 µm sized graphene and bilayer samples with suspended regions over the holes. By having both suspended and non-suspended regions, effects of the substrate on damage incurred by electron beam exposure can be evaluated. Figure 3.17(a) is an optical image and Fig. 3.17(b) a scanning electron micrograph.

Prior to exposure, contrast across the mono- and bilayer is uniform in both optical and electron microscopy, with a noticeable contrast difference in the suspended regions over the holes. Upon exposure of roughly 500 electrons per nm^2 over an area of 20 µm × 15 µm on both the mono- and bilayer, these areas show darker contrast in the electron micrograph, Fig. 3.17(c). The electron energy was 5 keV. It is well known that electron beam exposure in

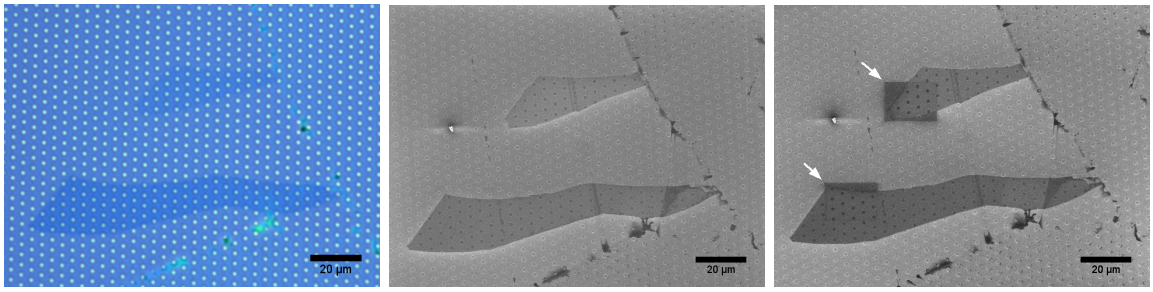

(a) Optical image (b) Electron micrograph (c) Electron micrograph post-exposure

Figure 3.17: Electron beam exposure of graphene (upper) and bilayer (lower) sample. Arrows indicate exposed regions.

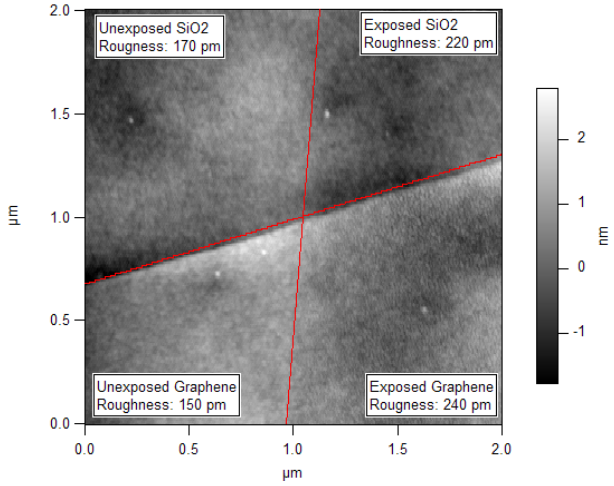

Figure 3.18: Roughness of graphene exposed to electron beam irradiation determined by atomic force microscopy.

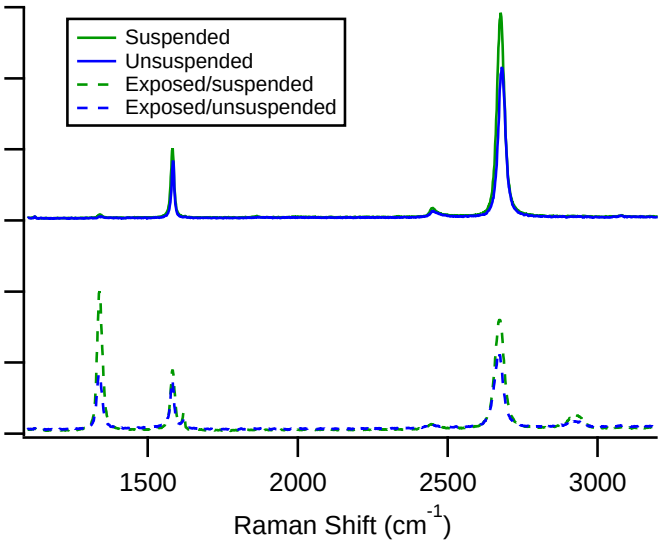

(a) Raman spectrum

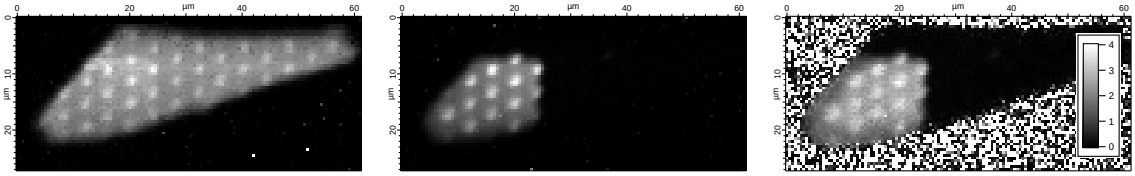

(b) Raman G map (c) Raman D map (d) Raman D/G map

Figure 3.19: Raman spectroscopy of effect of electron beam exposure on semi-suspended graphene sample.

high vacuum (above 1×10^{-6} Torr) results in deposition of a layer of amorphous carbon–the beam ionizes residual hydrocarbon gases in the chamber which are positively charged and attracted to the exposed, negatively charged surface [44]. This deposited carbon provides the additional contrast in the exposed regions indicated by the arrows in Fig. 3.17(c). Figure 3.18 is an atomic force microscopy image taken in AC mode (see Section 3.3 below) showing the enhanced roughness of exposed graphene due to hydrocarbon adsorption, increasing from 150 pm RMS to 240 pm. The phase image (not shown) also indicates that the exposed area has a different mechanical damping than the pristine graphene. The electron-beam induced deposition of hydrocarbon can also be observed by transmission electron microscopy [107].

Figure 3.19 shows Raman spectroscopy and Raman maps of the D band, G band, and D/G intensity ratio of the exposed and unexposed regions of the graphene sample. Both suspended and unsuspended unexposed regions (solid traces) show only prominent G and 2D peaks indicative of undefective graphene (Fig. 3.19(a)). A slightly higher 2D to G integrated intensity ratio is observed for the suspended sample. This 2D/G ratio is an indicator of the electronic quality of the sample [12], and is higher as expected in the suspended regions

which are free from substrate induced disorder.

In the exposed regions (dashed traces), a large D peak is apparent which dwarfs the G as well as 2D peaks. This D peak is not the Raman signal of the adsorbed hydrocarbons as no such signal is seen on the exposed substrate areas devoid of graphene (Fig. 3.19(b)). Comparing exposed spectra, the D/G ratio of the suspended region is greater than that of the unsuspended region. This indicates that the suspended regions are more susceptible to defect formation or that the substrate has a damage stabilizing effect. Such a stabilizing effect was suggested in the soft x-ray induced damage of graphite [165], where the bottom graphene layers may help reduce defect production in the uppermost, exposed layer.

Figure 3.19(d) is a map near showing the D to G intensity ratio over the entire sample, confirming that the suspended regions have higher D/G ratio. The D/G ratio is virtually zero in the unexposed region, equal to 2.60 ± 0.36 in the exposed, unsuspended region, and 3.28 ± 0.21 in the exposed, suspended region. Away from the graphene sheet, the Raman spectra have no D or G peaks and the ratio is meaningless, hence the noise surrounding the graphene sheet. Assuming the validity of Equation 3.2 for graphene samples, for an excitation wavelength of 514 nm one obtains a crystallite size of $L_a = 16.5$ nm per inverse unit D to G intensity ratio. For the suspended graphene, that is 5.0 nm and for the unsuspended graphene, 6.4 nm. The crystallite size is roughly 30% larger in the unsuspended graphene.

Results on the bilayer sample are similar to the monolayer, except that the D to G ratios are smaller. For the bilayer over holes, this ratio is 1.80 ± 0.12 and for the bilayer over SiO_2, 1.80 ± 0.12. The lower ratios suggest that damage may be limited to the upper graphene layer.

Hydrocarbon adsorbed on the graphene surface can catalyze defect formation under electron beam irradiation. This was observed directly with aberration corrected transmission electron microscopy (TEM), described in Section 3.4, on suspended graphene samples (it is not possible to look at samples on substrates thicker than several tens of nm with TEM). Regions with hydrocarbon adsorbates would readily form holes or defects under intense flux from the 80 kV TEM beam. A similar process should be more likely with the lower-voltage (1 kV to 30 kV) SEM beam as the scattering cross section for ionization of carbon is maximum around 1 keV (Univ. Tennessee-Knoxville Electron Solid Interaction Database). Chemical reactions between the already ionized adsorbed hydrocarbons and readily ionizable carbon in the graphene could introduce the defects detected by Raman spectroscopy.

There are several possibilities why suspended graphene appears to be more damaged under electron beam exposure. The first is that it is actually *not* more damaged, but that the measured D/G intensity is somehow enhanced for suspended samples relative to samples on a substrate. It is already the case that the G peak area is enhanced by a factor of 4/3 for the suspended sample and if the D peak area is enhanced by a different, larger factor, the ratio would also be greater. One can speculate that the G peak area enhancement of suspended samples may be because the atoms can more readily vibrate without the interaction of the SiO_2 substrate, but then why would the D peak area be enhanced by a different factor? In order to correlate these enhancements to different defect structures, atomically-resolved scanning probe microscopy of a sample similar to this one,

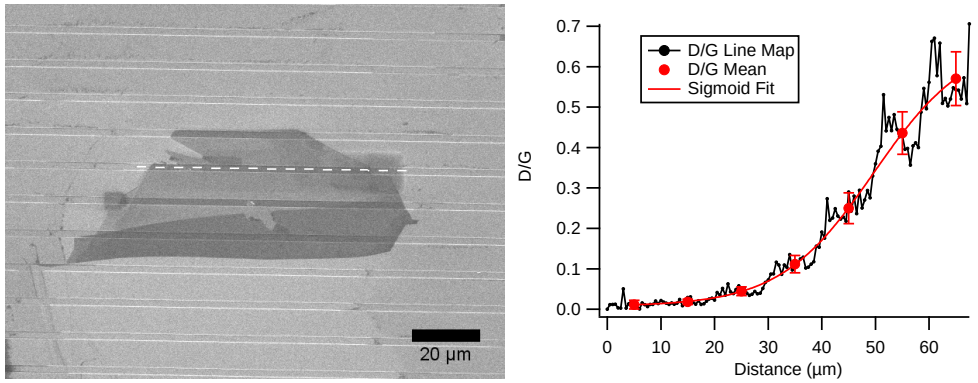

(a) Bilayer sample (b) D/G ratio and fit

Figure 3.20: Variation of D/G ratio as a function of position along bilayer sample exponentially exposed to electron beam radiation.

where the suspended and unsuspended regions are adjacent, is likely to be necessary. If the damage is equal, then the prefactor in Equation 3.2 would have to be different for suspended and unsuspended samples.

If however the suspended sample *is* more defected, there are several hypotheses. One is that in a suspended sample, one defect is more likely to result in formation of another defect. If the strain induced by a defect is larger in suspended graphene where out-of-plane displacement is possible, such strain could more easily encourage the formation of another defect nearby. In another scenario, the substrate could serve as an "anti-catalyst", reducing the defect producing chemical reaction between the adsorbed hydrocarbons and graphene. More thorough measurements, as a function of beam energy and flux, are necessary to test these and other hypotheses on the nature of the induced damage.

On another bilayer sample, the effect of varying the electron beam dosage was studied, Figure 3.20. The sample was exfoliated over micron wide trenches and adjacent 10 µm × 10 µm regions were exposed with an exponentially varying electron dose at 5 keV. The dosed regions can be seen in Fig. 3.20(a) as dark squares around the dashed line. Raman spectra were obtained over the trench along the dashed line at 0.5 µm increments and the D/G intensity ratio calculated as a function of position (black curve "D/G Line Map", Fig. 3.20(b)). Averaging the D/G ratio over each 10 µm length segment results in the curve "D/G Mean", which is well fit by a sigmoid function,

$$\frac{I_{\mathrm{D}}}{I_{\mathrm{G}}}(x) = \frac{\mu}{1+e^{-(x-x_0)/l}} = \frac{\mu}{1+(\xi_0/\xi(x))^{\nu}}, \tag{3.3}$$

where x is the position of the middle of each exposed square, $x_0 = 50$ µm is the halfway or inflection point, and $l = 8.7$ µm is the length scale over which the D/G ratio changes. The maximum D/G ratio predicted is $\mu = 0.66$. In terms of the exposure as a function of distance $\xi(x)$ the relevant fit parameters are $\xi_0 = 4600$ µC/cm^2 and $\nu = 1.1$. The predicted

saturation D/G ratio of 0.66 for the sigmoid function differs significantly from the D/G ratio of 1.8 measured in the previous suspended bilayer sample at a dosage of 8000 $\mu C/cm^2$. The D/G ratio of 0.66 is comparable however to that of the previous sample's unsuspended region, 0.9. Similar measurements, over a larger exposure range and at different accelerating voltages, could help reveal whether the D/G ratio actually does saturate at mC/cm^2 dosages and whether there is significant sample-to-sample variation in this saturation value.

3.3 Atomic Force Microscopy

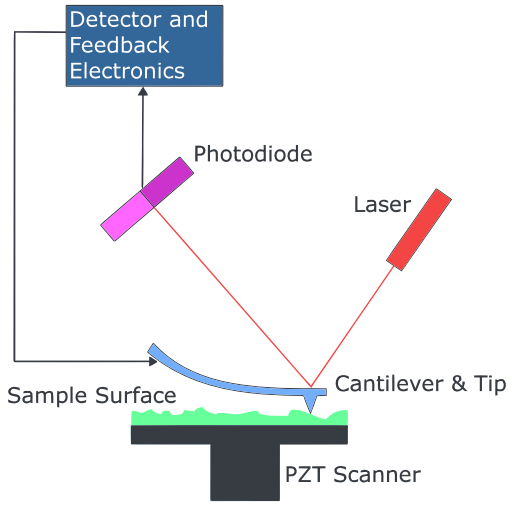

Figure 3.21: Block diagram of atomic force microscopy (AFM). Wikipedia.

Atomic force microscopy (AFM) is a type of scanning probe microscopy that uses the Lennard-Jones (r^{-6} plus r^{-12}) interaction between a nanoscale probe and a surface to map topography. An AFM is very similar to a phonograph, in that the movement of a cantilever tip (phonograph needle) is transduced into an electrical signal (music) giving information about the topography of the surface. A schematic of an AFM system is shown in Fig. 3.21. The sample surface is scanned underneath a cantilever tip by piezos (PZT Scanner). The deflection of the cantilever is measured by the reflection of laser light off the cantilever and onto a photodiode. The detector and feedback electronics use the measured deflection to adjust the z-height of the sample by applying voltages to the piezos. These height variations correspond to the sample surface topography. Piezos can provide sub-nanoscale actuation of the cantilever with a z-height resolution of less than 1 Å, and the optics can be designed to obtain high sensitivity to cantilever deflection.

The components of the Zettl group AFM system, an Asylum Research MFP3D, are shown in Fig. 3.22. The XY scanner is located on top of the large black box resting on the blue gyroscopic vibration isolator (Fig. 3.22(a)). Off to the side, a smaller black box with four legs sticking up is the Z scanner, which also houses the photodiode and light source. This is

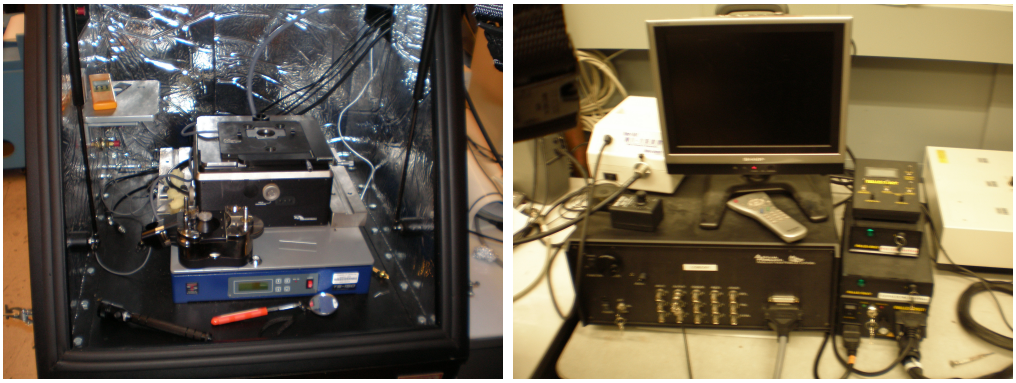

(a) Scanning Stage (b) Controller Box

Figure 3.22: Asylum Research MFP-3D atomic force microscope, Zettl group.

also where the silicon cantilever is mounted. The controller containing the voltage amplifiers to drive the piezos and feedback electronics to control the scanning is shown in Fig. 3.22(b).

There are many different modes of operation of an AFM, corresponding to different tip-sample forces such as magnetic, friction, or electrostatic as well as the nature of the drive and feedback loop. The most common imaging mode for topography measurements is noncontact or "AC" mode. This is often used instead of contact mode, described below, because it is less damaging to the surface (with smaller magnitude interaction force) and has good resolution. In this mode, the cantilever is driven by the piezos to vibrate near its natural frequency, usually between 50 300kHz. Just like a spring to which a dampener is attached, when the vibrating cantilever comes in contact with a surface, the resonant frequency is shifted and the vibration amplitude reduced. The feedback loop operates to adjust the z piezo height to keep the amplitude of vibration constant. When the vibration amplitude is reduced the piezo will pull the cantilever away from the surface to restore the setpoint amplitude. These height adjustments correspond to the surface topography.

Other modes of operation are magnetic force microscopy (MFM), where the cantilever tip is coated in a magnetic material. The tip is then magnetized with an external magnet and then used to scan a material with magnetic domains. The varying force on the cantilever due to the magnetic domains is converted to a magnetization map. In Kelvin probe microscopy (KPM), the surface is first scanned to obtain a topography map and then scanned a second time at a fixed height above the surface, usually several tens of nanometers. During the second scan, an alternate feedback loop is initiated which varies the voltage on the cantilever tip to keep the deflection on the cantilever zero. This implies that there is no local capacitive interaction between the cantilever and sample and the map produced gives the potential across the sample.

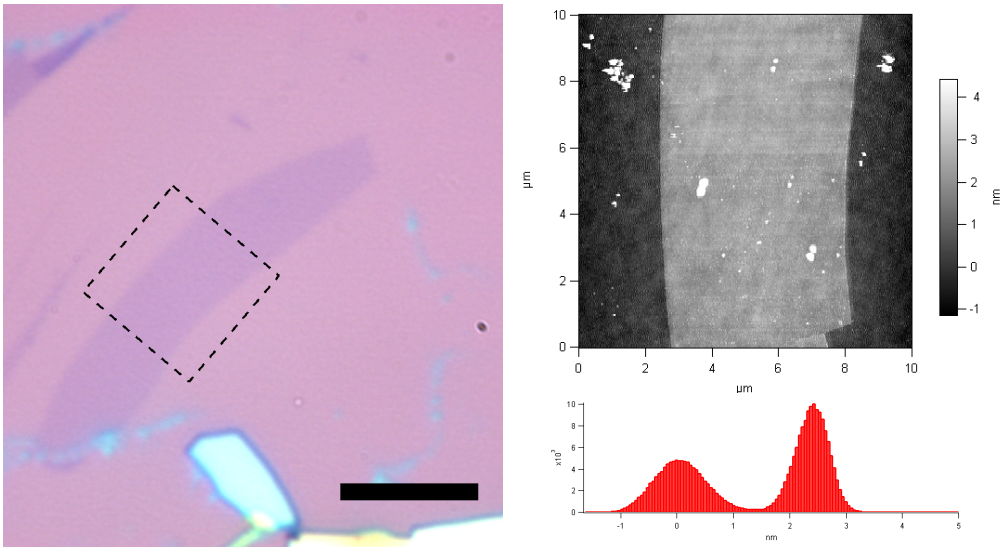

Figure 3.23: Tapping mode atomic force microscopy image of graphene sample. *Left*: optical image of graphene sample (scale bar, 10 µm). *Right, upper*: (**a**) tapping mode AFM topography of region indicated by dashed square in optical image. *Right, lower*: height histogram of topography image with two peaks corresponding to substrate and sample. Inferred graphene height 2.9 nm ± 0.8 nm.

3.3.1 Graphene Identification

Identifying graphene with AFM requires imaging in "contact" mode, where the cantilever tip is in constant contact with the surface. The feedback loop adjusts the height of the z piezo in order to keep the deflection on the cantilever constant. Hence the setpoint for the feedback loop is the force on the sample, proportional to the deflection by Hooke's law. The adjustments made by the feedback loop on the z piezo to keep the deflection constant correspond to the height profile of the line being scanned. As the cantilever tip is in constant contact with the surface, both sample and tip can be more readily damaged or modified. Any damage to the tip or adsorbed material on its surface will strongly influence the resulting image.

If graphene is imaged in AC mode, the apparent height difference between substrate and graphene sample can be erroneously large, as high as several nanometers, compared to the interlayer spacing of 0.335 nm. Several hypothesis have been proposed for why graphene appears "elevated" from the surface. One is that there is a thick layer of water between the substrate and graphene (Geim), although this does not explain why contact mode imaging works. Figure 3.23 shows an optical image and AC mode AFM topograph of a graphene sample. A histogram of the topography image shows two Gaussian peaks corresponding to the substrate (position 0.00 nm ± 0.66 nm) and sample (position 2.36 nm ± 0.42 nm) give a height value of 2.36 nm ± 0.78 nm, far from the expected for a monolayer.

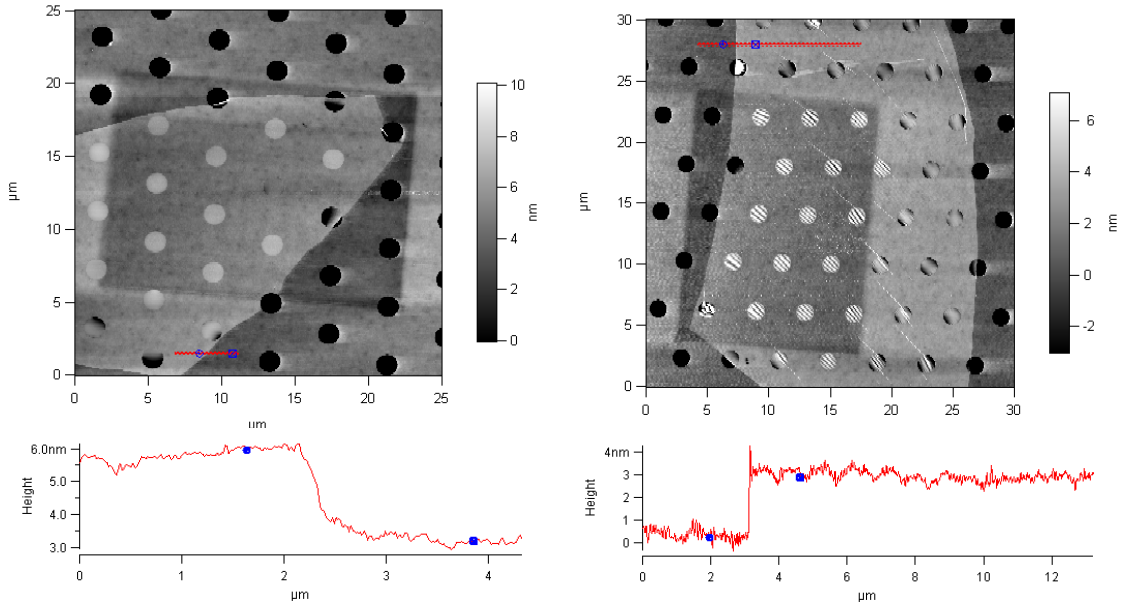

(a) Graphene sample (AC mode)

(b) Bilayer sample (AC mode)

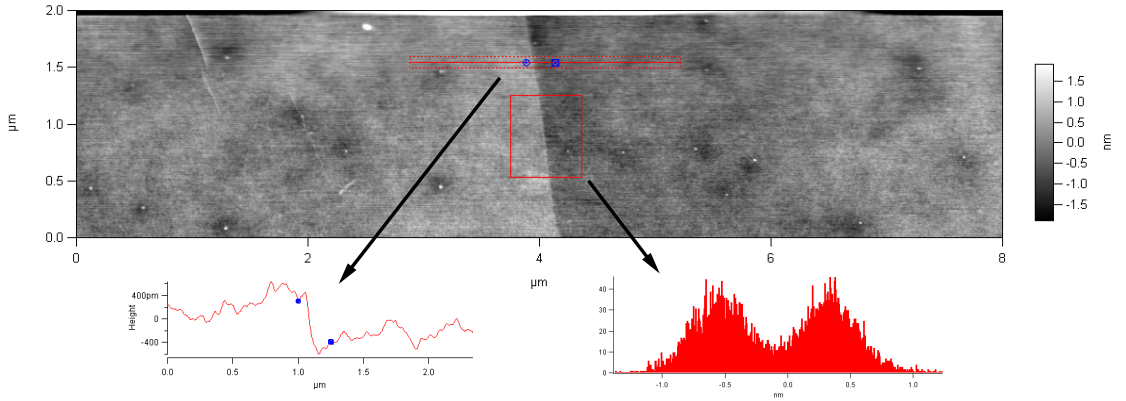

(c) Bilayer sample (contact mode)

Figure 3.24: Atomic force microscopy imaging of height of graphene and bilayer sample.

Figure 3.24 shows AC mode images of a another graphene sample and a bilayer sample with line scans to indicate sample thickness. These samples are the same exposed to an electron beam and studied by Raman spectroscopy in Section 3.2.3. The rectangular areas exposed to the beam are covered in hydrocarbons and give dark contrast in the AFM image. The line scan for both the graphene and bilayer sample indicates a height change of $2.6\,\mathrm{nm} \pm 0.2\,\mathrm{nm}$. This is eight times the graphene interlayer height and almost four times what was measured in the previous sample. It is clear that in all these samples the apparent height is not dominated by the contribution from few-layer graphite, and that the measured height depends sensitively on unknown factors.

In contrast, once the imaging mode is switched to contact, the bilayer thickness is determined to be 0.86(30) nm (Fig. 3.24(c)). Within the error, this is twice the interlayer thickness as expected. AC mode can still be used to determine thickness in special situations where the graphene is folded on itself or over another graphitic layer. For example a monolayer step height on graphite is the correct value with AC mode imaging. Hence one can determine the thickness of a sample if there is a fold by taking a line scan from an unfolded region to a folded region.

3.3.2 Imaging Suspended Samples

Another use of atomic force microscopy in relation to graphene is for imaging suspended samples. Due to strain induced during the exfoliation process, suspended graphene samples often have large-scale ripples, much like when covering a bowl with plastic wrap. With optical imaging, these ripples are sometimes discernible by their contrast if they are large enough, but it is in general difficult to tell if a sample is suspended. With SEM, especially when tilted, suspended samples and their ripples can be identified. However none of these techniques give a good measure of the height of the ripples, and this is where AFM can be useful. In addition, AFM is less invasive than SEM, where the sample is constantly bombarded by electrons.

Some of these ripple structures on few-layer graphite over holes are apparent in Fig. 3.24, and a variety of them are shown in Fig. 3.25 both on holes and trenches. The ripple height and period can vary from tens to hundreds of nanometers. The structure of these ripples can be explained classically from the tension distribution and the dimensions of the suspended area (L. Mahadevan, personal communication).

In order to image suspended samples with AFM, AC mode is preferable as it is less likely to induce collapse of the suspended area. Contact mode can also be used but scanning over a suspended edge should be avoided as that is likely to cause collapse. The setpoint in both cases should be set close to the free cantilever deflection (contact mode) or amplitude (AC mode) in order to minimize forcing.

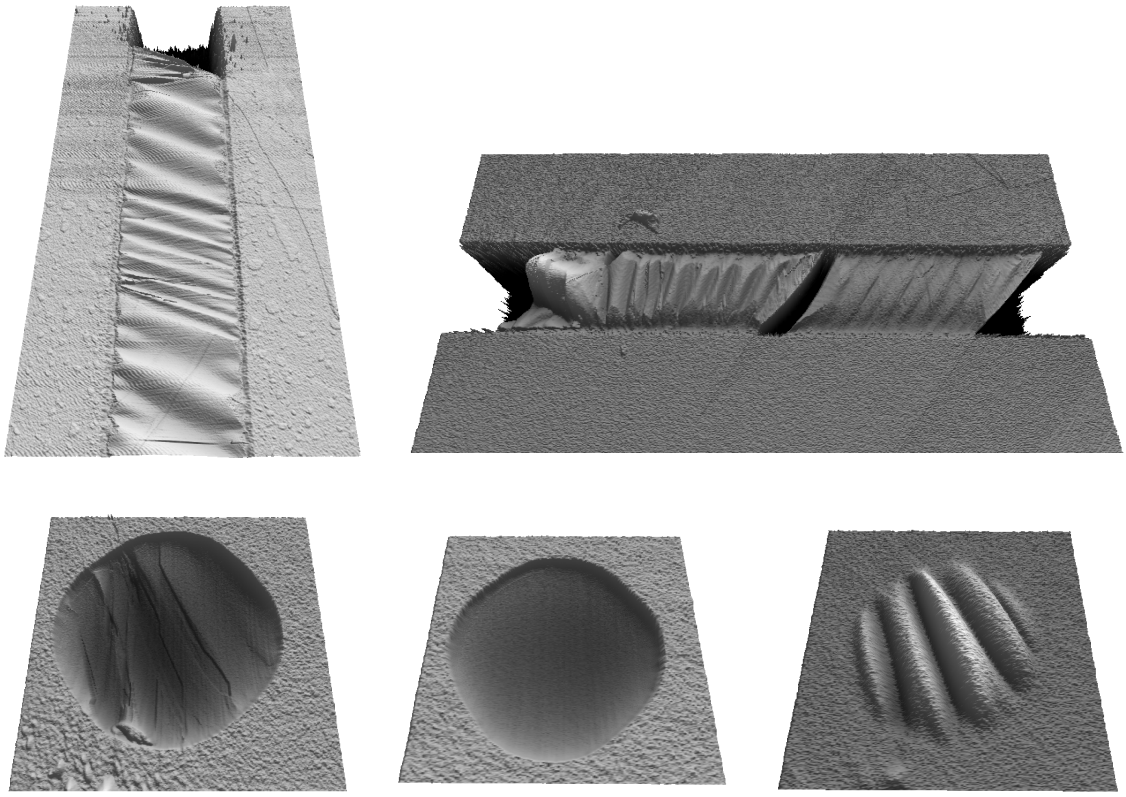

Figure 3.25: AFM images of graphene suspended over trenches and 1.8 µm diameter holes, showing effect of exfoliation induced tension.

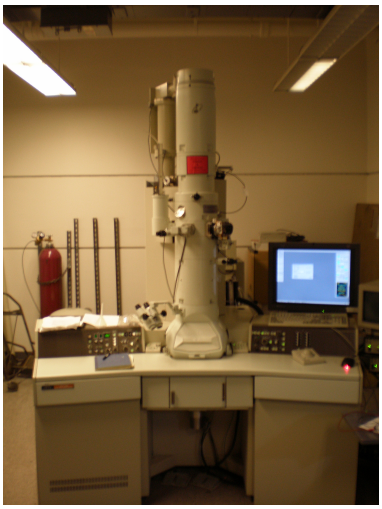

Figure 3.26: Zettl group JEOL 2100 transmission electron microscope.

3.4 Transmission Electron Microscopy

By using high-energy electrons for microscopy instead of light the imaging wavelength, given by the de Broglie relation $\lambda = hc/E$, can be reduced far below wavelengths in the visible spectrum and consequently the spatial resolution, on the order of λ, greatly improved. A transmission electron microscope (TEM) exploits this potential by accelerating electrons to voltages over 80 kV, where the wavelength is less than an angstrom. Electron optics, consisting of electromagnetic and electrostatic lenses, is used to direct, collimate, and focus the high-energy electrons onto a thin sample. Electrons that are not back scattered travel onward and hit a fluorescent screen where they can be imaged or photographed. A good introduction to TEM is the textbook by Williams and Carter [157].

Some limitations of TEM are that contrast is reduced for low atomic number elements which scatter less; and that thin samples (<10 nm) are required to image in transmission mode. Applied to graphene, these limitations imply that samples must be suspended and that longer image acquisition times are necessary to obtain good contrast. Jannik Meyer and others pioneered the techniques to suspend graphene and study it using transmission electron microscopy, including how to identify single layers [106], analyze adsorbates [108], and perform high-resolution lithography by electron-beam induced hydrocarbon deposition [107].

3.4.1 Graphene Atomic Dynamics

The traditional method of obtaining atomic resolution on surfaces and edges is scanning tunneling microscopy (STM) or atomic force microscopy (AFM). While there are several atomically-resolved AFM/STM studies of graphene [17, 127, 77], as well as studies of step edges in graphite [142], there are several problems in observing dynamics of the edge atoms with scanning probe techniques. First, typical scan speeds are on the order of minutes

to hours which may be too slow to capture the movement of atoms. Second, the highest resolution and stability is obtained at cryogenic temperature, where the dynamics may be frozen out. Finally, the sample is usually on a substrate, which can strongly influence the behavior of atoms both in the bulk and at the edge. In order to observe dynamics on a time scale of seconds, the only alternative to scanning probe microscopes with comparable spatial resolution is TEM. Indeed, the dynamics of atom columns comprised of heavy atoms were observed in this manner [102].

Traditional TEMs lack the necessary resolution at the low operating voltages required to avoid immediate sample damage. Previous 100-200 kV TEM studies of few-layer graphitic materials showed that some microscopes have difficulty resolving the lattice and are not capable of atomically resolving edges [21, 57, 79], making image interpretation ambiguous. By using the aberration-corrected, monochromated TEAM 0.5 transmission electron microscope [90], capable of sub-angstrom resolution even at 80 kV, we imaged every carbon atom in the lattice of suspended single-layer graphene [109]. Here we employ the same microscope to record the dynamics of carbon atoms on the edge of a hole in a graphene sheet. The sample was prepared as described previously [107] and details of the microscope configuration can be found in [109].

Movie S1, which can be downloaded from the Zettl group highlights page, shows the evolution of the hole within a suspended graphene sheet (stills in Fig. 3.28). Each frame averages one second of exposure and the frames themselves are four seconds apart. The carbon atoms are shown as white since the spherical aberration was chosen to be negative [148]. The spatial sampling is 26±4 pm/pixel, determined by fitting for the measured atomic positions and using the known atomic spacing of 1.42 Å. Figure 3.27(a) shows the first frame of the sequence. The hole, initially formed through prolonged irradiation by the electron beam, is clearly visible near the center of the frame, and is surrounded by the hexagonal carbon lattice. The structures lining the boundary of the frame are adsorbates most likely deposited during the process of suspending the graphene sheet. Every carbon atom in the lattice is resolved, including those at the edge of the hole. We assume the edge atoms are unterminated since the entire experiment, including creation of the hole, is carried out in the high vacuum of the microscope chamber. As the sheet is suspended, small drifts in the z direction can occasionally move it out of the focal plane of the microscope. To account for this, a focal adjustment was made between frames 29 and 30, which represents a time gap of less than one minute.

Figures 3.27(b) and (c), showing frames 9 and 10 of the movie, respectively, depict the basic mechanism by which the hole changes shape. While motion of the atoms is expected to occur faster than the one second sampling time in the experiment, it is the "meta-stable" configurations of the edge that are recorded. The red dashed line in Fig. 3.27(b) and (c) circles a hexagon which "loses" two atoms, indicated by red dots, as a result of either knock-on damage from the electrons in the beam or migration to vacant sites nearby. For an 80-keV incident electron, the maximum energy that can be transferred to a carbon atom is 15.8 eV [45]. The knock-on energy threshold for ejection of an in-lattice carbon atom with three bonds is 17 eV, corresponding to a beam energy of 86 keV [135], and hence those atoms

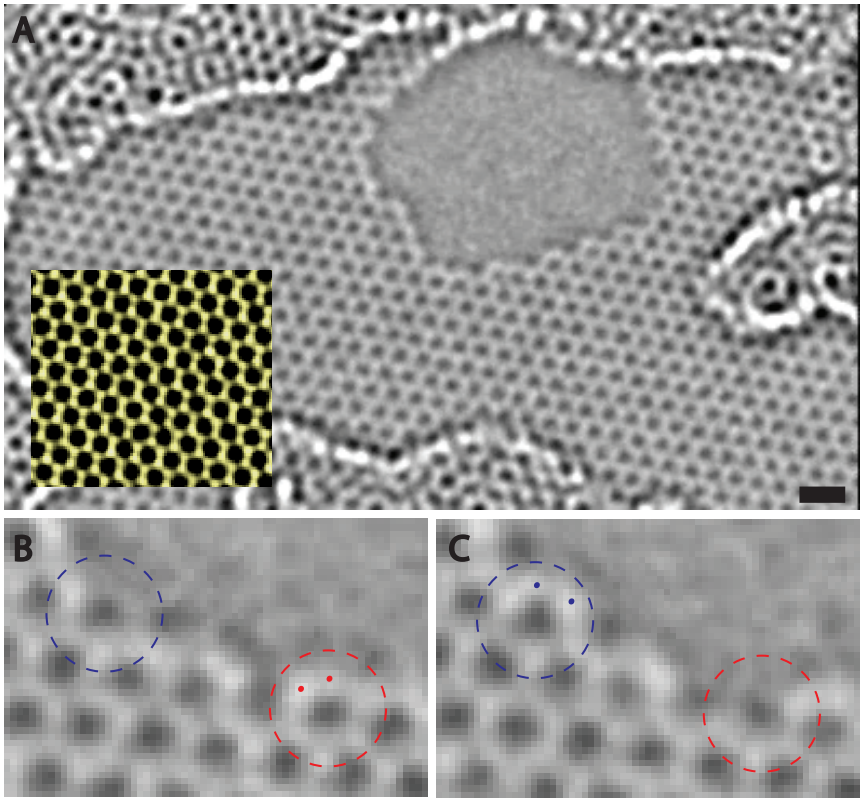

Figure 3.27: Atomically resolved hole in graphene.
(**A**) Aberration-corrected transmission electron microscope image of a hole in a single layer of graphene produced by prolonged irradiation (frame 1 of Movie S1). Individual carbon atoms are resolved as white spots. Structures lining the perimeter are adsorbates. Scale bar is 5 Å. Inset: Averaged series of images showing the atomically resolved graphene lattice. (**B**) and (**C**) Two still frames (9-10) in the evolution of the hole, with (**C**) following four seconds after (**B**). Two carbon atoms (red dots) are removed while two carbon atoms nearby (blue dots) bind to their neighbors to close a hexagon (circled). The measured lattice constant is 2.5±0.2 Å.

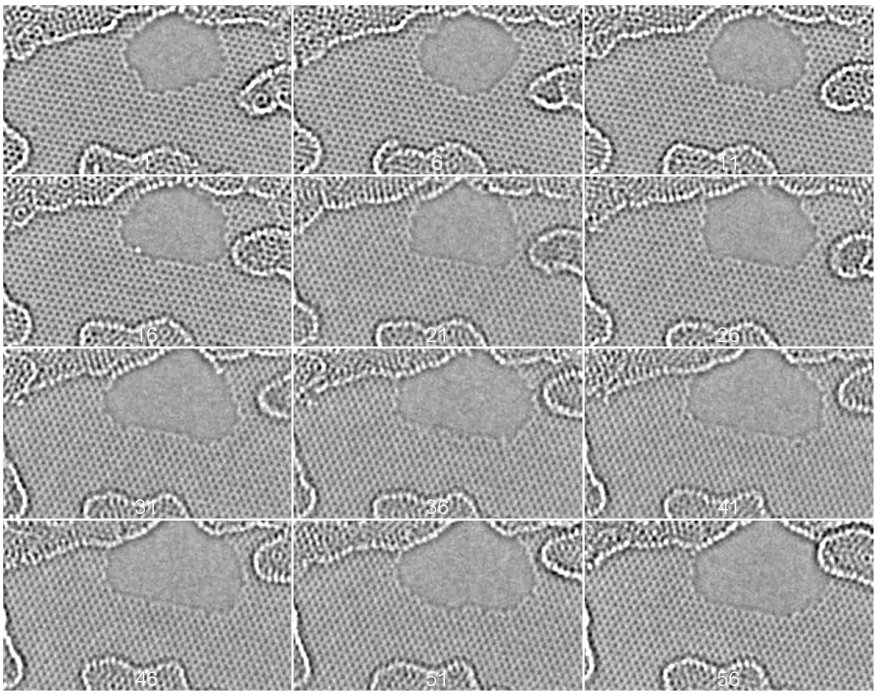

Figure 3.28: Stills from movie of atomic dynamics in graphene hole growth.

are not ejected. However this threshold drops below the maximum transfer energy to 15 eV for sites with a neighboring vacancy [31], and may be even less in our case where atoms at the edge may have several vacant next-nearest-neighbor sites. The lower energy mechanism of beam-induced ejection of atoms from the edge, as opposed to the surface, is referred to as sputtering and is responsible for the overall enlargement of the hole.

The energy barrier for migration of a carbon atom to various nearby vacant sites is expected to be less than the 15 eV necessary for sputtering. Indeed ab-initio density functional theory (DFT) calculations within the local density approximation give a barrier height of 0.3-6.6 eV for unterminated edges. This value does not change significantly when calculated for hydrogenated edge atoms. Because of the much smaller energy threshold for atom migration, these events should occur more frequently than hole enlargement, and this is what is observed. The movie and subsequent figures show that the hole growth time scale is on the order of minutes in contrast to less than a second for edge reconfiguration. Figs. 3.27(b) and (c) show the appearance of two carbon atoms (blue dots) at previously vacant sites. This may be a result of migration of the two atoms indicated by red dots or from another region of the hole. It is also possible that the region of the hole obscured by adsorbates acts as a carbon atom reservoir, which can replenish sites that are made vacant. Those adsorbates are likely rich in carbon and more reactive than graphene, providing atoms for "repair" of the lattice, but at a slower rate than beam-induced ejection leading to an overall growth of the hole. These competing mechanisms result in the rich dynamics observed in the movie.

To investigate whether a model can reproduce the experimental observations, we simulate the evolution of the graphene hole with a kinetic Monte Carlo method [152] (Section 3.4.2). We manually define a hole in a graphene lattice, and describe the edge dynamics in terms of three different mechanisms: the beam-induced ejection of carbon atoms along the edge, the addition of carbon atoms from a virtual reservoir, and the migration of dangling carbon atoms from one site to another. The ejection probability incorporates the effect of energy input from the electron beam. The addition probability, smaller than the ejection probability, accounts for the possibility of obtaining carbon atoms from either the imperfect vacuum in the microscope or adsorbates near the hole. These two probabilities are estimated to be much smaller than the migration probabilities and thus set by hand. The migration probabilities (up to third nearest neighbor sites) are determined by the factor , where is the relevant energy barrier height obtained from DFT calculations and is an effective temperature corresponding to the energy input from the electron beam. In the movie of simulated hole growth (Movie S2), the time step is not necessarily that of the experimental movie. The dynamics, as characterized by Figs. 3.29 and 3.30, are remarkably similar to that observed experimentally, and show the emergence of long-range order and the mechanism of edge reconfiguration.

Figure 3.29 shows typical examples from experiment of edge configurations with a high degree of order. The outlined region of the hole in Fig. 3.29(a) is entirely armchair, and that in Fig. 3.29(b) is entirely zigzag. These two configurations are defined in the inset diagrams. Each ordered edge spans about twelve hexagons. The existence of such long-range order indicates that these configurations are stable, at least for periods of time longer than the one second to capture the frame. Such long-range order is also observed in the simulation, as shown in Fig. 3.29(c) and (d), where a seven-hexagon armchair edge and a nineteen-hexagon zigzag edge are identified, respectively. Long armchair edges are much less prevalent than zigzag edges in the simulation. This is also the case experimentally, although not as pronounced, and results from the greater stability of the zigzag edge.

The beam-induced ejection of atoms, and resultant migration and edge reconfiguration, changes the shape of the hole, as shown in Fig. 3.30(a). An armchair sequence at a corner of the hole transforms over the course of four seconds, or one frame, into a zigzag sequence. The blue dots in the upper frame indicate two carbon atoms that were removed from the armchair edge and the red dots in the lower frame indicate four atoms added to form the zigzag edge. At a corner, or for a short segment, such a transformation would only involve the migration, addition, or removal, of a handful of atoms, but the exact sequence of events is unknown. For long, uniform segments such as in Fig. 3.29(b) or (d), where the edge is aligned with the zigzag direction of the lattice, a transformation to armchair is difficult. Similar behavior is again observed in the simulation, where the rearrangement of atoms can also interconvert armchair and zigzag edges. The simplest example of such an event is shown in Fig. 3.30(b), where one of three atoms on a zigzag edge (red dots, bottom frame) disappear and within four frames, two others appear (blue dots, upper frame) to form an armchair edge.

In Figure 3.31, we analyze the data in an attempt to understand the growth of the hole as a function of time and demonstrate the stability of the zigzag edge configuration.

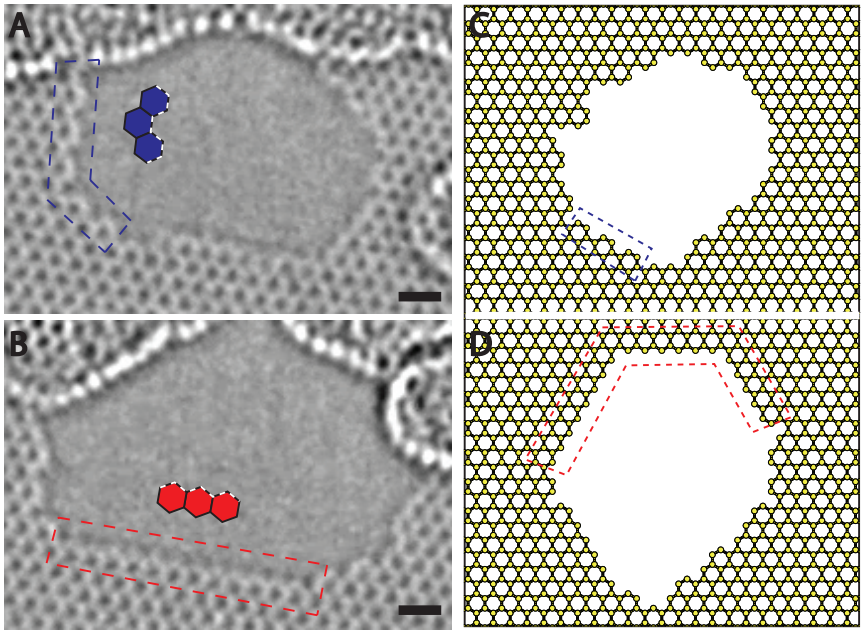

Figure 3.29: Edge configurations of hole in graphene.
Aberration-corrected transmission electron microscope image of (**A**) an armchair (frame 24) and (**B**) zigzag (frame 55) configuration of carbon atoms at the edge of a hole in graphene. The inset diagrams exemplify an armchair (blue hexagons, edge dashed) and zigzag (red hexagons) arrangement. The armchair edge, roughly 12 hexagons long, makes a 60° turn at the lower left-hand corner. The zigzag edge is a continuous segment 12 hexagons long. Examples of the emergence of long range order are (**C**), frame 113, with a seven hexagon armchair segment at the edge of the simulated hole and (**D**), frame 223, an extremely long (19 hexagon) zigzag edge interrupted by two 60° turns.

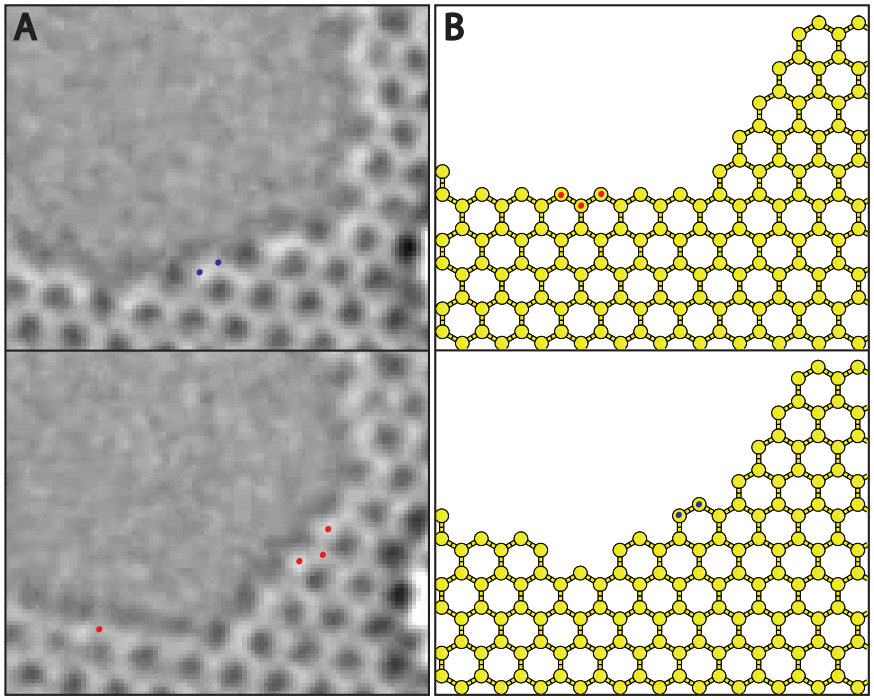

Figure 3.30: Reconfiguration of edge atoms in a hole in graphene.
(**A**) Conversion of an armchair edge (top) to a zigzag edge (bottom) over the course of two frames, 14 and 15, taken at 4 s interval. The two atoms marked by blue dots in the upper frame are gone in the lower frame, where four new carbon atoms are marked by red dots. The seven hexagon armchair edge is transformed into a nine hexagon zigzag edge with a 60° turn. The transformation occurs due to migration of atoms along the edge. (**B**) Similar behavior is observed in the kinetic Monte Carlo simulation of hole growth, where three zigzag atoms (red dots, top) from frame 235 disappear and two armchair atoms (blue dots, bottom) appear in frame 239. It is possible that one of the three red dotted atoms was ejected by the beam and the other two migrated to the positions marked by the blue dots to form an armchair edge.

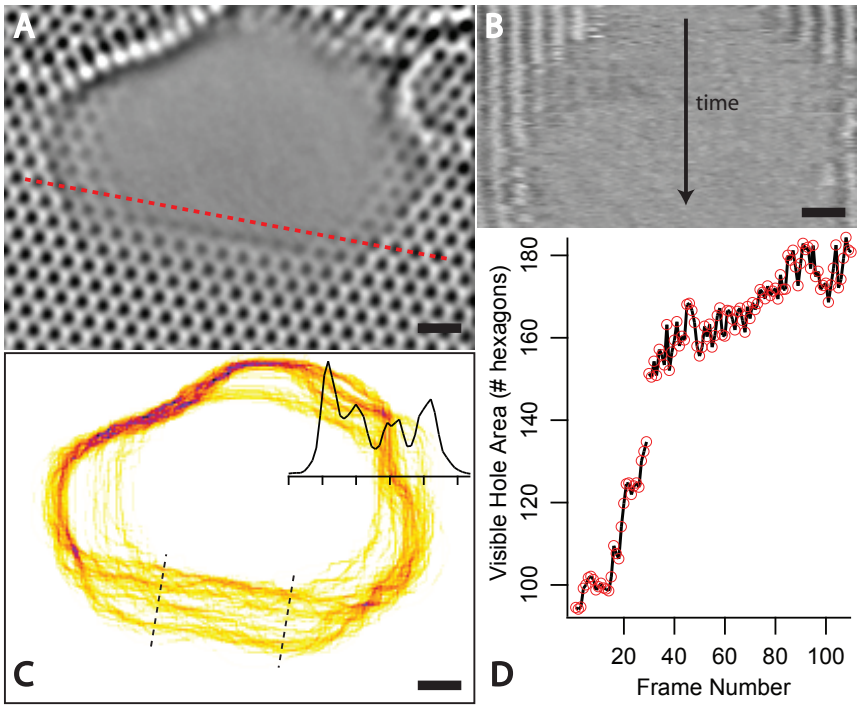

Figure 3.31: Analysis of growth of hole in graphene.
(**A**) Average intensity map constructed by averaging pixel values over all 110 frames of movie after frame registration. Faint hexagons in the interior have been gradually removed by knock-on damage from the electron beam. Scale bar is 5 Å. (**B**) Time development of the pixel values along the dashed line in (**A**). The left end of the dashed line corresponds to the left side of (**B**). The frame number increases from top to bottom, and the scale bar is 5 Åalong the x-axis (position) and 30 frames, or 120 s, along the y-axis (time). The opening of the hole is visible as a reduction in the number of black-and-white bands, corresponding to hexagons, scanning downward. (**C**) Average, over all frames, of the perimeter of the hole. Darker segments of lines correspond to regions through which the perimeter passed more often than lighter segments. The hole opened quickly in the horizontal direction, as observed in (**B**), but near the bottom edge, the presence of four dark bands indicates those configurations of the perimeter were more stable and the hole opened less quickly in the direction of the black dashed line. Scale bar is 5 Å. Inset: the profile of pixel values along the dashed line shows four peaks corresponding roughly to the graphene lattice constant. Tick spacing 2 Å. (**D**) The visible area of the hole, normalized by the area of a single hexagon, 5.17 $Å^2$, as a function of frame number. The missing line segment indicates the 30-second gap between frames 29 and 30.

Fig. 3.31(a) shows a flattened image averaging all 110 recorded frames. First the images are registered by taking the initial frame, isolating a region of the lattice far from the hole, and shifting all subsequent frames into alignment (Section 3.4.2, below). Then the pixel values are averaged over all frames to produce an image. The advantage of such a representation is that it will highlight structures along the edge which appear often, even though those structures may change rapidly from frame to frame. Faint hexagons are fleeting, located in regions where the hole quickly grew in size, whereas well-contrasted hexagons are more stable and existed throughout most of the recording. One observes that the most prominent edge structure is of the zigzag type, with the bottom and lateral sides of the hole aligned in the zigzag directions of the lattice. The faint hexagons are concentrated on the left and right sides of the hole, where the hole grew quickly. The red dashed line indicates a path of pixels along which the time development is shown in Fig. 3.31(b). The pixel values along the path are lined on the horizontal axis, with the vertical axis time, going from top to bottom. The hexagons are indicated by alternating bands of black and white, with the hole a uniform gray. Here one directly sees the growth of the hole along the cut in Fig. 3.31(a). The hole expands by roughly three hexagons both to the left and right within the first 50 frames, and then stabilizes with about two hexagons on the left side and one on the right. This stable configuration corresponds to the formation of zigzag edges on the left and right of Fig. 3.31(a). The lateral regions of the hole, which started with more armchair or mixed-type edges, stabilize in a state which is more zigzag in nature. A similar slice taken perpendicular to the bottom edge of the hole (not shown) indicates a slower growth of the hole in that direction, indicating that it is difficult to erode the long zigzag edge. To further analyze the hole growth, the outline of the hole was determined algorithmically for each frame. All such outlines were averaged over all frames to produce the image in Fig. 4 3.31(c). Faint lines indicate regions where the outline quickly changed shape and darker ones where the outline of the hole was more constant. The analysis of the lateral and bottom regions is similar to the above, except that one clearly sees four bands on the bottom (between dashed lines) aligned along the zigzag direction. This indicates once more that the hole was more stable along that direction, and the hexagons remained in place longer. An averaged line profile over those bands shows four peaks (inset, Fig. 3.31(c)), with a mean spacing of 2.1 Å, close to the lattice constant of 2.46 Å. Finally, in Fig. 3.31(d), the area within the hole, as determined from the outlines, is computed and plotted as a function of frame number. We see the sharp increase in area within the first 50 frames as the hexagons along the left and right edges of the hole are removed, and then the hole growth slows down as a more stable configuration and a larger hole is produced. This global analysis of the edge stability is complemented by a site-by-site analysis of the zigzag fraction (Fig. 3.33, below).

A simple model can account for the stability of zigzag edges observed in both experiment and simulation by considering the effect of ejecting an atom at the edge for each chirality (Fig. 3.32). Half of the atoms along a zigzag or armchair edge are bonded to two neighboring atoms, and the other half are bonded to three neighboring atoms. Naively, we expect the atoms most likely to be ejected by the electron beam are those with two neighboring atoms. The removal of such an atom from a zigzag edge leaves a vacancy without creating any

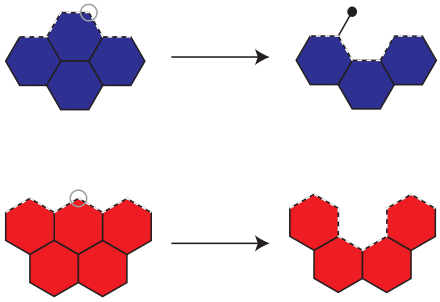

Figure 3.32: Schematic of zigzag stability.
For sites on the perimeter of the hole (dashed line), the electron beam is most likely to eject carbon atoms bonded to only two neighbors (circled, gray). In the case of an armchair edge, top, the removal of such an atom leaves behind a dangling atom, for which the barrier for migration along the edge is small (0.3-0.6 eV). In the case of a zigzag edge, the removal does not lead to a dangling atom, but to a vacancy or "missing" hexagon. The vacancy can be filled by dangling atoms, migrating from other sites, effectively repairing the edge. This mechanism of repair is less likely to occur for the armchair edge, where two atoms are needed to replace the first that was ejected by the electron beam, and the second that subsequently migrated away. Hence the zigzag edge is more stable than the armchair edge under electron beam exposure from the microscope.

dangling carbon atoms, those bonded to only a single neighbor. However the removal of such an atom from an armchair edge does leave a dangling carbon atom, which can easily migrate and fill a vacancy elsewhere on the edge, as the calculations predict (Section 3.4.2, below). For an armchair configuration, two atoms are needed to repair the edge: the atom that was ejected and the neighboring dangling atom which migrated away. In a zigzag edge, only the ejected atom needs replacement. Hence the zigzag edge is more stable under electron irradiation at this energy, and the argument holds even when the ejection of atoms along the edge with three neighbors is considered.

These images, simulations, and analysis show the complicated dynamics which occurs at the atomic edge of a single-layer graphene sheet. The TEAM microscope provides real-time atomic resolution, and the electron beam at 80 keV acts as an energy bath which allows the dynamics of edge reconstruction and hole growth to be observed. This study of the edge configuration demonstrates the stability of the armchair and zigzag arrangements, and quantifies their evolution with time. Although the reconfiguration occurs on a time scale on the order of seconds, with a comparable contribution of armchair and zigzag sites, the long-term stability of zigzag edges is elucidated through a time-average analysis and explained by a simple model.

3.4.2 Notes and Methods

Numerical Simulation

A kinetic Monte Carlo method [152] is used to investigate the dynamics of the graphene hole edge. This allows simulation of such a large system with modest computational power and time, but comes at the expense of being able to define a physical time scale as with more computationally intensive molecular dynamics methods. We simulate the ejection and the adsorption processes by randomly taking out and putting in, respectively, carbon atoms along the edge. In order to reproduce the growth of the graphene hole, we set the ejection probability to be larger than the adsorption probability. In addition, these two probabilities (which depend on the detailed experimental conditions) are set to be 2-3 orders of magnitude smaller than the migration probabilities of dangling carbon atoms along the edge in order to match the dynamics observed in the experiment. The actual values of the probabilities is unimportant, as the time scale for the transitions is not defined by the simulation. The energy barrier height of migration used in our simulation (see the main paper) is obtained from density functional theory calculations within the local density approximation for the exchange-correlation functional. According to our calculations, the energy barrier heights for taking out a carbon atom which has one bond and migrating it to various nearby sites range from 0.3 eV to 0.6 eV, significantly smaller than those corresponding to migration of carbon atoms having two or three bonds (6 eV to 12 eV). The barrier heights increase when calculated for hydrogen-terminated edge atoms, but the relative values are comparable, and we do not expect terminating groups to influence the overall behavior. From these results, we confirm that by far the dominant process in the dynamics of carbon atoms at the edge of a graphene hole is the migration of dangling carbon atoms along the edge.

Role of Temperature

The actual temperature rise expected in the suspended graphene specimen due to exposure by the electron beam in the microscope is minimal. This is because the beam current density is small ($45\,\mathrm{A/cm^2}$) and the thermal conductivity of graphene is extremely high ($>1000\,\mathrm{W\,m^{-1}\,K}$). From Fig. 4.11 of the standard transmission electron microscopy textbook [157], the temperature rise is much less than 100 degrees and the sample will not be far from room temperature. In effect, sputtering occurs due to a few "direct hits" of edge atoms by electrons in the beam, but overall the lattice absorbs little energy because there are few electrons in the beam and the high thermal conductivity of graphene easily dissipates the heat.

The effective temperature used in the calculation of the migration probabilities is not related to the actual temperature which depends on the distribution of phonons in the sample, but should be considered a "beam-induced" temperature taking into account the energy input by electrons in the beam. It will depend on the beam energy, beam intensity, and the cross sections of the various electron-electron interactions involved in the breaking of bonds by the beam.

Image Analysis

To produce the content of Figure 3.31, image analysis was done using the ImageJ program. First the movie frames were registered, or aligned, using the MultiStackReg plugin by B. L. Busse to account for a small drift during the microscope recording. In order to avoid registering on features such as the hole which change during the film, the entire film is first cropped to a clean section of the graphene lattice far from the hole. Then the MultiStackReg plugin is used to register these frames and the translation vectors saved. Only a translation transformation is allowed, and no rotations or projections. Finally the translation vectors are applied to align the frames in the original movie. The Z-Project stack function is then used to average all registered frames and produce Fig. 3.31(a). Figure 3.31(b) was produced using the Reslice function along the slice indicated in Fig. 3.31(a) on the registered frames. In Fig. 3.31(c), the strategy used to obtain the hole outlines was to isolate the region within the hole as background. This background identification was performed using the Subtract Background function, with a 10 pixel rolling ball radius, and checked options "Light Background", "Create Background (Don't Subtract)", and "Disable Smoothing." This produced a stack of images where the hole was identified in dark contrast. A subsequent thresholding of this stack and application of the Analyze Particles function (with "Show: Outlines" and "Summarize") produced both the outlines of the holes and the area contained within each one. Finally a z-projection was applied to the stack of outlines to produce Fig. 3.31(c) and the area data converted to produce Fig. 3.31(d).

Zigzag Fraction Time Development

The evolution of the number of sites that exhibit zigzag character is quantified in Fig. 3.33. Because of the atomic resolution provided by the transmission electron aberration-corrected microscope (TEAM), one can identify the positions of atoms along the edge in all frames. One can classify the different types of edge atoms, count the number of each type in every frame, and plot their development as a function of time. This analysis is complicated by the fact that the hole is partially obstructed by adsorbates and that defects such as Stone-Wales (pentagon-heptagon), octagon rings, or dangling atoms can sometimes occur along the edge. To get around those complications, only three different types of edge configurations are considered, and only those are counted. These configurations are shown in the inset to Fig. 3.33(a). The first hexagon, indicated in red, is zigzag, whereas the next two sites, in blue, are armchair hexagons. The gray hexagons are neighboring hexagons, and the dashed line indicates the location of the edge. The two blue hexagons, in alternation, form an armchair edge. The fraction of zigzag hexagons along the edge is plotted as a function of frame number (multiply by four to obtain time in seconds). The total number of sites counted per frame varies between 20 and 40 hexagons. We see that, contrary to expectation, there is no trend, either upward or downward, for the zigzag fraction. Instead the value fluctuates around a mean value (solid light blue line) with large excursions both above and below a standard deviation (light dashed blue line) from the mean.

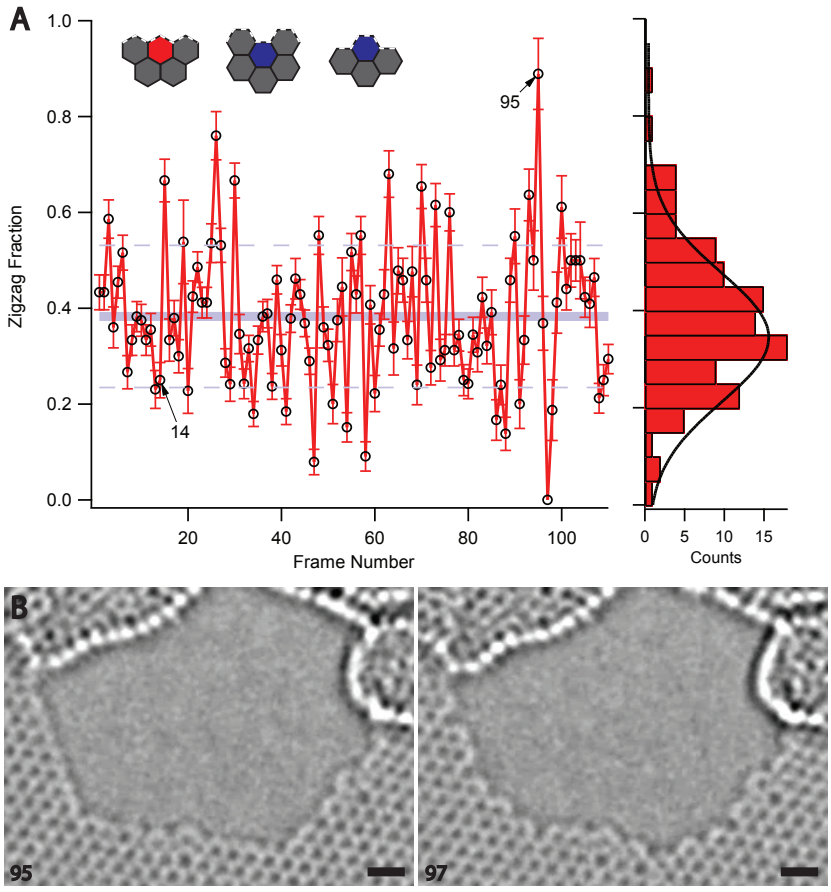

Figure 3.33: Schematic of zigzag stability.
(**a**) *Left*: Plot of the zigzag fraction of hexagons along the edge as a function of frame number. Inset diagram: a hexagon (red) is considered "zigzag" when surrounded by neighboring hexagons (gray) as in the first configuration, while hexagons (blue) in the other two configurations are considered "armchair". Any other configuration is ignored. The zigzag fraction fluctuates around the mean value $\mu = 0.38$ (light blue band), but there are jumps larger than the standard deviation $\sigma = 0.15$ (light blue dashed lines: $\mu \pm \sigma$) above and below the mean. The mean value expected for a random edge configuration is 1/3. *Right*: Histogram of zigzag fraction and Gaussian fit. (**b**) Frames 95 (left) and 97 (right) showing a transformation from an almost entirely zigzag-type edge to an armchair-type edge. Scale bar is 5 Å.

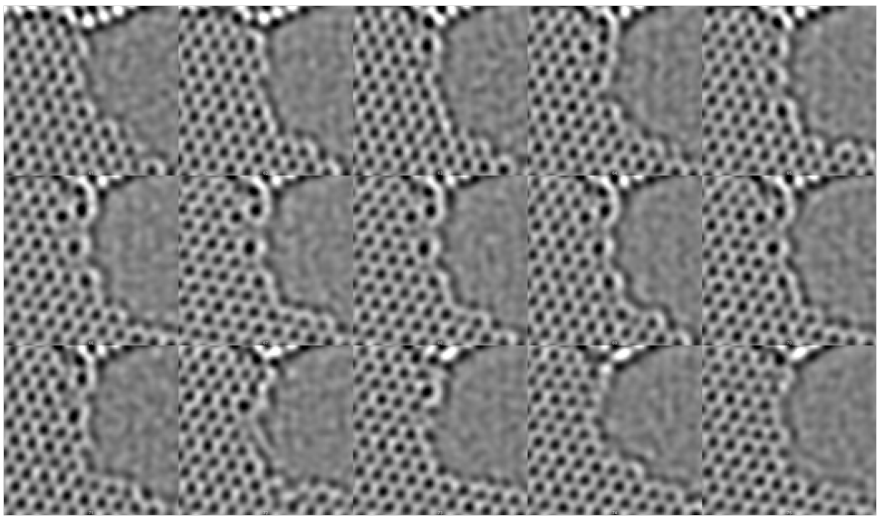

Figure 3.34: Pentaheptite edge structure.

For a completely random process, the zigzag fraction is expected to be one-third, as we only count three different configurations. The mean zigzag fraction is 38%, well within one standard deviation of the expected value. A Gaussian fit (black line) is plotted for comparison. The excursions indicate that long-range order is established, albeit briefly. The zigzag fraction at frame 95, 89%, is followed two frames later by an edge configuration with no zigzag hexagons at all. These two frames are shown in Fig. 3.31(b). One can see in frame 95, left, the predominance of zigzag sites, and two large defects on the bottom and right edges. In frame 97, eight seconds later, with the disappearance of several carbon atoms, the zigzag structure is completely gone. This local analysis reveals the speed with which the edge can be reconfigured, but does not show the global behavior and edge trend as displayed in Figure 3.31.

Other Extended Defects

Atomically resolved aberration corrected electron microscopy allows investigation of several different extended defects in a graphene crystal. An interesting edge structure which has been predicted by some theorists to be more stable than either the zigzag or armchair edge under certain circumstances (references in [93]) is pentaheptite. This is an alternating structure of five- and seven-membered rings. Although zigzag and armchair edges are predominant in Movie S1 considered previously, there are several frames where pentaheptite edges appear. A time-series development (frame order is left to right, then up-down) showing the formation and disappearance of a pentaheptite edge is given in Figure 3.34. A detailed analysis of this edge structure is given in a paper by Koskinen et al [93].

Another extended structure which can be induced by a missing atom or localized defect structure is a line defect. A segment of the entire graphene lattice may shift slightly to

reduce strain caused by the sudden formation of a point defect at a vertex consisting of one or several atoms. This can be difficult to detect by eye, as the overall hexagonal structure will be preserved. In order to elucidate such defects, processing of an image series is required. By subtracting each frame from the preceding one, changes are highlighted as regions of high contrast. If over the course of two frames one region of the image acquires large contrast, this indicates that a large number of atoms shifted position. This is what is observed in Figure 3.35. Fig. 3.35(a) shows two adjacent frames (first frame top; second frame bottom) from Movie S1 where a line defect has occurred. Visual inspection does not indicate where the line defect is located, although several point defects can be identified. The two images are registered using the region highlighted by the white square in the lower right of the frame and subtracted to give Fig. 3.35(b), the difference image. This difference image shows black where atoms stayed put and white where they moved. Unsurprisingly, the lower right of the frame is black since that is where the registry was performed. Elsewhere however, the image shows white dots over a large area where the atoms have moved in relation to the registry area. The short diagonal, dashed line separates the two domains. This is the location of the line defect. Fig. 3.35(c) shows the region around the defect line. In the right-hand frame, a white polygon has been drawn to show an unstrained graphene crystal structure. In the left-hand frame, corresponding to the upper frame in Fig. 3.35(a) the same polygon is superimposed. The shift in the atomic positions is clear. It is likely that this large strain has been caused by the defect pointed at by the black arrow, and results in the two domain difference image of Fig. 3.35(b). Theoretical calculations may be able to explain how such a localized defect can cause a large scale apparent relative shift in atomic positions, possible due to line defect formation or buckling.

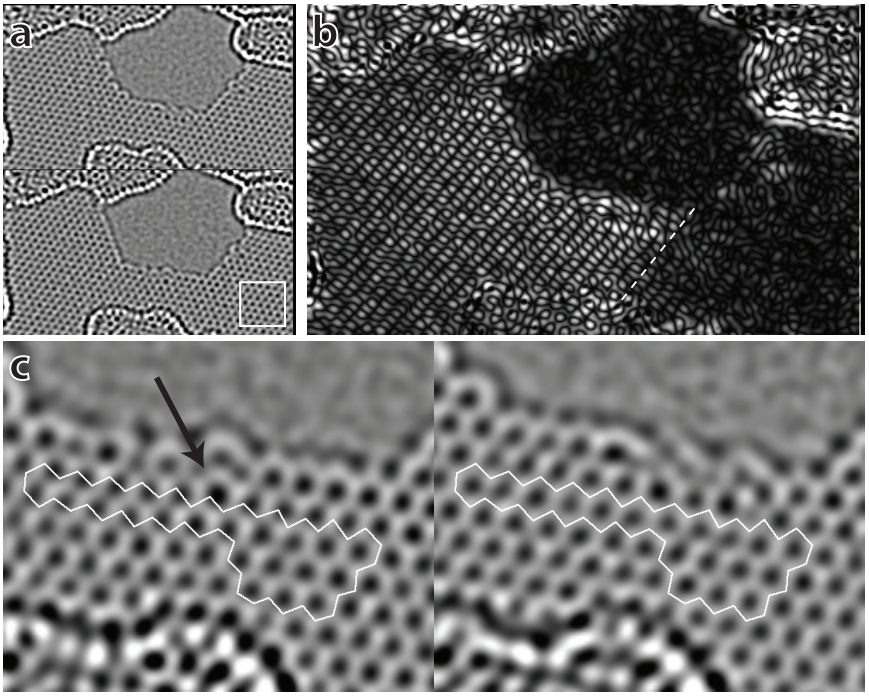

Figure 3.35: Extended defect induced by point defect.

Chapter 4

Manipulation

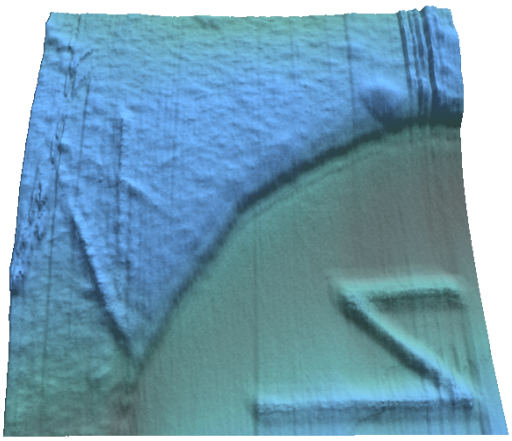

Figure 4.1: AFM image of graphene sample patterned with "Z" (suspended over hole) and "X" shapes by local anodic oxidation. Region is 1 1µm square.

Few experiments can be performed on graphene in its pristine exfoliated or synthesized form. Exfoliated samples are generally too small to be investigated as-is by anything other than focused optical microprobes (lasers) or scanning probes which function on insulating surfaces (AFM but not scanning tunneling microscopy). Synthesized samples can be arbitrarily large and would be amenable to experimentation, but the copper foil substrate to which they are firmly attached modifies their electronic properties. For both exfoliated and synthesized graphene, at least one electrical contact is necessary if the electric field effect is to be used to adjust the Fermi level. Hence almost all experiments with graphene require manipulating it in some way.

This chapter will cover three common ways to manipulate graphene to prepare a sample for an experiment. The first is lithography which is a general technique to define patterns

with features down to about 10 nm (electron beam lithography) or 1 µm(optical lithography). The second is deposition of electrodes for electrical measurements. The final method is etching and oxidation to define the active, or conducting area of a graphene device or otherwise shape it into a desired form. These techniques will not be discussed in generality but relevant references provided. Emphasis is placed on their specific application to the manipulation of graphene.

4.1 Lithography

Due to graphene's large surface-to-volume ratio, any lithography which involves solvents and polymers contacting the sample surface can adversely affect the device's electronic properties. Although conventional electron beam and optical lithography techniques can be used outright, special care must be taken to minimize depositing residues or damaging the graphene during processing. The surface of an oxidized silicon chip which has had graphite exfoliated onto it will invariably have tape residues or other gunk. Even if all solutions and resists are of exceptional purity and would not contaminate, the intrinsic on-chip residues will diffuse everywhere, including onto graphene when dissolved. Small modifications to a standard lithography process for device fabrication can help reduce the inevitable contamination. In addition, graphene devices can be annealed both externally and via Joule heating to remove contamination post fabrication.

In this section, graphene device patterning by electron-beam lithography will be discussed with details on ways to minimize contamination. For a general reference on microfabrication, consult the *Handbook of microlithography, micromachining, and microfabrication* [125]. In the second subsection, techniques to characterize contamination and examples of good and bad device fabrication are presented.

4.1.1 Patterning

Electron-beam lithography of graphene devices post optical identification for exfoliated samples, or synthesis for CVD graphene samples, involves seven steps. Spinning a special polymer resist to form a thin uniform film on the surface of the sample to be patterned; baking the resist to harden and solidify it; aligning the sample for proper patterning; exposing the resist to an electron beam in the desired pattern; developing the resist in a special chemical which selectively removes the exposed area (positive resist) or the negative of the exposed area (negative resist); processing the patterned areas for device fabrication, including electrode deposition or etching; and finally liftoff and/or PMMA strip, where the deposited thin film is removed and/or the remaining PMMA is dissolved.

The most important decision in this process is the choice of resist(s). Poly(methyl methacrylate) (PMMA, Microchem), known in commercial use as plexiglass, is the most common positive resist for electron beam lithography as it provides ultra-high resolution. The most common ultra-high-resolution negative resist is probably hydrogen silsesquiox-

ane (HSQ, Dow Corning FOX-12). A good reference to choose a resist is the Stanford Nanofabrication Facility E-Beam Resist website. In the following, only the use of single layer PMMA A4 resist will be covered, as this is the easiest and most reliable way to fabricate closely spaced contacts ($< 100\,\text{nm}$) of arbitrary width.

1. **Spinning**
   Before spinning resist, make sure that it is clean and unexpired. In order to avoid pouring it out each time from a 500 mL or 1 L stock bottle, store about 50 mL at a time in an all glass amber-colored reagent bottle with ground glass stopper (Wheaton). Frequent pouring from the stock bottle can contaminate the entire batch of PMMA. Seal the reagent bottle after each use with parafilm. Do not pour the PMMA out of the reagent bottle–use instead a disposable Pasteur pipette to transfer, taking care not to get any PMMA on the lid of the bottle. PMMA deposits on the lid will eventually dry out and the stopper will get stuck to the lid. This can be undone by inverting the bottle to dissolve the solids with the solvent (anisole or chlorobenzene) in the PMMA mixture, but could lead to contamination or solution inhomogeneity.

   Load the wafer chip with exfoliated graphene or synthesized graphene/copper foil onto the spin coater. The settings used to obtain a PMMA A4 film of roughly 200 nm is 3000 RPM for 30 s. Ready the Pasteur pipette which has been used to extract fresh PMMA from the reagent bottle near the sample. Squeeze out several drops away from the sample to remove any dust or particles at the pipette end. Now start the spinner and then quickly drop one to three drops per cm^2 onto the sample as it is spinning up. This will minimize the dissolution by solvents and subsequent diffusion of tape adhesive or other contaminants on the chip surface. When the drops hit the spinning sample, they are rapidly thinned and the solvent quickly evaporates, ejecting any briefly dissolved contaminants outward radially.

   Instead of using a Pasteur pipette, one can also use special syringes which have small-particle filters attached. This can be used to filter the PMMA mixture and is common practice in some research groups (Vincent Bouchiat, private communication).

2. **Baking**
   Once the PMMA has been spin-coated onto the sample, it needs to be baked. This is a straightforward procedure with a hotplate. However, it has been found that baking for a longer time than recommended greatly reduces post-development residues. Microchem, in their PMMA datasheet, give a recipe with a 60 s to 90 s bake time at 180 °C. This *should not* be followed. Instead bake for at least 30 min at 180 °C. A recipe requiring three minutes of baking had been followed for many years before it was realized that this left residues post-development. Place an inverted glass petri dish over the sample during baking to avoid dust deposition.

3. **Alignment**
   At this point, one should check in the optical microscope that the exfoliated graphene

sample has not folded over itself or disappeared as a result of the spinning process. This can sometimes occur depending on the adhesion of the sample to the oxide. This check as well as the following alignment step should not be not necessary for large area CVD synthesized graphene. However alignment of the desired contact pattern to a small graphene sample is necessary to obtain a working device! Conventionally this is done by doing a rough alignment first and then exposing an alignment pattern near the sample in the SEM. Then, having taken an optical photo of the alignment marks and sample, one can subsequently align with respect to those marks in the SEM before patterning the actual device geometry. However one can bypass the SEM alignment-mark patterning step by using instead a micromanipulator to directly scratch the PMMA near the sample, similarly to the process of microsoldering (Sec. 4.2.3). The mechanical scratch marks then serve for alignment just as electron-beam exposed alignment marks would but time is saved.

4. **Exposure**
   Proper electron beam exposure is critical both to prevent leaving residues and to achieve narrow linewidths. If the dosage is too small (usually less than $250\,\mu C\,cm^{-2}$), not all of the PMMA will be lifted off and some residue will remain in the exposed areas. If the dosage is too high (much greater than $400\,\mu C\,cm^{-2}$) the patterned features will be enlarged and shorts can occur between closely spaced contacts. At very large dosages, approaching $1000\,\mu C\,cm^{-2}$, PMMA can act as a negative resist (to acetone) and this will also leave residues in exposed areas.

   It is critical to run dosage tests regularly as the proper dosage can vary with time as the PMMA ages. If the required dosage has increased significantly, this is a good indicator that the PMMA is no longer good. To do a dosage test, pattern an array of doublets of closely spaced rectangles. After development, sputter a nanometer thin film of gold and inspect in the SEM. An alternative is to avoid sputtering gold and inspect with an AFM, but this is more time consuming. The doublet with proper dosage will have no residues in the interior of the exposed rectangles and the narrow unexposed line in between the two rectangles should be well defined (no bowing, no breaks, and desired width). For good PMMA on the FEI Sirion SEM in the Zettl group, proper dosage at 30 kV is around $325\,\mu C\,cm^{-2}$.

5. **Development**
   Once the PMMA has been exposed it needs to be developed. The exposed regions are damaged and are more readily dissolved by the developer. For PMMA, the developer used is a one-to-three mixture of methyl isobutyl ketone and isopropanol (MIBK:IPA, 1:3). Prepare sufficient developer in a small beaker. Using clean tweezers, hold the chip near a bottom corner and submerge in the developer. Shake it back and forth without letting go of the tweezers for 30 s. Have a squirt bottle of clean isopropanol on hand. At the end of the 30 s, pull out the chip, taking care that the tweezers are at the drip-down end of the chip and squirt vigorously with isopropanol to rinse the developer.

The isopropanol should run from the top of the chip to the bottom, accumulating at the tweezers and then dripping off. Capillary action between the tweezer ends will suck up developer and isopropanol. It is undesirable to have them run back down onto the sample. After squirting isopropanol for about 10 s to 15 s, blow dry with a N_2-gun, pointing it downward to force the evaporating alcohol to run down toward the bottom of the chip. Be careful when placing the chip down once it is dry because there may still be liquid resting between the tweezer ends that could run back onto the chip.

6. **Device Processing**
   This will be covered in the next two sections, where electrode deposition and etching are discussed.

7. **Liftoff/PMMA strip**
   Now that the patterned areas have been processed, it is time to remove the remaining PMMA. This PMMA layer has undergone all the preceding processing steps and can be difficult to remove. This is especially the case after device processing involving etching with certain reactive gases or the deposition of high melting point metals. The vigor with which one attempts to remove the PMMA must be balanced by the need not to damage the sample and electrical contacts, if any. The standard process for liftoff is to submerge the sample in a beaker of clean acetone. The acetone will slowly dissolve the PMMA, leaving the rest intact. In order to better remove PMMA residues which can stick preferentially to the graphene, the beaker of acetone and sample is placed in a water bath which is then heated between 60 °C to 80 °C. The acetone should not boil, but the additional heat will improve the stripping power and the induced convective currents may help avoid redeposition of dissolved contaminants. It is best to keep the beaker at an angle, with the sample chip resting almost vertically on the beaker walls. In this configuration heavy deposits in the solution will not tend to sink onto the sample as much as they would if the sample were horizontal. Or at least that is what one can imagine–there is a fair amount of speculative, untested steps in these recipes, but if it works one keeps it. Keep the sample under hot acetone for 5 15min. Make sure that there was enough acetone to start with as it will evaporate rapidly once hot. At this point grab the chip with clean tweezers in one hand and a squeeze-bottle of clean isopropanol in the other. As in the **Development** step, hold the sample near the bottom. Vigorously spray isopropanol onto the chip as you remove it from the acetone. It is extremely important to blast the chip with isopropanol before the hot acetone rapidly evaporates from the chip surface. The only way to reliably do this is to start spraying isopropanol onto the chip while it is still submerged but just under the level of the acetone. Remember to always spray downward. After 10 s of spraying, blow dry with nitrogen, running the evaporating isopropanol downward toward the tweezer end.

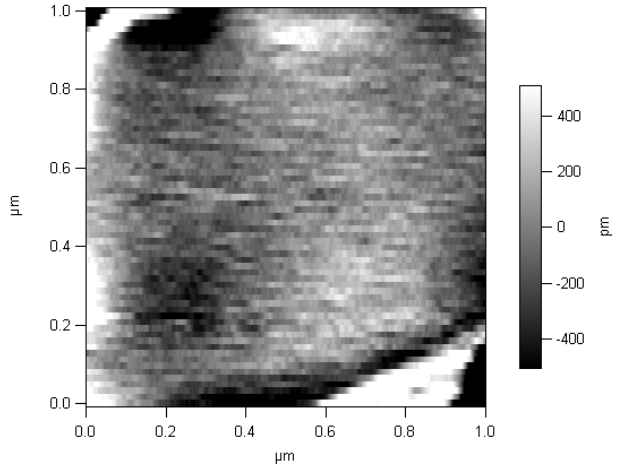

Figure 4.2: AFM contact mode topography of suspended few-layer graphite. Roughness in central area is 50 pm.

4.1.2 Evaluating Contamination

The best way to evaluate surface contamination is atomic force microscopy. However as a scanning probe technique, AFM can be time consuming. If patterned features have high aspect ratios, such as narrow and tall trenches, it can be impossible to image with conventional cantilever tips. In these cases scanning electron microscopy is a good alternative, but low atomic number elements such as organics will usually need to be coated with a thin metallic layer to be visible. This can be done quickly with a sputterer (Anatech).

If the surface residue grain size is extremely small (several nanometers), SEM is rendered useless, whereas roughness measurements in the AFM can still detect the contamination. A good demonstration of this is the electron-beam deposited hydrocarbons discussed in Section 3.2.3. The SEM micrograph, Fig. 3.17(c), shows darker contrast in the exposed areas but a priori it is not clear whether this is a charging effect due to the high electron dosage of the insulating silicon oxide or whether the surface has been contaminated or both. However an AFM scan, Fig. 3.18, shows that the roughness in the exposed areas is larger by about 90 pm. Although this is extremely small, about twice a Bohr radius, it is indicative of surface contamination. Indeed, imaging of electron-beam induced hydrocarbon by TEM confirms this [107].

Pristine non-suspended exfoliated graphene imaged by AC mode AFM should have a roughness of 150 pm. For pristine suspended samples, this roughness measurement should be limited by noise, and has been measured as small as 50 pm, Fig. 4.2. The roughness measured on a graphene sheet which has undergone lithography with proper exposure should be less than 300 pm (Fig. 4.4).

Figure 4.3 shows the effects of rinsing a pristine graphene sample in acetone. On the left is the pristine graphene sheet. The RMS roughness measured in a 1 µm × 1 µm square on

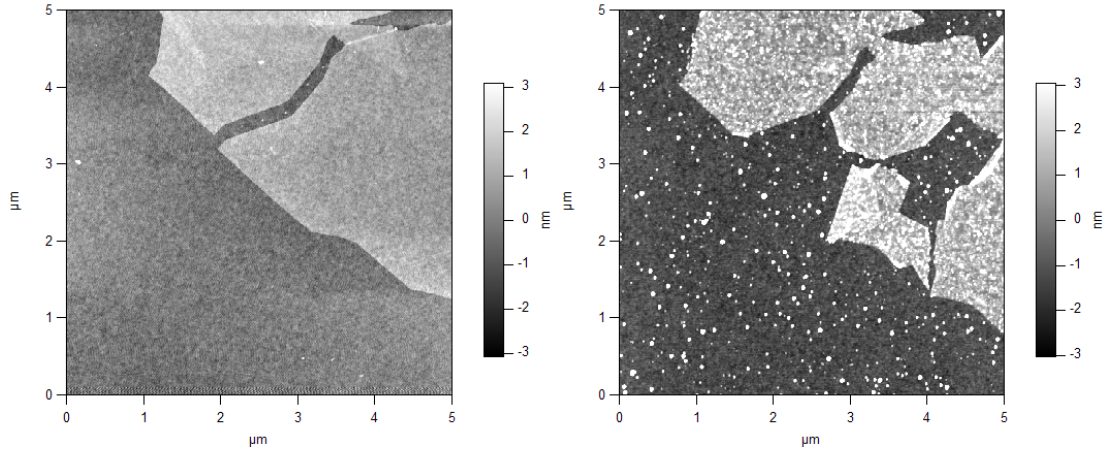

Figure 4.3: AFM topography evaluation of contamination of pristine graphene sheet due to acetone rinse.

the graphene is 344 pm and on the silicon oxide, 398 pm. It is normal for the on-graphene roughness to be smaller due to the draping of the graphene sheet over the hills and valleys of the amorphous oxide surface. The topography image after dipping the chip into a beaker full of clean acetone, shaking it, and then removing it and leaving it to dry is shown on the right. Many white spots are visible with heights of several nanometers. These are likely to be redeposited adhesive tape or other contaminants which had been dissolved by the acetone and then clumped together upon evaporation. The folding and ripping of the graphene sheet can be ignored and is likely due to the careless processing for demonstration purposes. The RMS roughness measured in a $1\,\mu m \times 1\,\mu m$ square on the dirtied chip is 1.01 nm for graphene and 1.11 nm for the SiO_2. From these images it is clear that liquid-phase processing of graphene samples needs to be done carefully to minimize contamination. It is also extremely important to evaluate contamination by SEM or AFM because optical imaging cannot detect it because of the small particle size and composition.

Scanning electron micrographs and atomic force microscopy of the effects of proper and improper dosing are shown in Figure 4.4. The test pattern shown was exposed at different dosages, increasing from the left toward the right, and then developed. A thin film of gold (1 nm) was sputter-coated prior to imaging the patterns in the SEM. A dosage of about $200\,\mu C\,cm^{-2}$, marked "Low exposure", clearly shows residues. The properly exposed test pattern (about $300\,\mu C\,cm^{-2}$) shows no residues and well-defined walls of roughly 50 nm width. The overexposed test pattern (about $400\,\mu C\,cm^{-2}$) shows no residues but bowing of the walls. Atomic force microscopy prior to sputtering indicates a roughness of about 375 pm for low exposure. At proper dosage, the roughness is reduced to about 250 pm.

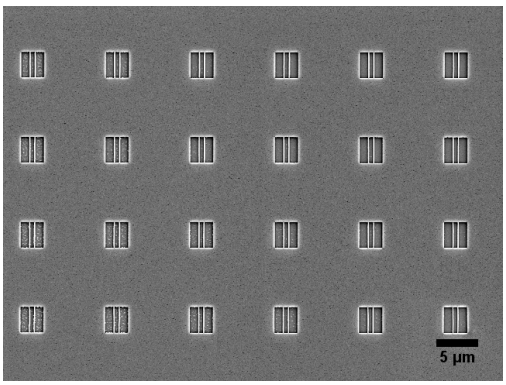

(a) Test pattern

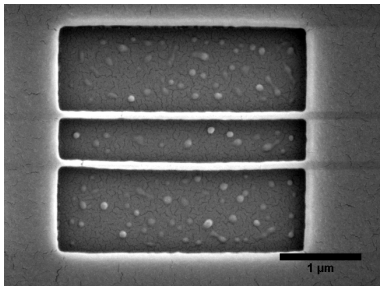

(b) Low exposure

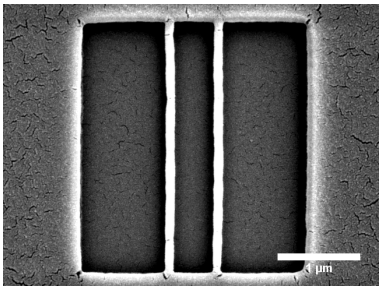

(c) Proper exposure

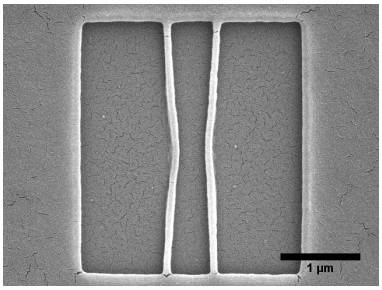

(d) Over exposure

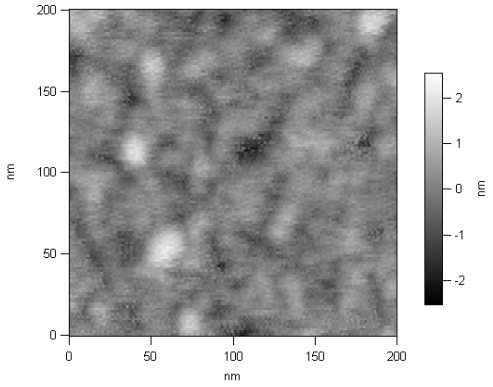

(e) AFM, low exposure

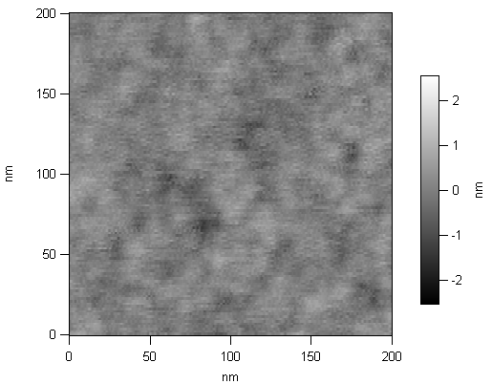

(f) AFM, proper exposure

Figure 4.4: Electron beam lithography exposure test. Scanning electron micrographs of test pattern with varying exposures. Atomic force microscopy of substrate roughness with proper and improper dosing.

(a) Electron-beam evaporator (b) Thermal evaporator

Figure 4.5: Thin-film deposition systems. Zettl group wiki.

4.2 Electrode Deposition

Several different techniques that can be used to attach electrodes onto graphene samples to investigate electronic transport properties are described below. The conventional technique is to do lithography followed by thin film deposition. One can avoid doing polymer-based lithography on a sample and contaminating it by using stencil-mask evaporation, but this precludes having closely spaced electrodes or fine features (less than several microns). An alternative which also keeps samples clean but does not require any thin-film evaporators is microsoldering, in which small contacts are soldered onto a sample under a microscope using micromanipulators. This has the same limitations on feature size as stencil masks, but it is more difficult to produce complex electrode geometries.

4.2.1 Thin Film Deposition

Two common means to deposit thin films are electron beam evaporation and thermal evaporation. Both rely on heating the evaporation source to the point where atoms are ejected from the surface of the source and onto the sample. They differ in how the source is heated, but are similar in most other aspects. Another technique which is not covered here is sputtering, in which a source is bombarded by ions with the aid of electromagnetic fields, resulting in the ejection of atoms as well as atomic clusters at the surface of the source. Although there is some heating of the source when sputtering the mechanism is not thermal but mechanical, similar to sandblasting. For this reason, sputtering is desirable for depositing materials with high melting points such as refractory metals and ceramics. A less conventional technique for thin film deposition is atomic-layer deposition (ALD), which is

more similar to chemical vapor deposition (2.2) than any of the other techniques.

In the following a brief description of the functioning of electron beam and thermal evaporators is given along with recipes and results for their use in making different types of thin films relevant for graphene electronic devices. These include normal metals, superconducting metals, and gate dielectrics. A good reference of evaporation techniques and parameters for various materials is the Thin Film Evaporation Guide.

Electron Beam Evaporation

In an electron-beam evaporation system, for example shown in Fig. 4.5(a), a tungsten filament is elevated to high temperatures by Joule heating which causes thermal emission of electrons. A fixed electric field is used to accelerate these electrons to an energy of 5 keV and electromagnets are used to focus and steer them onto the evaporation source. The beam spot size can be controlled between 0.1 cm to 1 cm. The intense electron flux causes localized heating of the material, be it metallic or insulating. Once the local temperature is high enough, the atoms "boil" off and travel ballistically in a high vacuum chamber onto the sample, where they quickly cool and form the thin film.

- **Au**
  Gold is a useful metal for forming electrical contacts because it has high conductivity and does not oxidize. It can be used as a capping layer to prevent oxidation of covered layers. It is relatively easy to evaporate by electron beam evaporation, but nonuniform heating can cause spitting. Spitting will show up as beads of gold interspersed in the thin film and is likely a result of bubbles in the molten gold popping and spewing a large assembly of atoms. In order to keep spitting down heating needs to be uniform, which can be difficult with electron beam evaporation. Keep the spot large and sweep it at a high frequency in order to minimize thermal gradients.

  Gold is usually evaporated with a graphite or vitreous carbon crucible. This eventually results in carbonaceous surface contamination because of the non-zero but small solubility of carbon in gold (Fig. 2.15). The gold nugget will lose its luster and develop a dark matte coating. This can be removed by sanding the surface or one can try heating in air/oxygen or piranha etching.

  Gold deposition by thermal evaporation is preferred. If it is deposited with an electron beam, evaporate dirty surface layers before opening the shutter.

- **Cr**
  Chromium is an important material for contact fabrication because it sticks readily to most materials, including graphene and oxides. It forms a strong adherent film which is difficult to remove mechanically, such as by scratching. Although it is a transition metal with a relatively high melting point (1890 °C), it sublimes at low pressures and can be evaporated easily with low beam currents. Chromium crystal chunks can be loaded in a vitreous carbon crucible. The chromium will eventually form a greenish

oxide sheen which should be evaporated first before opening the shutter. Otherwise, replace the chromium source as it is inexpensive.

- **Pd**
  Palladium is an excellent material to form transparent contacts to graphene [60]. It can be used as a thin interfacial layer between graphene and another material such as gold or aluminum in order to improve contact resistance. It is not as easy to evaporate as gold and is much more easily contaminated by the crucible. Recommended crucibles are alumina (Al_2O_3) and BeO, but alumina crucibles eventually alloy with the palladium and form a dull oxide before cracking and breaking. Beryllium oxide has not been tested.

  It is best to evaporate the palladium quickly with higher beam currents rather than slowly with low currents as this can be unstable. Palladium will also spit vigorously.

- **Al**
  Aluminum is important as an easily processed type-I superconducting metal. It is a desirable material for making Josephson junctions due to its long coherence length ($>1\,\mu m$). Evaporation of aluminum can be tricky, as it tends to alloy with most materials. The recommended crucible for electron beam evaporation is alumina, but this will result in eventual oxidation of the aluminum source itself. When evaporating, it is highly unstable.

- **Ru**
  Like most refractory metals, ruthenium is difficult to evaporate. Fortunately it has the lowest melting point of the platinum group of elements at 2700 °C and can be evaporated by electron beam evaporation. Thin ruthenium films can be used for graphene chemical vapor deposition (Section 2.2). Although vitreous carbon is the recommended crucible, experience has shown that graphite crucibles work better and do not form holes as easily. Ruthenium slugs should fill the crucible at least halfway to avoid damaging the crucible. Ruthenium is expensive and hard to evaporate, so it is best to evaporate once onto a large area rather than several times onto small ones. Once the chamber pressure is at 1×10^{-6} Torr, degas the ruthenium by ramping up the beam current slowly, letting the pressure go up and return before increasing further. It will degas significantly. Once the ruthenium is properly degassed, the observed deposition rate at the crystal monitor should be zero. The ruthenium will finally start to evaporate at high beam currents and should be stable if properly degassed. In the Zettl group evaporator (Fig. 4.5(a)), which has a 3 kW gun, the deposition rate is $0.3\,\text{Å}\,s^{-1}$ to $0.4\,\text{Å}\,s^{-1}$ at the max current of 500 mA. Monitor the evaporation closely because the ruthenium may shift away from the beam, which will result in rapid hole burning of the crucible and possible damage to the hearth. Radiative heating will increase the chamber temperature significantly if there are no radiation shields, so allow time for cooling down the chamber cool down before venting.

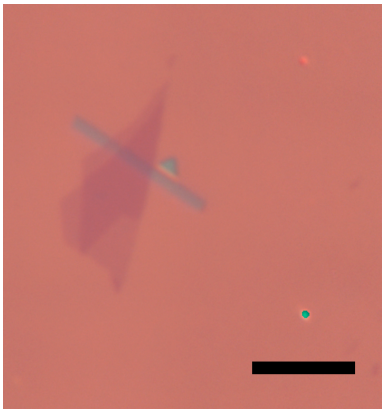

(a) ALD, optical image

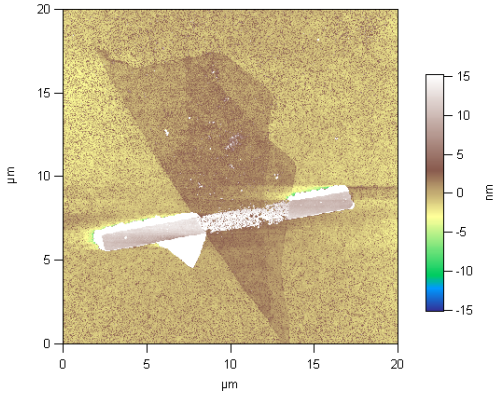

(b) ALD, AFM topography

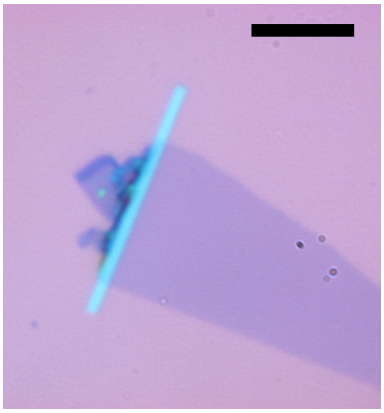

(c) E-beam, optical image

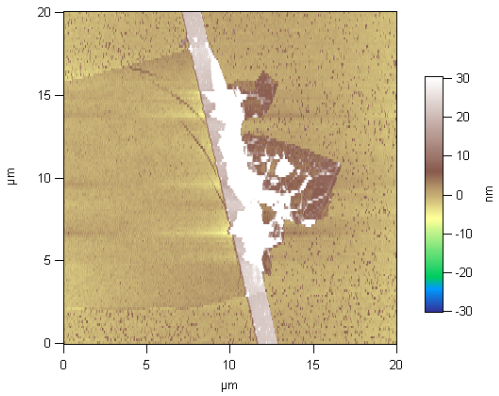

(d) E-beam, AFM topography

Figure 4.6: Alumina deposition on bilayer graphene by atomic layer deposition (ALD) (a,b) and on trilayer graphene by electron beam evaporation (c,d). Scale bar in optical images, 10 µm.

- **Dielectrics**
  Common dielectrics such as SiO_2 and Al_2O_3 are readily evaporated by an electron-beam. In fact this is a preferred method for making top-gates (with alumina) on graphene devices as near-ideal breakdown voltage can be obtained, and mobilities are not unacceptably affected. In contrast to atomic layer deposition, alumina evaporated in the e-beam evaporator will stick to the graphene surface and form a continuous film as shown in Fig. 4.6

Thermal Evaporation

In thermal evaporation, the source material is heated either directly by passing a large current through it or indirectly by being in good thermal contact with a carrier heated in

this manner. It requires specially designed boats or filaments of conducting material with resistance matched to the output of the system power supply and the potential for good thermal contact to the source (in the case of indirect heating). Because of these reasons, it is less versatile than electron beam evaporation and most high melting point materials cannot be thermally evaporated. On the other hand, Joule heating can provide much more uniform heating than an electron beam as well as allow evaporation of large quantities which can be advantageous.

The Zettl group MBraun thermal evaporator is shown in Fig. 4.5(b). It has a liquid nitrogen cooled, rotating sample stage and the capacity to evaporate two different source materials at a time. It is the preferred means to evaporate the following materials.

- **Au**
  The uniform heating profile, compared to the electron-beam evaporator, avoids spitting and produces uniform, flat films. Alumina-coated tungsten boats with an exposed tungsten central region work well (R.D. Mathis part S35B-AO-W). Evaporation is extremely easy and stable. Molybdenum boats also work, but the gold can creep around the edge.

- **Cu**
  Copper is similar to gold in ease and quality of thermal evaporation. Molybdenum boats are recommended for copper and works fine. Films as thick as 1 µm have been deposited by thermal evaporation for CVD graphene growth.

- **Al**
  Aluminum can be deposited by thermal evaporation and is easier than electron beam evaporation. Three standard Al pellets (Kurt Lesker, 1/8" diameter by 1/4" length) or 4" of 40-mil diameter wire (VWR Part AA43427-G5) are loaded in a basket heater (R.D. Mathis or part ME17-3X.025W at Kurt Lesker). Evaporation proceeds quickly and should be stopped before the entire source is evaporated. The small quantity of source material does not allow for evaporation of thick films. The aluminum alloys with the tungsten and the heater must be discarded after several uses as it becomes too brittle.

- **Pd**
  Bob at R.D. Mathis, (562) 426-7049, suggests using boat S4-.015W similarly to Ti below. He recommends a slow ramp (4 min) to melt the palladium, and then a quick evaporation. The boat should be reusable, but the palladium will corrode the tungsten. He said alumina coated boats could work too, but alumina crucibles have led to contamination in the electron-beam evaporator. A possible Al_2O_3 coated boat for this purpose is S21-AO-W.

- **Ti**
  Titanium can be evaporated thermally, but this is difficult as it has a high melting

point. There are several suggestions for heaters: a titanium filament (Duniway part TSP-12-PE); boat S4-.015W with small Ti pellets that lie below the lip of the groove; a 0.5 mm tungsten filament (R.D. Mathis) tungsten filament (W filaments at RDMathis) in 0.127 mm Ti wire (VWR AA10391-G5); one-two standard Ti pellets inside a wire heater (same as Al above).

- **In, Sn**
  Indium and tin are two soft metals with low melting points which are useful as superconductors. They can be evaporated easily both by thermal and electron-beam evaporation, however they do not form continuous films if deposited onto substrates at room temperature (Fig. 2.16). The auto-assembly of small, closely spaced islands can be exploited for experiments [87]. If a continuous film is desired, the substrate should be cooled.

Atomic Layer Deposition

Atomic layer deposition (ALD) is similar to low-pressure chemical vapor deposition (LP-CVD) in that vapor phase reactants undergo a chemical reaction at a hot surface in an evacuated chamber. The main differences are that in ALD, the reactants are introduced in small bursts with the reaction at the heated surface proceeding one atomic layer at a time, and that the chamber temperatures are in general lower. ALD makes conformal coats, unlike with the line-of-sight evaporation techniques discussed above. Because of this it is often used to make high-quality dielectric coatings of materials such as alumina with low pinhole-density.

ALD does not work well on graphene without external priming (such as polymer coating) of the surface because of the inertness of graphene. Figure 4.6 shows a comparison of alumina deposition on graphene by ALD and electron-beam evaporation. Although the ALD alumina film appears good on the SiO_2 in the AFM image, it looks porous and discontinuous on the graphene and could not be used as a dielectric for a graphene top-gate. Other groups (Kim, Goldhaber-Gordon) have succeeded in ALD Al_2O_3 top gates on graphene but with initial priming. It is not clear what ALD chemistry is directly suitable for graphene.

4.2.2 Stencil Masking

Stencil masking refers to evaporating a thin film through a mask which has patterns lithographed into it. In comparison to standard electron-beam lithography, a hard prepatterned mask takes the role of the patterned PMMA. Stencil masks can be fabricated by doing conventional lithography on a silicon, silicon oxide, or silicon nitride substrate and then etching completely through the patterned regions. Then the mask is aligned onto the sample, using either a professional mask alignment system or a home-built one using micromanipulators similar to the one discussed below for microsoldering (Section 4.2.3). The film is then evaporated onto the sample through those unmasked regions (Fig. 4.7). While stencil masks

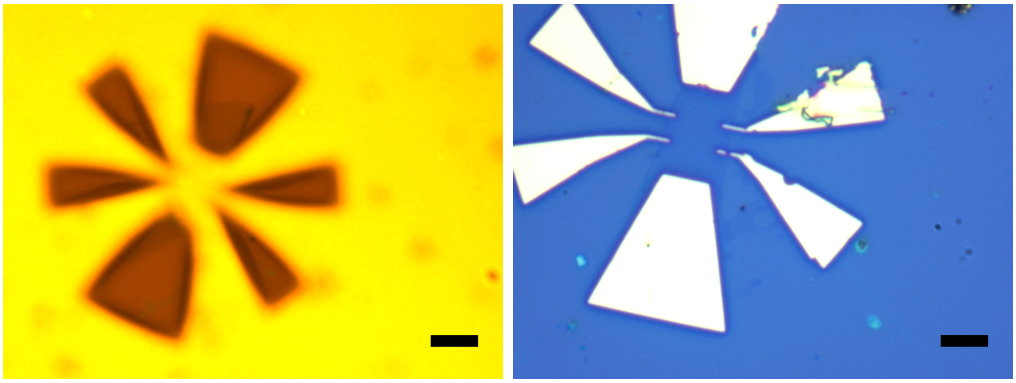

(a) (b)

Figure 4.7: Alignment of shadow mask over graphene sample and device post-evaporation. Scale bars 10 µm.

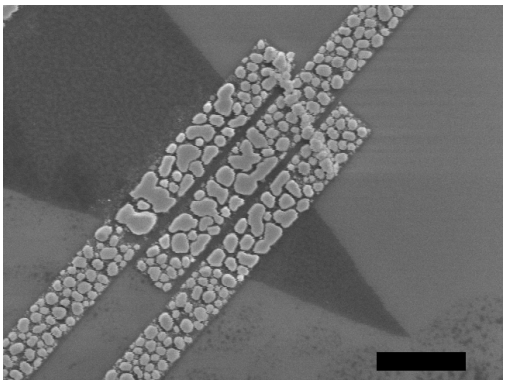

Figure 4.8: Diffusion of evaporated indium on patterned region of graphene and SiO_2. Larger islands over graphene indicate longer diffusion lengths than on SiO_2. Scale bar 2 µm

are useful in that wet-processing of the sample is avoided and contamination minimized, it has several drawbacks. First, the desired pattern must be simply connected–there cannot be any holes. For example, a Corbino disk stencil mask is not possible. Second, the pattern feature size is limited by two factors: because the mask must be etched completely through, it is difficult to have narrow features using thick masks; if the mask is not in close contact with the sample, evaporants will pass at an angle under the masked regions and features will be broadened. Finally, since the masks cannot be too thick, they are prone to breaking during alignment, transportation, or worst, evaporation. Despite these drawbacks, for simple contact geometries, stencil masks are ideal for graphene as they avoid contaminating the sample.

When using stencil masks with graphene, care must be taken in the choice of evaporant material. Due to the inertness of the graphene surface, many evaporated metals will hit the

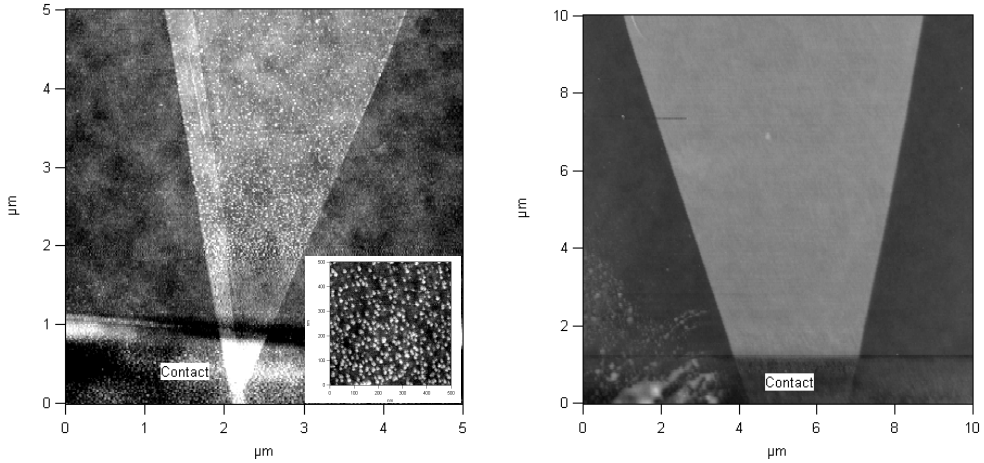

(a) Au (b) Au/Cr

Figure 4.9: Comparison of deposition of Au and Au/Cr through stencil mask onto few-layer graphite samples. Gold diffuses onto sample whereas chromium does not.

graphene surface and migrate substantial distances of up to tens of microns. This diffusion distance will be determined by the kinetic energy of the incident particles, their thermalization to the substrate, and the graphene-evaporant surface interaction. The diffusion length is longer on graphene than on SiO_2 for indium (Fig. 4.8) and probably for other materials as well. Substrate cooling can reduce diffusion, but adds complexity to the evaporator system.

Gold evaporated through a stencil mask onto graphene will travel several tens of microns and room-temperature evaporation should be avoided (Fig. 4.9). Titanium, often used as an adhesion layer, has also been observed to migrate on graphene. Chromium however adheres well to graphene even at room temperature and can be used as a contact material by itself or as an interfacial layer.

4.2.3 Microsoldering

The conventional method of electrically contacting nanostructures, as described above, is electron-beam lithography. While having good resolution, the procedure is complex, expensive, and time-consuming. Moreover, as demonstrated the polymer resists and solvents used in the process leave residues that contaminate the sample or device. As a result, often the major contribution to the device resistance is not from the sample itself, but from the contact [138]. Other lithography-free contacting techniques (see Section 4.2.2) have been attempted, but they have their own drawbacks and have not been widely used. An alternative method, effectively a miniaturization of soldering, allows making sub-micron sized, ohmic contacts to nanostructures of even single-atom thickness such as graphene. The technique is simple, inexpensive, rapid, and entirely avoids sample contamination.

Figure 4.10 shows the main components of the microsoldering setup: a micromanipulator,

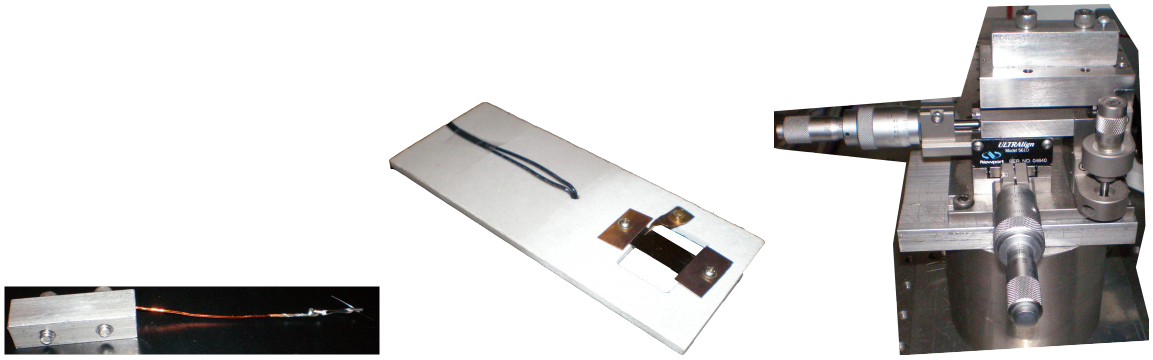

(a) Solder tip holder (b) Heater (c) Micromanipulator

Figure 4.10: Components of a microsoldering setup.

a heated sample holder, and a soldering tip holder. A photo of the setup along with a schematic is shown in Figure 4.11; and a photo showing the entire microscope in proximity to the micromanipulator is Fig. 3.2. The micromanipulator is a heavy duty three-axis precision motion stage, Newport 561 ULTRAlign. The soldering tip holder is stiff copper wire fixed with a set screw onto an aluminum block which is machined to fit onto the micromanipulator. At the far end of the copper rod is a small soldering tip holder, which can be a small hole and set screw machined into the copper or a professional microprobe holder accessory from a probe station soldered to the end. This soldering tip holder will house an etched tungsten wire or commercial probe tip (for example Signatone, Inc.) which will be used for soldering. The set screw should loosely clamp the copper rod onto the aluminum block to dampen vibrations. Other vibration-dampening mechanisms could also be incorporated into the design, but a loose set screw works very well. The heated sample holder is fabricated out of a commercial machinable ceramic (alumina from McMaster-Carr), a degenerately doped silicon wafer chip, and beryllium-copper contacts attached to low-resistance wires (black in photo). The degenerately doped silicon serves as a thin and flat heating element suitable for insertion under the microscope objective and keeps the sample planar for observation. A major problem with doped silicon is the strong temperature dependence of the resistance, and a thin film of nichrome (Ni-Cr) deposited on a silicon chip can be used instead. Beryllium copper (BeCu) thick foil contacts clamp the chip firmly and provide a good contact. The wires supplying current are firmly anchored at the underside onto a stainless steel nut and screw in electrical contact with the BeCu. The optical microscope should have long working distance objectives to allow insertion of the soldering tip above the sample.

The sample to be contacted is placed on the holder along with a small bead of indium. The temperature of the holder is then raised to 170 °C, roughly twenty degrees above indium's melting point. The indium serves as the low-melting point solder. The room-temperature tungsten tip, attached to the holder, is inserted into the molten bead using the microscope and micromanipulator XYZ translation stages, and a spike of solder is slowly pulled out.

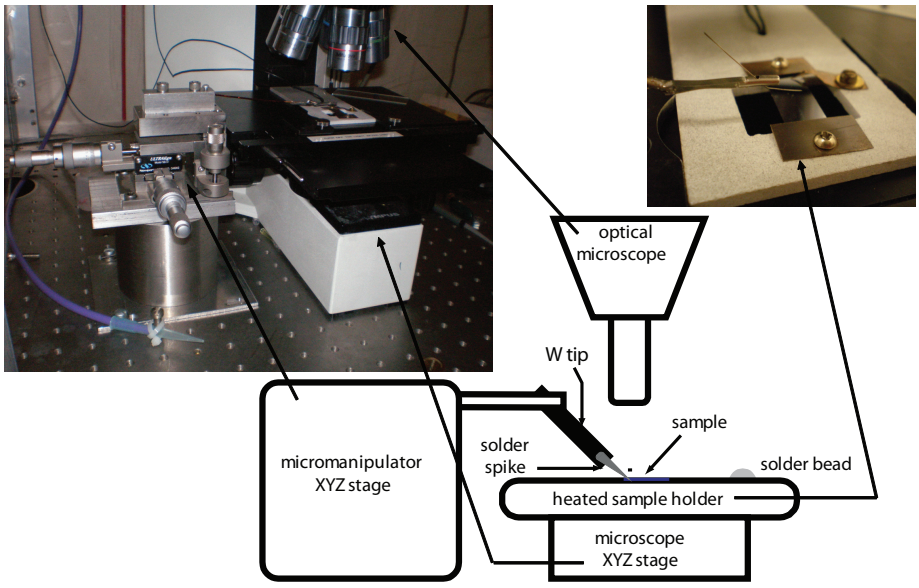

Figure 4.11: Schematic of microsoldering setup.

Sub-micron spike tips (Fig. 4.12) are possible with careful adjustment of the temperature and pullout rate. The sample and spike tip are then successively positioned and aligned under the microscope using both XYZ stages. The microscope stage is then quickly raised, fusing the solder spike onto the sample as it comes into contact. Once all contacts are made, the sample heater is turned off and the contacts solidify to produce a device (Fig. 4.13). A video of the procedure can be provided on request (caglargirit@gmail.com).

Several low-temperature melting point alloys of indium and tin (Indalloy 1E, 4, 121, 182, 290) have also been used to make contacts. Indium is desirable because of its good adhesion to numerous surfaces, including silicon oxide. Flux and flux-bearing solders are avoided so as to keep the sample free of residues. In fact flux, as well as inert or forming gases which would normally be required to make a good bond, are unnecessary with this technique. Since the tungsten tip which draws out the solder spike is at room temperature, oxidation of the solder spike is minimal [133]. Sample oxidation is also negligible for carbon nanostructures, since oxidation in air is significant only above 350 °C [85, 80, 27], and for these materials only solders with eutectic or melting points in the range 118 °C to 280 °C are used. Ultimately, once the procedure is fine-tuned, the nano-solder contacts are extremely reliable.

Using this technique electrical contact can be made to exfoliated graphene sheets down to about 10 µm in size. Several images of microsoldered graphene devices with two terminals is shown in Fig. 4.13. The separation between contacts can be as small as several microns.

Figure 4.14 shows the source-drain current I_{sd} of a nano-soldered graphene device measured as a function of applied voltage V_{sd} in the range ± 10 V at room temperature in ambient conditions. The IV characteristic is linear even up to such high source-drain voltage. The resistance of the device, from the linear fit (dashed line), is 5.7 kΩ. The inset, an IV trace

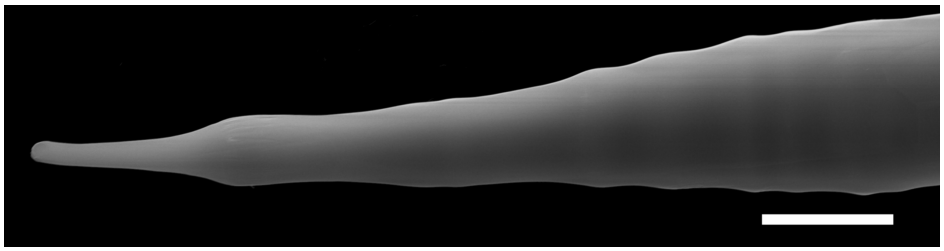

(a) Tip 1 (Scale bar 5 µm)

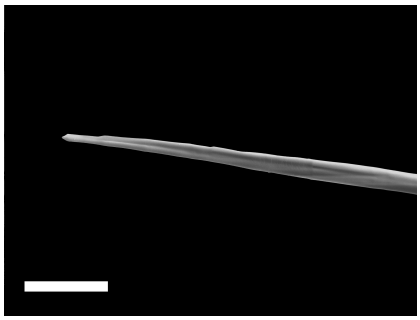

(b) Tip 2 (Scale bar 5 µm)

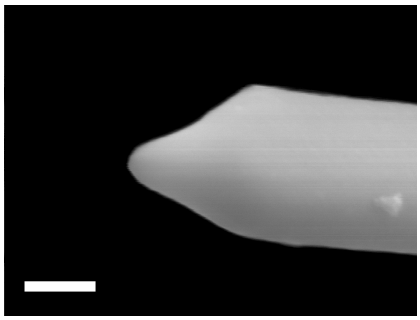

(c) Tip 2 (Scale bar 200 nm)

Figure 4.12: Indium microsolder spike tips.

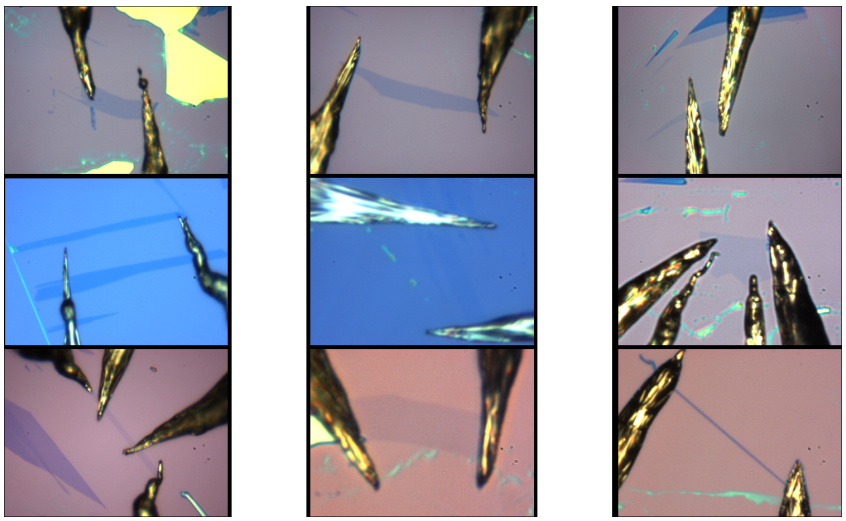

Figure 4.13: Optical images of two and four terminal microsoldered graphene and few-layer graphite devices. Sample sizes are 10 µm to 100 µm.

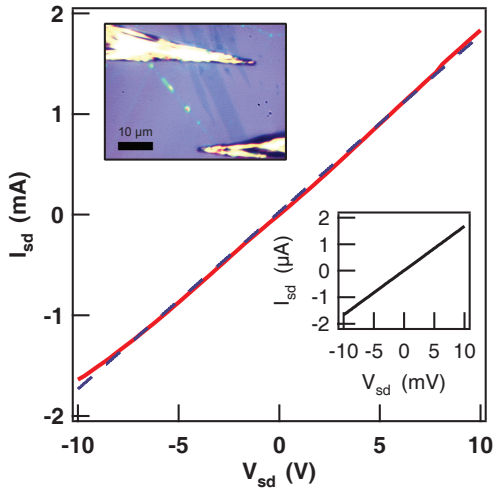

Figure 4.14: Source-drain current-voltage characteristic of microsoldered graphene device. Source-drain voltage V_{sd} is swept from $-10\,\mathrm{V}$ to $10\,\mathrm{V}$. Device is shown in inset optical image (contrast enhanced). Dashed line is linear fit to resistance of $5.7\,\mathrm{k\Omega}$. Inset plot is low-bias IV curve of same device, with a resistance of $6.0\,\mathrm{k\Omega}$. The back-gate voltage $V_{bg} = 0$ V.

taken in the range $V_{sd} = \pm 10\,\mathrm{mV}$, gives a low-bias resistance of $6.0\,\mathrm{k\Omega}$, differing by 5% despite the one-thousand times smaller range in V_{sd}. Taking the device geometry into account, a lower bound on the current carrying capacity of single layer graphene in air on a silicon oxide substrate can be placed at $390\,\mathrm{A\,m^{-1}}$ (where per meter refers to the sheet width) or $120\,\mathrm{MA/cm^2}$ bulk assuming a sheet thickness of 3.35 Å, the graphite interlayer spacing. This bulk current carrying capacity is more than one-hundred times that of a superconductor [54]. Since our value is a lower bound, it is quite probable that the actual limit is comparable to that of multi-wall carbon nanotubes [154], roughly $1 \times 10^9\,\mathrm{A/cm^2}$. In vacuum ($1 \times 10^{-5}\,\mathrm{mbar}$), current densities in graphene as high as $500\,\mathrm{A\,m^{-1}}$ have been observed without device failure. Assuming uniform power dissipation, the power density of the device in Fig. 4.14 is $16\,\mathrm{kW/cm^2}$, more than two orders of magnitude larger than present processor heat flux [47]. With such high current carrying capacities and power densities, graphene electronics as envisaged, for example by Berger et al. [13], are expected to operate reliably at far higher power levels than possible for conventional Si-based devices.

Figure 4.15(a) shows the two-terminal conductances G' of four soldered graphene devices as a function of back-gate voltage V_{bg} at room-temperature in vacuum. All graphene samples, identically prepared and solder contacted are remarkable in that their Dirac points V_D – the location of the conduction minimum – are within five volts of $V_{bg} = 0$ V without any annealing or processing. This is in contrast to the early literature of electron-beam lithographed devices [141], where V_D in the tens of volts were common. The clean, solder-contacted samples, without lithography residues to charge the sample and shift the Dirac point away

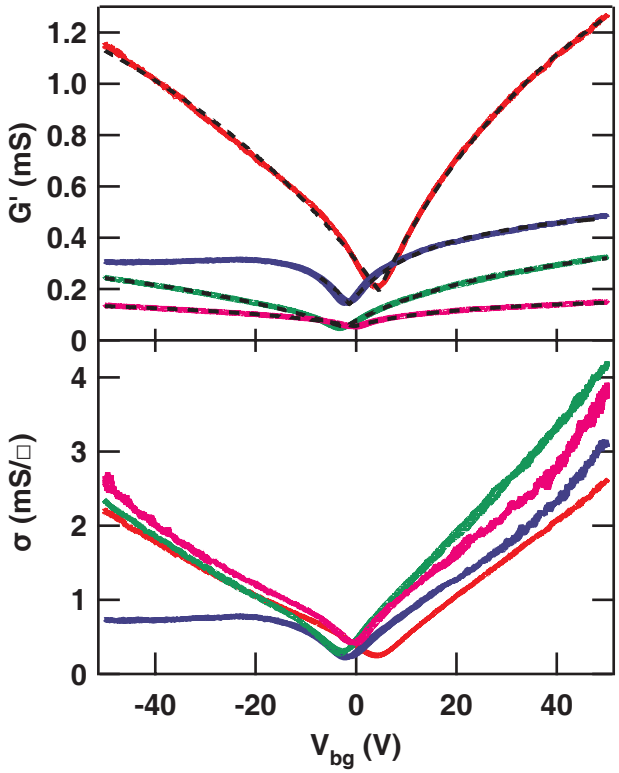

Figure 4.15: Back-gate voltage sweeps of microsoldered graphene device.
(**a**) Two-terminal conductance G' of four solder-contacted graphene devices measured as a function of back-gate voltage V_{bg}. The dashed black-lines are fits to the data with a Drude model modified to account for the electric field effect and the contact resistance. (**b**) Intrinsic sheet conductivities for the same devices obtained by subtracting the contact resistance as determined from the fits and accounting for the device aspect ratios. Gate voltage is swept both ways, showing negligible hysteresis.

from zero, are at least neutral, if not undoped. This is an important indication of how processing parameters influence device characteristics.

Although these are two terminal measurements, one can nevertheless estimate the effective, or device, mobility, the minimum conductivity, and the contact resistance with a simple model. The Drude equation for conductivity, $\sigma = en\mu$ with n the carrier density and μ the mobility is related to the conductance by $\sigma = GL/W$. The experimentally measured conductance G' includes the contact resistance R_c via $1/G' = R_c + 1/G$. For graphene in a standard transistor geometry, the carrier density depends on the back-gate voltage as $n = c'|V_{bg} - V_D|/e$, where the specific capacitance c' for a 300 nm silicon oxide gate thickness is $115\,\mathrm{aF/\mu m^2}$. Finally, a phenomenological parameter σ_D is added to account for the non-zero minimum conductance and allow differing electron and hole mobilities μ_e ($V_{bg} > V_D$) and μ_h ($V_{bg} < V_D$) to obtain

$$\frac{1}{G'} = R_c + \frac{L/W}{c'\mu_{e,h}\,|V_{bg} - V_D| + \sigma_D} \tag{4.1}$$

The aspect ratio, L/W, is determined from optical images of the devices. In general, this model will overestimate the contact resistance as any intrinsic sub-linearity in the conductance-gate voltage curves [73] will contribute to R_c. While the data can be fit to more fundamental theories [2], the simple model suffices here to characterize the graphene devices.

Figure 4.15(b) plots the intrinsic device conductivity, $\sigma = L/W(1/G' - R_c)$, as a function of applied back-gate voltage V_{bg}, where the contact resistance R_c is extracted from the fits (Fig. 4.15(a), dashed black lines). The conductivity curves are relatively linear for almost all the devices, indicating ohmic contact. Note that it is clear from the plots that the mobilities (slopes of the curves) and minimal conductivities are roughly the same for all devices. The electron mobilities range from $(4500 \text{ to } 6200)\,\mathrm{cm^2\,V^{-1}\,s^{-1}}$ and hole mobilities range from $(3000 \text{ to } 3600)\,\mathrm{cm^2\,V^{-1}\,s^{-1}}$, showing much less variation than in electron-beam lithography defined devices [141], probably due to the absence of residues. The minimal conductivities are 210 µS, 230 µS, 300 µS, and 440 µS. The contact resistance per lead, over nine devices, varied from 190 Ω to 1700 Ω, with mean 680 Ω standard deviation 450 Ω, comparable to the best electron-lithography fabricated devices [132].

The lack of adsorbates on the sample surface as a result of microsoldering is shown in Figure 4.16. The microsolder electrode is in the lower left of the image and appears white due to its large diameter (>1 µm) which dwarfs features such as the graphene on the substrate. However the graphene sample edge can be recognized in the lower right, despite "shadow" effects from the electrode. No adsorbates are found on the graphene surface and the roughness is determined to be <0.2 nm as for pristine uncontacted samples.

The solder contact method can also be used to contact nanotubes and nanowires. SEM can be used to locate multi-wall carbon nanotubes relative to predefined optically visible markers. The soldering technique, as described above, can then be used by positioning the leads relative to the markers. However a better method would be to use a piezo micromanipulator inside the SEM itself, along with a heated sample stage, and solder the contacts in

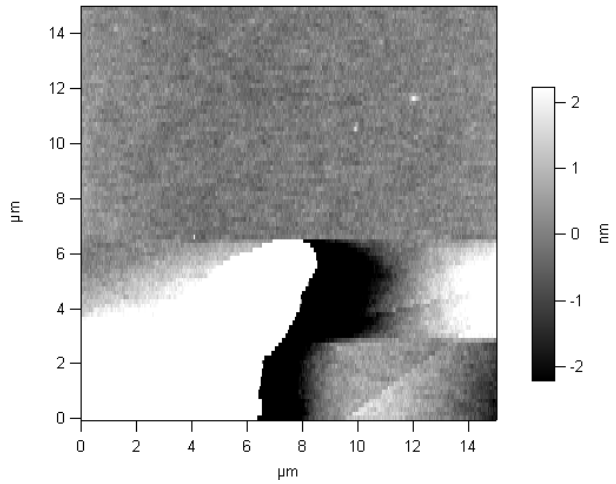

Figure 4.16: AFM topography of microsoldered graphene sample. Electrode white area at bottom left. Graphene roughness is 0.2 nm RMS.

situ. Other applications of the solder technique are wirebonding and stencil mask alignment. To wirebond devices which already have leads, fine wire is placed near the leads and then a solder spike is deposited, with the sample stage hot, over both lead and wire. When the heater is turned off, the solidified spike fixes the wire to the substrate and provides electrical contact to the lead. The wirebonding and sample soldering can also be performed in a single step, with the solder spike both contacting the sample and fixing the wire. To align stencil masks, a similar process is used. The mask is placed on top of the substrate, over the sample, and soldered at the corners. The micromanipulator is then used to push the mask into alignment, and the heater turned off to fix the mask.

Microsolder contacts are a simple, efficient means of producing functional nanostructure devices based on graphene, nanotubes, or other materials. Not only are the contacts ohmic, but the resultant devices are clean and the device characteristics consistent. The contacts, capable of sustaining large currents without failure, allow investigation of high-bias electronic transport properties.

4.3 Etching

In order to shape graphene into point contacts, narrow ribbons, hall bars, or other device geometries it needs to be etched. Conventionally, etching is performed post-patterning with a plasma etcher (reactive ion etching, RIE) or liquid solvent. A resist or sacrificial layer serves as a stop mask, and prevents those areas from reacting with the etchant. The selectivity of the process is defined as the rate at which the target material is etched over the etch rate of the stop mask. Because of the atomic thickness of graphene, selectivity is somewhat irrelevant. Graphene can be readily etched with a short oxygen plasma. Liquid phase etching

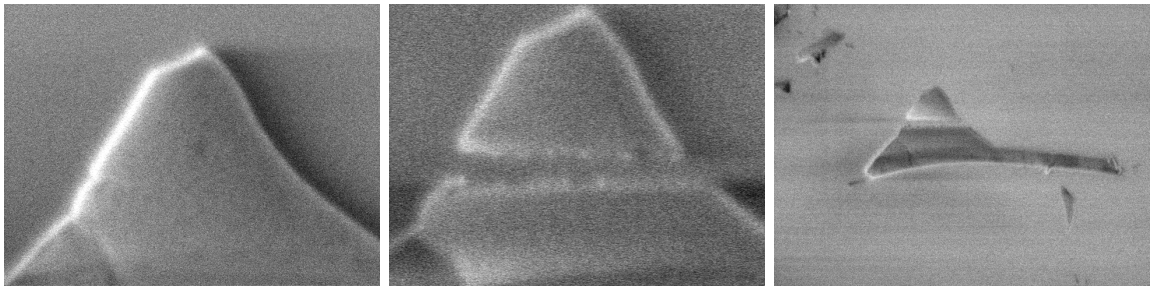

Figure 4.17: Cutting few-layer graphite with an electron beam in the SEM.

is more complicated as graphene is more resistant to organic solvents than polymer mask materials such as PMMA. A good reference on different conventional etch processes is "Etch rates for micromachining processing" [158].

These techniques have the same contamination problem for graphene as any process that requires putting a mask such as PMMA in close contact with it. Alternatives which can avoid contamination while maintaining fine patterning resolution are desirable. One such technique is focused ion-beam (FIB) milling, in which gallium ions are accelerated and focused onto a surface, "milling" it away. Although some gallium contamination occurs near the milled areas, resolution can be very good (7 nm). FIB systems are often incorporated in SEMs as a means of simultaneously or sequentially (without breaking vacuum) observing the sample and milling it. FIB was successfully used to pattern and etch graphene in collaboration with Andrew Minor at the National Center for Electron Microscopy (on the FEI Strata 235 Dual Beam FIB). It was not pursued further as a means to make clean graphene point contacts. A reference on FIB milling of graphite is Dujardin et al [43].

4.3.1 Electron-Beam Cutting

Cutting of multi-wall nanotubes by electrons in a scanning electron microscope was demonstrated by Yuzvinsky et al [161]. Despite the potential to contaminate graphene by hydrocarbon adsorption as a result of imaging in the SEM (Section 3.2.3), cutting graphene with an electron beam has the potential to make extremely fine features (<10 nm). Cutting occurs selectively at graphene exposed to intense low-energy electrons (0.5 keV to 5 keV) as a result of chemical reactions with residual oxygen and water gas in the chamber. In a likely scenario the low energy electrons ionize the residual gas and/or graphene which allows an oxidation reaction to take place, removing carbon atoms. It is necessary to allow pure water into the SEM chamber with a leak valve (MDC Vacuum) in order for the cutting to occur. Figure 4.17 shows SEM micrographs of a few-layer graphite sample on SiO_2 cut with this technique.

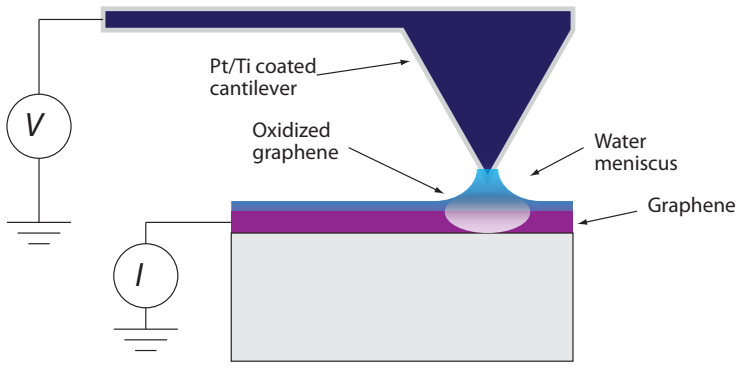

Figure 4.18: Schematic of local anodic oxidation (LAO) to define insulating regions in graphene.

4.3.2 Local Anodic Oxidation

Local anodic oxidation (LAO) is a technique to locally oxidize a conducting material. It is similar to the anodization process used commercially to coat metals with thick protective oxide layers. The material to be anodized serves as the anode of an electrochemical cell and an applied negative bias induces oxidation. For the most common process, anodization of aluminum, the total reaction is [4]

$$2\,\mathrm{Al} + 3\,\mathrm{H_2O} \longrightarrow \mathrm{Al_2O_3} + 3\,\mathrm{H_2}. \tag{4.2}$$

A similar reaction can occur with carbon, whose electrochemistry is described in detail in the book by Kinoshita [89].

$$\mathrm{C_2^+CO_3^{2-}} \longrightarrow 3\,\mathrm{CO_2} + 4\,\mathrm{e^-} \qquad \text{Anode} \tag{4.3}$$

$$\mathrm{O_2} + 2\,\mathrm{CO_2} + 4\,\mathrm{e^-} \longrightarrow 2\,\mathrm{CO_3^{2-}} \qquad \text{Cathode} \tag{4.4}$$

$$\mathrm{C} + \mathrm{O_2} \longrightarrow \mathrm{CO_2} \qquad \text{Solution} \tag{4.5}$$

The conventional product is carbon dioxide (CO_2). Partial oxidation or other processes may also occur in the case of graphene, and this product is called GO (graphene oxide). It was synthesized long before the extraction of graphene and has been reviewed in detail by Ruoff et al [39] and recently imaged with high-resolution aberration-corrected transmission electron microscopy (Section 3.4) [62] .

In the case of local anodic oxidation with an atomic force microscope, the electrochemical cell is formed by the tip of the cantilever (cathode), the thin water layer that coats all surfaces in ambient conditions and forms a meniscus between the sample and tip, and the sample itself (anode). A schematic is shown in Figure 4.18. When a negative bias is applied to the cantilever tip ($V \lesssim -3\,\mathrm{V}$) in contact with the grounded graphene sample, oxidation commences. The drain current I can be monitored with a current amplifier to indicate the onset of oxidation (Fig. 4.19(b)). LAO has been used to pattern many metals (Ti, Al, Nb),

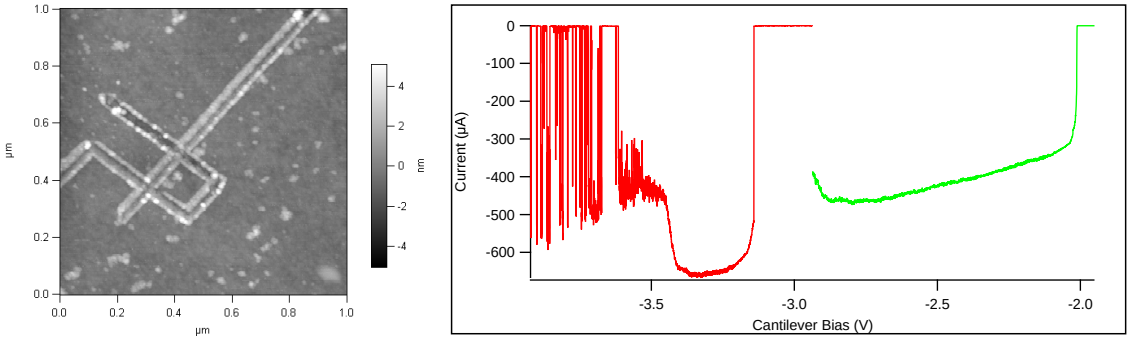

(a) LAO graphene cutting

(b) LAO graphene IV

Figure 4.19: (a) AFM topography of LAO patterned graphene sample (42 nm line width). (b) Current voltage characteristic for local anodic oxidation at two different points on graphene sample.

conventional semiconductors (GaAs, Si), graphite [81], and graphene [155, 104, 59]. A review of the technique, its dependence on experimental parameters, and its use for patterning different materials is Held et al [70].

LAO is usually performed in contact mode, although tapping mode operation has been demonstrated [76]. The contact-mode cantilever should have a strong, chemically inert conductive coating such as platinum (MikroMasch Ti-Pt coating). Another more expensive option is conducting diamond coated cantilevers such as Nanosensors NDT-CONTR. These are much more resistant to damage during oxidation but have larger tip radii, 100 nm compared to 40 nm for the Pt/Ti ones. Tip radius of curvature is not the only parameter determining resolution. The oxidation linewidth is also a function of humidity, bias, tip-sample distance, and scan speed [70].

Figure 4.19(a) shows a graphene sample patterned into a line and sickle shape by LAO. The graphene sample to be oxidized is first imaged in contact mode with the same cantilever to be used for lithography. Then using a lithography panel built-in to the AFM control software (Asylum Research MFP3D) the desired shape is drawn and overlaid on the image. The tip bias, deflection setpoint (related to tip-sample distance), and scan speed are entered and lithography initiated. Typical values for the tip bias are $-3\,\mathrm{V}$ to $-7\,\mathrm{V}$; for the deflection setpoint one to two times that used for imaging; and for the scan speed between $10\,\mathrm{nm\,s^{-1}}$ to $1000\,\mathrm{nm\,s^{-1}}$. In Fig. 4.19(b), the IV characteristic for two different point-oxidations (green and red curves) is shown. As the negative bias is increased (right to left), after the onset of conduction the IV is relatively linear, with a tip-sample resistance of $5.1\,\mathrm{k\Omega}$ (green) and $8.3\,\mathrm{k\Omega}$ (red). Once oxidation begins, the current rapidly goes down to zero. Afterwards it may fluctuate rapidly ($V \lesssim -3.5$ V) which may be due to intermittent conduction before the region under the tip is oxidized. After the threshold oxidation voltage is determined, the bias for subsequent patterning can be set a volt or so more negative. Then there should be no current measured without sensitive electronics as the Faradaic current

during oxidation is small (picoamperes) and brief (milliseconds) [94].

The appearance of the patterned region post-oxidation depends both on the AFM imaging mode and the lithography parameters. Scanning the sample in contact mode directly after oxidation results in images such as Fig. 4.19(a), where in addition to the patterned shape there appears to be "dirt" on the surface. This dirt is the oxidized graphene that has been pushed to the sides by the cantilever during scanning. When GO clumps dragged by the cantilever stick strongly enough to the surface to overcome the lateral force, the cantilever passes over the clump and there appear white blobs of diameter 1 nm to 10 nm. If scanning is continued the GO will be pushed completely out of the scan region (Fig. 4.20(a)) and the graphene surface cleaned. If the cantilever deflection setpoint is decreased to increase the downward force, cleaning will occur faster but care must be taken not to rip the graphene sheet. Once the GO is gone, the patterned areas will appear as cuts in the graphene (Fig. 4.20(b)) and be at lower elevation, that of the substrate. If the deflection setpoint is kept small, the GO can be imaged without pushing it away but it is difficult to keep it unperturbed. To do so, after patterning in contact mode the cantilever should be exchanged for a non-contact one and imaging switched to AC mode. Then the GO will remain in the patterned area and appear as bloated graphene, Figs. 4.1 and 4.21, with a height of several nanometers.

Of the many parameters in LAO that can be varied to change pattern resolution, one of the easiest to control is cantilever bias. Larger negative biases will result in wider linewidths. The cut in Fig. 4.19(a) is 42 nm wide. In comparison, the two cuts in Figure 4.20(b) performed at larger biases are wider at 101 nm and 170 nm. The scan speed also influences linewidths, with faster patterning resulting in finer lines up to a point where oxidation becomes discontinuous and alignment of the pattern unreliable due to piezo jerk.

An important factor determining linewidths is one that is not commonly controlled unless the AFM is housed in a cleanroom: humidity. The size of the water meniscus (Fig. 4.18) depends on the relative humidity as well as the cantilever tip radius. If the AFM is housed in a chamber that can be closed, wider lines can be obtained simply by putting a beaker of hot water inside and finer lines by putting in fresh desiccant. The relative humidity can be monitored with a hand-held, battery-operated psychrometer (McMaster-Carr part no. 3823K31).

Figure 4.20 shows the use of LAO to pattern graphene devices to make insulating regions. In Fig. 4.20(a), the graphene surrounding an electrode (white) is in the process of being decoupled electrically from the rest of the sheet by oxidizing the perimeter of a rectangle centered at the electrode. The GO has been pushed away by contact mode imaging and is not visible. The patterned lines appear as cuts in the graphene. A 500 nm × 500 nm scan where two cuts meet is shown in Fig. 4.20(a). A pristine graphene nanobridge of width 46 nm separates the two cuts. Clean point contacts and nanoribbons such as this cannot be fabricated by lithography and this is the appeal of LAO for graphene device fabrication (Section 6.2). In Fig. 4.20(c), which is taken in AC mode, two cuts across a graphene sample isolate contacts above and below the sample (not shown). The upper image is the topography whereas the lower one is phase. Although the cuts are identifiable in the topography image,

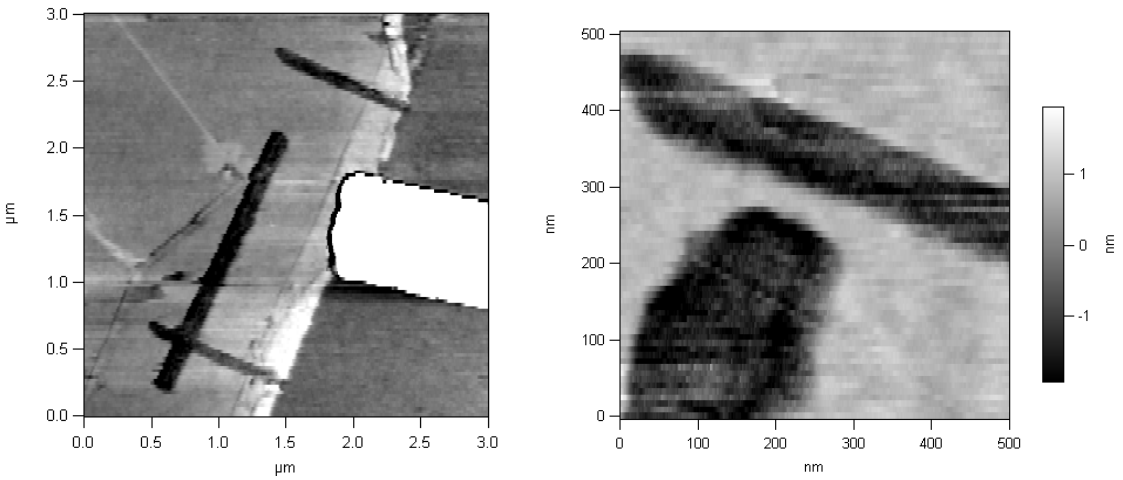

(a) Isolating electrode

(b) Isolating electrode, zoom in

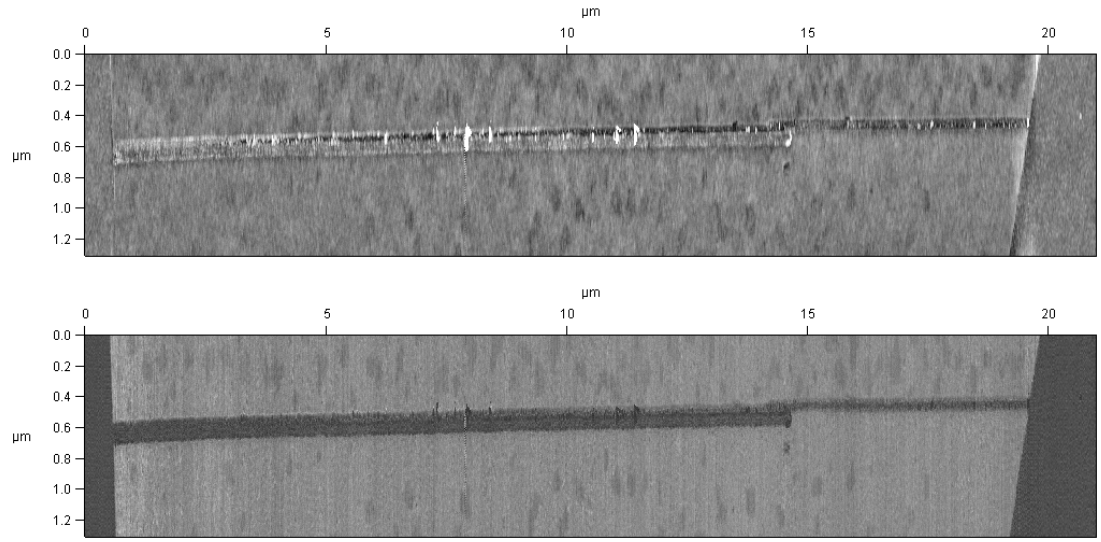

(c) Cut in graphene, topography (upper) and phase (lower)

Figure 4.20: AFM images of graphene devices after patterning with local anodic oxidation. Isolating graphene from an electrode (a,b, contact mode AFM) and cutting a graphene device across a line (c, AC mode AFM).

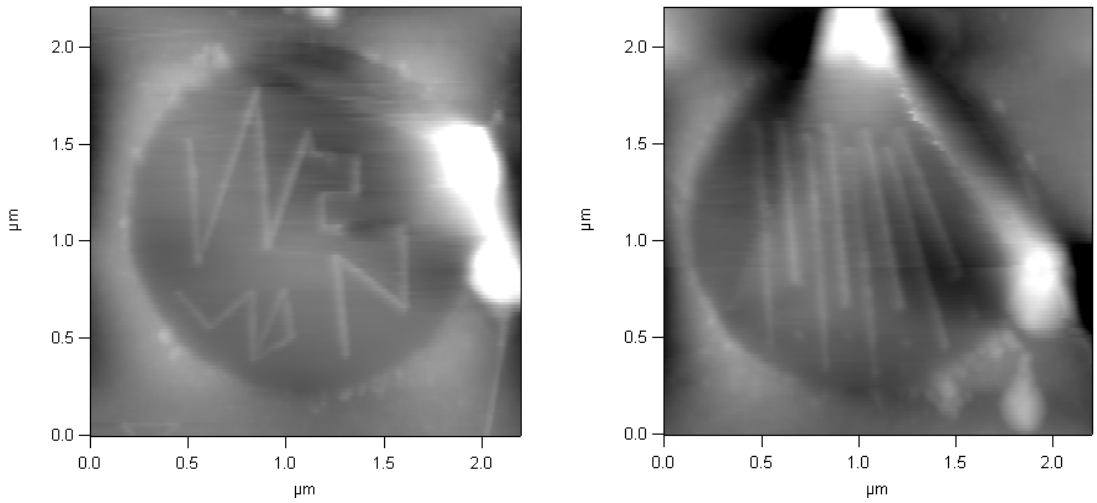

Figure 4.21: AC mode AFM images of suspended few-layer graphite patterned by local anodic oxidation. See also Fig. 4.1.

it is much more clear in the phase image. In AC mode, the phase gives information about the tip-sample interaction. It is clear that the tip-sample interaction in the cut (phase 48°) is similar to that on the SiO_2 substrate, whereas the oscillation damping over graphene is different (phase 62°) likely because it is more inert than the oxide.

Local anodic oxidation can also be performed on suspended samples, including both few-layer graphite (Fig. 4.21 and graphene (not shown). On suspended few-layer graphite the procedure is not different from unsuspended samples except that if the oxidation depth reaches the bottom-most layer, structural integrity can be compromised. Depending on the sample thickness, this can be a concern or not. On suspended graphene samples, oxidation will readily result in breaking, especially if there is tension.

Part II

Conduction Quantization in Graphene

Chapter 5

Ballistic Transport Theory

The aim of this chapter is to lay the theoretical foundation to describe conductance quantization in general and then apply it to calculate the ballistic transport properties of massless Dirac fermions. First the quantization of the conductance of a perfect ballistic wire connected to two charge reservoirs is derived. The transmission of an imperfect conducting channel is presented and related to the conductivity of a disordered one-dimensional wire as described by the Drude model. The multi-channel Landauer-Büttiker formalism is introduced which describes wide conductors and can be applied to unpatterned ballistic graphene devices. The transmission coefficients for massless Dirac fermions in a simple geometry and potential are calculated. From these transmission coefficients, important transport parameters including the conductance, Fano factor, and current-phase relation are determined. Finally, modifications to the calculations for real graphene devices are considered.

5.1 Conductance Quantization

Following Imry [75], we can derive the conductance of an ideal one dimensional conductor, Figure 5.1(a). The channel is tied to two large electron reservoirs on the right and left and

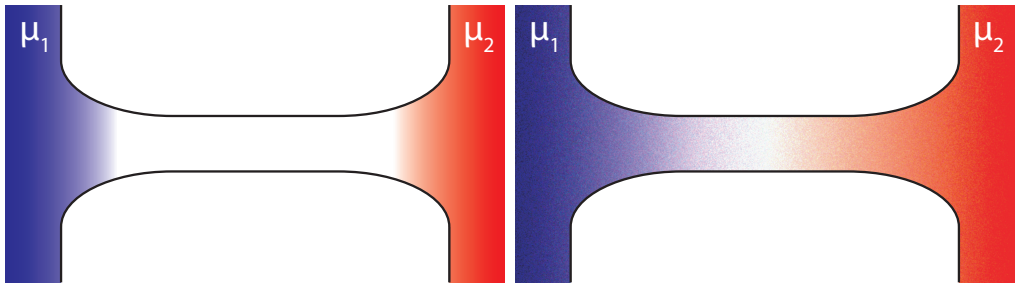

(a) Ballistic (b) Disordered

Figure 5.1: Potential drop across ballistic and disordered one-dimensional conductor.

has no scatterers contained within it or at the ends. The electron distributions deep inside the reservoirs are described by the Fermi function with chemical potential μ_1 on the left and $\mu_2 < mu_1$ on the right. The modes in the channel are indexed by a transverse wavevector and the condition that only the energy of the lowest mode lies below the Fermi level of the contacts ensures that the channel is effectively one-dimensional. In one-dimension, the density of states for a single polarization is calculated as

$$M = \frac{L}{2\pi}k_F, \qquad \frac{dn}{d\mu} = \frac{d}{d\mu}\left(\frac{M}{L}\right) = \frac{dk}{d\mu}\frac{d}{dk}\left(\frac{k}{2\pi}\right) = \frac{1}{\hbar}\left(\frac{d\omega}{dk}\right)^{-1}\frac{1}{2\pi} = \frac{1}{hv}, \tag{5.1}$$

where M is the total number of states, k_F is the Fermi wavevector, and $v = v_F$ is the velocity in the direction of the channel at the Fermi surface. The current can then be calculated as

$$I = ev\Delta\mu\frac{dn}{d\mu} = ev(\mu_1 - \mu_2)\frac{2}{hv} = \frac{1}{h}e(\mu_1 - \mu_2) \tag{5.2}$$

The electrochemical potential difference in terms of voltages V_1 and V_2 applied to the left and right reservoirs respectively is just $\Delta\mu = \mu_1 - \mu_2 = e(V_1 - V_2)$. This gives the conductance $G = I/V$ as

$$G = \frac{e^2}{h}, \tag{5.3}$$

the conductance quantum for a single nondegenerate channel. This universal value is a result of the cancellation of the group velocity v in the product of the 1D density of states cancels that in the current.

In the case of spin degeneracy, we have $G_0 = 2e^2/h$, which is what has been measured in quantum point contacts in clean GaAs 2DEGs [150]. This is equivalent to 77.48 µS or a resistance of 12 907 Ω. In the following discussion, we will always assume spin degeneracy and include the factor of two in G_0.

All of the voltage drop occurs at the ends of the wire, and the electrochemical potential inside the wire is constant. This is depicted in Fig. 5.1(a), where the potential drop is color coded. Despite the absence of scatterers in the channel, the two-terminal resistance measured at the large reservoirs gives a finite conductance because of the finite density of states of the one-dimensional wire. Inside the channel there are only right-moving electronic states, giving a reduced density of electrons and an effective electrochemical potential reduced relative to μ_1, the potential measured deep in the left reservoir. The in-channel potential is influenced equally by the left and right reservoirs and is equal to $\frac{1}{2}(\mu_1 + mu_2)$.

The derivation presented here makes strong requirements on having ideal reservoirs and smooth contacts connecting them to the narrow channel, but the conductance quantization can be calculated similarly without these restrictions and for other situations as well [52].

5.1.1 Scattering

The conductance formula $G_0 = 2e^2/h$ can be modified to account for scatterers inside the channel by introducing a transmission probability T. This is the probability that an

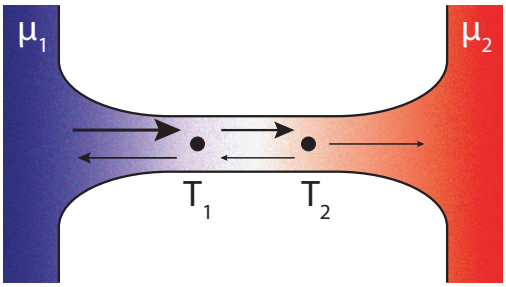

Figure 5.2: Calculating the total transmission for two scatterers with individual transmissions T_1 and T_2.

electron will enter from the left and exit at the right. The transmission T reduces the details of the scatterer, such as the exact form and shape of the potential profile, to a single number between zero and one sufficient to calculate the conductance. This two-terminal conductance measured between the two reservoirs in the presence of scattering in the channel is

$$G = G_0 T = \frac{2e^2}{h} T. \tag{5.4}$$

A ballistic channel has perfect transmission, $T = 1$. Landauer, who originally developed the notion of conductance as transmission, calculated the conductance for the case of noninvasive probes measuring the voltage drop inside the channel, and not at the reservoirs. Then one obtains [95]

$$G' = G_0 \frac{T}{1-T} = \frac{2e^2}{h} \frac{T}{1-T}. \tag{5.5}$$

As expected this gives infinite conductivity for perfect, ballistic transmission as the voltage drop inside the channel is zero. As soon as there is scattering however the conductance is finite and there will be a potential drop inside the channel. The resistance of the perfect channel occurs only at the contacts; it is equal to $R_c = R_0 = 1/G_0 = h/2e^2$ and is in series with the in-channel resistance $1/G' = R_c(1-T)/T$. Thus the total resistance including the contacts and the channel in which there is scattering is $R_c + 1/G'$ which is just equal to G (Eq. 5.4). As soon as scattering is significant, $T \ll 1$, the in-channel resistance and the resistance measured at the reservoirs will be equal ($R_c \ll 1/G' \approx 1/G$).

5.1.2 Relation to Drude Model

We can treat the case of a long one-dimensional wire in which there are many scatterers. One expects for such a disordered conductor that the potential profile looks like Fig. 5.1(b). First assume there are two scatterers in series in the channel with transmissions T_1 and T_2, as in Fig. 5.2. What is the total transmission T_{12}? Due to the multiple scattering between the two sites it is not simply $T_1 T_2$. We can calculate this from the resistance, which adds

in series, and is equal to $R_i = 1/G_i' = R_0(1-T_i)/T_i$ for each scatterer (Eq. 5.5). The total two-terminal resistance as measured by voltage probes deep in the reservoirs, R_{12} is just

$$R_{12} = R_c + R_1 + R_2 = R_0\left(1 + \frac{1-T_1}{T_1} + \frac{1-T_2}{T_2}\right). \tag{5.6}$$

This resistance can also be written as the sum of the contact resistance R_c plus the resistance, $R_{12}' = R_0(1-T_{12})/T_{12}$ as measured by voltage probes inside the channel and surrounding the two scatterers:

$$R_{12} = R_c + R_{12}' = R_0\left(1 + \frac{1-T_{12}}{T_{12}}\right). \tag{5.7}$$

From these two equations we can determine T_{12} as a function of T_1 and T_2,

$$\frac{1-T_{12}}{T_{12}} = \left(\frac{1-T_1}{T_1} + \frac{1-T_2}{T_2}\right) \tag{5.8}$$

$$T_{12} = \frac{T_1 T_2}{T_1 + T_2 - T_1 T_2} \tag{5.9}$$

From these last equations it is seen that when a scatterer with transmission T_i is added to a series of scatterers with total transmission T, the transmission is modified as $(1-T)/T \to (1-T)/T + (1-T_i)/T_i$. If each scatterer is identical, $T_i = T$, and there are N of them, then the total transmission is just $N(1-T)/T$. If there are roughly ℓ'/L scatterers per unit length, then we have for the total resistance of the channel

$$R = R_c + R_0 N\frac{1-T}{T} = R_0\left(1 + \frac{L}{\ell'}\frac{1-T}{T}\right). \tag{5.10}$$

We can now relate this equation derived for a one-dimensional channel with many scatterers in the transmission formalism to the 1D Drude expression for the conductivity. The Drude conductivity is $\sigma = en\mu$, where n is the carrier density and μ the mobility. We can express the carrier density in 1D simply as $n = 2 \cdot 2\pi k_F$, where k_F is the Fermi wavevector and there is a factor of two for spin degeneracy. The mobility can be written $\mu = e\tau/m^*$ with τ the scattering time. The effective mass can be calculated from the band dispersion as $m^* = \hbar k_F/v_F$. Combining these relations and using the fact that $G = \sigma/L$ in one dimension, we have for the Drude conductance

$$G_{\mathrm{D}} = G_0\frac{\ell}{L} \tag{5.11}$$

where the mean free path $\ell = v_F\tau$. This means the total "transmission" of the channel in the Drude model is $T_{\mathrm{D}} = \ell/L$. Does the resistance $R_{\mathrm{D}} = 1/G_{\mathrm{D}}$ include the contact resistance R_c? In the limit of validity of the Drude model, $\ell \ll L$, the resistance R_{D} is so much larger

than R_c that it does not matter. We can determine the transmission per scatterer T by setting R_D equal to the resistance determined in Eq. 5.10 and ignoring contact resistance,

$$R_\mathrm{D} = R_0 \frac{L}{\ell} = R_0 \frac{L}{\ell'} \frac{1-T}{T} \rightarrow T = \frac{\ell}{\ell + \ell'}. \tag{5.12}$$

We see that if the mean free path is much larger than the separation between scatterers ℓ' then the transmission T must be close to perfect. We can also determine what the transmission would have to be if the scatterer separation and mean free paths were approximately equal, $\ell \approx \ell'$. In this case $T \approx 1/2$, which means that at each scatterer the incident particle has an equal chance of being reflected or transmitted.

5.1.3 Dirac Channel

The derivation of the conductance quantization formula, Eq. 5.3, nowhere incorporates the nature of the quasiparticles involved in transport. This is because the group velocity $\frac{1}{\hbar} dE/dk$ falls out of the calculation and thus the quasiparticle energy dispersion is irrelevant. However, the state degeneracy of the quasiparticles *does* appear in the prefactor and in the case of graphene, due to sublattice or "pseudospin" degeneracy, there is an additional factor of 2:

$$G_\mathrm{Dirac} = 4e^2/h. \tag{5.13}$$

Thus in a ballistic graphene quantum point contact, one would expect to see quantization steps (next Section 5.1.4) that are twice the height one would observe for a conventional 2DEG [150].

The condition that the channel be one-dimensional also includes implicitly the quasiparticle energy dispersion. For the fundamental transverse mode described by a wavevector $k_0 = \pi/W$, the energy E_0 for a Schrödinger channel (parabolic energy dispersion) is different from that of the Dirac channel:

$$\text{Schrödinger: } E_0 = \frac{\hbar^2 k_0^2}{2m^*} \tag{5.14}$$

$$\text{Dirac: } E_0 = \hbar k_0 c^*, \tag{5.15}$$

where W is the width of the channel, m^* the effective mass of a Schrödinger quasiparticle, and c^* the effective speed of light for a massless Dirac quasiparticle. Putting in values for GaAs ($m^* = 0.067 m_e$) and graphene ($c^* \approx c/300$) we obtain a critical channel width at which the energies E_0 are equal, $W_\mathrm{crit} \approx 3\,\mathrm{nm}$, corresponding to an energy of 380 meV. For wider channels, the lowest transverse mode energy will be larger for a graphene channel than for a GaAs channel. This means that for all channel widths that can be realistically fabricated with current technology, the energy scaling favors graphene. For example for $E_0 = 100\,\mathrm{meV}$ which significantly exceeds room temperature $kT_\mathrm{RT} \approx 25\,\mathrm{meV}$, the graphene channel width would be 21 nm. This could potentially be fabricated with ultra high-resolution electron-beam

lithography (Sec. 4.1) or local anodic oxidation (Sec. 4.3.2). However for a GaAs channel of equivalent lowest subband energy, the width would need to be 7 nm, which cannot be reasonably fabricated by these technique. Since kT should be much lower than E_0 to obtain a one-dimensional conductor, given equivalent mean free paths and channel geometry, one expects a graphene device to demonstrate better single-mode quantization than a GaAs device.

5.1.4 Landauer-Büttiker Formalism

The previous results can be generalized to multiple conduction channels as well as to more than two probes or sources at the device. This is known as the Landauer-Büttiker formalism and has been used to explain electronic transport measurements in a variety of systems, including multi-terminal ballistic GaAs 2DEG devices. This formalism is described in detail in the books by Ferry [52] and Datta [34].

For the two-terminal case in which there is more than one transverse mode below the Fermi level of the contacts, instead of having a single number T specifying the transmission, one has a probability amplitude matrix t. The basis for this matrix is the transverse eigenmodes of the channel, with the size of the matrix $M \times M$ if there are M states below the Fermi level. The entries of t correspond to the probability amplitudes for transmission of the incident wave functions into the outgoing wave functions. The transmission probabilities for scattering are then given by $\mathrm{T} = tt^\dagger$ now a matrix. The conductance can then be written as

$$G = G_0 \,\mathrm{Tr}(tt^\dagger) = \frac{2e^2}{h}\,\mathrm{Tr}(\mathrm{T}). \tag{5.16}$$

If one can diagonalize the matrix T into its eigenvalues T_i, the conductance is simply

$$G = \frac{2e^2}{h}\sum_{i=0}^{M} T_i, \tag{5.17}$$

where the number of channels M is given by

$$M = \left\lfloor \frac{k_F W}{\pi} \right\rfloor = \left\lfloor \frac{W}{\lambda_F/2} \right\rfloor. \tag{5.18}$$

In the case where all channels have perfect transmission $T_i = 1$, this becomes $G = MG_0$.

The seminal experiments on quantum point contacts by van Wees [150] and Wharam [156] directly showed the conductance quantization of multiple ballistic channels. By tuning an electrostatic split-gate to deplete the carriers under it, a conduction geometry similar to Fig. 5.1 was created in a GaAs 2DEG. The mean free path greatly exceeded the junction length and so transport was ballistic. By tuning the carrier density in the reservoirs they could control the number of occupied transverse modes in the narrow channel. They saw that each time a new subband was occupied, the conductance increased by G_0, producing

a staircase in a plot of conductance versus carrier density. The experiment and results are reviewed by van Houten in *Physics Today* [149].

Equation 5.16 can be used to calculate the conductance of channels containing many subbands $M \gg 1$, thus allowing transport parameters of two-dimensional sheets such as graphene to be determined as well.

5.2 Dirac Transmission Coefficients

For a one-dimensional channel, if the scattering potential and boundary conditions are known, one first calculates the eigenmodes of the channel and then "stitches" the wavefunction together at the boundaries with the wavefunctions at both leads. Continuity of the wavefunction and its first derivative must be satisfied at the interfaces between regions for the Schrödinger equation. However massless Dirac fermions are *not* described by the Schrödinger equation and the boundary conditions and matching conditions are different. In general the eigenmodes will also be different but in some cases, such as for the plane wave, the form (k-dependence) is identical but there is a spinor multiplication factor.

The transmission coefficients were calculated analytically by Tworzydło et al [147] for the case of the graphene device geometry of Figure 5.3(a) by making several simplifying assumptions. The first is that the electrodes plus underlying graphene are replaced by a graphene sheet with the same width but a much larger potential than the graphene in the "active" area. Since the width is constant the transverse modes are identical in both the leads and the electrodes. This prevents mixing of modes at the sample/electrode interface and the transmission matrix T is already diagonalized.

The assumption that the graphene-electrode potential is $V_\infty \gg V_g$ makes the analytical calculation possible but in a subtle way. The potential in the active area is controlled by the gate voltage V_g and this determines the magnitude of the Fermi wavevector there by $k_F(V_g) = \sqrt{\pi n(V_g)}$, where we assume the Dirac point is at 0 V (electric field effect). The number of transverse modes M in the active area is roughly $k_F(V_g)W/\pi$ and the transverse wavevectors q_m are related to the Fermi wavevector by $k_F^2 = q_m^2 + k_x^2$, where k_x is the longitudinal wavevector in the direction pointing between the electrodes. There will also be evanescent modes in the active area for $m > M$ or equivalently $q_m > k_F(V_g)$ such that k_x is imaginary. These modes will have exponentially decaying wavefunctions along the direction of the current. For a given propagating or non-evanescent mode $q_{m'}$ in the active area, by the assumption that the graphene-electrode potential is $V_\infty \gg V_g$, the corresponding Fermi wavevector in the graphene-electrode will have a much larger longitudinal component $\sqrt{k_F^2(V_\infty) - q_{m'}^2} \sim k_F(V_\infty)$ compared to the transverse component. In addition short transverse wavelength modes at the graphene-electrode such that $k_F(V_g) < q < k_F(V_\infty)$ will only couple to evanescent modes in the active area and will contribute very little to the transmission. This allows us to ignore the contribution to the wavefunction in the graphene-electrodes from terms in the Dirac equation with σ_y, the transverse direction, and ultimately allow an analytic calculation as well as removing V_∞ from the final expression for the transmission

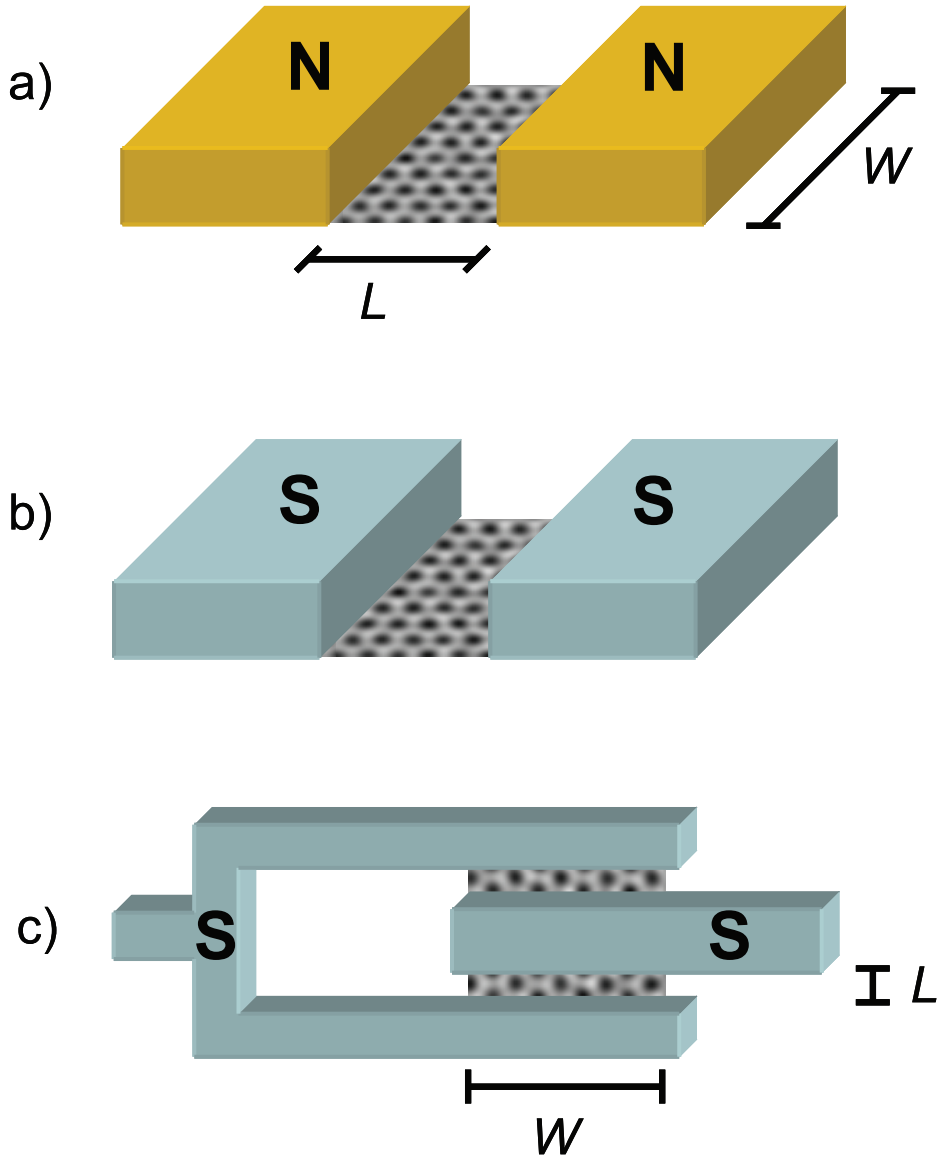

Figure 5.3: Schematic of two-terminal graphene device geometries for measurement of conductance, Fano factor, critical current, and current-phase relation (back-gate electrode not shown).
(a) normal electrodes, for measurements of conductance and Fano factor, **(b)** superconducting electrodes with a single junction for measuring critical current, **(c)** superconducting electrodes with two junctions and loop (superconducting quantum interference device), for measuring critical current-phase relation.

coefficients.

The exact number of transverse modes that correspond to non-evanescent wavefunctions in the active area is given by $M = \lfloor k_F(V_g)W/2 - 1/2 \rfloor$. Note that there is an extra one-half in this equation compared to the conventional expression for the number of modes, Eq. 5.18. This is a characteristic of Dirac fermions and is a result of the different boundary conditions imposed on those particles. Consider the boundary conditions for confinement of a particle in a box with walls at infinite potential. It is well know that for a Schrödinger particle the wavefunction is zero at the walls but this is not true for a Dirac fermion, where it is is *finite* [3]. As the Dirac equation is first order, the discontinuity in the potential is converted to a discontinuity in the wavefunction which is zero outside but finite at the edge. For the second-order Schrödinger equation, one only has a discontinuity in the first derivative. The discontinuity in the wavefunction is satisfied by a phase shift in the eigenstates. For the massless Dirac fermion in a box [3], instead of eigenstates of the form $\sin(q_m y)$ one has eigenstates of the form $\sin(q_m y - \pi/4)$. The boundary condition for q_m is modified from $q_m W = \pi m$ to $q_m W = \pi/2 + \pi m$. Thus at the box edges the wavefunction $\sin(q_m W - \pi/4) = \pm 1/\sqrt{2}$ is not zero.

The boundary condition for matching wavefunctions at the interfaces between two regions is also different for Dirac fermions. Instead of matching continuity of the wavefunction and its derivative as for the Schrödinger case one only needs to match continuity of both components of the Dirac wavefunction. In this way the probability flux is preserved at the interface. By virtue of the fact the Dirac equation is first order, the expression for the probability flux does not involve derivatives of ψ (Sec. A.2) and only wavefunction continuity is required.

Once these boundary conditions are specified and the simplifying assumptions made, one can solve the Dirac equation for the transmission coefficients. The derivation is shown in detail in the appendix to Tworzydło's `arXiv.org` version arXiv:cond-mat/0603315v3 of their published paper [147]. Making the following definitions,

$$\theta_F \equiv k_F(V_g)L \tag{5.19}$$

$$\theta_m \equiv q_m L = (m + 1/2)\pi L/W, \tag{5.20}$$

the simplified form of the transmission coefficients in dimensionless form is:

$$T_m = \left(1 + \frac{\sin^2\left(\sqrt{\theta_F^2 - \theta_m^2}\right)}{(\theta_F/\theta_m)^2 - 1} \right)^{-1} . \tag{5.21}$$

Figure 5.4 shows a plot of the transmission coefficients. It is assumed that $W \gg L$, making $\theta_m \propto L/W$ essentially a continuous variable. Below the line $\theta_F = \theta_m$, which corresponds to evanescent modes $q_m < k_F$, the transmission is zero (black), except near the origin where the Fermi level is approximately zero corresponding to the Dirac point. Here the transmission can be almost unity for the modes with long transverse wavelengths even though the wavefunction decays longitudinally. This can be shown by taking $\theta_F \to 0$ which gives a transmission $T_m(\theta_F = 0) = \mathrm{sech}^2(\theta_m)$, plotted in Fig. 5.5(a).

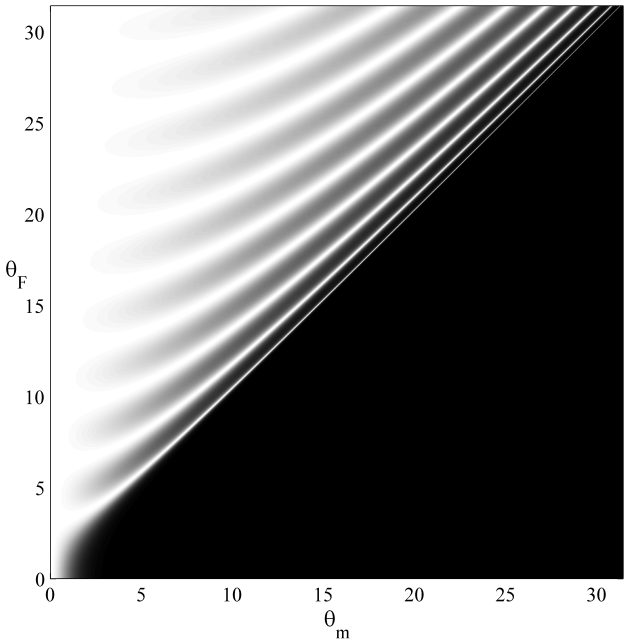

Figure 5.4: Transmission coefficients T_m for wide and short ballistic graphene device. Plotted as a function of Fermi angle related to the gate voltage by $\theta_F = k_F(V_g)L$ and transverse mode angle $\theta_m = q_m L$. Black corresponds to zero transmission and white to unity transmission.

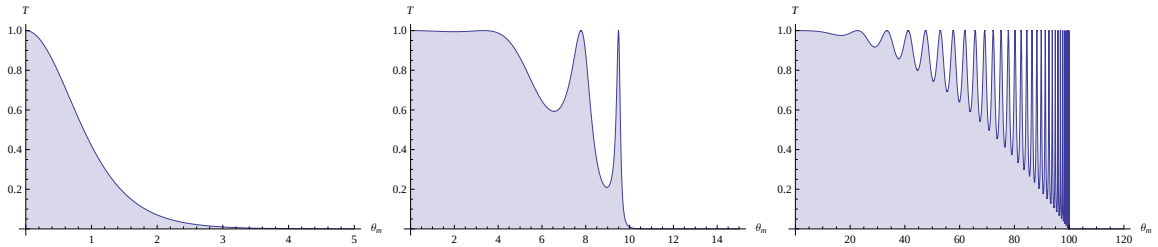

(a) Dirac point ($\theta_F = 0$) (b) $\theta_F = 10$ (c) $\theta_F = 100$

Figure 5.5: Transmission coefficients for transverse modes in a graphene sheet at different gate voltages.

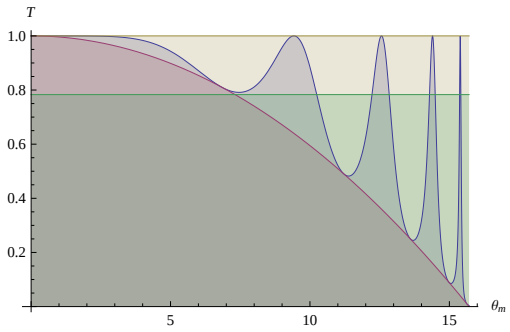

Figure 5.6: Transmission coefficients for transverse mode with $\theta_m = 5\pi$ (blue) along with lower envelope given by $T = (k_x/k_F)^2$ (purple) and the area equivalent given by $T = 0.783$ (green).

Figure 5.5 also plots the transverse mode dependence of the transmission for two other gate voltages, one intermediate from the Dirac point, and the other far from the Dirac point. The plots away from the Dirac point confirm that the transmission of evanescent modes with $\theta_m > \theta_F$ is negligible. Many resonances, or peaks which reach perfect transmission, are evident. The number of resonances at a given gate voltage is equal to $\lfloor \theta_F/\pi \rfloor$ and occur at values $\theta_m = \sqrt{\theta_F^2 - (n\pi)^2}$ for integer n. This is exactly the condition that the longitudinal wavevector $k_x L = n\pi$ and is similar to the resonant transmission through a finite potential well at bound-state energies of the well.

The lower envelope of the transmission curves is $1 - (\theta_m/\theta_F)^2$, which is shown in Fig. 5.6 for $k_F = 5\pi$. This is just $T = (k_x/k_F)^2$, which is maximized when the longitudinal wavevector $k_x = k_F$ at $q_m = 0$ and decreases to zero at $q_m = k_F$. Without the resonances, the transmission for a given transverse mode would just be proportional to the square of the longitudinal component of the Fermi wavevector. For the Fermi level away from the Dirac point $|k_F| > 0$, the total area of the transmission curve can be well approximated by $0.7831 k_F$. The rectangle of equivalent area is shown in green in Fig. 5.6.

5.3 Transport Parameters

Once the transmission coefficients have been determined, many transport parameters such as the conductance and Fano factor can be obtained. In some sense, the transmission coefficients contain all the information necessary to predict the results of a two probe resistance measurement. In the following, the conductance and current phase relation will be given as a function of the transmission coefficients and then calculated numerically for graphene short-and-wide junctions as in Fig. 5.3. Further application of the transmission coefficients to other types of measurements is discussed by Imry [75].

As an example of a non-trivial measurable quantity described by transmission coefficients, the Fano factor describes correlations between quasiparticles. It can be determined from

noise measurements and in the case of graphene, two groups have published a shot noise characterization [36, 33]. It can be expressed in terms of the transmission coefficients as:

$$F = \frac{\sum_{m=0}^{M} T_m(1-T_m)}{\sum_{m=0}^{M} T_m}. \tag{5.22}$$

There is a signature of ballistic quasiparticles in the Fano factor for graphene [147] but it is most evident at the Dirac point which makes it difficult to demonstrate [33].

5.3.1 Conductance

As described above the conductance is just the quantum of conductance G_0 times the trace of T, the transmission matrix. In terms of the eigenvalues T_i of T this is $G_0 \sum T_i$. For the graphene transmission coefficients with an extra factor of two for sublattice degeneracy this gives

$$G = \frac{4e^2}{h} \sum_{m=0}^{\infty} \left(1 + \frac{\sin^2\left(\sqrt{\theta_F^2 - \theta_m^2}\right)}{(\theta_F/\theta_m)^2 - 1} \right)^{-1} \tag{5.23}$$

where the number of transverse modes in the leads is taken to be infinity since $V_\infty \gg V_g$. This sum can be converted to an integral in the limit where the transverse mode spacing is infinitesimally small, i.e. $W \gg L$. In this limit θ_m becomes a continuous variable and the weight of each each term in the sum is $d\theta_m \cdot W/L\pi$. The integral expression is then

$$G = \frac{4e^2}{\pi h} \frac{W}{L} \int_0^{\infty} d\theta_m \left(1 + \frac{\sin^2\left(\sqrt{\theta_F^2 - \theta_m^2}\right)}{(\theta_F/\theta_m)^2 - 1} \right)^{-1}. \tag{5.24}$$

The integral can be calculated analytically at the Dirac point from the previous expression for the transmission $T_m(\theta_F = 0) = \mathrm{sech}^2(\theta_m)$ and is simply equal to one. Even though the Fermi level is essentially zero and hence also the carrier density, the conductance is *non-zero* as one would expect from a Drude model. The current is carried entirely by evanescent modes. The conductivity at the Dirac point, σ_D has a universal value $4e^2/\pi h \sim 1/20\,273\,\Omega^{-1}$. In contrast to a ballistic graphene ribbon which would have a quantized conductance of $4e^2/h$ for a single mode, the short-and-wide ballistic graphene device has a quantized *conductivity* that is $1/\pi$ times the Dirac conductance quantum. In the early measurements on graphene devices the Dirac point conductivity was on the order of $4e^2/h$ and those results were interpreted in this context [111, 116]. Miao et al [111] especially used the scaling of the Dirac point conductivity with aspect ratio to claim that their shortest devices were ballistic and

had conductivity converging on $4e^2/\pi h$. However these claims were unfounded as later studies showed that the Dirac point conductivity depends sensitively on doping [2] and could be much higher. Recent results on clean suspended devices with long mean free paths show conductivity approaching $4e^2/\pi h$ from above but are still a factor of two away [41].

For other gate voltages, the conductance can be calculated numerically. Since the contribution to the conductance of evanescent modes away from the Dirac point is minimal, the upper range of ∞ for the integral in Eq. 5.24 can be replaced with θ_F. Near the Dirac point but not at θ_F where the calculation is analytic, the upper range of integration can be fixed at 2π without any loss of accuracy. The resulting gate-voltage dependence of the conductivity over the entire gate-voltage range is shown in Figure 5.7. This plot assumes a device length $L = 50\,\text{nm}$, which has been achieved experimentally with electron-beam lithography, and a standard SiO_2 substrate with $\epsilon = 3.9$ dielectric constant and $d = 300\,\text{nm}$ thickness.

We claimed before that the sum of the transmission coefficients away from the Dirac point can be well approximated by $0.7831k_F$. Call the ideal constant of proportionality $\gamma \approx 0.7831$. Then for the conductance away from the Dirac point $G_{\bar{D}}$ we have

$$G_{\bar{D}} = \frac{4e^2}{\pi h}\frac{W}{L}\gamma k_F \tag{5.25}$$

which is linearly proportional to the Fermi wavevector. Since the number of modes is $M \approx k_F(V_g)W/2$, we can rewrite

$$G_{\bar{D}} = \frac{8e^2}{\pi h}\frac{1}{L}\gamma M. \tag{5.26}$$

Each channel effectively adds $8e^2/\pi h \cdot 1/L$ to the conductance. It is interesting that despite the channel being ballistic the contribution to the conductance from each transverse mode is inversely dependent on the sample length. Since $k_F(V_g) \propto \sqrt{V_g}$, the ballistic graphene transfer characteristic σ vs. V_g will go as $\sqrt{V_g}$ away from the Dirac point.

The sublinear gate-voltage dependence should be modulated by small conductance oscillations of which there are roughly five as expected from the channel length and the number of transverse modes that appear at the maximum gate voltage $\pm 50\,\text{V}$, $\sim \theta_{F,\max}/pi$. Each conductance peak corresponds to the introduction of a new longitudinal conduction mode $k_x L \sim n\pi$. These conductance oscillations which will be detectable in only the shortest graphene junctions as well as the $\sqrt{V_g}$ gate voltage dependence are the two signatures of ballistic transport in graphene devices of this geometry.

5.3.2 Current Phase Relation

If the leads to the graphene sample are superconducting, as in Fig. 5.3(b) and (c), a Josephson junction is created with the graphene as the weak link (Chapter 7). The superconducting leads at each end of the graphene sample will have a well-defined phase as a result of condensing into a macroscopic superfluid. Differences in these phases drive a current even

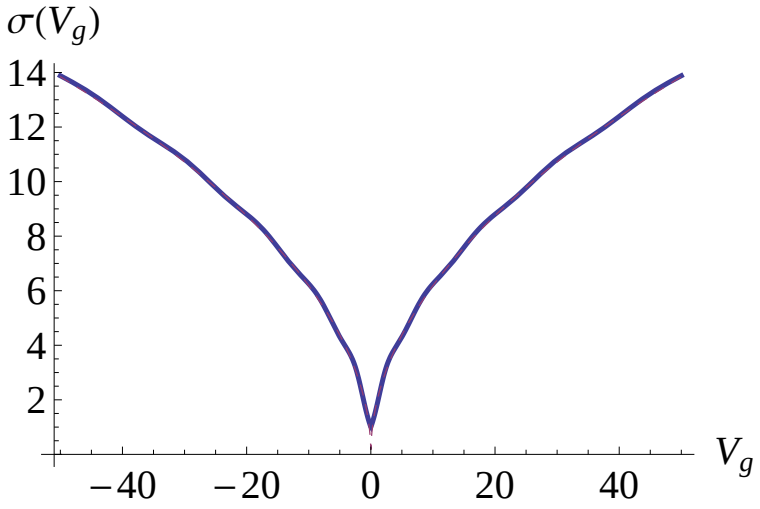

(a) Full voltage range

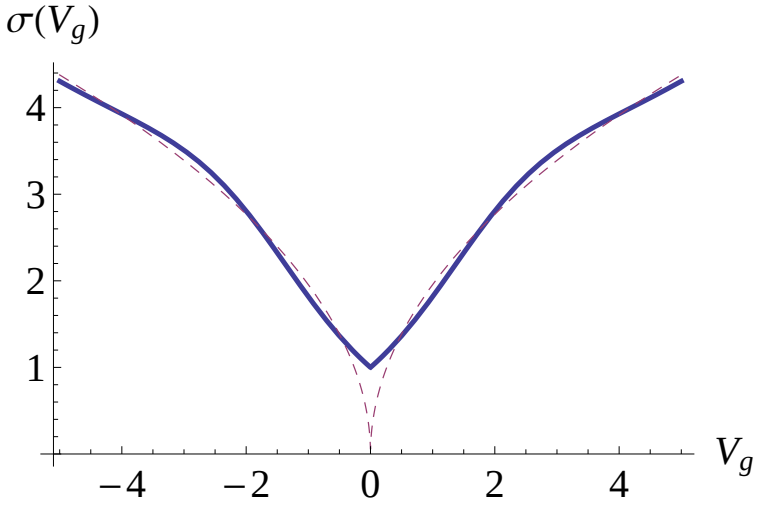

(b) Near Dirac point

Figure 5.7: Theoretical conductivity of a short-and-wide ballistic graphene sheet as a function of gate voltage.
The length L of the junction is 50 nm, the SiO_2 substrate dielectric constant is 3.9 and thickness 300 nm. Conductivity is given in units of $4e^2/\pi h$. Least squares fit to the conductivity proportional to $\sqrt{V_g}$ also shown (red dashed line).

in the absence of a voltage. This "supercurrent" will flow with zero applied voltage up to a certain critical current that depends on the properties of the carrier quasiparticles in the weak link and can be calculated from the transmission coefficients. First the current-phase relation $I(\phi)$ describing the dependence of the supercurrent on the phase difference between the superconducting leads is written. The Josephson junction adjusts this phase difference to maximize the supercurrent to I_c, the critical current. Higher currents passed through the junction will result in a non-zero voltage drop across it.

The current phase relation, in terms of transmission coefficients T_m is

$$I(\phi) = \frac{e\Delta_0}{2\hbar} \sum_{m=0}^{M} \frac{T_m \sin(\phi)}{\sqrt{1 - T_m \sin^2(\phi/2)}} \tag{5.27}$$

where Δ_0 is the zero-temperature superconducting energy gap of the leads [10]. The first calculation using the transmission coefficients determined for a ballistic graphene Josephson junction was Titov et al [145] followed by others [14, 32]. Much like with the conductance, the form of $I(\phi, \theta_F)$ can only be obtained analytically at the Dirac point. Taking $\theta_F = 0$, substituting $T_m = \mathrm{sech}^2(\theta_m)$ into Eq. 5.27 and turning the sum into a integral over θ_m ($W \gg L$) as before, one has for the current phase relation,

$$I(\phi) = \frac{e\Delta_0}{\hbar} \frac{W}{\pi L} \cos(\phi/2) \operatorname{arctanh}(\sin(\phi/2)) \tag{5.28}$$

which has a maximum value the critical current I_c given by

$$I_c = 1.33 \frac{e\Delta_0}{\hbar} \frac{W}{L\pi}. \tag{5.29}$$

Finally one can also determine the product of the normal state resistance and critical current, $I_c R_n = 2.08\Delta_0/e$. This voltage is on the order of the Josephson energy which is the energy to break Cooper pairs traveling through the weak link.

The form of the current-phase relation at the Dirac point is the same as that of a dirty metallic weak link [145, 101]. This is interesting in that the ballistic Dirac fermions at the Dirac point behave like nonrelativistic electrons with short mean free path.

Away from the Dirac point, the current-phase relation can be calculated numerically similarly to the conductance. The current-phase relation for several different gate voltages near the Dirac point in the same device geometry as before ($L = 50\,\mathrm{nm}$, $\epsilon = 3.9$, $d = 300\,\mathrm{nm}$) is shown in Figure 5.8(a). There are several distinguishing features. The phase which maximizes the critical current, $\phi_c(V_g)$, shifts with gate voltage. This can be seen by eye from the position of the maxima of the sinusoid-like curves in Fig. 5.8(a). It is made clear in Fig. 5.8(d), where a color map of the current-phase relation is presented as a function of Fermi angle $\theta_F(V_g) = k_F(V_g)L$ instead of V_g. The extremizing phase is traced over the color map and shows oscillations decaying with increasing θ_F. The maximum peak-to-peak difference is roughly 20°. Far from the Dirac point the magnitude is much smaller. Much like in the normal case, the maximum critical current varies as the square root of the gate

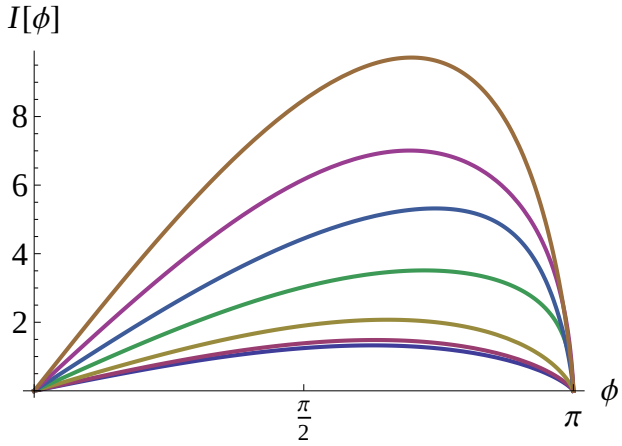

(a) Current-phase relation

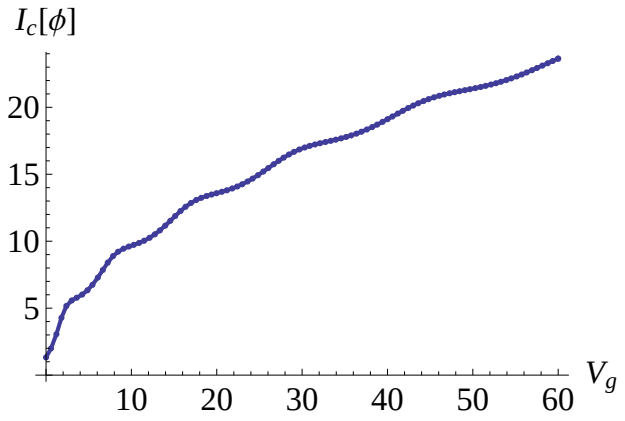

(b) Critical current vs gate voltage

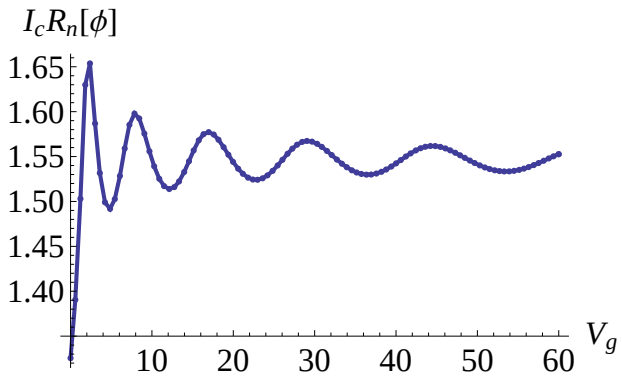

(c) I_cR_n product

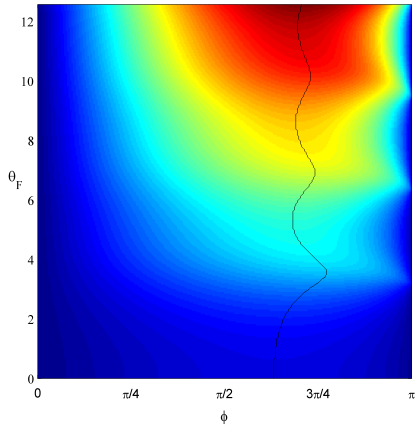

(d) Current-phase relation color map

Figure 5.8: Theoretical current-phase relation of a short-and-wide ballistic graphene sheet as a function of gate voltage.
The length L of the junction is 50 nm, the SiO_2 substrate dielectric constant is 3.9 and thickness 300 nm. Currents in units of $e\Delta_0/2\hbar$. **(a)** The current-phase relation is plotted for gate voltages near Dirac point $V_g = 0, 0.16, 0.64, 1.44, 2.56, 5.76, 10.24$ V (upward). **(b)** Critical current as a function of gate voltage and I_cR_n product (**c**). **(d)** Map of current-phase relation showing location of current extremizing phase, ϕ_c. Plotted as a function of $\theta_F = k_F(V_g)L$.

voltage far from the Dirac point and shows similar resonances (Fig. 5.8(b)). The product of the maximum critical current and the normal state resistance also shows small oscillations as a function of gate voltage (Fig. 5.8(c)). All these features are signatures of ballistic transport in a short-and-wide graphene Josephson junctions. The current-phase relation, which is identical to the diffusive metal junction case at the Dirac point, is not identical to either that or the ballistic metal junction relation away from the Dirac point. Indeed while the critical phase does oscillate and sometimes approach closer to $\pi/2$, the value in the ballistic metal limit [101], it does not

Using the same current-phase relation, we can also determine the expected critical current modulation with flux and gate-voltage of an ideal, ballistic graphene superconducting quantum interference device (SQUID, Ch. 7). This is shown in Figure 5.9. With respect to a conventional tunnel-junction based dc-SQUID, there are some distinguishing features. First the modulation of the critical current with flux is not complete. The critical current does not reach zero at any value of the flux or gate voltage. Second there is a cusp at the critical current minima. Both these features could not appear simultaneously in a tunnel junction SQUID, although other type of weak link SQUIDs such as those with normal metals could look similar. The overall modulation with gate voltage should follow the results above for the critical current.

5.4 Considerations for Real Devices

The approximations made for the potentials, leads, and modes involved in calculating the transport parameters of the previous sections can be improved to account for more realistic devices. These refinements result in models which reproduce some of the oft-seen features in transport measurements in graphene, including the conduction asymmetry between the electron and hole branches. Several groups [72, 24, 49] have modified the effective potential profile across the graphene device to account for doping by contacts. The contact-doping due to the work function differences and charge transfer between graphene and electrodes for common metals has been calculated by Giovannetti [60]. The considerations in these papers and the models developed therein improve upon the simple, yet easily calculable one presented in this chapter. Further analysis of the data presented in the following chapters would benefit from more realistic graphene transport models.

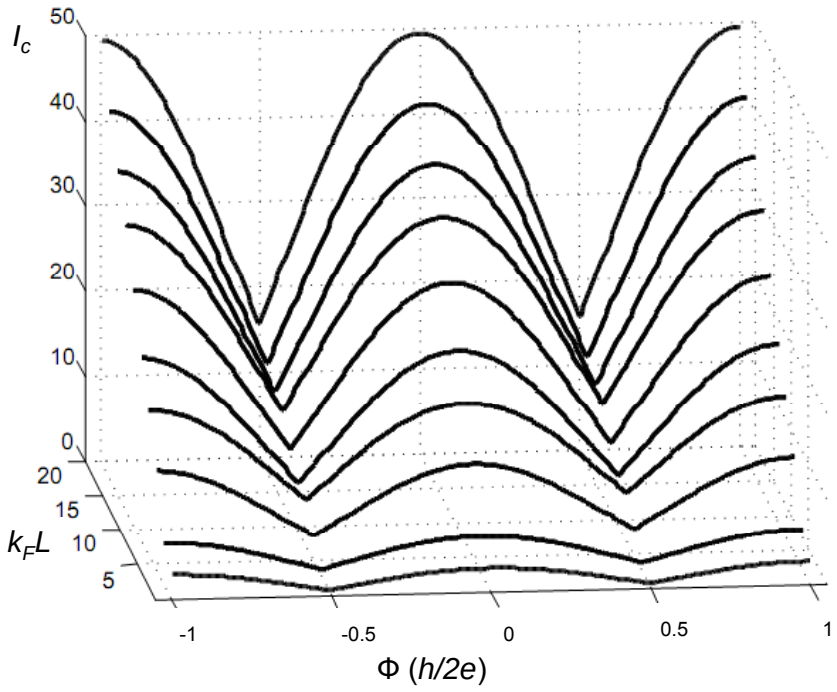

Figure 5.9: Theoretical flux and gate-voltage modulation of ideal ballistic graphene superconducting quantum interference.
Gate voltage units in radians calculated from Fermi angle $\theta_F = k_F(V_g)L$ and current in units of $e\Delta_0/2\hbar$.

Chapter 6

Point Contact

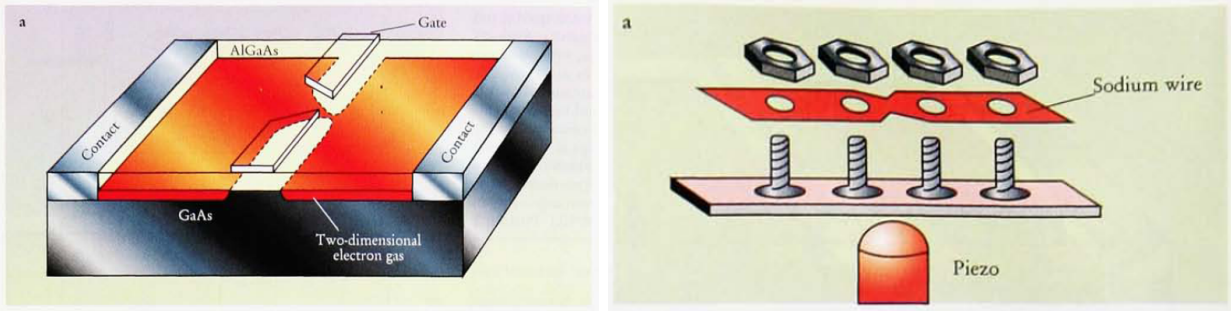

(a) 2DEG QPC

(b) Break junction QPC

Figure 6.1: Two types of quantum point contacts which exhibit conductance quantization. From van Houten et al, *Physics Today* [149].

A point contact is a device in which one electrode is attached to another at a single point. This can be done for example by gently pushing a metal whisker or etched tip onto a flat counter-electrode until it just makes contact. Another technique is to pull a single fine wire from both ends until it almost breaks–this is called a break junction (Fig.6.1(b)). The interest in such devices is that the diameter of the wire W at the contact point can be extremely small, down to the width of several atoms. When this width is comparable to the Fermi wavelength λ_F, the quantum properties of the electron manifest themselves. This type of device is called a quantum point contact (QPC). Indeed in Chapter 5 it was shown that such techniques channel can exhibit conductance quantization, in which the measured conductance occurs in multiples of $G_0 = 2e^2/h$. The number of conducting channels is roughly the width divided by the Fermi wavelength. In a break junction as the wire is pulled and the point contact width decreases, the number of conducting channels is modified and steps can be seen in the conduction.

In metals the Fermi wavelength is on the order of a nanometer. The fabrication of a point contact at this scale is extremely difficult and lithographic techniques, if they exist, would be complicated. Sophisticated alternatives have been developed which allow some measure of control and reliability but the experiments are difficult and the interpretation can be controversial. In addition, the intrinsic carrier density in metals is so large that it is impossible to tune it externally.

For these reasons it is desirable to use a semiconductor instead of a metal. In a semiconductor the Fermi wavelengths can be much larger and can potentially be tuned with the electric field effect or by inserting dopants. An ideal semiconductor system is GaAs, in which engineering of layers by molecular-beam epitaxy can produce a two-dimensional electron gas (2DEG) that not only exhibits high mobility but whose carrier density can easily be tuned with the field effect. An important advantage of high-quality GaAs 2DEGs is that the mean free paths are long ($>1\,\mu$m). Scattering within the point contact would ruin conductance quantization. In a GaAs 2DEG, electrostatic gates define the point contact by depleting carriers along a line separating two regions except at a single point. This type of gate is called a split-gate and the device is shown in Fig. 6.1(a). By adjusting the split-gate voltage near the conduction-band edge, the effective width of the point contact can be controlled, determining the number of conduction channels. Van Wees and Wharam independently measured conductance quantization in such systems in the late eighties [150, 156]. Their results and those on metallic point contacts is reviewed in the article by van Houten and Beenakker [149].

Graphene is also a 2D electronic system, but unlike GaAs, the graphene band structure does not have a gap (Ch. A). This means that alternatives to electrostatic depletion must be used to define the point contact. There are several possible to do so which all rely on removing or chemically modifying the graphene to make it insulating in the undesired areas. Unfortunately this means that the constriction width cannot be controlled. However one can still adjust the overall Fermi wavelength by changing the back-gate voltage *or* envision putting local gates at the point contact to change the Fermi wavelength locally. Two techniques to define point contacts in graphene will be covered in this chapter: patterning followed by etching, and local anodic oxidation (Ch. 4). Results on one graphene point contact device is presented. Due to scattering in the channel, conduction is not quantized and Coulomb-blockade like behavior was seen.

6.1 Etched QPC

6.1.1 Experimental Details

Graphene samples were obtained by micromechanical exfoliation (Ch. 2) and high-resolution electron beam lithography used to pattern a geometry similar to Fig. 6.1(a). Multiple point contacts were designed on the sample graphene flake, Fig. 6.2(a). Once the resist was developed, an oxygen plasma was used to etch the patterned areas. Graphene is readily removed

with a reactive ion etch and processing parameters are not crucial. Different shapes of point contacts were fabricated, including conventional symmetric bridges as well as tapered asymmetric ones. Lithography patterns were polygon fills, but this is not the optimal geometry. Single-pass lines with a short break should have been used instead as this can give narrower widths. Other groups have subsequently used that technique [146] to obtain smaller constrictions. Once the constriction width is too small, edge disorder effects dominate transport characteristics.

Once the graphene has been etched, electrodes are patterned and deposited, Fig. 6.2(b). The electrode material is Au/Cr, with the approximately 5 nm film of chromium serving as an adhesion layer, without which the gold does not stick well to the graphene. The gold thickness is about 45 nm. Good device fabrication and deposition techniques are necessary to obtain a small contact resistance (Sec. 4.2). At worst the resistance between a measurement probe and the entry to the point contact should be comparable to the resistance quantum, $4/e^2h$, about 6 kΩ. Ideally it should be much less than a kΩ but this requires a large inverse aspect ratio $W'/L' \gg 1$ of the region between the electrode and the point contact.

Figures 6.2(c) through (e) show close-up SEM micrographs of fabricated point contacts. The smallest point-contact width varied between 40 nm to 150 nm. The energies corresponding to lowest subband population are then 50 meV to 200 meV. If the channels are clean, this would imply that the lowest subband is almost completely occupied at room temperature. For a GaAs point contact of identical width, this would not be the case. The preferable energy scaling for graphene point contacts was discussed in Section 5.1.

At cryogenic temperatures, the contribution to conduction from higher subbands is virtually non-existent. Thermal broadening of features is also minimized. More importantly, scattering from thermally activated sources such as phonons should be greatly reduced, increasing the mean free path. In dirty lithographed devices such as the early fabricated ones shown here, the phonon contribution to scattering is negligible and the resistance shows a very weak dependence on temperature. This is because of the large amount of surface disorder from the lithography process (see Sec. 3.3) and the charged impurities in the substrate. In comparison, for suspended devices or clean devices on good substrates the phonon contribution *is* significant and a strong temperature dependence of the conductivity is observed.

Once a graphene sample with multiple point contacts has been fabricated and electrodes deposited, the device is loaded into a cryogenic probe station, shown in Fig. 6.3. The four probe arms, central chamber where the sample is loaded, optical telescope with camera (black column), and transfer line insert are visible in the photo. The flow-cryostat probe station has several advantages compared to a conventional bath cryostat with hard-wired connections to devices. One can take measurements on a large number of devices limited only by the size of the cold plate (5 cm × 5 cm). In addition no wirebonding of electrodes is necessary. This can avoid inadvertent device damage due to static discharge or other reasons during bonding. With proper grounding of the measuring probes, the probe station is less risky for sensitive devices such as point contacts. The lowest temperatures obtained with the probe station are 4.2 K at the sample stage and 9 K for the radiation shield.

To contact a device, the beryllium gold probe station tips were grounded and then lowered

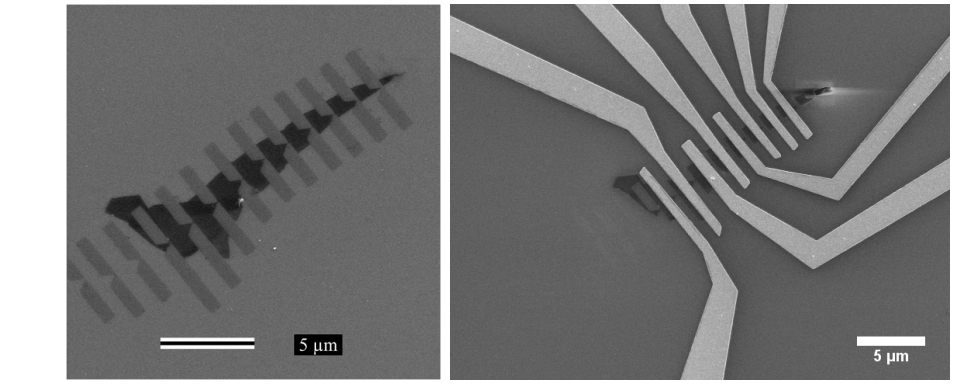

(a) (b)

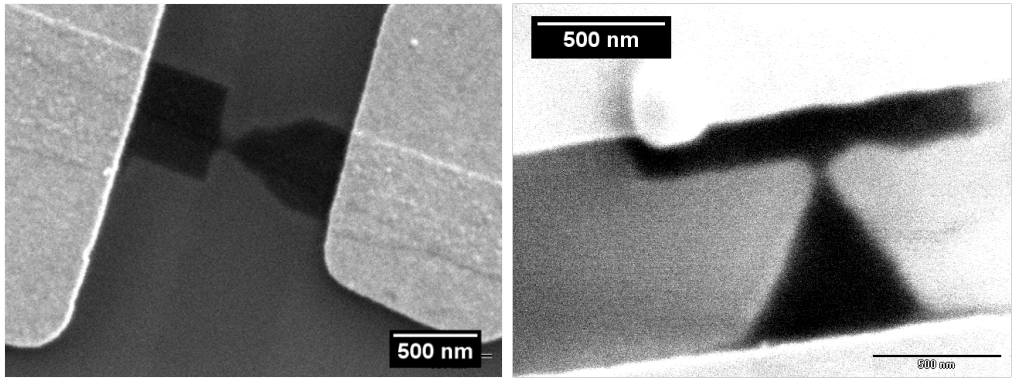

(c) (d)

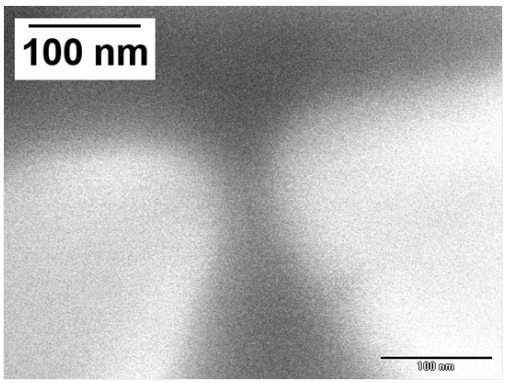

(e)

Figure 6.2: Scanning electron micrographs of graphene point contact devices. **(a)** Few-layer graphite sample post patterning and oxygen plasma etch. **(b)** Subsequent patterning and electrode deposition. **(c),(d)** Close up micrographs of point contacts and electrodes of different samples. **(e)** Extreme close up on point contact in (d).

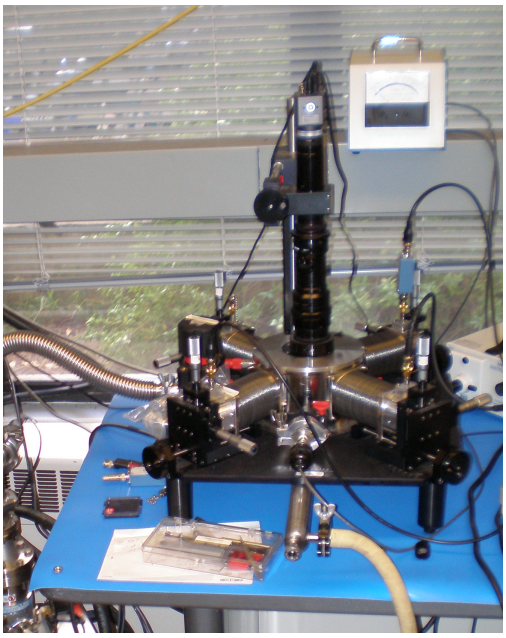

Figure 6.3: Four-terminal cryogenic (liquid helium) probe station.

onto lithographed pads connected to electrodes near the graphene point contact. Measurements were take in a two-terminal configuration, with current sourcing and voltage sensing performed outside of the probe station. A lock-in amplifier, as well as current and voltage preamplifiers were used to amplify small signals. A DAQ card controlled by LabView was used to generate small sinusoidal wavefunctions with a DC offset for differential conductance measurements with the lock-in. Another output on the DAQ card was used to control the gate voltage signal between $\pm 10\,\mathrm{V}$. For a wider range, a high voltage configurable voltage supply was used. Data was analyzed offline in Igor Pro.

6.1.2 Results

Figure 6.4 shows different transport measurements on the graphene point contacts. The IV curves between $\pm 100\,\mathrm{mV}$ is shown at several gate voltages in Fig. 6.4(a). The curves are non-ohmic and have step-like features indicating an activated conduction process. Near the room temperature Dirac point, $-12\,\mathrm{V}$, the IV curve is flat with a conductance of $8.5\,\mathrm{nS}$ corresponding to a resistance of $0.1\,\mathrm{G\Omega}$. Away from the Dirac point the conductance increases by orders of magnitude, but the dependence is not smooth on gate voltage (data not shown). At $6.7\,\mathrm{V}$ the small bias conductance is $7.6\,\mu\mathrm{S}$, a thousand times larger than at $-12\,\mathrm{V}$.

In Fig. 6.4(a), the zero-bias conductance is plotted for another device as a function of gate voltage at liquid nitrogen ($77\,\mathrm{K}$) and liquid helium ($4.2\,\mathrm{K}$) temperatures. The gate voltage range is small ($\pm 10\,\mathrm{V}$) and the sweep has been performed in both directions. The high temperature conductance shows a small ($10\,\mu\mathrm{S}$) sinusoidal variation of conductance

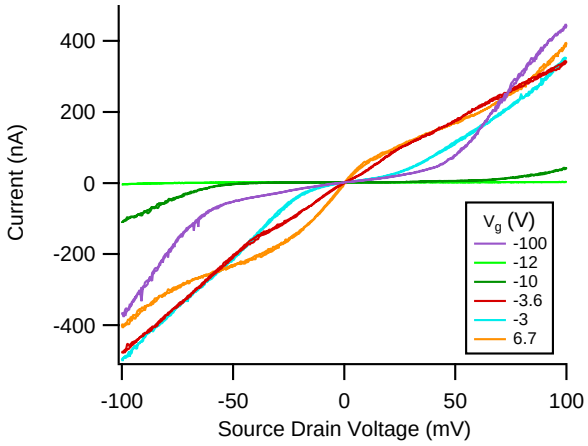

(a) IV curve

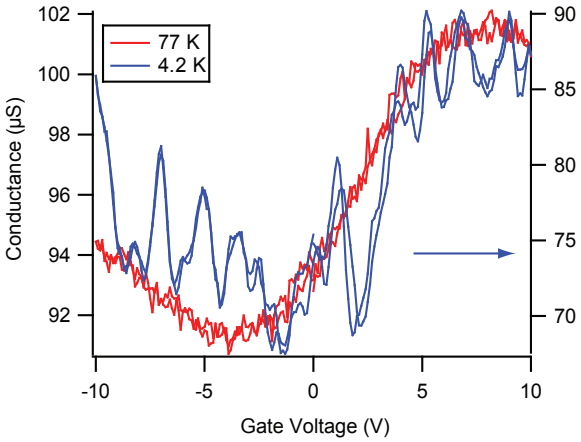

(b) Temperature dependence

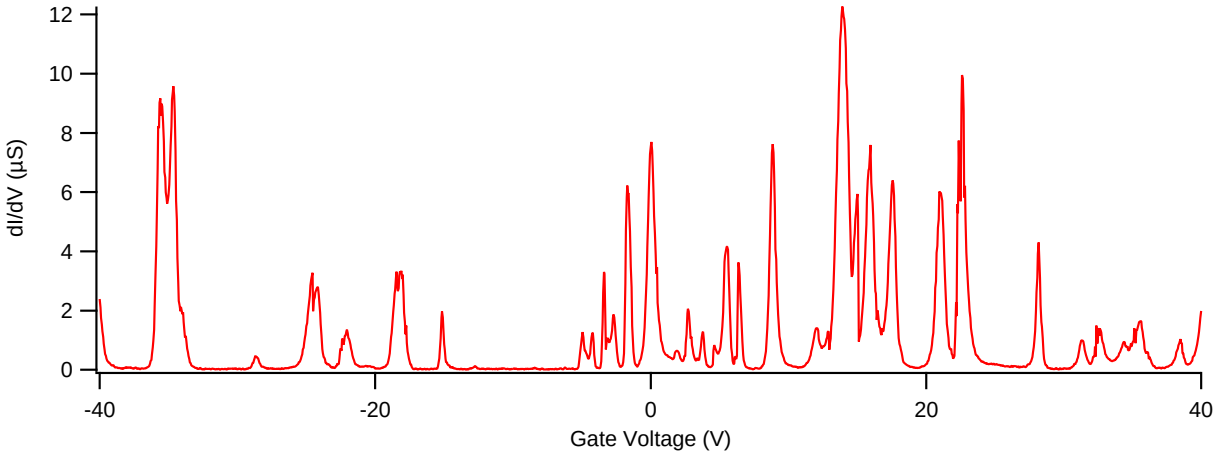

(c) Coulomb oscillations

Figure 6.4: Electronic transport measurements on etched graphene point contact devices. Measurements at 4.2 K unless noted.

with gate voltage voltage and some noise. Although a dip in the conductance near zero gate voltage would be a sign of the Dirac point in a macroscopic graphene sample, the conductance decreases again near 10 V indicating that the gate voltage dependence is not a band structure effect. When the temperature is lowered, the overall conductance is decreased by about 16 µS (blue curve is plotted on the right-hand axis). The large scale conductance variation present at higher temperature remains but is superimposed with a series of narrower peaks. These peaks are reproducible and have widths on the order of a few volts. Some periodicity is evident.

Fig. 6.4(c) shows the full gate voltage dependence of zero-bias conductance (dI/dV) at 4.2 K for another device. Here the peaks are extremely narrow and can be separated by large regions of zero conductance. There is no identifiable periodicity to the peak structure, and the peak widths vary from less than one volt to several volts.

Figure 6.5 shows 2D plots of the differential conductance as a function of gate voltage and source-drain voltage bias, $\frac{dI}{dV}(V_g, V_s)$, for three different devices. The gate voltage varies across a small range, ±10 V. Fig. 6.5(a) is the differential conductance map for the device in Fig. 6.4(b). The data presented there corresponds to a slice at $V_S = 0$ in the map. The region of low conductance, approximately $0.9G_0$, centered at roughly −3 V on the backgate has a width of several millivolts and can be identified as the Dirac point. The peaks observed at low temperature in Fig. 6.4(b) correspond to the lateral corners of the faint white diamonds in the dI/dV map. Although the spacing between these corners is somewhat regular, fainter diamonds appear to be overlapping.

Fig. 6.5(b) and (c) show differential conductance maps for two other samples. In Fig. 6.5(b), many intersecting diamonds are visible and the conductance modulation is not strong. The Dirac point is off to the right above 10 V. The sample in Fig. 6.5(c) is in the opposite regime. The conductance modulates essentially to zero and large well-defined diamonds are apparent. The Dirac point for this sample appears to be off to the left, below −10 V. There is also a lower conductance region to the right above 10 V. Although the diamonds are well defined, they are aperiodic.

6.1.3 Discussion

The features of the IV curves, differential conductance dependence on gate voltage, and 2D differential conductance maps indicate Coulomb blockade without well defined single islands. Transport is not ballistic despite conductivities on the order of G_0 in the on state. Most likely multiple transport channels with low transmission are contributing in parallel. Scattering within the channel as well as at the entrance and exit are producing localized states with a range of confinement and charging energies. When the source-drain bias increases and passes over a new energy level in a localized state in the channel, the current increases rapidly. When the source-drain voltage is intermediate between levels, a current plateau is observed. As there are multiple localized states of different sizes in series as well as parallel, the level structure is complex, and leads to a complicated gate voltage dependence of conductance as in Fig. 6.4(c). Similarly to the source-drain bias, when the gate voltage tunes the Fermi level

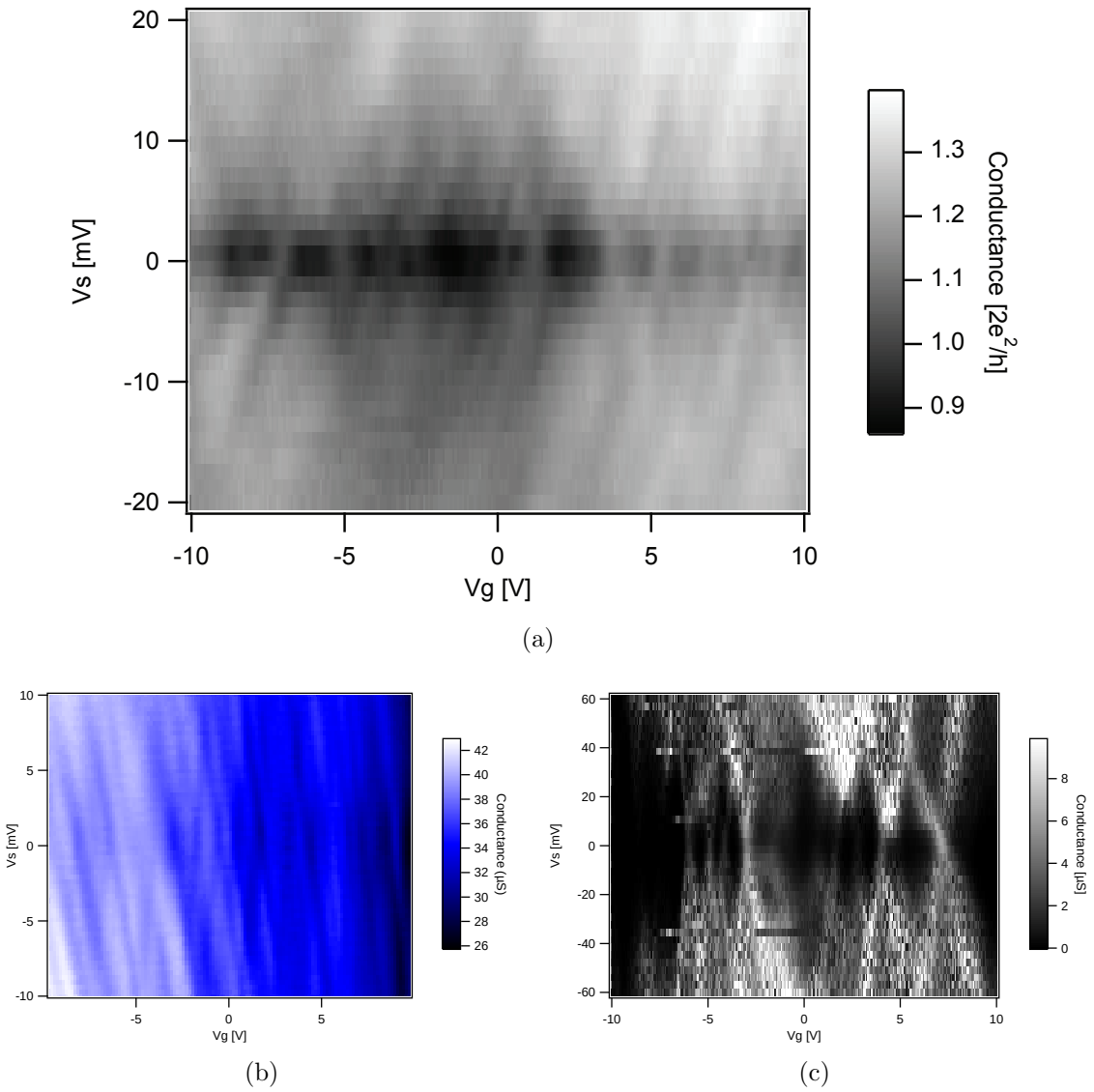

Figure 6.5: Coulomb blockade behavior of three different graphene etched point contacts at 4.2 K.

of the contacts to resonance with a localized state, the conductance increases. In between states, the conductance is virtually zero.

The first phenomenon that results in localized states with discretely spaced energy levels is 1D confinement. This is the familiar quantum particle-in-a-box. The second is the electrostatic energy of a discrete charged particles in a confined area, called the charging or Coulomb energy. The energy for confinement E_b and charging E_c are

$$E_b = \hbar c^* \frac{\pi}{d} \qquad\qquad E_c = \frac{e^2}{2C} = \frac{e^2}{2c'd^2} \tag{6.1}$$

where d is a characteristic dimension which in the case of the devices considered here, is bounded from above by the constriction width, $W \sim 40\,\mathrm{nm}$ to $150\,\mathrm{nm}$. It is certainly smaller however due to the effects of scatterers. The specific capacity $c' = C/A$ is determined by the substrate geometry and for the standard values $\epsilon = 3.9$, $d = 300\,\mathrm{nm}$), is equal to about $115\,\mathrm{aF\,\mu m^{-2}}$. This makes the crossover length $d_c = e^2/(\pi\hbar c^* c')$ roughly 340 nm. This implies that the effects in graphene point constrictions are solely due to charging and do not arise from confinement. For a conventional 2DEG, the confinement energy would instead have an inverse d^2 dependence. In this case the charging energy exceeds the confinement energy for all d with reasonable effective masses.

The question is why does a constriction show Coulomb blockade? The graphene has *not* been patterned into an island and one hoped for good transmission into the channel in order to observe ballistic transport properties. However scattering in and at the ends of the channel effectively produce a series of charging islands and this results in the observed aperiodicity in the Coulomb diamonds. This process is depicted in Figure 6.6.

Coulomb blockade phenomena in graphene has been investigated since its discovery, although early measurements were on thicker samples [19]. Since then, it has been studied in graphene samples with increasingly small islands. Ponomarenko [124] et al observed room-temperature charging and confinement effects. There is already a review on graphene single-electron transistors in press [74] (2010).

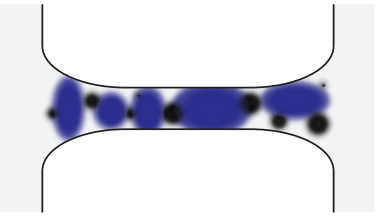

Figure 6.6: Depiction of charging island formation in graphene point contacts. The black dots are scattering sites such as charged impurities in the substrate. Blue regions represent localized states in graphene. Based on Todd et al [146].

6.2 Local Anodic Oxidation QPC

Graphene point contacts can also be made by local anodic oxidation (LAO), described in detail in Section 4.3.2. In the LAO process, an atomic force microscope (AFM) is used to oxidize patterns on a graphene sheet, thereby defining nonconducting regions. Point contact devices fabricated by LAO are different in many respects from those patterned by plasma etching. The most important is that they can be clean if the electrodes are also deposited in a way which avoids lithography, such as by stencil mask evaporation (Sec. 4.2.2). In addition to cleanliness, with LAO the conductance of the graphene device can be monitored during the oxidation process, albeit at room-temperature ambient conditions. This can in principle allow controlling the width and conductance of the point contact region. Finally, the AFM tip itself provides a local probe of graphene's electronic properties via techniques such as scanning gate microscopy (SGM) and Kelvin probe microscopy. With a suitable conducting tip (such as doped diamond) one can also measure directly the tip-drain resistance.

Initially, the motivation was to detect at room temperature conductance quantization by slowly oxidizing a graphene sample from one end to the other. In the moments before the graphene sheet is completely cut and the constriction width approaches zero, the lowest transverse mode energy should exceed room temperature. Although it may be possible to observe this in clean samples, due to substrate-induced disorder, no such quantization was observed in the measurements. The diffusive transport results can be fit to an analytic solution of the Laplace equation obtained by conformal mapping. The capability to pattern an ideal two-dimensional conductor and simultaneously record the conductance is interesting in itself.

6.2.1 Experimental Details

Exfoliated graphene samples were produced and identified as usual. Electrodes were then deposited by several means, including lithography, stencil-mask evaporation, and microsoldering (Sec. 4.2.3). Lithographed devices were sometimes cleaned post fabrication by scanning an AFM tip in contact mode over the sample for a half-hour. This would remove most adsorbed material without damaging the sheet. Stencil-mask evaporated devices were clean except for a few samples in which the electrode material had diffused across the graphene during electron-beam evaporation (Sec. 4.2.2). Microsoldered devices were always clean.

The devices were then mounted on a home-built PC-board designed for electronic access to samples while scanning in the AFM. Source and drain electrodes on the sample were wirebonded to pads on the PCB. A back-gate connection was also made to be able to vary the carrier density via the electric field effect. Once the sample was mounted in the AFM and the microscope aligned and stabilized, an initial contact-mode scan of the graphene sheet and electrodes provided a reference image. The graphene could then be patterned into the desired point contact geometry.

For electrical measurements, the two terminal conductance was measured either by ap-

plying a small fixed bias to the source terminal, allowing larger bandwidth, or with a small low-frequency signal for lock-in detection with enhanced sensitivity. In both cases, a current preamplifier was attached between drain and ground to monitor the conductance $G = I/V_s$ and read out directly for DC measurements or fed to the lock-in amplifier for AC measurements. In a few samples with four electrodes, a voltage preamplifier was used to amplify the signal at the inner, voltage sense terminals. The output was fed back to the AFM through its front panel inputs to be able to precisely link the conductance to the position of the cantilever tip on the sample. Feedback or triggering on these inputs could also be programmed with the AFM computer interface to produce constrictions of predetermined conductance although this was not done.

At any point the gate voltage dependence of the device conductance $G(V_g)$ could be measured. This can be used to identify shifts in the Dirac point over time which occurs in ambient conditions. If the environment in the AFM chamber was modified to control oxidation parameters, such as by increasing or decreasing humidity, the Dirac point could shift quickly (several volts per minute) before stabilizing or exceeding the gate voltage range.

In some samples, scanning gate microscopy (SGM) was used to identify the point contact and make local gate measurements. In SGM, the device conductance is measured as the conducting cantilever tip passes above the sample at a fixed height. The tip acts as a local gate modulating the carrier density in the region underneath. For a wide sheet, SGM should not show any effects because the tip doping is localized. However when the tip passes over the point contact, through which all current passes, the carrier density modulation strongly affects the conductance.

6.2.2 Results

Figure 6.7 shows a graphene point contact fabricated by local anodic oxidation. The six palladium electrodes deposited by stencil mask evaporation frame the exfoliated graphene sample in the optical image, Fig. 6.7(a). The source and drain pads as well as the two sense electrodes on the left were successfully wirebonded to allow a four-terminal measurement. Unfortunately due to a problem with the dielectric, the backgate could not be used above $\pm 5\,\mathrm{V}$.

The graphene shorts between the sense electrodes on the right and the lower electrode were first disconnected by LAO. At this point the AFM was centered between the four sense electrodes and aligned horizontally to the region traced by the square in the optical image. Fig. 6.7(b) shows a contact-mode AFM scan of the area. The four sense electrodes are shown in white and the polygonal graphene sample appears as a dark gray. The palladium, like gold and other metals in the absence of a chromium adhesion layer, had migrated across the graphene surface during evaporation. Although not visible in the contact-mode image, it is clear in the tapping mode post-cut topography.

Once the conductance measurement was setup and initiated, the cut was made as shown in Fig. 6.7(c), halfway between the sense electrodes. In order to avoid issues with aligning two cuts, a single cut is used to produce a point contact at an edge of the sheet. The measurement

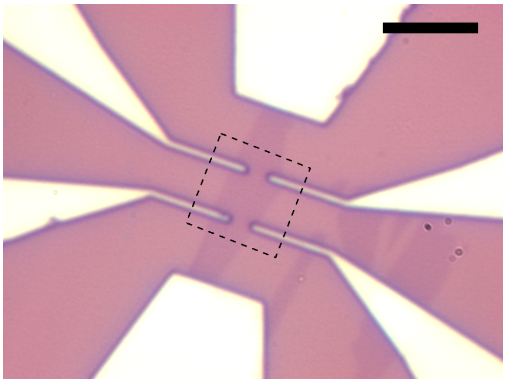

(a) Optical image

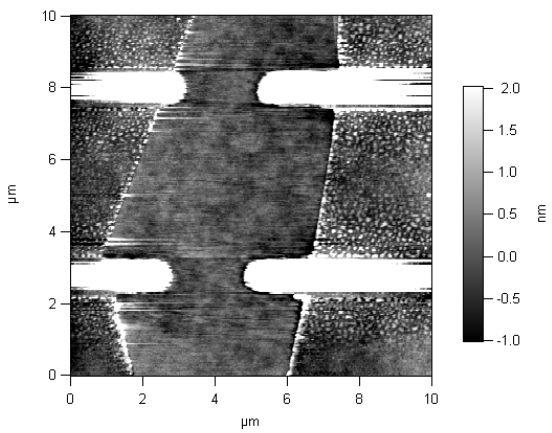

(b) AFM topography, pre cut

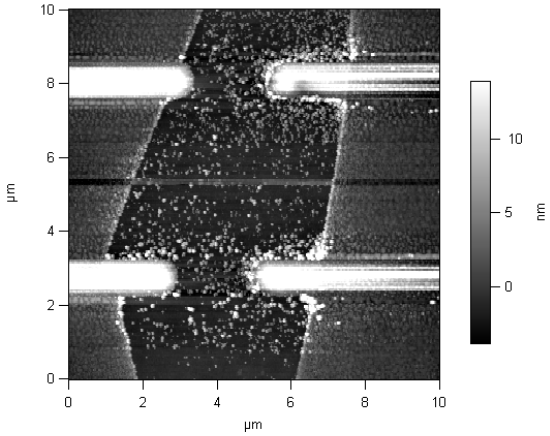

(c) AFM topography, post cut

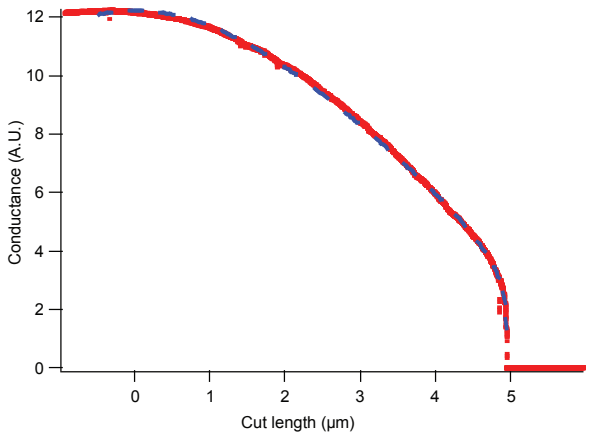

(d) Conductance vs cut length

Figure 6.7: Fabrication of graphene point contact and conductance measurement during cut. Optical scale bar 10 µm.

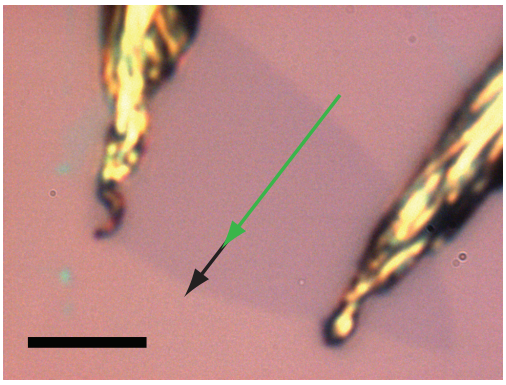

(a) Optical image

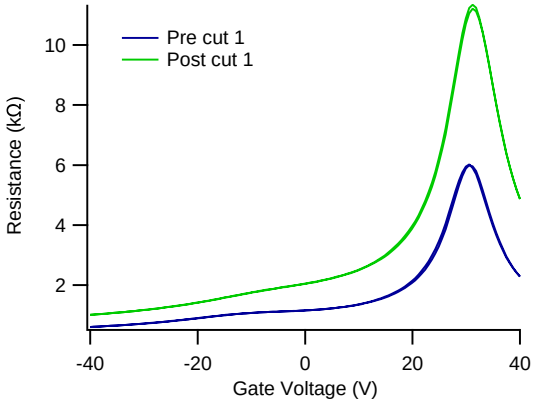

(b) Resistance vs gate voltage

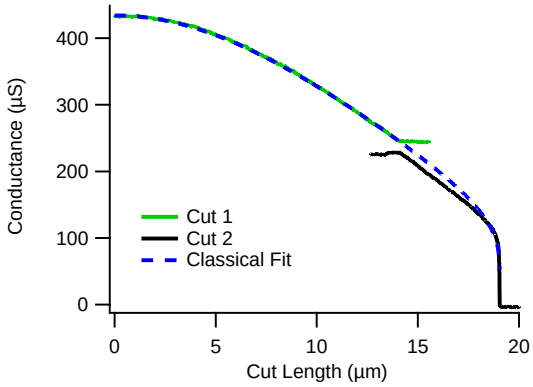

(c) Conductance vs cut length

Figure 6.8: Conductance vs gate voltage and conductance vs cut length for LAO patterned graphene point contact.
Optical scale bar 10 µm. AFM images of cut, Fig. 4.20(c).

of the conductance during the cut is shown in Fig. 6.7(d). The conductance rises slightly in the beginning and then gently decreases downward almost until the end, where it sharply falls to zero. When the cut is halfway across the sheet, the conductance is only about 80% its initial value. In fact the conductance only reaches half its initial value when there is only 500 nm left in the sheet, roughly one-tenth its initial width. Superimposed on the curve is a fit to the data, explained in the discussion below. There is no sign of conductance quantization in the few subband limit near the end of the cut. In µS the graphene conductance quantum is at 154 µS.

Figure 6.8 shows a second graphene device which has been patterned into a point contact by LAO. This device was already presented in Section 4.3.2, where the LAO technique was described. AFM images of the cut can be found in Fig. 4.20(c). Fig. 6.8(a) is an optical image of the device. The electrodes are indium deposited by microsoldering which keeps the

surface of the sample extremely clean. In this sample, a first cut was made, and then the gate voltage characteristic was measured. Afterwards a second cut completely isolated the two electrodes. The cuts are indicated by arrows in the optical image, with green preceding black.

Figure 6.8(b) is the gate voltage characteristic before and after making the first cut. The resistance is plotted as a function of gate voltage. Possibly as a result of measuring in ambient conditions, the Dirac point is at 31 V, indicating p-doping. However one can see that the Dirac point position has not shifted between the initial measurement and the measurement post cut 1. It is also a possibility that doping from the substrate or another impurity source has resulted in the large shift. It is remarkable that even in air with the sample completely exposed to water and oxygen the device mobility is fit to more than $2500\,\mathrm{cm^2\,V^{-1}\,s^{-1}}$.

After the first cut, the resistance has increased almost by a factor two at the Dirac point despite being only 60% larger elsewhere ($V_g \sim -14\,\mathrm{V}$). If the sample were completely homogeneous one would expect the scaling of the resistance with cut length to be independent of gate voltage. Heterogeneous doping however could change this picture by making the effects of local variations in the Dirac voltage more prominent. Electron-hole puddles [103, 162] which are responsible for charge inhomogeneity have a comparable length scale (1 µm) but would not cause such a large shift. A Dirac point shift of 30 V corresponds to an additional charge density of $2 \times 10^{12}\,\mathrm{cm^{-2}}$ which is an order magnitude larger than what has been observed for electron hole puddles.

Figure 6.8(c) shows the conductance as a function of cut length for the two cuts. The curve is very similar to the one for the previous sample. At the end of the first cut, with roughly one-third of the sheet width remaining, the conductance is still not half its initial value. A shift in the conductance between stopping the first cut and starting the second one is apparent. This is likely due to adsorption of dopants during the pause. The same fitting function, without any free parameters, matches well the data. No quantization features are observed at the knee at zero conductance.

Finally, Figure 6.9 shows scanning gate microscopy results on an LAO patterned few-layer graphite point contact device. An optical image of the microsoldered device is shown in Fig. 6.9(a) with the point contact region highlighted in the middle where the sheet is single layer. Fig. 6.9(b) shows an AFM contact-mode topography scan zoomed into the square in the optical image. The surface is pristine as the oxidized graphene over the cut has been pushed away by scanning. The two thick black lines are long cuts that have been made to confine the current to flow only in the central area. There one can identify several small constrictions. These constrictions are magnified in another AFM topography map, Fig. 6.9(c). There are five in total and they range in width from 20 nm to 80 nm. The constrictions in the upper half of the scan show some oxidized graphene around the cuts because they had not yet been cleaned. These small constrictions were produced by placing the cantilever over the desired spot and applying a short negative voltage pulse relative to the sample. This would oxidize a small patch under the tip and two such patches define a constriction.

Fig. 6.9(e) shows the scanning gate microscopy data. After a topography image is made

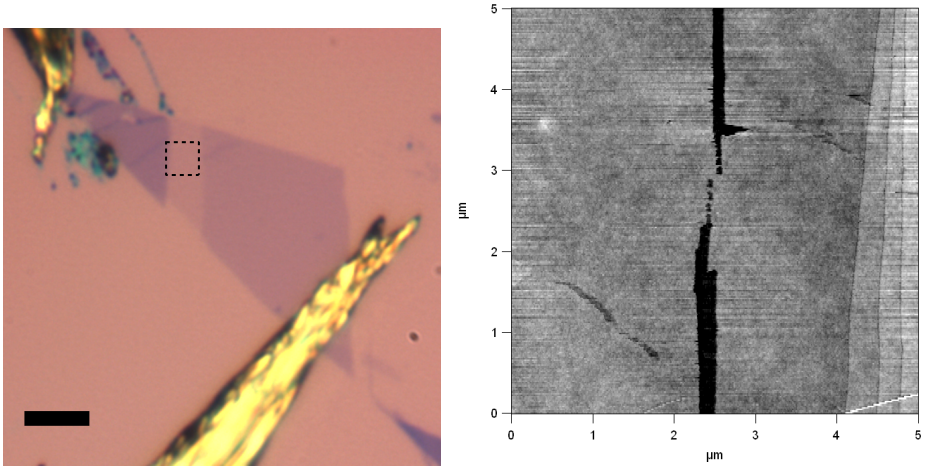

(a) (b)

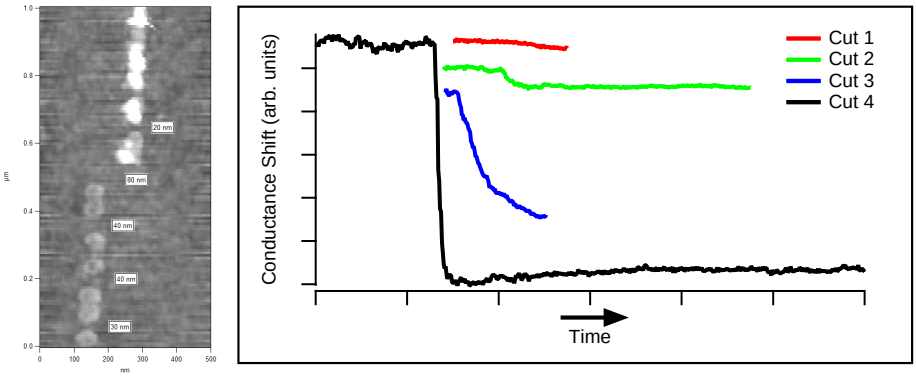

(c) (d)

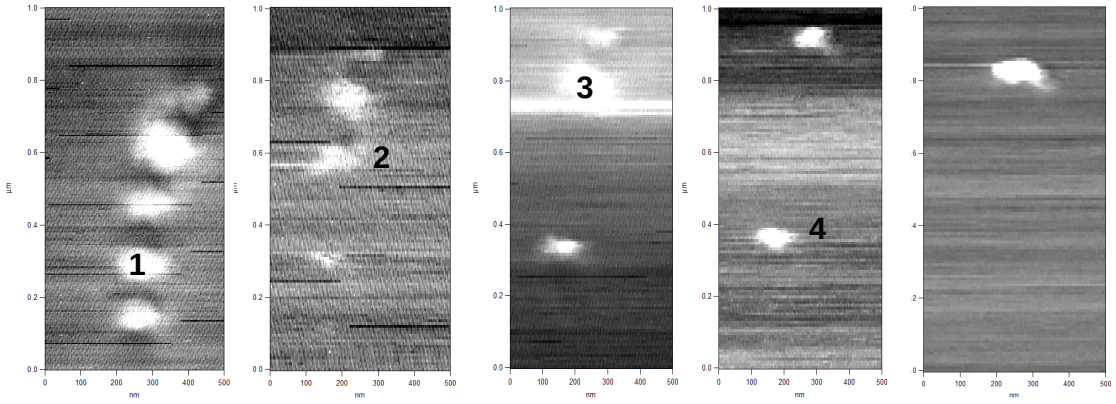

(e)

Figure 6.9: Scanning gate microscopy of parallel point contacts being cut. Optical scale bar 10 µm. Details in text.

the tip passes a second time over the sample, but at a fixed height above, following the profile of the surface. During this second scan a voltage is applied to the tip making it act as a local gate. The conductance is simultaneously measured and plotted as a function of position in the five scans. Since most of the voltage drop and the highest current density is at the constriction, when the tip passes on top and locally dopes it, the conductance is strongly modified. These shifts in conductance are shown by the white blobs located at the constrictions. Locally changing the carrier density elsewhere does not have an effect as the current density away from the constriction is relatively small. Going from left to right, four of the point contacts are cut by LAO. The 20 nm constriction is the last one to remain in the fifth scan. This point contact in the first scan appears faint and has the smallest contribution to the total current. This is expected as it is the narrowest constriction with the largest effective resistance. Note that there is an offset between images. This is due to drift over the small scan area. In Fig. 6.9(d) the conductance is monitored as each point contact is cut, going from top to bottom (curves have been offset). The first cut has a minimal effect on the conductance as expected from the removal of one resistor from a set of equivalent ones in parallel. However as more and more point contacts are remove, the conductance must inevitably go down. This is the case with the last cut resulting in a shift in conductance more than twenty times the first. When the 80 nm constriction is removed in cut 3 the conductance decrease is because this is the widest of the point contacts.

6.2.3 Discussion

The smooth dependence of the conductance on the constriction width can be understood by assuming diffusive conduction and solving the Laplace equation for the device geometry. This can be done numerically using a partial differential equations solver but another technique was used. Since the device shape is roughly a polygon, the technique of conformal mapping can be applied [114]. Conformal mapping allows solving the Laplace equation by finding a complex analytic function which maps the device geometry onto a rectangle. There are dictionaries of such transformations [92] developed for solving electrostatics problems before the advent of computers. If the function is analytic, it satisfies the Laplace equation and so does its inverse. This means that one can use the inverse transform applied to the simple isopotentials of the rectangle to obtain the more complicated isopotentials of the desired device. In addition the aspect ratio L/W of the rectangle given by the forward transform is the resistance of the original device. That the transform is analytic ensures that the derived isopotentials are correct and by construction so are the boundaries. In the case of a closed, or bounded, geometry such as the point contact a closed form expression for the transform cannot be obtained, but an integral expression can be easily written. These are called Schwarz-Christoffel maps and the integral expression can be calculated rapidly numerically. The advantage of using the Schwarz-Christoffel transform instead of the partial differential equation is the large decrease in computation time when the solution is required for a continually varying geometry. In contrast to a PDE solver, there is no mesh which needs to be recomputed and refined for each geometry. Only coefficients in the integral

Schwarz-Christoffel transform corresponding to the polygon vertices need to be modified. Software to calculate the transform under MATLAB is available for free from T. A. Driscoll, SC Toolbox.

The solution is plotted in Figure 6.10 for several different idealized point contact geometries. The geometry is indicated in Fig. 6.10(a). The black lines are twenty equally spaced isopotentials (vertically oriented) and field lines (horizontally oriented). If the left edge of the geometry is taken at potential $V = 1$ and the right edge $V = 0$, then the spacing between potentials is $V = 1/21 \approx 0.05$. The number of isopotentials contained between any two points divided by twenty is roughly the fraction of the entire device resistance that would be measured by two voltage probes at those points. In the series of plots (b)-(g), which decrease in the width w from left to right, the isopotentials are seen to congregate on the point contact. One can see that for the smallest point contact, Fig. 6.10(g) with $l = 0.01, w = 0.001$, all of the voltage drop occurs in the point contact since no isopotentials are visible. The geometry comparable to the smallest point contacts fabricated in graphene by the LAO technique is Fig. 6.10(f), where $l = w = 0.01$ and $w/W \approx 0.01$. In the actual devices, the sheet width is roughly 10 µm and the constriction dimension is 100 nm, giving the same ratios l/w and w/W.

The aspect ratio of the rectangle to which a given device geometry maps conformally is called the conformal modulus. It is equal to the normalized square resistance–the unit square has resistance one and a rectangle with aspect ratio L/W has resistance L/W. The unitless conductance, g, which is the inverse of the conformal modulus r is given for the different geometries of Fig. 6.10. The smallest point contact, Fig. 6.10(g), has the lowest conductance, $g = 0.07$, and this is the conductance that would be measured were the conductivity of the material $1/\square$. Looking at Fig. 6.10(e) with $l = 0.01, w = 0.1$, a cut constricting current to a region one-thousandth the area of the entire square and one-tenth the width, the conductance $g = 0.44$ is only about half that before the cut! This is a remarkable and counterintuitive result[1]. Our intuition leads us to believe the conductance will depend on the width w of the cut from a naive expectation that such a cut will also sever the current flow lines. This would indeed be the case for a quasi-1D situation consisting of many resistors in parallel where the current could not bend and flow through another path. This of course is not the case for a true 2D conductor and the situation is more complicated.

To understand what occurs in our geometry and fit the measured data over the entire cut range with an analytic formula, the work of P.M. Hall titled "Resistance calculations for thin film patterns" is extremely useful [67, 68]. With conformal mapping he obtained the resistance of various thin film conducting rectangles modified by adding or removing regular geometric shapes. In the limit where the rectangle length is infinite, he determined analytically the difference in the resistance of the sheet with and without the geometric modification. The modification he considered that matches this experiment is a nick at the side of the rectangle that can span the whole width. He treats the nick as infinitesimally

[1]The author's colleagues were not convinced until he measured the resistance of a partially scratched thin metal film on a glass slide!

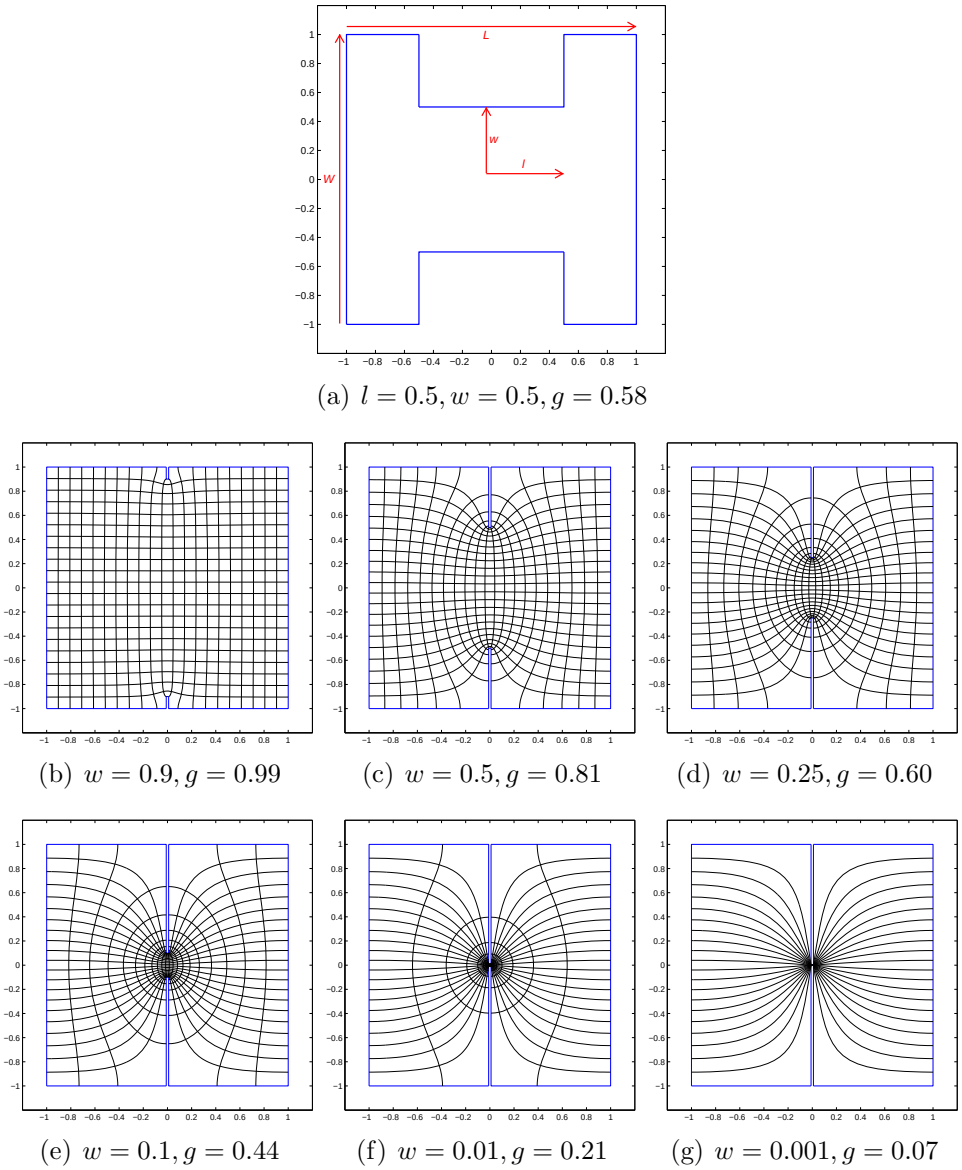

(a) $l = 0.5, w = 0.5, g = 0.58$

(b) $w = 0.9, g = 0.99$ (c) $w = 0.5, g = 0.81$ (d) $w = 0.25, g = 0.60$

(e) $w = 0.1, g = 0.44$ (f) $w = 0.01, g = 0.21$ (g) $w = 0.001, g = 0.07$

Figure 6.10: Solution to the Laplace equation for a classical point contact. Geometry shown in (**a**). Equally spaced isopotentials (vertically oriented) and field lines (horizontally oriented) are shown in black. The series (**b**)-(**g**) shows the effect of decreasing the width w while keeping $l = 0.01$ constant. The unitless, normalized conductance g is the conductance of the device geometry assuming a unitless material conductivity of $1/\square$ and is the inverse of the conformal modulus. Created using Schwarz-Christoffel conformal mapping software (SC Toolbox).

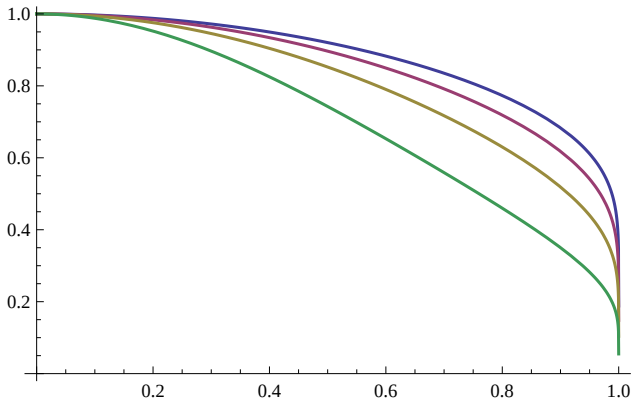

Figure 6.11: Normalized fit to conductance versus cut distance data on graphene point contact devices fabricated by local anodic oxidation.
The function plotted is $1/(N + \log\sec(x\pi/2)$, where $N = L/W$ is the number of squares in the pristine uncut sheet. $N = 1, 2, 3, 4$ is plotted (from bottom to top).

narrow, corresponding to $l \to 0$, which is compatible with our case because l is much smaller than the inter-electrode separation L. When the distance between the electrodes and the location of the geometric modification is long on a characteristic length scale set by the modification, he showed that the errors in the "infinite rectangle" approximation are small. For this reason, we can compare his formula obtained for the resistance of an infinitely long rectangle with a nick at one side with the conductance vs cut distance data obtained on graphene point contacts. The dimensionless formula for the conductance is

$$g(x) = \frac{1}{N + \log\sec(\pi x/2)} \tag{6.2}$$

where the dimensionless conductance with $x = 0$ (no cut) is $g(0) = 1/N = W/L$ and in terms of the normalized spatial coordinate x, the width of the sheet is $x = 1$ such that $g(1) = 0$. N is the aspect ratio of the sheet, L/W, or equivalently the number of squares in the context of resistance per square. The actual conductance is given by $\sigma g(x)$ with σ the conductivity. The aspect ratio N is the only parameter in the equation and it is not fitted for since it is measured from the device images. Figure 6.11 plots this function for different square resistances $N = 1, 2, 3, 4$. It is almost identical under scaling both the x and g axes to the data obtained experimentally in Figs. 6.7 and 6.8 for the given device aspect ratio. There are no fitting parameters. The graphene sheet on a substrate even at the smallest length scale of the experiment, 100 nm, behaves as a diffusive conductor obeying the Laplace equation. With conformal mapping, the conductance dependence on the point contact geometry can be explained entirely.

Chapter 7

Superconducting Quantum Interference Device

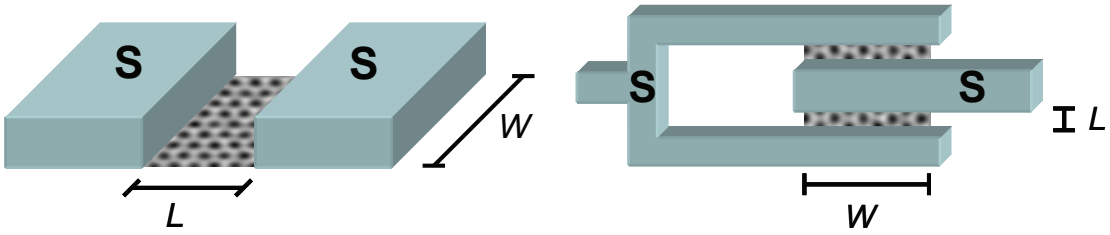

(a) Graphene Josephson junction (b) Graphene SQUID

Figure 7.1: Graphene-superconductor hybrid device geometries.

7.1 Introduction

In the previous chapters, the two-terminal conductance of graphene devices was explained theoretically in the ballistic limit and measured experimentally and analyzed in the diffusive limit. The dependence of the conductance on carrier density, or indirectly the back-gate voltage $G(V_g)$, as well as geometric properties or other considerations allow identifying the transport regime. To aid in determining whether transport is ballistic, one can make measurements that go beyond the conductance. Several possible signatures of ballistic transport in graphene were discussed in Chapter 5, where graphene-superconductor hybrid geometries such as in Figure 7.1 were considered.

By having closely spaced superconducting electrodes instead of normal metallic ones, an additional probe of the transport regime can be introduced: ϕ, the phase difference between the two superconducting electrodes. In a sense each electrode in the superconducting state

can be described by a macroscopic wavefunction and ϕ is the difference in their phases. That this type of junction would carry a finite current at zero voltage, called supercurrent, was predicted by Brian Josephson and an elegant derivation of the effect can be found in Feynman's lecture series, Vol. 3, Ch. 21 [53]. Such a Josephson junction with graphene is called an SGS junction, for superconductor-graphene-superconductor, and is represented in Fig. 7.1(a). The condition that a supercurrent can flow is that the inter-electrode separation L be less than the zero-temperature superconducting coherence length ξ_0, which measures the mean separation between two electrons in a Cooper pair and also sets the length scale over which the superconducting wavefunction can vary appreciably. For a superconductor such as aluminum, ξ_0 is on the order of a micron.

By putting two Josephson junctions in a loop as in Fig. 7.1(b), called a dc superconducting quantum interference device (dc-SQUID), one can control the phase difference $\Delta\phi = \phi_1 - \phi_2$ with an applied magnetic flux. The transport parameter is then $I_c(V_g, \Delta\phi)$ instead of $G(V_g)$, where I_c is the critical current, the maximum current that can be passed at zero voltage. The variation in the critical current with $\Delta\phi$ depends on the properties of the charge carriers in the *weak link*, the material between the superconducting electrodes, and can serve to identify the transport regime.

Josephson determined that for a weak link consisting of a thin insulating oxide, called a superconducting tunnel junction, the current-phase relation is

$$I(\phi) = I_c \sin(\phi). \tag{7.1}$$

Details of the Josephson effect and its applications can be found in Tinkham's superconductivity book [144]. We can reproduce Josephson's equation from the general equation stated in Chapter 5 in terms of the transmission coefficients T_m, Eq. 5.27,

$$I(\phi) = \frac{e\Delta_0}{\hbar} \sum_{m=0}^{M} \frac{T_m \sin(\phi)}{\sqrt{1 - T_m \sin^2(\phi/2)}}$$

by substituting a constant transmission $T_t \ll 1$ describing a low-transparency tunnel interface. The zero-temperature energy gap of the superconductor comprising the electrode is Δ_0, related to the superconducting transition temperature T_c by $\Delta_0 \approx 1.764 kT_c$ for common type-1 BCS superconductors such as aluminum. Since the transmission per channel is small, the term in the denominator is approximately unity and we obtain Eq. 7.1 with $I_c \approx e\Delta_0 M T_t/2\hbar = \pi\Delta_0 G_n/2e$, where G_n is the normal state resistance $G_n = 2e^2/h \cdot MT_t$. This gives the product $I_c R_n = \pi\Delta_0/2e$, which is the exact Ambegaokar-Baratoff result [144] for zero temperature.

Given the current-phase relation $I(\phi)$, one can calculate the dependence of the current on the phase difference $I_S(\Delta\phi)$ for the SQUID in Fig. 7.1(b) with two identical junctions by summing the currents through each one,

$$I_S(\phi_1, \phi_2) = I(\phi_1) + I(\phi_2), \tag{7.2}$$

and then expressing it in terms of the phase difference $\Delta\phi = \phi_1 - \phi_2$ and sum $\theta = \phi_1 + \phi_2$,

$$I_S(\Delta\phi, \theta) = I\left(\frac{\theta + \Delta\phi}{2}\right) + I\left(\frac{\theta - \Delta\phi}{2}\right). \tag{7.3}$$

The current is then maximized over θ to give the SQUID critical current. In the case of a tunnel junction with $I(\phi) = I_c \sin(\phi)$, this gives $I_S(\Delta\phi) = 2I_c|\cos(\Delta\phi/2)|$. For other current-phase relations, the SQUID critical current modulation can be determined numerically. It is shown in the case of a ballistic graphene SQUID in Chapter 5, Fig. 5.9, along with the gate voltage dependence. Indicators of ballistic transport in the shape of this modulation curve are also discussed there.

To relate the phase difference $\Delta\phi$ to the applied flux Φ, we note that in order for the superconducting condensate wavefunction to be single valued over the loop containing the two Josephson junctions, we must have $\Delta\phi = 2\pi\Phi/\Phi_0 + 2\pi n$ for integer n, where Φ_0 is the flux quantum $h/2e$, 2.07 fWb. The flux term in this expression comes from the fundamental fact that a quantum particle acquires a phase proportional to the line integral of the vector potential A along the path it travels [53]. The integral over a closed loop of the vector potential is just the magnetic flux Φ and since it is applied externally, this constrains the phase difference $\Delta\phi$ such that the total phase acquired over the loop is a multiple of 2π. This is why this device is called a superconducting interferometer. In the case of a tunnel-junction dc-SQUID the supercurrent modulation becomes $I_S(\Phi) = 2I_c|\cos(\pi\Phi/\Phi_0)|$. With loop areas of 10 µm, the field modulation period is 207 µT which is easily applied by a small coil electromagnet.

In the following, the fabrication and operation of a superconducting quantum interference device formed by a single graphene sheet contacted with aluminum/palladium electrodes in the geometry of a loop is described. The supercurrent in this device is modulated via an applied magnetic field in addition to the gate voltage. The results are analyzed with both a ballistic graphene and diffusive tunnel-junction model and fit some of the characteristics of both, showing that graphene SQUIDs are a useful probe of electronic transport in graphene.

7.2 Experimental Details

Graphene samples are produced by mechanical exfoliation of graphite flakes on oxidized silicon wafers (SiO_2(285 nm)/Si++) (Ch. 2) and devices fabricated using conventional high-resolution electron-beam lithography (Ch. 4). The two graphene Josephson junctions that form the SQUID are patterned side by side on the same graphene sheet in a tuning fork geometry. A schematic is shown in Fig. 7.1(b) which also defines the junction geometry parameters length L and width W. Graphene samples were selected to have rectangular shape with widths between 4 µm to 15 µm. The electrode gap length was patterned to be as short as possible and was at or below 100 nm. Actual device images, including optical and scanning electron microscopy, are shown in Figure 7.2. Since the active area of the device is small, multiple SQUIDs are fabricated on the same sample as in Figs. 7.2(a)-(c). In some

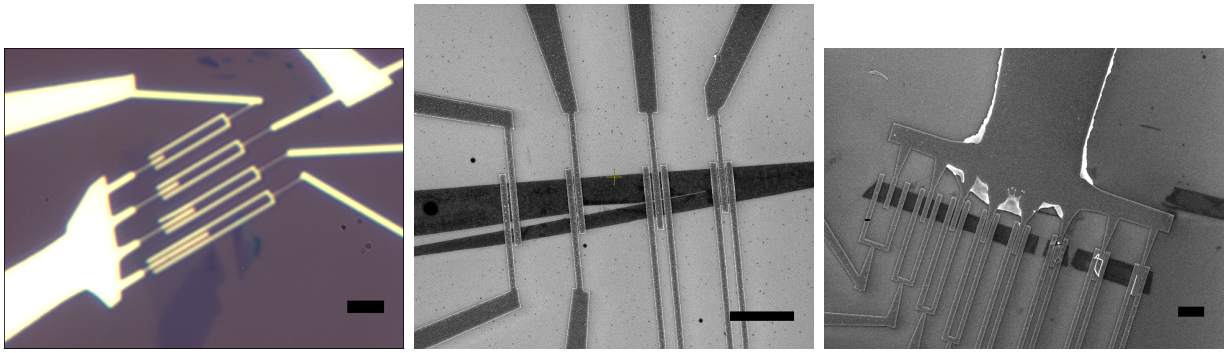

(a) Optical (b) SEM (c) SEM

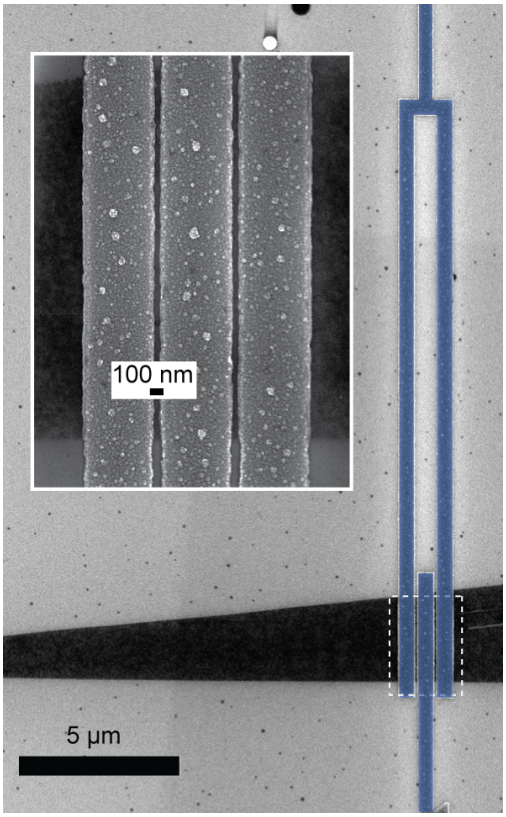

(d) SEM, single SQUID, false colored

Figure 7.2: Graphene superconducting interference devices. Scale bars 5 µm unless indicated.

cases a common drain was patterned to maximize the number of devices per sample, but in this case noise is increased. The loop area was patterned to be about $10\,\mu m^2$, equivalent to an applied field periodicity of $207\,\mu T$.

Fig. 7.2(d) shows a close-up of one SQUID, with the inset showing the spacing between the electrodes. As the two Josephson junctions are fabricated side by side, the electronic properties of the graphene sheet such as doping and mobility should be similar at each junction. In addition no patterning and etching steps are necessary to make the junction widths identical as exfoliated samples generally have constant widths over the approximately $2\,\mu m$ length of the two junctions. The width of the electrodes is $0.5\,\mu m$ to minimize flux pinning and they extend onto both sides of the graphene sheet. Since adhesion to graphene is poor without the use of chromium (Sec. 4.2) anchoring the electrodes at both ends to the SiO_2 substrate helped to improve contact to the graphene. Without this anchoring, leads would often detach from graphene during liftoff. The gaps between the electrodes which define the junctions are patterned to be very short ($L = 50\,nm$) and wide ($W > 1\,\mu m$) with an inverse aspect ratio W/L of at least ten. The gaps are made short in an attempt to reach the ballistic transport limit where the mean free path $\ell > L$. Wide junctions help obtain large critical currents which should reduce the effect of thermal noise. With an aspect ratio of at least ten one can make the simplifying assumption in calculations that the mode spacing is continuous (Ch. 5).

Exposure tests should be performed prior to lithography (Sec. 4.1) because with short gaps and wide, closely spaced contacts, the electron proximity effect is important and proper dosage will be reduced relative to well spaced patterns. Dosing effects on a SQUID test geometry are shown in Fig. 4.4. Once the devices are patterned and the resist developed, a $3\,nm$ interfacial layer of palladium, followed by a $50\,nm$ thick aluminum layer is deposited by electron-beam evaporation or thermal evaporation. Details of evaporation can be found in Sec. 4.2. Though palladium is a normal metal, superconducting charge carriers from the aluminum top layer can transit through this thin layer which is used to obtain a reliable, low resistance contact to the graphene sheet [72, 60]. The Si^{++} layer serves as an electrostatic back gate common to both junctions and must be highly degenerately doped ($1\,m\Omega\,cm$ to $5\,m\Omega\,cm$) to function at dilution temperatures.

Figure 7.3 shows the experimental setup, including cryostat, sample box, and readout electronics. The cryostat, shown in Fig. 7.3(a), is a cryogen-free dilution refrigerator (Veri-Cold, now Oxford Instruments) with a base temperature of $T \sim 20\,mK$. It is equipped with shielded, differential wiring (both resistive and superconducting) filtered with multiple stages of copper powder (for frequencies $>1\,GHz$) and discrete element low-pass filters (for frequencies $0.01\,MHz$ to $100\,MHz$) [15]. The sample box, Fig. 7.3(b), consists of a copper box with thick (1/8-1/4") walls to attenuate low frequency noise; a PC-board with 25 connections filtered with surface-mount LCR filters and a chip mount or bonding surface for sample connections; and a superconducting coil mounted to the backside of the PCB used to apply magnetic fields. Multi-filamentary niobium-titanium wire is wound into a solenoid (1300 turns) of 1/2-inch diameter resulting in a superconducting electromagnet with a field of $0.320\,G\,mA^{-1}$ at the surface and $0.185\,G\,mA^{-1}$ at a distance of 1/8-inch. Two

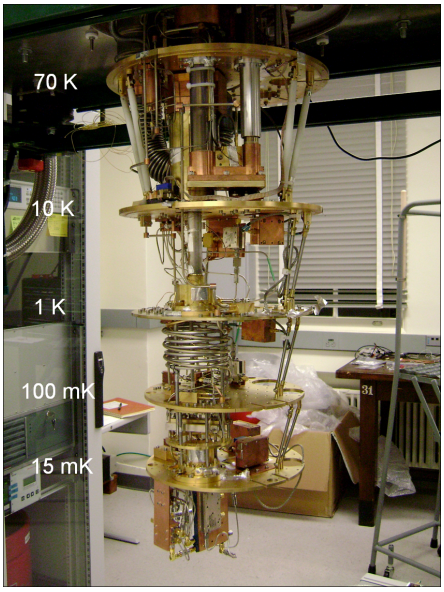

(a) Dry cryostat

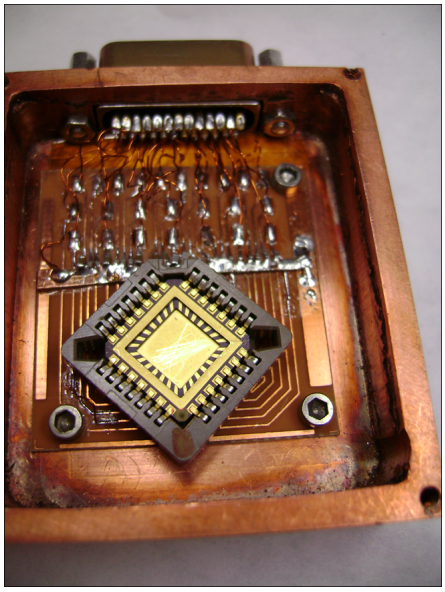

(b) Sample box

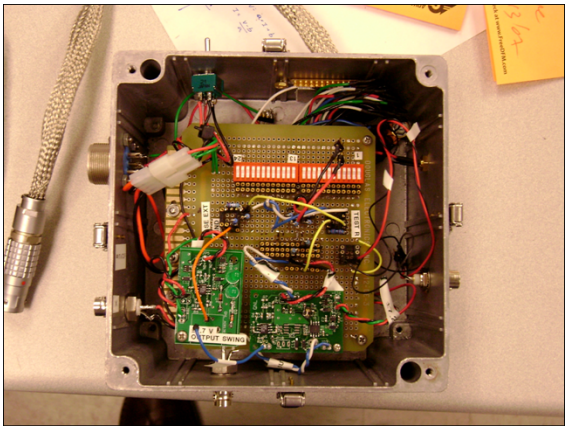

(c) Electronics

Figure 7.3: Experimental setup: cryostat, sample box, and readout electronics.

aluminum/silicon wires are wirebonded for redundancy from the PCB to each of four pads per device. Two pads serve as current source and the other two as voltage sense providing for a pseudo-fourwire measurement since the electrodes join together before reaching the sample. In some cases as a result of lithography error or bonding failure sense and source are bonded on the same pad. This makes for a pseudo-fourwire measurement with the sense point even further back, at the bonding pad. Care must be taken when wirebonding not to destroy the device, create a short in the gate, or run out of bond-pad space without making a successful bond. Adequate practice, good grounding, and proper bonding parameters are necessary. The sample box is mounted to the mixing chamber of the cryostat at $T \approx 20\,\mathrm{mK}$.

The amplifier and readout electronics is comprised of a low-frequency, low-noise amplifier/buffer mounted at room-temperature inside the cryostat (not shown) connected to an external box with additional amplifiers, buffers, voltage dividers, bias resistor, and switchboard (Fig. 7.3(c)). An arbitrary signal generator is used to supply DC bias and low-frequency AC signals to the box, which buffers, voltage divides, and passes it through a bias resistor delivering current of 0.01 µA to 10 µA to the filtered cryostat lines. A voltage preamplifier amplifies the voltage sense signal, buffers it, and delivers it to the output of the box. A National Instruments DAQ board is used to digitize the output signal and is interfaced to a data acquisition computer with LabView. The gate voltage signal is filtered in the box and delivered through unfiltered lines to the sample. The current bias for the electromagnet (up to roughly 50 mA or 1.5 mT) is passed through independent copper lines down to the 4 K plate and then through Nb-Ti wire to the sample box.

7.3 Results

Figure 7.4 shows the gate-voltage dependence of the resistance of the device in Fig. 7.2(d) above the aluminum electrode transition temperature and the transition to the zero resistance state as the temperature is lowered. All subsequent results will be on this device unless stated. The $R(V_g)$ characteristic Fig. 7.4(a) shows a sharp peak at the Dirac point at $V_{d1} = 1.25\,\mathrm{V}$ and another smaller hump at $V' \approx 33\,\mathrm{V}$. In addition to these two resistance maxima, there is an oscillatory modulation of the resistance away from the humps. It is difficult to fit this curve as described in Sec. 4.2.3 for two reasons. Since the two devices are in parallel, unless the junctions are identical, the fit contains twice as many parameters as for a single junction. The parameters include the contact resistances, which must be non-negligible since the device resistance is extremely low, as well as the aspect ratios for each junction, their respective Dirac points, mobilities, etc. An attempt to match the curve with a single junction fitting function does not work and with twice the parameters it is difficult to have confidence in the results. In addition electrode doping effects are likely since the gap is so short [72, 49]. Interestingly, the shape of the conductance-gate voltage characteristic, with a Dirac point near zero and another, wider hump farther away is similar to the calculations presented in [49]. However in their model they treated the case of a doped graphene sheet in contact with intrinsic graphene electrodes, and their calculations for the metallic electrode

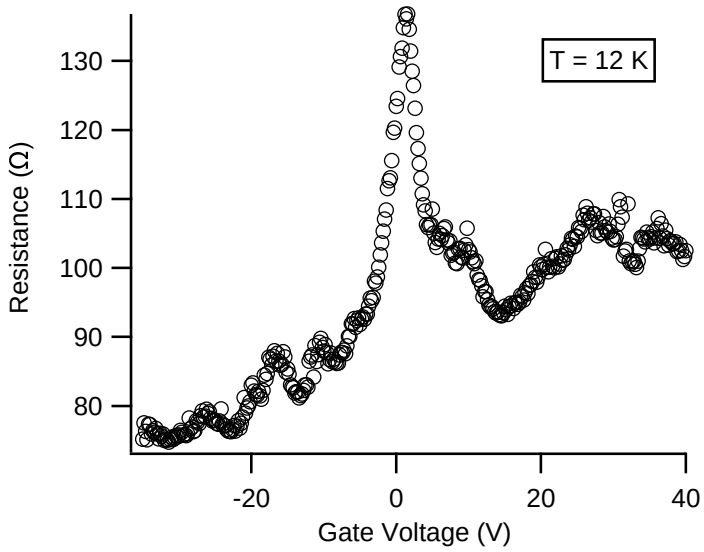

(a) $R(V_g)$ at $T = 12\,\mathrm{K}$

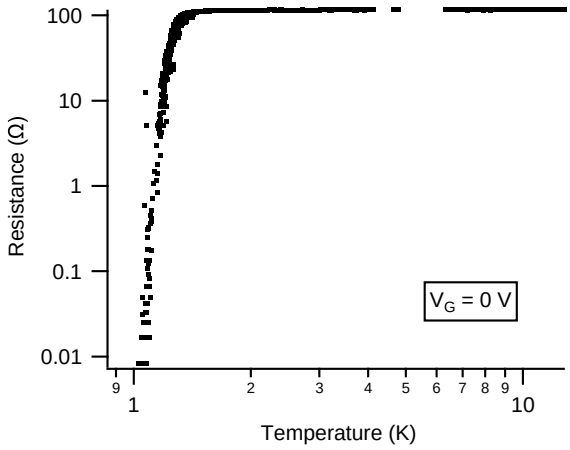

(b) Log-log cooldown plot

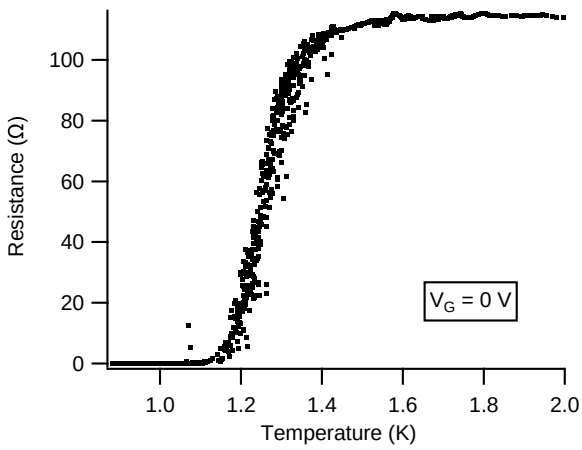

(c) $R(T)$ at transition

Figure 7.4: Transition to zero-resistance state of graphene superconducting quantum interference device and resistance vs. gate voltage in the normal state above transition.

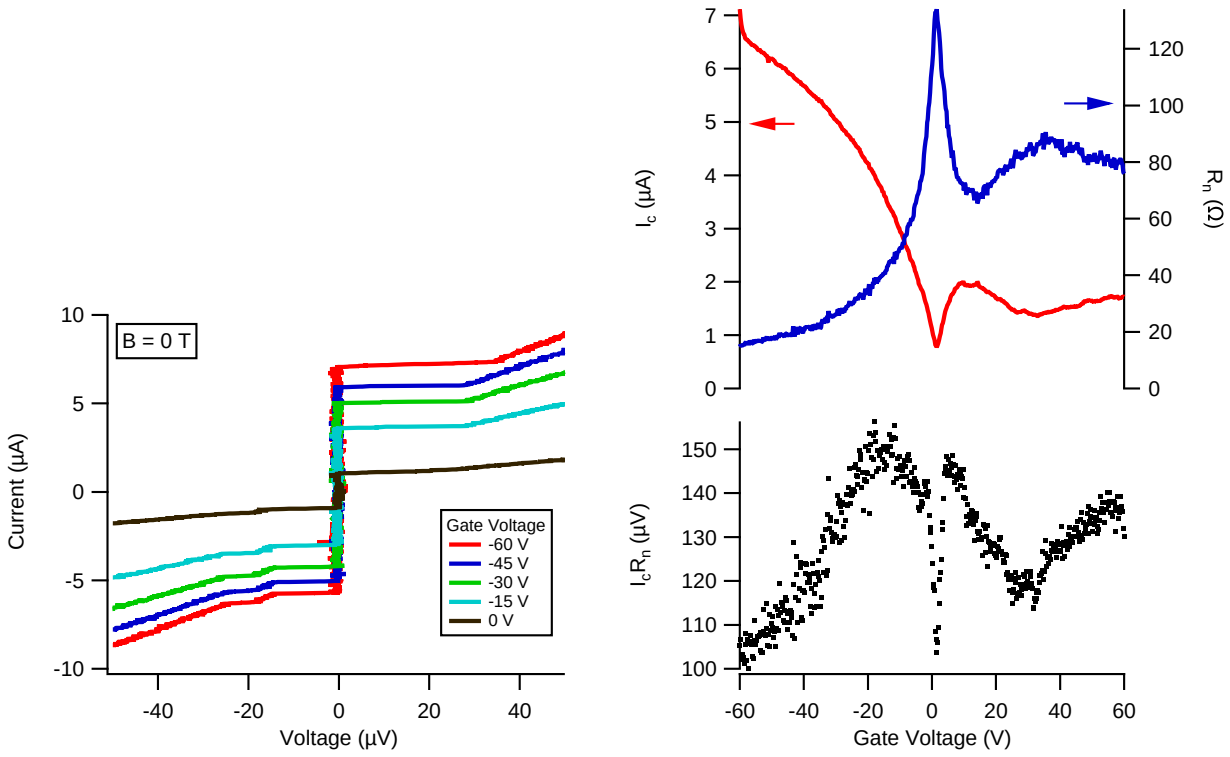

(a) IV curves at different V_g

(b) Critical current and I_cR_n product

Figure 7.5: Transport properties in supercurrent-carrying state of graphene superconducting quantum interference device ($T = 20\,\mathrm{mK}$).

case do not have two humps.

In Figs. 7.4(b) and (c) the resistance of the same device is plotted, both as $\log(R)$ vs. $\log(T)$ across a large range and as $R(T)$ across the aluminum/palladium electrode transition temperature T_c ~1.1 K. Between 2 K to 10 K there is a constant normal state resistance and then near 2 K the dip to the zero-resistance state begins. The transition is not sharp and occurs between 1.1 K and 1.8 K. The broadness of the transition and the enhanced conductivity above T_c may be related to fluctuation or finite-size effects but does not fit the Azlamasov-Larkin theory [144]. That the resistance falls to zero close to T_c is a sign of a strong proximity effect [58] and should be a result of the short junction length as well as having high transparency contacts due to the thin palladium interfacial layer. Previous experiments on graphene Josephson junctions with aluminum contacts [40] but larger gaps (>200 nm) showed the emergence of a supercurrent only at $T < 0.2\,\mathrm{K}$. Experiments with long superconductor-normal metal-superconductor SQUIDs [5] have shown that the onset of proximity-effect induced superconductivity occurs at much lower temperatures than the superconducting transition of the electrodes.

Figure 7.5 shows the transport properties at base temperature, $T = 20\,\mathrm{mK}$, at zero

applied magnetic field. From the IV curves at different gate voltages, there is a clear supercurrent with the transition to the finite voltage state occurring at critical currents between about 1 µA to 7 µA. The sample is current-biased, with the current swept toward positive values. The hysteresis in switching current is not shown and two retrapping events are seen at negative bias which can be attributed to electrode heating effects as they do not show gate voltage dependence [110, 30]. In the top panel of Fig. 7.5(b), the critical current has been extracted by averaging the transition threshold from a series of IV curves and plotted as a function of gate voltage (red curve). The modulation of the critical current I_c with gate voltage is similar to that of a 2DEG Josephson field-effect transistor [131]. However, due to the finite minimal resistivity of graphene, the critical current cannot be turned off completely. The values for I_c are one-thousand times larger than what has been observed in carbon nanotube Josephson junctions [29, 78] and the critical current density I_c/W is as high as 1 A m^{-1} per junction, roughly a factor of ten larger than previous graphene Josephson junctions [42, 69]. As the I_cR_n product must be on the order of Δ_0, the critical current increases as the gate voltage is shifted away from the Dirac point V_{d1}. The critical current roughly follows the inverse of the $R(V_g)$ plot Fig. 7.4(a). R_n is plotted in blue in the top panel of Fig. 7.5(b) along with I_c and follows the shape of $R(V_g)$ except for an offset most likely related to a contact resistance in the normal state. R_n is extracted by computing the slope of the IV curves at a bias current intermediate between the last multiple Andreev reflection and the transition of the electrodes to the normal state (explained below). Finally the product I_cR_n is plotted in the bottom panel of Fig. 7.4(b). Since the two junctions are in parallel, this product can be related to the individual $I_{ci}R_{ni}$ by

$$I_cR_n = (I_{c1} + I_{c2})\frac{R_{n1}R_{n2}}{R_{n1} + R_{n2}} = \frac{(I_{c1}R_{n1})R_{n2} + (I_{c2}R_{n2})R_{n2}}{R_{n1} + R_{n2}} \tag{7.4}$$

which is a weighted sum of the two $I_{ci}R_{ni}$. In the case where the product $I_{ci}R_{ni} = V_0$ is the same for each junction, the total $I_cR_n = V_0$ as well. However if the $I_{ci}R_{ni}$ are unequal but comparable, then only in the limit of large asymmetry will I_cR_n reduce to the $I_{ci}R_{ni}$ product of the least resistive member. Since the junction asymmetry, from subsequent data, is intermediate, it is difficult to interpret the I_cR_n product as one can with a single Josephson junction [40, 69].

Figure 7.6 is a map of differential resistance dV/dI versus bias current (y-axis) and gate voltage (x-axis). The data was obtained by numerically differentiating a series of averaged IV curves measured at gate voltages in the range $|V_g| < 60$ V. The central dark region corresponds to the zero-voltage state. The SQUID critical current is demarcated by the yellow dashed line, and is equivalent to the $I_c(V_g)$ plot in the top panel of Fig. 7.5(b). Transport processes which involve multiple reflections of charge carriers at the superconductor/graphene interface result in the conversion of electrons and holes to Cooper pairs (multiple Andreev reflection, MAR) and give rise to a subharmonic gap structure [91]. These MAR processes occur at sub-multiples of an energy gap $2\Delta_g$ and are shown by three white dashed lines which are constant voltage contours at $2\Delta_g/ne$ for integer n. The contours were determined as follows: first the IV data was inverted to determine voltage at a given current bias and

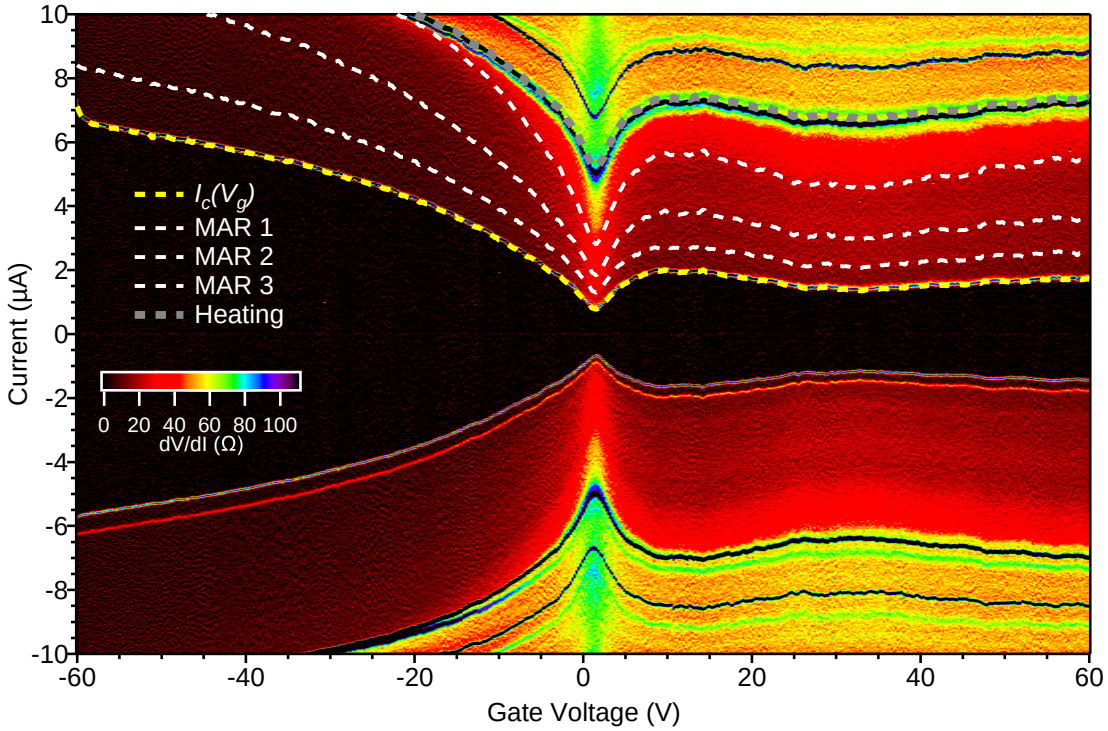

Figure 7.6: Map of differential conductance dV/dI as a function of source-drain bias current and gate voltage.

gate voltage. Then voltages were selected whose contours on the dV/dI plot matched the dip preceding the faint white differential resistance peaks. These are more easily visible in the bottom half of the map at negative current bias. These dips correspond to maxima in the differential conductance and indicate the resonance condition for the multiple Andreev reflection process. The one labeled "MAR 1", for $n = 1$, occurs at $2 \cdot \Delta_g/e \approx 150\,\mu\text{V}$; "MAR 2", $n = 2$, at $1 \cdot \Delta_g/e \approx 80\,\mu\text{V}$; and "MAR 3", $n = 3$, at $2/3 \cdot \Delta_g/e \approx 50\,\mu\text{V}$. The effective gap Δ_g is approximately $75\,\mu\text{eV}$ and is reduced relative to $\Delta_0 = 1.7654kT_c \approx 167\,\mu\text{eV}$ from the superconducting transition at $T_c \approx 1.1\,\text{K}$. This discrepancy may be due to sample heating effects in the finite voltage state which reduce the effective gap. We can estimate the effective temperature T' from the mean-field dependence on the gap by $\Delta_g/\Delta_0 \approx 1.74(1 - T'/T_c)^{1/2}$ to obtain $T' \approx 1\,\text{K}$ which is surprisingly close to the transition temperature. It is likely that with the large current densities being passed through the graphene sheet, heating is significant. This effect has been studied in detail in SNS junctions [30]. The heating hypothesis would also explain why the MAR features disappear progressively for large negative gate voltages ($V_g \lesssim 5\,\text{V}$) when the critical current rapidly increases. Since the power scales as I^2R_n with R_n roughly constant the heating will be more significant at larger currents. Despite heating effects, the small value of the effective energy gap is comparable to that found for similar Al/Pd contacts on nanotubes [29].

There is an additional contour line that is indicated in the differential resistance plot as "Heating" and at which there is a peak in the dV/dI. This line corresponds to a constant power contour at $P_c = 2.5\,\text{nW}$, or a power density of $1.3\,\text{W}\,\text{cm}^{-2}$ taking the area between the electrodes. At this level of power dissipation in the graphene, the contacts are sufficiently heated to be driven normal and the discontinuity in the IV curves result in a peak in the dV/dI map. It is not surprising that MAR features disappear as one approaches this critical power contour. The normal state resistance $R_n(V_g)$ from Fig. 7.5(b) is determined by inverting the differential resistance at points between the last MAR feature at constant voltage $2\Delta_g/e$ and the P_c contour line.

At negative biases, one can also identify the MAR features and the critical power peak in the differential resistance. In addition there are two switches in voltage at negative current bias and these are the palladium contact effects mentioned earlier that lack gate dependence.

Next the effects of applying a magnetic field are presented. Figure 7.7(a) shows the IV characteristic at fixed gate voltage, $V_g = 0\,\text{V}$, for different values of applied flux $\Phi/\Phi_0 = 0, 1/8, 3/8, 1/2$. As described above, the magnetic flux through the SQUID loop induces a phase difference between the two Josephson junctions and interference between their supercurrents results in a variation of the total critical current with applied field. In a symmetric SQUID with no loop inductance the critical current varies as $I_S(\Phi) = 2I_c|\cos(\pi\Phi/\Phi_0)|$ and is maximum at $\Phi = 0$ and zero at $\Phi = \Phi_0/2$ with a period $\Phi_0 \approx 2.07\,\text{fWb}$. In the IV curve, the maximum supercurrent occurs at $\Phi = 0$ because offsets due to stray fields have been corrected. The value of the maximum critical current at zero gate voltage and zero applied flux is $1.60\,\mu\text{A}$. At $\Phi = \Phi_0/2$, the critical current is reduced to $1.17\,\mu\text{A}$, only 73% of its maximum value. This indicates that the junctions are highly asymmetric, as the maximum critical current for one junction cannot completely cancel out the maximum critical current

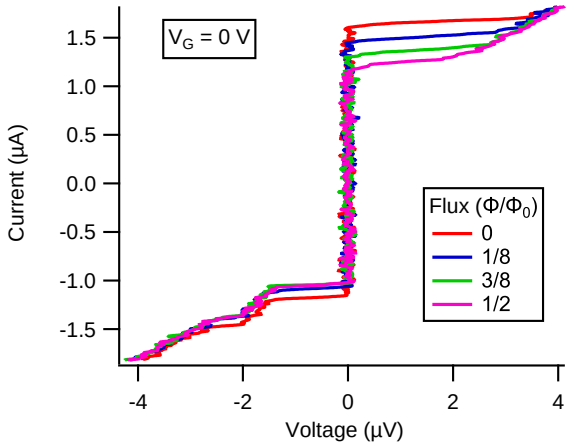

(a) IV curves at different magnetic flux

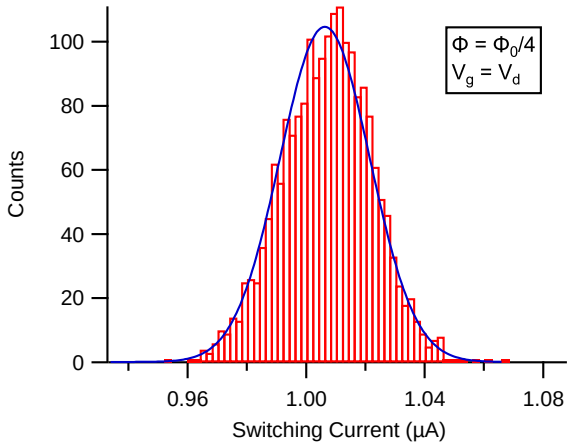

(b) Switching histogram at $\Phi = \Phi_0/4$, $V_g = V_d$

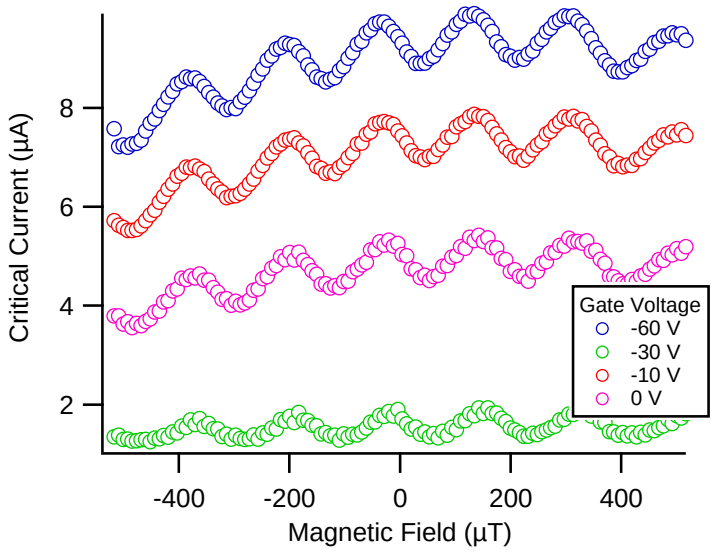

(c) Flux modulation at different gate voltages

Figure 7.7: Magnetic flux modulation of critical current in graphene superconducting quantum interference device.

of the other junction.

In Fig. 7.7(b) a switching histogram is shown. The switching current, the point at which the SQUID develops a non-zero voltage, is collected for a large number of IV sweeps. The histogram of the distribution of switching currents can be fit with a Gaussian of mean 1.01 µA and width 22 nA, roughly 2% of the mean switching current. The true critical current I_0 is the upper limit of this histogram at zero temperature. In the preceding and ensuing discussion, what is referred to as the measured critical current is in actuality the mean switching current. In an ideal situation where the electronic temperature is equal to the bath temperature and both are much lower than the Josephson energy, $E_J = h\bar{I}_c/2e$, the form of the switching histogram is not Gaussian, but tilted toward I_0. This is because although thermal fluctuations can allow switching at lower currents than I_0, switching cannot occur higher than I_0. The details of switching histograms and using them to determine the "escape rate", which is inversely related to the lifetime of the zero voltage state, can be found in Fulton and Dunkleberger [55].

Fig. 7.7(c) shows the critical current modulation as a function of flux at several gate voltages including $V_g = 0$ V. The plotted current is the mean switching current determined as in Fig. 7.7(b) for all values of gate voltage and applied field. The sinusoid-like variation has a periodicity of $\Delta B \approx 190$ µT which implies an effective loop area $\Delta B/\Phi_0 \approx 11$ µm^2. This value is in good agreement with the geometric loop area of approximately 10 µm^2. The modulation depth is incomplete for all gate voltages. The absolute depth is larger at higher critical currents and is a minimum at the Dirac point. In addition to this asymmetry, there is a slight tilt in the direction of increasing field to the sinusoid-like modulation shape. This is indicative of inductance in the loop. Both the asymmetry and inductance will be discussed in detail in the next section.

Figure 7.8(a) shows the effects of changing both the magnetic field and the gate voltage on the critical current of the graphene SQUID. The tunability of the flux modulation depth and height with gate voltage implies a new kind of SQUID. The magnetometry properties of the unshunted graphene dc-SQUID can be characterized by two quantities. The first is the transfer function, or magnetometry gain, given by the maximum slope of the critical current vs flux, $dI_c/d\Phi(V_g)$. Because of the finite loop inductance, the maximum slope occurs at flux slightly higher than $\Phi_0/4$. The magnetometry gain is determined by differentiating along the flux direction plots such as Fig. 7.7(c) or Fig. 7.8(a) and determining the maximum value. In Fig. 7.8(b) it is plotted for several values of the gate voltage and follows the critical current dependence on gate voltage. This is the same device as previously but the characteristics, such as the Dirac point, have slightly changed as a result of thermal cycling. The magnetometry gain is minimum at the Dirac point (1.3 µA/Φ_0) and maximum at $V_g = -60$ V (4.0 µA). Although the gain in a standard dc SQUID can be adjusted by changing the flux bias, Φ, with the graphene SQUID it can be controlled with the gate voltage instead. The only possible advantage of gate voltage gain control is to be able to stay at $\Phi \approx \Phi_0/4$ in order to preserve the same dynamic range, the fractional flux range $\Delta\Phi/\Phi_0$ over which the gain will not vary appreciably. At $\Phi \approx \Phi_0/4$, the critical current modulation is the most linear and hence the slope constant over a wider range.

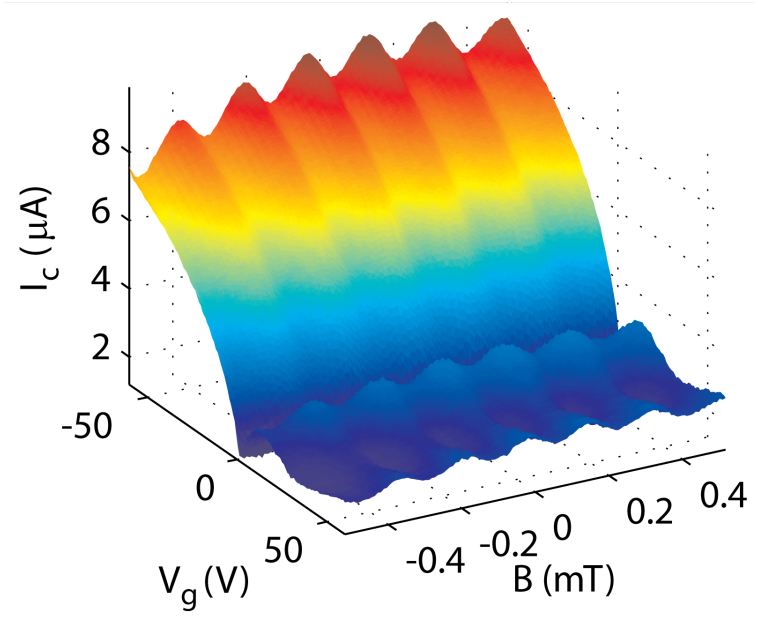

(a) Critical current variation with gate voltage and magnetic field

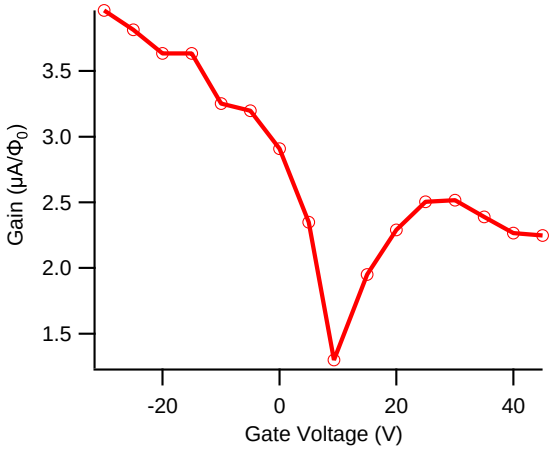

(b) Magnetometry Gain

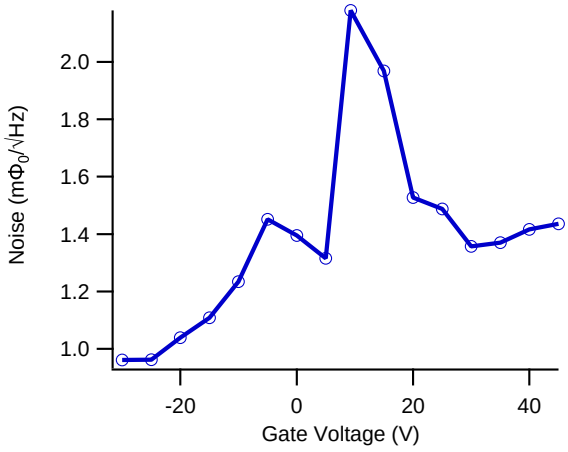

(c) Magnetometry Noise

Figure 7.8: Summary of graphene superconducting quantum interference device operation and application to magnetometry.

When the flux bias is changed in a conventional SQUID the dynamic range is reduced because of the sinusoidal nature of the critical current modulation. SQUIDs in magnetometry applications are often shunted with a resistor to convert the critical current to a more easily measurable voltage. In graphene SQUIDs inadvertently fabricated with such a shunt resistor (10 Ω to 100 Ω) a transfer function of 10-100 $\mu V/\Phi_0$ has been measured, comparable to that of typical resistively shunted dc SQUIDs [28].

The second quantity characterizing the graphene dc-SQUID is the magnetometry detection noise, which is the minimum amount of flux that can be detected in a 1 Hz bandwidth, given in units of $\Phi_0/\sqrt{\text{Hz}}$. This is shown in Fig. 7.8(c). A switching histogram such as Fig. 7.7(c) is used to determine the magnetometry noise. The width in amperes of the switching distribution at the maximum gain flux bias point $\Phi \approx \Phi_0$ is divided by the product of the gain and measurement bandwidth. This bandwidth is roughly 100 Hz for the construction of histograms. The noise for the graphene SQUID is in the $m\Phi_0/sqrt$Hz range, which is relatively high compared to typical values in the $\mu\Phi_0/sqrt$Hz range. The origin of this noise is not understood but it is likely that it comes from either improperly filtered gate voltage bias or magnetic field bias lines. At the Dirac point, the gain is minimized while the noise is maximized. Performance improves away from the Dirac point.

In Figure 7.9, the critical current modulation with magnetic field is shown for the previous device, as well as two others (b-c). At high magnetic fields, the flux can penetrate into the junction area of the SQUID where the graphene is sandwiched between electrodes. This flux penetration causes interference between the supercurrent flowing in each junction and reduces the critical current in a distinctive Fraunhofer pattern [144], similar to optical diffraction through a single rectangular slit. The first Fraunhofer-type pattern shown, Fig. 7.9(a), is a 2D map of IV curves versus applied magnetic field at $V_g \approx -60$ V for the previous device. The modulation of the switching current (for positive current bias) and retrapping current (for negative bias) has a slowly varying envelope. The pinch-off point for the envelope is somewhere near 2.8 mT which corresponds to an area of 0.7 µm^2. For the 3.8 µm width of the junctions, this corresponds to an $L \approx 200$ nm, which is comparable to the true electrode gap. In Fig. 7.9(b) the Fraunhofer type modulation has been extracted from current sweeps for another sample which was inadvertently shunted by a small resistor (1 Ω to 10 Ω). It is plotted as a function of the current through the magnetic field bias solenoid for several gate voltages. Since the SQUID is shunted, the Fraunhofer pattern looks flipped vertically. In Fig. 7.9(c), a single period of the sinusoid-like critical current modulation is shown for another device at gate voltages near and far from the Dirac point. Here the critical current modulation has a much larger depth than the device discussed throughout this section, with the minimum at 0.4 µA only one-third that at the maximum, 1.5 µA.

7.4 Discussion

In order to understand the critical current variation with flux for the graphene SQUIDs presented in the previous section two ingredients are necessary. First the simple model for a

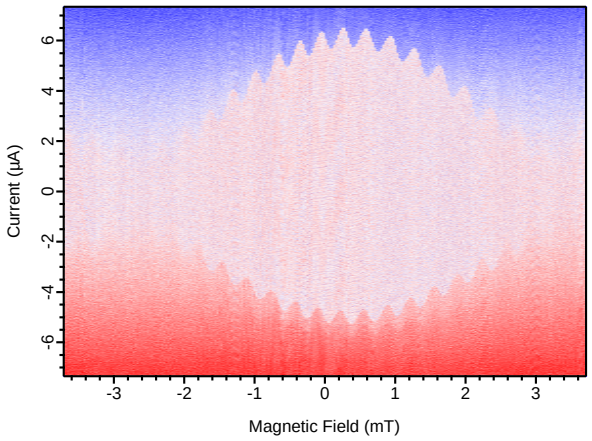

(a) Fraunhofer pattern

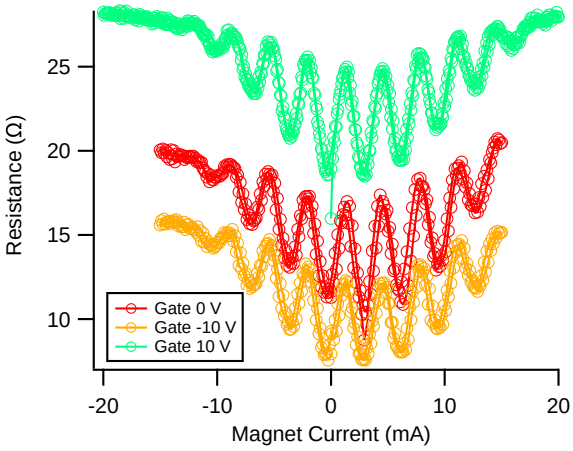

(b) Fraunhofer pattern, shunted SQUID

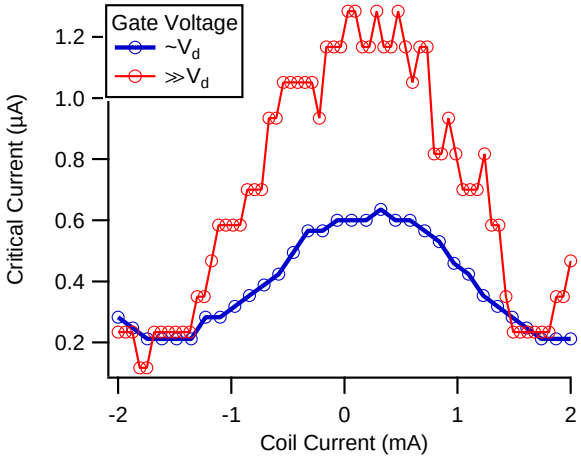

(c) Critical current vs Coil current

Figure 7.9: Critical current as a function of magnetic field in three different graphene superconducting quantum interference devices.

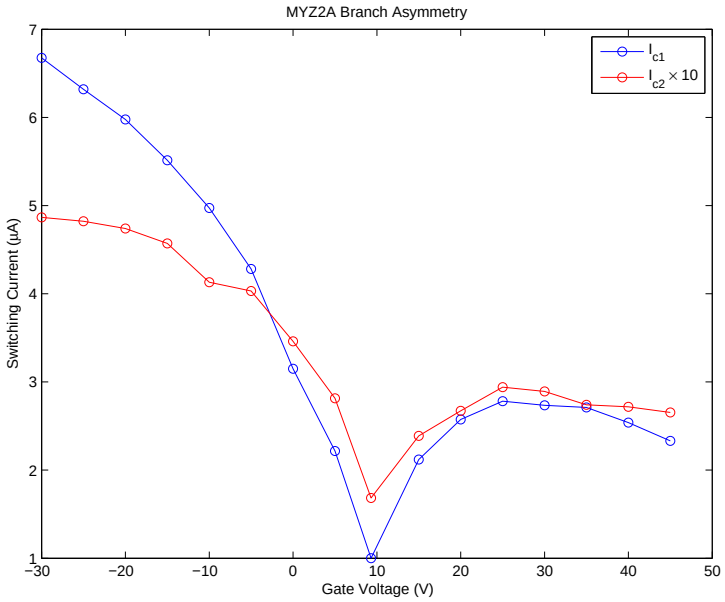

Figure 7.10: Determination of individual critical currents in asymmetric graphene SQUID.

tunnel junction dc SQUID presented in the introduction, $I_S(\Phi) = 2I_c|\cos(\pi\Phi/\Phi_0)|$, assumes both junctions are identical with critical current I_c. By allowing for different maximum critical currents in each junction, I_{ci}, the formula for an asymmetric tunnel junction dc SQUID can be derived,

$$I_S(\Phi) = \sqrt{(I_{c1} - I_{c2})^2 + 4I_{c1}I_{c2}\cos^2(\pi\Phi/\Phi_0)}. \tag{7.5}$$

The maximum supercurrent attained is easily seen to be $I_{c1} + I_{c2}$ and the minimum $I_{c1} - I_{c2}$ assuming $I_{c1} > I_{c2}$. The modulation depth is then $(I_{c1} - I_{c2}) - (I_{c1} - I_{c2}) = 2I_{c2}$ and the fractional modulation is $2I_{c2}/(I_{c1} + I_{c2}) \approx 2I_{c2}/I_{c1}$ in the case of large asymmetry. The individual I_{ci} can be determined for a general current phase relation by determining the modulation depth $2I_{c2}$ and mean value $((I_{c1} + I_{c2}) + (I_{c1} - I_{c2}))/2 = I_{c1}$ from the measured data.

A plot of the individual critical currents for the device of the previous section, "MYZ2A," is shown in Fig. 7.10. To first order $I_{c1} \approx 10I_{c2}$ which is not surprising given the small flux modulation depth compared to the large critical current variation with gate voltage. Since $R_{ni}(V_g) \propto 1/I_{ci}(V_g)$, in the limit of large asymmetry with two junctions in parallel, the critical current dependence on gate voltage will be dominated by the contribution from I_{c1}. The modulation depth as a function of flux however is determined by I_{c2}. If the two curves in Fig. 7.10 are divided to determine the asymmetry factor $\gamma \equiv I_{c2}/I_{c1}$, then γ does depend on gate voltage. This is not surprising since only if the Dirac points and mobilities for each junction were identical would γ be a constant independent of gate voltage.

Assuming for the time being a sinusoidal current-phase relation the data for sample MYZ2A can be fit with Eq. 7.5. The results are shown in Figure 7.11 for gate voltages

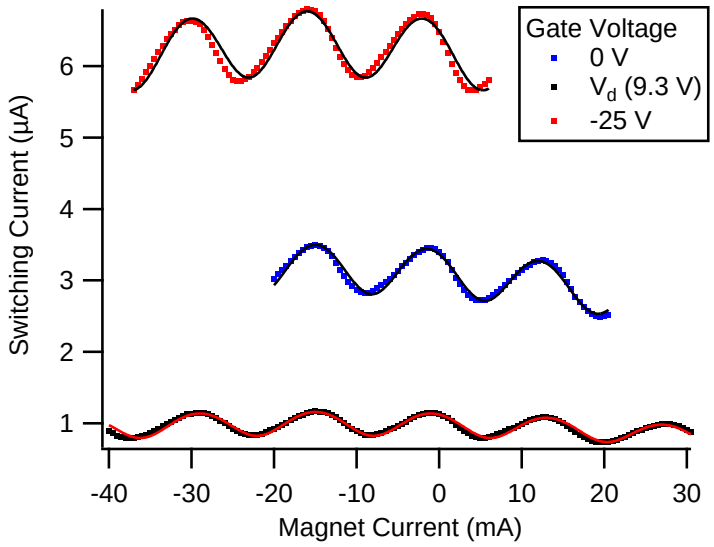

Figure 7.11: Fitting of critical current-magnetic field data for asymmetric graphene SQUID MYZ2A with an asymmetric tunnel junction flux modulation characteristic with zero loop inductance.

$V_g = 0, 9.3, -25$ V which includes the Dirac point $V_d \approx 9.3$ V. Although the fit has the correct period, the slight tilt or skew in the sinusoid-like modulation is not captured by Eq. 7.5, which has Φ inversion symmetry $I_S(\Phi) = I_S(-\Phi)$ due to the even $\cos(\pi\Phi/\Phi_0)$ term. For this reason the black fit lines tend to lag behind the peaks in the data and fall ahead of the troughs (in the direction of increasing magnet current). To reproduce the skewed sinusoid-like modulation one must account for the inductance of the loop. The supercurrent flowing through the loop will produce its own magnetic flux $\Phi' = (L_1 I_{c1} - L_2 I_{c2})$ assuming an inductance L_i in each arm of the loop. For a symmetric SQUID, this additional flux will be zero at a peak in the flux modulation where I_{c1} and I_{c2} interfere constructively. Thus the position of the maxima will not change. However at the troughs in the flux modulation characteristic, where I_{c1} and I_{c2} interfere destructively, Φ' will be maximized and the trough will occur at lower applied flux Φ. This results in the skewed sinusoid of Fig. 7.11. The flux Φ' must be added to the flux Φ applied externally when determining the condition that the wavefunction be single valued:

$$\Delta\phi = \frac{2\pi(\Phi + \Phi')}{\Phi_0} + 2\pi n. \tag{7.6}$$

When L_i is not substantially smaller than Φ_0/I_{ci}, the SQUID modulation characteristic will be skewed. The inductance of a single rectangular loop of given wire radius and dimensions can be calculated online (Inductance Calculator) or found in Grover [65]. The dimensions of the loop for the tuning fork graphene SQUID devices are 10 µm × 3 µm with an electrode thickness 50 nm. This gives for the geometric inductance L_0 between 10 pH to 20 pH. For the

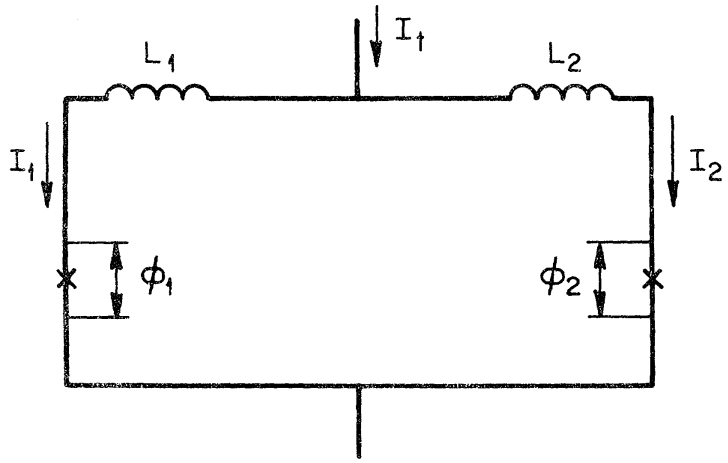

Figure 7.12: Schematic for the asymmetric SQUID with loop inductance, from [56].

observed critical current range 0.1 µA to 7 µA (from Fig. 7.10), $\alpha \equiv 2\pi L_0 I_c/\Phi_0 \approx 0.01$-0.44 which means inductance effects can be important.

Fulton, Dynes, and Dunkleberger describe in detail the solution for the flux modulation characteristic of an asymmetric SQUID with loop inductance [56]. Their device schematic is shown in Fig. 7.12. In their paper they describe a graphical approach which can be easily implemented on a computer.

We can refine the fit of Fig. 7.11 to include inductances L_1 and L_2 with respective dimensionless parameters $\alpha_i \equiv L_i I_{ci}/\Phi_0$. Two examples of fits to one period of flux modulation are shown in Figs. 7.13(a) and (b), for gate voltage at the Dirac point and far away. The error bars for the mean switching currents are determined from the width of histograms such as in Fig. 7.7(b). As evident from Fig. 7.8(c), the error bars are larger for the curve at the Dirac point $V_g = V_d = 9.3\,\mathrm{V}$ than far from it, at $V_g = -40\,\mathrm{V}$. Both fits have similar values for the inductance parameters α_i. At the Dirac point $\alpha_1(V_d) = 0$, $\alpha_2(V_d) = 0.15$ gives zero for the inductance of the "strong" arm, which contributes the larger critical current I_{c1}, and $L_2(V_d) = \alpha_2(V_d)/2\pi \cdot \Phi_0/I_{c1}(V_d) \approx 330\,\mathrm{pH}$ for the "weak" arm with small critical current $I_{c1}(V_d) \approx 0.15\,\mu\mathrm{A}$ (from Fig. 7.10). This inductance is more than an order of magnitude larger than the geometric estimate. The fit at $V_g = -40\,\mathrm{V}$ gives a similar $\alpha_2(-40\mathrm{V}) = 0.17$ but with the higher $I_{c2}(-40\mathrm{V}) \approx 0.9\,\mu\mathrm{A}$, the inductance L_2 is 62 pH, which is only a factor three higher than the geometric estimate.

The fitting results for many gate voltages is shown in Fig. 7.13(c), with the addition of the loop inductance accounting well for the skew in the critical current modulation. The extracted parameters α_i are shown for the gate voltage range $-30\,\mathrm{V}$ to $50\,\mathrm{V}$ in Fig. 7.13(d). Although α_1 is roughly constant and zero throughout, α_2 varies between 0.15 and 0.35 but is clustered around 0.2. The inductances $L_2(V_g)$ inferred from α_2 and the weak critical current I_{c2} are larger than expected from the geometric inductance estimate. In addition the fact that α_2 is almost constant and does not show a dependence with gate voltage

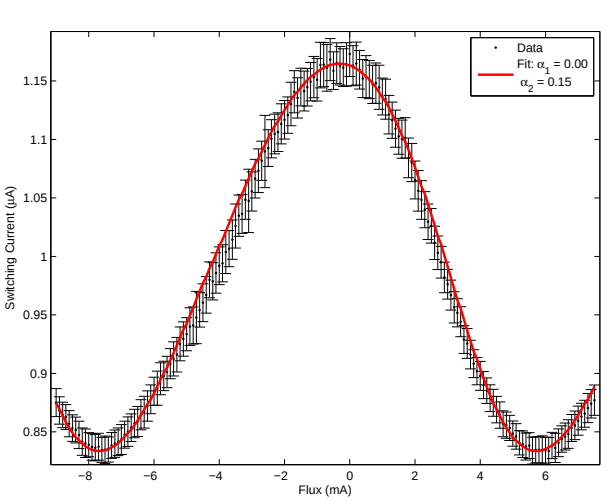

(a) Fit for $V_g = V_d = 9.3\,\mathrm{V}$

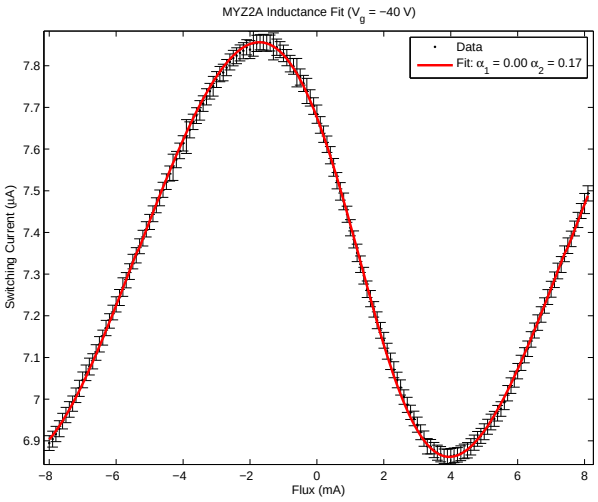

(b) Fit for $V_g = -40\,\mathrm{V}$

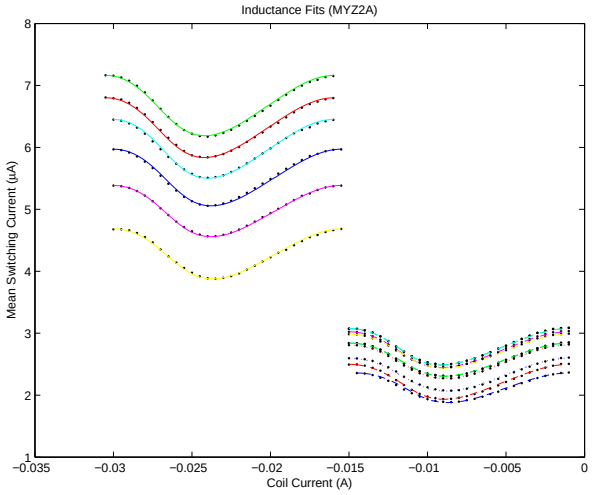

(c) Fit for many gate voltages

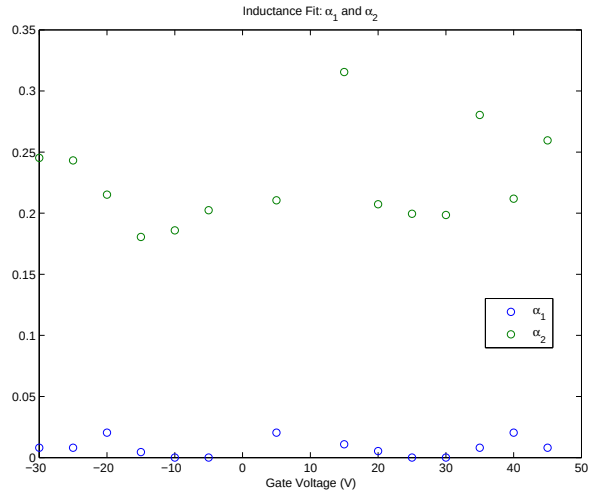

(d) Inductance parameters $\alpha_i = L_i I_{ci}/\Phi_0$

Figure 7.13: Fit to flux modulation data of graphene SQUID MYZ2A with asymmetric double-junction model with loop inductance and sinusoidal current-phase relation.

similar to $R_n(V_g)$ which is inversely related to critical current leads one to believe that the inductance is not purely geometric. It is possible that a non-sinusoidal current-phase relation for the superconductor-graphene-superconductor Josephson junction can account for these discrepancies. However it is unlikely that the simplified ballistic current-phase relation calculated in Ch. 5 is the proper one as this does not fit the flux modulation data well (not shown). It is interesting that in the limit of even larger asymmetry between the junctions $I_{c1} \gg I_{c2}$, and if the geometric loop inductance could be minimized, the measured flux modulation would be a direct measurement of $I_{c2}(\Delta\Phi_2)$ [56]. This could be a means to determine the diffusive graphene current-phase relation experimentally.

Bibliography

[1] D. S. L. Abergel, A. Russell, and V. I. Fal'ko. Visibility of graphene flakes on a dielectric substrate. *Applied Physics Letters*, 91(6):063125–3, 2007.

[2] S. Adam, E. H. Hwang, V. M. Galitski, and S. Das Sarma. A self-consistent theory for graphene transport. *Proceedings of the National Academy of Sciences*, 104(47):18392–18397, 2007.

[3] P. Alberto and et al. Relativistic particle in a box. *European Journal of Physics*, 17(1):19, 1996.

[4] R. S. Alwitt. Anodizing, 2002. http://electrochem.cwru.edu/encycl/art-a02-anodizing.htm.

[5] L. Angers, F. Chiodi, G. Montambaux, M. Ferrier, S. Guron, H. Bouchiat, and J. C. Cuevas. Proximity dc squids in the long-junction limit. *Physical Review B*, 77(16):165408, 2008.

[6] W. J. Arnoult and R. B. McLellan. The solubility of carbon in rhodium ruthenium, iridium and rhenium. *Scripta Metallurgica*, 6(10):1013–1018, 1972. doi: DOI: 10.1016/0036-9748(72)90163-9.

[7] N. W. Ashcroft and N. D. Mermin. *Solid state physics*. Holt, New York,, 1976.

[8] C. Beenakker and C. Schonenberger. Quantum shot noise. *Physics Today*, 56(5):37–42, 2003.

[9] C. Beenakker and H. van Houten. Quantum transport in semiconductor nanostructures. *arXiv:cond-mat/0412664v1*, 2004.

[10] C. W. J. Beenakker. Universal limit of critical-current fluctuations in mesoscopic josephson junctions. *Physical Review Letters*, 67(27):3836, 1991.

[11] C. Bena and G. Montambaux. Remarks on the tight-binding model of graphene. *New Journal of Physics*, 11(9):095003, 2009.

[12] S. Berciaud, S. Ryu, L. E. Brus, and T. F. Heinz. Probing the intrinsic properties of exfoliated graphene: Raman spectroscopy of free-standing monolayers. *Nano Letters*, 9(1):346–352, 2008. doi: 10.1021/nl8031444.

[13] C. Berger, Z. Song, X. Li, X. Wu, N. Brown, C. Naud, D. Mayou, T. Li, J. Hass, A. N. Marchenkov, E. H. Conrad, P. N. First, and W. A. de Heer. Electronic confinement and coherence in patterned epitaxial graphene. *Science*, 312(5777):1191–1196, 2006.

[14] A. M. Black-Schaffer and S. Doniach. Self-consistent solution for proximity effect and josephson current in ballistic graphene sns josephson junctions. *Physical Review B*, 78(2):024504, 2008.

[15] K. Bladh, D. Gunnarsson, E. Hurfeld, S. Devi, C. Kristoffersson, B. Smalander, S. Pehrson, T. Claeson, P. Delsing, and M. Taslakov. Comparison of cryogenic filters for use in single electronics experiments. *Review of Scientific Instruments*, 74(3):1323–1327, 2003.

[16] K. I. Bolotin, F. Ghahari, M. D. Shulman, H. L. Stormer, and P. Kim. Observation of the fractional quantum hall effect in graphene. *Nature*, 462(7270):196–199, 2009. 10.1038/nature08582.

[17] V. W. Brar, Y. Zhang, Y. Yayon, T. Ohta, J. L. McChesney, A. Bostwick, E. Rotenberg, K. Horn, and M. F. Crommie. Scanning tunneling spectroscopy of inhomogeneous electronic structure in monolayer and bilayer graphene on sic. *Applied Physics Letters*, 91(12):122102–3, 2007.

[18] M. Bttiker. Four-terminal phase-coherent conductance. *Physical Review Letters*, 57(14):1761, 1986.

[19] J. S. Bunch, A. M. van der Zande, S. S. Verbridge, I. W. Frank, D. M. Tanenbaum, J. M. Parpia, H. G. Craighead, and P. L. McEuen. Electromechanical resonators from graphene sheets. *Science*, 315(5811):490–493, 2007.

[20] P. Burset, A. L. Yeyati, and A. Martn-Rodero. Microscopic theory of the proximity effect in superconductor-graphene nanostructures. *Physical Review B*, 77(20):205425, 2008.

[21] J. Campos-Delgado, J. Romo-Herrera, x, Manuel, X. Jia, D. A. Cullen, H. Muramatsu, Y. A. Kim, T. Hayashi, Z. Ren, D. J. Smith, Y. Okuno, T. Ohba, H. Kanoh, K. Kaneko, M. Endo, H. Terrones, M. S. Dresselhaus, and M. Terrones. Bulk production of a new form of sp2 carbon: Crystalline graphene nanoribbons. *Nano Lett.*, 8(9):2773–2778, 2008.

[22] L. G. Cancado, K. Takai, T. Enoki, M. Endo, Y. A. Kim, H. Mizusaki, A. Jorio, L. N. Coelho, R. Magalhaes-Paniago, and M. A. Pimenta. General equation for the

determination of the crystallite size l[sub a] of nanographite by raman spectroscopy. *Applied Physics Letters*, 88(16):163106–3, 2006.

[23] A. H. Castro Neto, F. Guinea, N. M. R. Peres, K. S. Novoselov, and A. K. Geim. The electronic properties of graphene. *Reviews of Modern Physics*, 81(1):109, 2009.

[24] J. Cayssol, B. Huard, and D. Goldhaber-Gordon. Contact resistance and shot noise in graphene transistors. *Physical Review B*, 79(7):075428, 2009.

[25] C. Chen, S. Rosenblatt, K. I. Bolotin, W. Kalb, P. Kim, I. Kymissis, H. L. Stormer, T. F. Heinz, and J. Hone. Performance of monolayer graphene nanomechanical resonators with electrical readout. *Nat Nano*, 4(12):861–867, 2009. 10.1038/nnano.2009.267.

[26] J. Chen, C. Jang, M. S. Fuhrer, E. Williams, and M. Ishigami. Charged impurity scattering in graphene. *arXiv:0708.2408v1*, 2007.

[27] X. H. Chen, C. S. Chen, Q. Chen, F. Q. Cheng, G. Zhang, and Z. Z. Chen. Non-destructive purification of multi-walled carbon nanotubes produced by catalyzed cvd. *Materials Letters*, 57(3):734–738, 2002.

[28] J. Clarke and A. I. Braginski. *The SQUID handbook*. Wiley-VCH, Weinheim, 2004.

[29] J. P. Cleuziou, W. Wernsdorfer, V. Bouchiat, T. Ondarcuhu, and M. Monthioux. Carbon nanotube superconducting quantum interference device. *Nat Nano*, 1(1):53–59, 2006. 10.1038/nnano.2006.54.

[30] H. Courtois, M. Meschke, J. T. Peltonen, and J. P. Pekola. Origin of hysteresis in a proximity josephson junction. *Physical Review Letters*, 101(6):067002, 2008.

[31] V. H. Crespi, N. G. Chopra, M. L. Cohen, A. Zettl, and S. G. Louie. Anisotropic electron-beam damage and the collapse of carbon nanotubes. *Physical Review B*, 54(8):5927, 1996.

[32] J. C. Cuevas and A. L. Yeyati. Subharmonic gap structure in short ballistic graphene junctions. *Physical Review B*, 74(18):180501, 2006.

[33] R. Danneau, F. Wu, M. F. Craciun, S. Russo, M. Y. Tomi, J. Salmilehto, A. F. Morpurgo, and P. J. Hakonen. Shot noise in ballistic graphene. *Physical Review Letters*, 100(19):196802, 2008.

[34] S. Datta. *Electronic transport in mesoscopic systems*. Cambridge University Press, Cambridge ; New York, 1995.

[35] R. de Picciotto, H. L. Stormer, L. N. Pfeiffer, K. W. Baldwin, and K. W. West. Four-terminal resistance of a ballistic quantum wire. *Nature*, 411(6833):51–54, 2001. 10.1038/35075009.

[36] L. DiCarlo, J. R. Williams, Y. Zhang, D. T. McClure, and C. M. Marcus. Shot noise in graphene. *Physical Review Letters*, 100(15):156801, 2008.

[37] M. S. Dresselhaus. Lecture notes for mit course 6.732: Solid state physics, 2001. http://stuff.mit.edu/afs/athena/course/6/6.732/www/.

[38] M. S. Dresselhaus, G. Dresselhaus, R. Saito, and A. Jorio. Raman spectroscopy of carbon nanotubes. *Physics Reports*, 409(2):47–99, 2005. doi: DOI: 10.1016/j.physrep.2004.10.006.

[39] D. R. Dreyer, S. Park, C. W. Bielawski, and R. S. Ruoff. The chemistry of graphene oxide. *Chemical Society Reviews*, 39(1):228–240, 2010. 10.1039/b917103g.

[40] X. Du, I. Skachko, and E. Y. Andrei. Josephson current and multiple andreev reflections in graphene sns junctions. *Physical Review B*, 77(18):184507, 2008.

[41] X. Du, I. Skachko, A. Barker, and E. Y. Andrei. Approaching ballistic transport in suspended graphene. *Nat Nano*, 3(8):491–495, 2008. 10.1038/nnano.2008.199.

[42] X. Du, I. Skachko, F. Duerr, A. Luican, and E. Y. Andrei. Fractional quantum hall effect and insulating phase of dirac electrons in graphene. *Nature*, 462(7270):192–195, 2009. 10.1038/nature08522.

[43] E. Dujardin, T. Thio, H. Lezec, and T. W. Ebbesen. Fabrication of mesoscopic devices from graphite microdisks. *Applied Physics Letters*, 79(15):2474–2476, 2001.

[44] R. F. Egerton, P. Li, and M. Malac. Radiation damage in the tem and sem. *Micron*, 35(6):399–409, 2004. doi: DOI: 10.1016/j.micron.2004.02.003.

[45] R. F. Egerton, F. Wang, and P. A. Crozier. Beam-induced damage to thin specimens in an intense electron probe. *Microscopy and Microanalysis*, 12(1):65–71, 2006. Times Cited: 5.

[46] D. C. Elias, R. R. Nair, T. M. G. Mohiuddin, S. V. Morozov, P. Blake, M. P. Halsall, A. C. Ferrari, D. W. Boukhvalov, M. I. Katsnelson, A. K. Geim, and K. S. Novoselov. Control of graphene's properties by reversible hydrogenation: Evidence for graphane. *Science*, 323(5914):610–613, 2009.

[47] M. J. Ellsworth. Chip power density and module cooling technology projections for the current decade. In *Thermal and Thermomechanical Phenomena in Electronic Systems, 2004. ITHERM '04. The Ninth Intersociety Conference on*, volume 2, pages 707–708 Vol.2, 2004.

[48] K. V. Emtsev, A. Bostwick, K. Horn, J. Jobst, G. L. Kellogg, L. Ley, J. L. McChesney, T. Ohta, S. A. Reshanov, J. Rohrl, E. Rotenberg, A. K. Schmid, D. Waldmann, H. B. Weber, and T. Seyller. Towards wafer-size graphene layers by atmospheric pressure graphitization of silicon carbide. *Nat Mater*, 8(3):203–207, 2009. 10.1038/nmat2382.

[49] D. B. Farmer, R. Golizadeh-Mojarad, V. Perebeinos, Y.-M. Lin, G. S. Tulevski, J. C. Tsang, and P. Avouris. Chemical doping and electronhole conduction asymmetry in graphene devices. *Nano Letters*, 9(1):388–392, 2008. doi: 10.1021/nl803214a.

[50] A. C. Ferrari. Raman spectroscopy of graphene and graphite: Disorder, electron-phonon coupling, doping and nonadiabatic effects. *Solid State Communications*, 143(1-2):47–57, 2007. doi: DOI: 10.1016/j.ssc.2007.03.052.

[51] A. C. Ferrari, J. C. Meyer, V. Scardaci, C. Casiraghi, M. Lazzeri, F. Mauri, S. Piscanec, D. Jiang, K. S. Novoselov, S. Roth, and A. K. Geim. Raman spectrum of graphene and graphene layers. *Physical Review Letters*, 97(18):187401, 2006.

[52] D. K. Ferry, S. M. Goodnick, and J. P. Bird. Transport in nanostructures, 2009.

[53] R. P. Feynman, R. B. Leighton, and M. L. Sands. *The Feynman lectures on physics*. Pearson/Addison-Wesley, San Francisco, definitive edition, 2006.

[54] S. Frank, P. Poncharal, Z. L. Wang, and W. A. de Heer. Carbon nanotube quantum resistors. *Science*, 280(5370):1744–1746, 1998.

[55] T. A. Fulton and L. N. Dunkleberger. Lifetime of the zero-voltage state in josephson tunnel junctions. *Physical Review B*, 9(11):4760, 1974.

[56] T. A. Fulton, L. N. Dunkleberger, and R. C. Dynes. Quantum interference properties of double josephson junctions. *Physical Review B*, 6(3):855, 1972.

[57] M. H. Gass, U. Bangert, A. L. Bleloch, P. Wang, R. R. Nair, and A. K. Geim. Free-standing graphene at atomic resolution. *Nat Nano*, 3(11):676–681, 2008. 1748-3387 10.1038/nnano.2008.280 10.1038/nnano.2008.280.

[58] P.-G. d. Gennes. *Superconductivity of metals and alloys*. Advanced book classics. Advanced Book Program, Perseus Books, Reading, Mass., 1999.

[59] A. J. M. Giesbers, U. Zeitler, S. Neubeck, F. Freitag, K. S. Novoselov, and J. C. Maan. Nanolithography and manipulation of graphene using an atomic force microscope. *Solid State Communications*, 147(9-10):366–369, 2008. doi: DOI: 10.1016/j.ssc.2008.06.027.

[60] G. Giovannetti, P. A. Khomyakov, G. Brocks, V. M. Karpan, J. van den Brink, and P. J. Kelly. Doping graphene with metal contacts. *Physical Review Letters*, 101(2):026803, 2008.

[61] A. A. Golubov, M. Y. Kupriyanov, and E. Ilichev. The current-phase relation in josephson junctions. *Reviews of Modern Physics*, 76(2):411, 2004. Copyright (C) 2010 The American Physical Society Please report any problems to prola@aps.org RMP.

[62] C. Gomez-Navarro, J. C. Meyer, R. S. Sundaram, A. Chuvilin, S. Kurasch, M. Burghard, K. Kern, and U. Kaiser. Atomic structure of reduced graphene oxide. *Nano Letters*, 10(4):1144–1148, 2010. doi: 10.1021/nl9031617.

[63] D. Graf, F. Molitor, K. Ensslin, C. Stampfer, A. Jungen, C. Hierold, and L. Wirtz. Spatially resolved raman spectroscopy of single- and few-layer graphene. *Nano Letters*, 7(2):238–242, 2007. doi: 10.1021/nl061702a.

[64] W. Greiner. *Relativistic quantum mechanics : wave equations*. Springer, Berlin ; New York, 3rd edition, 2000.

[65] F. W. Grover. *Inductance calculations : working formulas and tables*. Dover Publications, Mineola, N.Y., 2004.

[66] A. Gupta, G. Chen, P. Joshi, S. Tadigadapa, and Eklund. Raman scattering from high-frequency phonons in supported n-graphene layer films. *Nano Letters*, 6(12):2667–2673, 2006. doi: 10.1021/nl061420a.

[67] P. M. Hall. Resistance calculations for thin film patterns. *Thin Solid Films*, 1(4):277–295, 1968. doi: DOI: 10.1016/0040-6090(68)90046-1.

[68] P. M. Hall. Resistance calculations for thin film rectangles. *Thin Solid Films*, 300(1-2):256–264, 1997. doi: DOI: 10.1016/S0040-6090(96)09495-3.

[69] H. B. Heersche, P. Jarillo-Herrero, J. B. Oostinga, L. M. K. Vandersypen, and A. F. Morpurgo. Bipolar supercurrent in graphene. *Nature*, 446(7131):56–59, 2007. 10.1038/nature05555.

[70] R. Held, T. Heinzel, P. Studerus, and K. Ensslin. Nanolithography by local anodic oxidation of metal films using an atomic force microscope. *Physica E-Low-Dimensional Systems & Nanostructures*, 2(1-4):748–752, 1998.

[71] Y. Hernandez, V. Nicolosi, M. Lotya, F. M. Blighe, Z. Sun, S. De, I. T. McGovern, B. Holland, M. Byrne, Y. K. Gun'Ko, J. J. Boland, P. Niraj, G. Duesberg, S. Krishnamurthy, R. Goodhue, J. Hutchison, V. Scardaci, A. C. Ferrari, and J. N. Coleman. High-yield production of graphene by liquid-phase exfoliation of graphite. *Nat Nano*, 3(9):563–568, 2008. 10.1038/nnano.2008.215.

[72] B. Huard, N. Stander, J. A. Sulpizio, and D. Goldhaber-Gordon. Evidence of the role of contacts on the observed electron-hole asymmetry in graphene. *Physical Review B*, 78(12):121402, 2008.

[73] E. H. Hwang, S. Adam, and S. D. Sarma. Carrier transport in two-dimensional graphene layers. *Physical Review Letters*, 98(18):186806–4, 2007.

[74] T. Ihn, J. Gttinger, F. Molitor, S. Schnez, E. Schurtenberger, A. Jacobsen, S. Hellmller, T. Frey, S. Drscher, C. Stampfer, and K. Ensslin. Graphene single-electron transistors. *Materials Today*, 13(3):44–50, 2010. doi: DOI: 10.1016/S1369-7021(10)70033-X.

[75] Y. Imry and R. Landauer. Conductance viewed as transmission. *Reviews of Modern Physics*, 71(2):S306, 1999. Copyright (C) 2010 The American Physical Society Please report any problems to prola@aps.org RMP.

[76] B. Irmer, M. Kehrle, H. Lorenz, and J. P. Kotthaus. Nanolithography by non-contact afm-induced local oxidation: fabrication of tunnelling barriers suitable for single-electron devices. *Semiconductor Science and Technology*, 13(8A):A79–A82, 1998. Suppl. S 111MY Times Cited:1 Cited References Count:11.

[77] M. Ishigami, J. H. Chen, W. G. Cullen, M. S. Fuhrer, and E. D. Williams. Atomic structure of graphene on sio2. *Nano Lett.*, 7(6):1643–1648, 2007.

[78] P. Jarillo-Herrero, J. A. van Dam, and L. P. Kouwenhoven. Quantum supercurrent transistors in carbon nanotubes. *Nature*, 439(7079):953–956, 2006. 10.1038/nature04550.

[79] X. Jia, M. Hofmann, V. Meunier, B. G. Sumpter, J. Campos-Delgado, J. M. Romo-Herrera, H. Son, Y.-P. Hsieh, A. Reina, J. Kong, M. Terrones, and M. S. Dresselhaus. Controlled formation of sharp zigzag and armchair edges in graphitic nanoribbons. *Science*, 323(5922):1701–1705, 2009.

[80] W. Jiang, G. Nadeau, K. Zaghib, and K. Kinoshita. Thermal analysis of the oxidation of natural graphite – effect of particle size. *Thermochimica Acta*, 351(1-2):85–93, 2000.

[81] P. Jin Gyu, Z. Chuck, L. Richard, and W. Ben. Nano-machining of highly oriented pyrolytic graphite using conductive atomic force microscope tips and carbon nanotubes. *Nanotechnology*, (40):405306, 2007.

[82] A.-S. Johansson, J. Lu, and J.-O. Carlsson. Tem investigation of cvd graphite on nickel. *Thin Solid Films*, 252(1):19–25, 1994.

[83] I. Jung, M. Pelton, R. Piner, D. A. Dikin, S. Stankovich, S. Watcharotone, M. Hausner, and R. S. Ruoff. Simple approach for high-contrast optical imaging and characterization of graphene-based sheets. *Nano Letters*, 7(12):3569–3575, 2007. doi: 10.1021/nl0714177.

[84] M. I. Katsnelson, K. S. Novoselov, and A. K. Geim. Chiral tunnelling and the klein paradox in graphene. *Nat Phys*, 2(9):620–625, 2006. 10.1038/nphys384.

[85] B. Kelly, B. Marsden, K. Hall, D. Martin, A. Harper, and A. Blanchard. Irradiation damage in graphite due to fast neutrons in fission and fusion systems. *International Atomic Energy Agency HTGR Knowledge Base*, IAEA-TECDOC–1154, 2000.

[86] B. T. Kelly. *Physics of graphite*. Applied Science Publishers, London ; Englewood, N.J., 1981.

[87] B. M. Kessler, c. O. Girit, A. Zettl, and V. Bouchiat. Tunable superconducting phase transition in metal-decorated graphene sheets. *Physical Review Letters*, 104(4):047001, 2010.

[88] K. S. Kim, Y. Zhao, H. Jang, S. Y. Lee, J. M. Kim, K. S. Kim, J.-H. Ahn, P. Kim, J.-Y. Choi, and B. H. Hong. Large-scale pattern growth of graphene films for stretchable transparent electrodes. *Nature*, 457(7230):706–710, 2009. 10.1038/nature07719.

[89] K. Kinoshita. *Carbon : electrochemical and physicochemical properties*. Wiley, New York, 1988.

[90] C. Kisielowski, B. Freitag, B. M., H. van Lin, S. Lazar, G. Knippels, P. Tiemeijer, M. van der Stam, S. von Harrach, M. Stekelenburg, M. Haider, S. Uhlemann, H. Muller, P. Hartel, B. Kabius, D. Miller, I. Petrov, E. A. Olson, T. Donchev, E. A. Kenik, A. Lupini, J. Bentley, S. J. Pennycook, I. M. Anderson, A. Minor, A. Schmid, T. Duden, V. Radmilovic, Q. Ramasse, M. Watanabe, R. Erni, E. A. Stach, P. Denes, and U. Dahmen. Detection of single atoms and buried defects in three dimensions by aberration-corrected electron microscope with 0.5- information limit. *Microscopy and Microanalysis*, 14:469–477, 2008.

[91] T. M. Klapwijk, G. E. Blonder, and M. Tinkham. Explanation of subharmonic energy gap structure in superconducting contacts. *Physica B+C*, 109-110:1657–1664, 1982. doi: DOI: 10.1016/0378-4363(82)90189-9.

[92] H. Kober. *Dictionary of conformal representations*. Dover Publications, [New York], 1957.

[93] P. Koskinen, S. Malola, and H. Hkkinen. Evidence for graphene edges beyond zigzag and armchair. *Physical Review B*, 80(7):073401, 2009.

[94] H. Kuramochi, F. Perez-Murano, J. A. Dagata, and H. Yokoyama. Faradaic current detection during anodic oxidation of the h-passivated p-si(001) surface with controlled relative humidity. *Nanotechnology*, 15(3):297–302, 2004. 807VW Times Cited:22 Cited References Count:24.

[95] R. Landauer. Spatial variation of currents and fields due to localized scatterers in metallic conduction. *IBM Journal of Research and Development*, 44(1):251–259, 2000.

[96] C. Lee, X. Wei, J. W. Kysar, and J. Hone. Measurement of the elastic properties and intrinsic strength of monolayer graphene. *Science*, 321(5887):385–388, 2008.

[97] M. P. Levendorf, C. S. Ruiz-Vargas, S. Garg, and J. Park. Transfer-free batch fabrication of single layer graphene transistors. *Nano Letters*, 9(12):4479–4483, 2009. doi: 10.1021/nl902790r.

[98] X. Li, W. Cai, J. An, S. Kim, J. Nah, D. Yang, R. Piner, A. Velamakanni, I. Jung, E. Tutuc, S. K. Banerjee, L. Colombo, and R. S. Ruoff. Large-area synthesis of high-quality and uniform graphene films on copper foils. *Science*, page 1171245, 2009.

[99] X. Li, W. Cai, L. Colombo, and R. S. Ruoff. Evolution of graphene growth on ni and cu by carbon isotope labeling. *Nano Letters*, 9(12):4268–4272, 2009. doi: 10.1021/nl902515k.

[100] X. Li, X. Wang, L. Zhang, S. Lee, and H. Dai. Chemically derived, ultrasmooth graphene nanoribbon semiconductors. *Science*, 319(5867):1229–1232, 2008.

[101] K. K. Likharev. Superconducting weak links. *Reviews of Modern Physics*, 51(1):101, 1979. Copyright (C) 2010 The American Physical Society Please report any problems to prola@aps.org RMP.

[102] A. V. Martin, K. Ishizuka, C. Kisielowski, and L. J. Allen. Phase imaging and the evolution of a gold-vacuum interface at atomic resolution. *Physical Review B*, 74(17), 2006.

[103] J. Martin, N. Akerman, G. Ulbricht, T. Lohmann, J. H. Smet, K. von Klitzing, and A. Yacoby. Observation of electron-hole puddles in graphene using a scanning single-electron transistor. *Nat Phys*, 4(2):144–148, 2008. 10.1038/nphys781.

[104] S. Masubuchi, M. Ono, K. Yoshida, K. Hirakawa, and T. Machida. Fabrication of graphene nanoribbon by local anodic oxidation lithography using atomic force microscope. *Applied Physics Letters*, 94(8):082107–3, 2009.

[105] R. B. McLellan. Invited review: Thermodynamics of solid solutions. *Materials Science and Engineering*, 9:121–140, 1972. doi: DOI: 10.1016/0025-5416(72)90025-0.

[106] J. C. Meyer, A. K. Geim, M. I. Katsnelson, K. S. Novoselov, D. Obergfell, S. Roth, C. Girit, and A. Zettl. On the roughness of single- and bi-layer graphene membranes. *Solid State Communications*, 143(1-2):101–109, 2007. 0038-1098 doi: DOI: 10.1016/j.ssc.2007.02.047.

[107] J. C. Meyer, C. O. Girit, M. F. Crommie, and A. Zettl. Hydrocarbon lithography on graphene membranes. *Applied Physics Letters*, 92(12):123110–3, 2008.

[108] J. C. Meyer, C. O. Girit, M. F. Crommie, and A. Zettl. Imaging and dynamics of light atoms and molecules on graphene. *Nature*, 454(7202):319–322, 2008. 0028-0836 10.1038/nature07094 10.1038/nature07094.

[109] J. C. Meyer, C. Kisielowski, R. Erni, M. D. Rossell, M. F. Crommie, and A. Zettl. Direct imaging of lattice atoms and topological defects in graphene membranes. *Nano Letters*, 8(11):3582–3586, 2008. doi: 10.1021/nl801386m.

[110] F. Miao, W. Bao, H. Zhang, and C. N. Lau. Premature switching in graphene josephson transistors. *Solid State Communications*, 149(27-28):1046–1049, 2009. doi: DOI: 10.1016/j.ssc.2009.01.035.

[111] F. Miao, S. Wijeratne, Y. Zhang, U. C. Coskun, W. Bao, and C. N. Lau. Phase-coherent transport in graphene quantum billiards. *Science*, 317(5844):1530–1533, 2007.

[112] D. L. Miller, K. D. Kubista, G. M. Rutter, M. Ruan, W. A. de Heer, P. N. First, and J. A. Stroscio. Observing the quantization of zero mass carriers in graphene. *Science*, 324(5929):924–927, 2009.

[113] R. R. Nair, P. Blake, A. N. Grigorenko, K. S. Novoselov, T. J. Booth, T. Stauber, N. M. R. Peres, and A. K. Geim. Fine structure constant defines visual transparency of graphene. *Science*, 320(5881):1308–, 2008.

[114] T. Needham. *Visual complex analysis*. Clarendon Press, Oxford, 2000.

[115] Z. H. Ni, H. M. Wang, J. Kasim, H. M. Fan, T. Yu, Y. H. Wu, Y. P. Feng, and Z. X. Shen. Graphene thickness determination using reflection and contrast spectroscopy. *Nano Letters*, 7(9):2758–2763, 2007. doi: 10.1021/nl071254m.

[116] K. S. Novoselov, A. K. Geim, S. V. Morozov, D. Jiang, M. I. Katsnelson, I. V. Grigorieva, S. V. Dubonos, and A. A. Firsov. Two-dimensional gas of massless dirac fermions in graphene. *Nature*, 438(7065):197–200, 2005. 10.1038/nature04233.

[117] K. S. Novoselov, A. K. Geim, S. V. Morozov, D. Jiang, Y. Zhang, S. V. Dubonos, I. V. Grigorieva, and A. A. Firsov. Electric field effect in atomically thin carbon films. *Science*, 306(5696):666–669, 2004.

[118] K. S. Novoselov, D. Jiang, F. Schedin, T. J. Booth, V. V. Khotkevich, S. V. Morozov, and A. K. Geim. Two-dimensional atomic crystals. *Proceedings of the National Academy of Sciences of the United States of America*, 102(30):10451–10453, 2005.

[119] K. S. Novoselov, Z. Jiang, Y. Zhang, S. V. Morozov, H. L. Stormer, U. Zeitler, J. C. Maan, G. S. Boebinger, P. Kim, and A. K. Geim. Room-temperature quantum hall effect in graphene. *Science*, page 1137201, 2007.

[120] K. S. Novoselov, E. McCann, S. V. Morozov, V. I. Fal/'ko, M. I. Katsnelson, U. Zeitler, D. Jiang, F. Schedin, and A. K. Geim. Unconventional quantum hall effect and berry/'s phase of 2[pi] in bilayer graphene. *Nat Phys*, 2(3):177–180, 2006. 10.1038/nphys245.

[121] C. Oshima and A. Nagashima. Ultra-thin epitaxial films of graphite and hexagonal boron nitride on solid surfaces. *Journal of Physics-Condensed Matter*, 9(1):1–20, 1997.

[122] C.-H. Park, Y.-W. Son, L. Yang, M. L. Cohen, and S. G. Louie. Electron beam supercollimation in graphene superlattices. *Nano Letters*, 8(9):2920–2924, 2008. doi: 10.1021/nl801752r.

[123] M. A. Pimenta, G. Dresselhaus, M. S. Dresselhaus, L. G. Cancado, A. Jorio, and R. Saito. Studying disorder in graphite-based systems by raman spectroscopy. *Physical Chemistry Chemical Physics*, 9(11):1276–1290, 2007. 10.1039/b613962k.

[124] L. A. Ponomarenko, F. Schedin, M. I. Katsnelson, R. Yang, E. W. Hill, K. S. Novoselov, and A. K. Geim. Chaotic dirac billiard in graphene quantum dots. *Science*, 320(5874):356–358, 2008.

[125] P. Rai-Choudhury. *Handbook of microlithography, micromachining, and microfabrication*. SPIE Press monograph. SPIE Optical Engineering Press ; Institution of Electrical Engineers, Bellingham, Wash., USA London, UK, 1997.

[126] S. Roddaro, P. Pingue, V. Piazza, V. Pellegrini, and F. Beltram. The optical visibility of graphene: interference colors of ultrathin graphite on sio2. *Nano Letters*, 7(9):2707–2710, 2007. doi: 10.1021/nl071158l.

[127] G. M. Rutter, J. N. Crain, N. P. Guisinger, T. Li, P. N. First, and J. A. Stroscio. Scattering and interference in epitaxial graphene. *Science*, 317(5835):219–222, 2007.

[128] A. Rycerz, J. Tworzydlo, and C. W. J. Beenakker. Valley filter and valley valve in graphene. *Nat Phys*, 3(3):172–175, 2007. 10.1038/nphys547.

[129] R. Saito, A. Jorio, A. G. Souza Filho, G. Dresselhaus, M. S. Dresselhaus, and M. A. Pimenta. Probing phonon dispersion relations of graphite by double resonance raman scattering. *Physical Review Letters*, 88(2):027401, 2001.

[130] K. Sato, R. Saito, Y. Oyama, J. Jiang, L. G. Canado, M. A. Pimenta, A. Jorio, G. G. Samsonidze, G. Dresselhaus, and M. S. Dresselhaus. D-band raman intensity of graphitic materials as a function of laser energy and crystallite size. *Chemical Physics Letters*, 427(1-3):117–121, 2006. doi: DOI: 10.1016/j.cplett.2006.05.107.

[131] T. Schapers. *Superconductor/Semiconductor Junctions*, volume 174/2001 of *Springer Tracts in Modern Physics*. Springer Berlin / Heidelberg, 2001.

[132] F. Schedin, A. K. Geim, S. V. Morozov, E. W. Hill, P. Blake, M. I. Katsnelson, and K. S. Novoselov. Detection of individual gas molecules adsorbed on graphene. *Nat Mater*, 6(9):652–655, 2007. 1476-1122 10.1038/nmat1967 10.1038/nmat1967.

[133] H. Schoeller, J. Kim, S. Park, and J. Cho. Thermodynamics and kinetics of oxidation of pure indium solders. In V. P. Atluri, S. Sharan, C.-P. Wong, and D. Frear, editors, *Advanced Electronic Packaging*, volume 968 of *Mater. Res. Soc. Symp. Proc.*, Warrendale, PA, 2007.

[134] A. V. Shytov, M. I. Katsnelson, and L. S. Levitov. Atomic collapse and quasi-rydberg states in graphene. *Physical Review Letters*, 99(24):246802, 2007.

[135] B. W. Smith and D. E. Luzzi. Electron irradiation effects in single wall carbon nanotubes. *Journal of Applied Physics*, 90(7):3509–3515, 2001.

[136] Y.-W. Son, M. L. Cohen, and S. G. Louie. Half-metallic graphene nanoribbons. *Nature*, 444(7117):347–349, 2006. 10.1038/nature05180.

[137] M. Sprinkle, D. Siegel, Y. Hu, J. Hicks, A. Tejeda, A. Taleb-Ibrahimi, P. Le Fvre, F. Bertran, S. Vizzini, H. Enriquez, S. Chiang, P. Soukiassian, C. Berger, W. A. de Heer, A. Lanzara, and E. H. Conrad. First direct observation of a nearly ideal graphene band structure. *Physical Review Letters*, 103(22):226803, 2009.

[138] E. Stern, G. Cheng, J. F. Klemic, E. Broomfield, D. Turner-Evans, C. Li, C. Zhou, and M. A. Reed. Methods for fabricating ohmic contacts to nanowires and nanotubes. *Journal of Vacuum Science and Technology B*, 24(1):231–236, 2006.

[139] E. Sutter, P. Albrecht, and P. Sutter. Graphene growth on polycrystalline ru thin films. *Applied Physics Letters*, 95(13):133109–3, 2009.

[140] P. W. Sutter, J.-I. Flege, and E. A. Sutter. Epitaxial graphene on ruthenium. *Nat Mater*, 7(5):406–411, 2008. 10.1038/nmat2166.

[141] Y. W. Tan, Y. Zhang, K. Bolotin, Y. Zhao, S. Adam, E. H. Hwang, S. Das Sarma, H. L. Stormer, and P. Kim. Measurement of scattering rate and minimum conductivity in graphene. *Physical Review Letters*, 99(24):246803, 2007.

[142] L. Tapaszto, G. Dobrik, P. Lambin, and L. P. Biro. Tailoring the atomic structure of graphene nanoribbons by scanning tunnelling microscope lithography. *Nat Nano*, 3(7):397–401, 2008. 1748-3387 10.1038/nnano.2008.149 10.1038/nnano.2008.149.

[143] C. Thomsen and S. Reich. Double resonant raman scattering in graphite. *Physical Review Letters*, 85(24):5214, 2000.

[144] M. Tinkham. *Introduction to superconductivity*. McGraw Hill, New York, 2nd edition, 1996.

[145] M. Titov and C. W. J. Beenakker. Josephson effect in ballistic graphene. *Physical Review B*, 74(4):041401, 2006.

[146] K. Todd, H.-T. Chou, S. Amasha, and D. Goldhaber-Gordon. Quantum dot behavior in graphene nanoconstrictions. *Nano Letters*, 9(1):416–421, 2008. doi: 10.1021/nl803291b.

[147] J. Tworzydł o, B. Trauzettel, M. Titov, A. Rycerz, and C. W. J. Beenakker. Sub-poissonian shot noise in graphene. *Physical Review Letters*, 96(24):246802, 2006.

[148] K. W. Urban. Studying atomic structures by aberration-corrected transmission electron microscopy. *Science*, 321(5888):506–510, 2008.

[149] H. van Houten and C. Beenakker. Quantum point contacts. *Physics Today*, 49(7):22–27, 1996.

[150] B. J. van Wees, H. van Houten, C. W. J. Beenakker, J. G. Williamson, L. P. Kouwenhoven, D. van der Marel, and C. T. Foxon. Quantized conductance of point contacts in a two-dimensional electron gas. *Physical Review Letters*, 60(9):848, 1988.

[151] L. M. Viculis, J. J. Mack, and R. B. Kaner. A chemical route to carbon nanoscrolls. *Science*, 299(5611):1361–, 2003.

[152] A. Voter. Introduction to the kinetic monte carlo method, 2006.

[153] P. R. Wallace. The band theory of graphite. *Physical Review*, 71(9):622, 1947.

[154] B. Q. Wei, R. Vajtai, and P. M. Ajayan. Reliability and current carrying capacity of carbon nanotubes. *Applied Physics Letters*, 79(8):1172–1174, 2001.

[155] L. Weng, L. Zhang, Y. P. Chen, and L. P. Rokhinson. Atomic force microscope local oxidation nanolithography of graphene. *Applied Physics Letters*, 93(9):093107–3, 2008.

[156] D. A. Wharam and et al. One-dimensional transport and the quantisation of the ballistic resistance. *Journal of Physics C: Solid State Physics*, 21(8):L209, 1988.

[157] D. B. Williams and C. B. Carter. *Transmission electron microscopy : a textbook for materials science*. Plenum Press, New York, 1996.

[158] K. R. Williams, K. Gupta, and M. Wasilik. Etch rates for micromachining processing-part ii. *Microelectromechanical Systems, Journal of*, 12(6):761–778, 2003.

[159] A. F. Young and P. Kim. Quantum interference and klein tunnelling in graphene heterojunctions. *Nat Phys*, 5(3):222–226, 2009. 10.1038/nphys1198.

[160] P. Y. Yu and M. Cardona. *Fundamentals of semiconductors : physics and materials properties*. Springer, Berlin ; New York, 2nd updated ed edition, 1999.

[161] T. D. Yuzvinsky, A. M. Fennimore, W. Mickelson, C. Esquivias, and A. Zettl. Precision cutting of nanotubes with a low-energy electron beam. *Applied Physics Letters*, 86(5):053109–3, 2005.

[162] Y. Zhang, V. W. Brar, C. Girit, A. Zettl, and M. F. Crommie. Origin of spatial charge inhomogeneity in graphene. *Nat Phys*, 5(10):722–726, 2009. 1745-2473 10.1038/nphys1365 10.1038/nphys1365.

[163] Y. Zhang, V. W. Brar, F. Wang, C. Girit, Y. Yayon, M. Panlasigui, A. Zettl, and M. F. Crommie. Giant phonon-induced conductance in scanning tunnelling spectroscopy of gate-tunable graphene. *Nat Phys*, 4(8):627–630, 2008. 1745-2473 10.1038/nphys1022 10.1038/nphys1022.

[164] Y. Zhang, Y.-W. Tan, H. L. Stormer, and P. Kim. Experimental observation of the quantum hall effect and berry's phase in graphene. *Nature*, 438(7065):201–204, 2005. 10.1038/nature04235.

[165] S. Y. Zhou, c. O. Girit, A. Scholl, C. J. Jozwiak, D. A. Siegel, P. Yu, J. T. Robinson, F. Wang, A. Zettl, and A. Lanzara. Instability of two-dimensional graphene: Breaking sp2 bonds with soft x rays. *Physical Review B*, 80(12):121409, 2009.

Appendix A

Graphene Theory

A.1 Band Structure

Graphene is a honeycomb network of carbon atoms (Fig. 1.2) which is described by the hexagonal lattice with two-atom basis shown in Figure A.1(a). The interatomic spacing is $a = 1.42\,\text{Å}$ and the lattice constant $|\boldsymbol{a}_i| = a\sqrt{3} = 2.46\,\text{Å}$. The Brillouin zone is hexagonal (Fig. A.1(b)) and has two inequivalent points of high symmetry, the "Dirac" points K and K', where the Fermi surface lies. Graphene's honeycomb structure has the most symmetrical planar crystallographic group and has the lowest coordination number (only three nearest neighbor atoms) in two dimensions. In crystallographic notation it is referred to as p6m or in orbifold notation *632 (Wikipedia: wallpaper groups). It has six reflections, through axes connecting K-K, K-K', K'-K', M-M, M'-M', and M"-M". Points M' and M" are not indicated in Fig. A.1(b) but are located at the intersection of the reciprocal lattice vectors $\boldsymbol{b}_i$ and the Brillouin zone edge. In addition to the reflections, there is one six-fold rotation axis at Γ, two three-fold rotation axes at K and K', and three two-fold rotation axes at M, M', and M".

To solve for the electronic band structure, the tight-binding method is used [7], in which the wavefunction is written as a Bloch function of atomic orbitals [11]

$$|\psi, \boldsymbol{k}\rangle = \frac{1}{\sqrt{2N}} \sum_n e^{i\boldsymbol{k}\cdot\boldsymbol{R}_n} \chi_n(\boldsymbol{k}), \tag{A.1}$$

where $\chi_n(\boldsymbol{k})$ is a pseudospinor describing the wavefunction at lattice site R_n composed of orbitals of the A and B atoms. It be written in Dirac braket notation as

$$\chi_n(\boldsymbol{k}) = \begin{pmatrix} c_+(\boldsymbol{k}) \\ c_-(\boldsymbol{k}) \end{pmatrix}_n = c_+(\boldsymbol{k})\,|+, n\rangle + c_-(\boldsymbol{k})\,|-, n\rangle\,. \tag{A.2}$$

The two kets $|\pm, n\rangle$ are the atomic orbitals at atom A (+) and B (−) of lattice site R_n, centered at positions denoted by $R_n^{\pm}$. The spatial dependence of these kets can be expressed as $\langle \boldsymbol{r}|\pm, n\rangle = \phi(\boldsymbol{r} + \boldsymbol{R}_n^{\pm})$. The atomic wavefunction $\phi(\boldsymbol{r})$ is the carbon p_z orbital. The complex numbers $c_{\pm}(\boldsymbol{k})$ are the coefficients of the linear combination of A and B wavefunctions

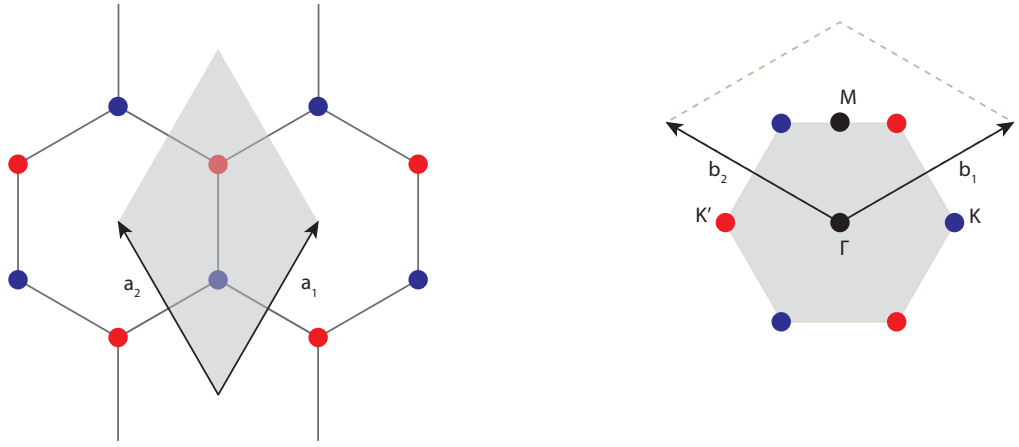

(a) Hexagonal lattice (b) Brillouin zone

Figure A.1: Graphene lattice with primitive cell (**a**, shaded 60°-rhombus) and reciprocal lattice with first Brillouin zone (**b**, shaded hexagon).
Indicated are translation vectors ($\boldsymbol{a}_i$,$\boldsymbol{b}_i$), two-atom basis defining sublattices A (blue dots) and B (red dots), and points of high symmetry in reciprocal space (Γ,M,K,K'). Interatomic spacing is $a = 1.42\,\text{Å}$, with $|\boldsymbol{a}_i| = a\sqrt{3}$ and $|\boldsymbol{b}_i| = 4\pi/(3a)$.

comprising $\chi_n(\boldsymbol{k})$ and satisfy the normalization condition $\chi_n^\dagger(\boldsymbol{k})\chi_n(\boldsymbol{k}) = 1$. However it is only an approximate equality $|c_+(\boldsymbol{k})|^2 + |c_-(\boldsymbol{k})|^2 \approx 1$ since there will be some small but non-zero nearest-neighbor overlap $\langle +, n|-, n\rangle$. In the tight binding calculation however this overlap is neglected.

The tight-binding Hamiltonian is

$$\mathrm{H} = -t \sum_{\langle nm \rangle} (|+, n\rangle \langle -, m| + |-, m\rangle \langle +, n|) \tag{A.3}$$

which connects nearest-neighbors indexed by sites $\langle nm \rangle$ by the transfer integral $t \approx 2.8\,\text{eV}$ [23]. Note that nearest-neighbor interaction only allows hopping between sublattices. To solve for the coefficients $c_\pm(\boldsymbol{k})$, we first apply the Hamiltonian onto the eigenstate $|\psi, \boldsymbol{k}\rangle$ which is just $E(\boldsymbol{k})\,|\psi, \boldsymbol{k}\rangle$. Braketing this with $\langle \pm, n|$ gives

$$E(\boldsymbol{k})\,\langle \pm, n|\psi, \boldsymbol{k}\rangle = \frac{1}{\sqrt{2N}} E(\boldsymbol{k}) e^{i\boldsymbol{k}\cdot R_n} c_\pm(\boldsymbol{k}). \tag{A.4}$$

Now we calculate the same overlap $\langle \pm, n|\,\mathrm{H}\,|\psi, \boldsymbol{k}\rangle$ but by applying the Hamiltonian to the left on $\langle \pm, n|\,\mathrm{H}$,

$$\langle \pm, n|\,\mathrm{H} = -t(\langle \mp, n| + \langle \mp, n'| + \langle \mp, n''|) \tag{A.5}$$

where the first term is due to the nearest neighbor at the same lattice site $\boldsymbol{R}_n$ and the remaining terms are from the nearest neighbors in adjacent lattice sites n', n''. For the A

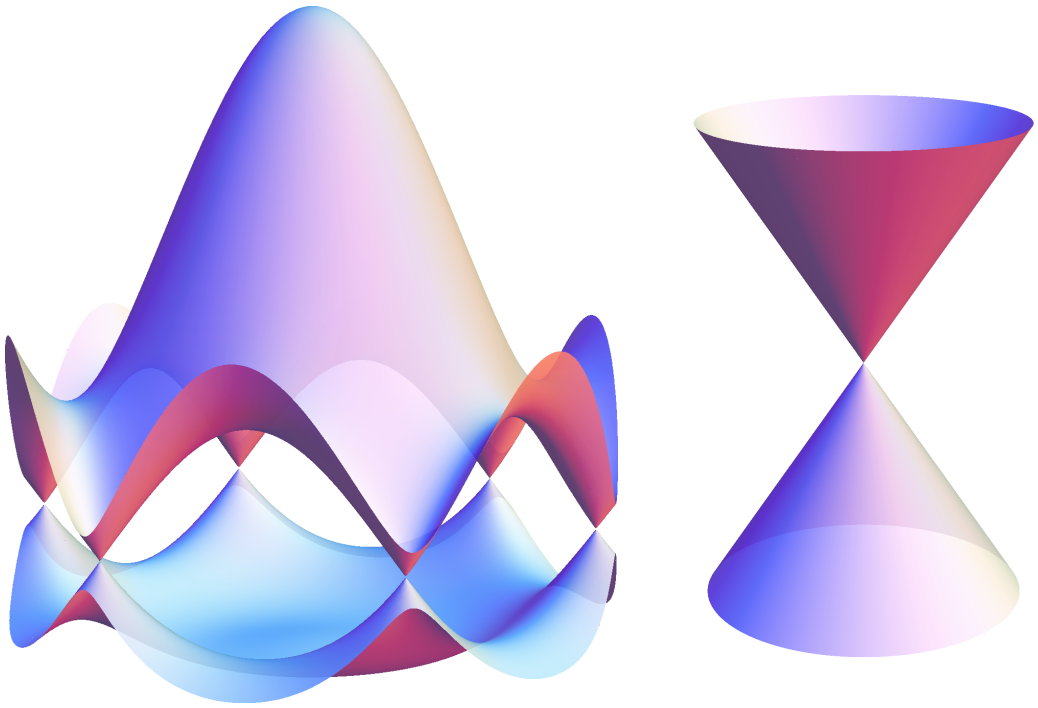

(a) Full Brillouin zone (b) Dirac cone (K,K' point)

Figure A.2: Next-nearest tight-binding band structure of graphene.
Six conical regions are K and K' points in Brillouin zone, referred to as Dirac cones.

(+) atoms (blue dots in Fig. A.1(a)), n' and n'' index the unit cells shifted by $-\boldsymbol{a}_1$ and $-\boldsymbol{a}_2$ from site $\boldsymbol{R}_n$. For the B (−) atoms (red dots), n' and n'' index unit cells shifted by $+\boldsymbol{a}_1$ and $+\boldsymbol{a}_2$. We then apply $\langle \pm, n|\,\mathrm{H}$ to $|\psi, \boldsymbol{k}\rangle$,

$$\langle \pm, n|\,\mathrm{H}\,|\psi, \boldsymbol{k}\rangle = \frac{-t}{\sqrt{2N}} e^{i\boldsymbol{k}\cdot\boldsymbol{R}_n}\left(1 + e^{\mp i\boldsymbol{k}\cdot\boldsymbol{a}_1} + e^{\mp i\boldsymbol{k}\cdot\boldsymbol{a}_2}\right) c_{\mp}(\boldsymbol{k}) \tag{A.6}$$

and equating the two expressions for $\langle \pm, n|\,\mathrm{H}\,|\psi, \boldsymbol{k}\rangle$, Eqs. A.4 and A.6, we have

$$E(\boldsymbol{k}) c_{\pm}(\boldsymbol{k}) = -t\left(1 + e^{\mp i\boldsymbol{k}\cdot\boldsymbol{a}_1} + e^{\mp i\boldsymbol{k}\cdot\boldsymbol{a}_2}\right) c_{\mp}(\boldsymbol{k}). \tag{A.7}$$

By defining $f(\boldsymbol{k}) = 1 + e^{-i\boldsymbol{k}\cdot\boldsymbol{a}_1} + e^{-i\boldsymbol{k}\cdot\boldsymbol{a}_2}$, the Hamiltonian in the $|\pm, n\rangle$ basis can be written

$$\mathrm{H}(\boldsymbol{k}) = \begin{pmatrix} 0 & -tf(\boldsymbol{k}) \\ -tf^*(\boldsymbol{k}) & 0 \end{pmatrix} \tag{A.8}$$

which is easily diagonalized to give the eigenvalues

$$E(\boldsymbol{k}) = \pm t\sqrt{3 + 2\cos(k_x a\sqrt{3}) + 4\cos(k_x a\sqrt{3}/2)\cos(3k_y a/2)}, \tag{A.9}$$

where the + sign refers in this case to the conduction band and the − to the valence band.

A plot of the band structure is shown in Figure A.2, where next-nearest neighbor interactions have also been included [23]. The six points of intersection are the K and K' points and are located at zero energy. These points define the Fermi surface and separate the valence and conduction bands.

To simplify the Hamiltonian further and determine the coefficients $c_{\pm}(\boldsymbol{k})$, define $\theta(\boldsymbol{k})$ such that $f(\boldsymbol{k}) = E(\boldsymbol{k})e^{i\theta\boldsymbol{k}}$. Then the Hamiltonian can be rewritten

$$\mathrm{H}(\boldsymbol{k}) = |E(\boldsymbol{k})| \begin{pmatrix} 0 & e^{-i\theta(\boldsymbol{k})} \\ e^{i\theta(\boldsymbol{k})} & 0 \end{pmatrix} \tag{A.10}$$

from which one can easily solve for $c_{\pm}(\boldsymbol{k})$ and obtain the pseudospinor

$$\chi_n(\boldsymbol{k}) = \begin{pmatrix} 1 \\ \pm e^{i\theta(\boldsymbol{k})} \end{pmatrix}_n, \tag{A.11}$$

where the signs refer to the conduction band (+) and valence band (−). The total wavefunction can then be written

$$|\psi, \pm, \boldsymbol{k}\rangle = \frac{1}{\sqrt{2N}} \sum_n e^{i\boldsymbol{k}\cdot\boldsymbol{R}_n} \begin{pmatrix} 1 \\ \pm e^{i\theta(\boldsymbol{k})} \end{pmatrix}_n. \tag{A.12}$$

A.2 Dirac Equation

In order to analyze the low-energy excitations, we need to expand the Hamiltonian H at the Dirac points K and K' where the energy is zero. The locations of theses points are

$$\mathbf{K} = \frac{1}{3}(\boldsymbol{b}_1 - \boldsymbol{b}_2) \tag{A.13}$$

$$\mathbf{K}' = \frac{1}{3}(\boldsymbol{b}_2 - \boldsymbol{b}_1) \tag{A.14}$$

so that their components parallel to the space lattice vectors $\boldsymbol{a}_i$ are

$$\mathbf{K} \cdot \boldsymbol{a}_1 = 2\pi/3 \qquad \mathbf{K} \cdot \boldsymbol{a}_2 = -2\pi/3 \tag{A.15}$$

$$\mathbf{K}' \cdot \boldsymbol{a_1} = -2\pi/3 \qquad \mathbf{K}' \cdot \boldsymbol{a_2} = 2\pi/3. \tag{A.16}$$

We can now calculate $f(\boldsymbol{k})$ for small wavevectors $\boldsymbol{q}$ near the K and K' points $\boldsymbol{k}_+ = \mathbf{K} + \boldsymbol{q}$, $\boldsymbol{k}_- = \mathbf{K}' + \boldsymbol{q}$,

$$f(\boldsymbol{q}) = 1 + e^{\pm i2\pi/3} e^{-i\boldsymbol{q}\cdot\boldsymbol{a}_1} + e^{\mp i2\pi/3} e^{-i\boldsymbol{q}\cdot\boldsymbol{a}_2} \tag{A.17}$$

$$\approx 1 + e^{\pm i2\pi/3}(1 - i\boldsymbol{q}\cdot\boldsymbol{a}_1) + e^{\mp i2\pi/3}(1 - i\boldsymbol{q}\cdot\boldsymbol{a}_2) \tag{A.18}$$

$$= \mp\frac{\sqrt{3}}{2}\boldsymbol{q}\cdot(\boldsymbol{a}_1 - \boldsymbol{a}_2) + \frac{i}{2}\boldsymbol{q}\cdot(\boldsymbol{a}_1 + \boldsymbol{a}_2) \tag{A.19}$$

and substituting in $\boldsymbol{a}_i$,

$$f(\boldsymbol{q}) = (\mp q_x + iq_y)3a/2. \tag{A.20}$$

The energy corresponding to the wavevector $\boldsymbol{q}$ is found by substituting into $E(\boldsymbol{q})$ in Eq. A.7 to obtain $E(q) = \pm\hbar c^* q$ where the effective speed of light $c^* = 3ta/2 \approx c/300$. This is the linear energy dispersion characteristic of massless particles.

To finally show that the Hamiltonian is the massless Dirac, or Weyl, equation describing massless spin-half particles, we rewrite it at the K point using the expansion for $f(\boldsymbol{q})$,

$$\mathrm{H}(\boldsymbol{q}) = \hbar c^* \begin{pmatrix} 0 & q_x + iq_y \\ q_x - iq_y & 0 \end{pmatrix} = \hbar c^* \boldsymbol{\sigma}\cdot\boldsymbol{q} \tag{A.21}$$

with a similar equation for the states at the K' point. In the last equality the Pauli matrices have been used to put it in a form identical to the Weyl equation describing massless spin-half neutrinos. The analog of spin for the massless Dirac fermions in graphene is the pseudospin χ describing the weight of the wavefunction on the A and B sublattice. From here on all of the methods and results of relativistic quantum mechanics can be applied, with c^* the effective speed of light and the role of spin replaced by pseudospin [64].